Utah Center for Water Resources Research
Annual Technical Report
FY 2015

Introduction

The Utah Center for Water Resources Research (UCWRR) is located at Utah State University (USU), the Land Grant University in Utah, as part of the Utah Water Research Laboratory (UWRL). It is one of 54 state water institutes that were authorized by the Water Resources Research Act of 1964. Its mission is related to stewardship of water quantity and quality through collaboration with government and the private sector.

The UCWRR facilitates water research, outreach, design, and testing elements within a university environment that supports student education and citizen training. The UCWRR actively assists the Utah Department of Environmental Quality (UDEQ), the Utah Department of Natural Resources (UDNR), the State Engineers Office, all 12 local health departments, and several large water management agencies and purveyors in the state with specific water resources problems. In FY 15, the UWRL expended a total of nearly $10 million in water research support. USGS Section 104 funds administered through the UCWRR accounted for approximately one percent of this total. These funds were used for research addressing water management problems, outreach, information dissemination, strategic planning, water resources, and environmental quality issues in the State of Utah. Five research projects were funded in FY15 with USGS 104 funds. These projects are respectively entitled, (1) "Estimating Crop Water Use with Remote Sensing: Development of Guidelines and Specifications," (2) "Capturing Aerial Imagery on the San Rafael River, Utah, using an Unmanned Aerial Vehicle (UAV) to Monitor and Assist in Evaluating Restoration Efforts," (3) "Managing Western Irrigation systems in the Face of Urbanization," (4) "Information Systems for Landscape Water Conservation," and (5) "Biofiltration of Utah Municipal Drinking Water."

These projects dealt with the following water management issues: (1) Developing a framework for estimating crop water use using remote sensing through a standardized approach, thus providing guidelines and specifications for applying certain evapotranspiration (ET) models and producing ET products that are acceptable to the USGS WaterSmart program and the scientific and user community; (2) Using an inexpensive unmanned aerial vehicle (UAV) to provide high resolution, up to date aerial imagery in support of restoration schemes ongoing in the San Rafael River in South Central Utah and determining the accuracy and limitation of this platform for providing digital elevation and terrain models in place of more conventional, and more expensive, approaches; (3) Identifying key opportunities and challenges faced by irrigation companies as they adapt to changes in land use and urban pressure and helping them understand and adapt to changes associated with the urbanization of an irrigated agricultural landscape; (4) Developing methods for analyzing historical water billing data to assist cities, counties, and state agencies in reducing municipal water demand throughout the State of Utah, and (5) Evaluating biofiltration as an effective way to reduce organic matter and potential disinfection by-product production in Utah drinking water. These projects all involved collaboration of local, state, and federal water resources agency personnel.

Research Program Introduction

Irrigated agriculture is the largest consumptive water user in the western United States. Estimates of crop water use can be improved through more accurate evapotranspiration (ET) estimates. A USGS-supported research project developed a framework for estimating crop water use using remote sensing through a standardized approach that provided guidelines and specifications that, if followed in order, could be applied to certain models and produce ET products that are acceptable to the USGS WaterSmart program and the scientific and user community. This research reviewed and tested candidate remote sensing–based ET models to establish model performance and determine the uncertainty associated with the application of these models. A set of study sites was selected from within the 17 western United States representing different climatic regions, and a variety of spatial and point datasets were utilized. A meeting was held with USGS personnel to discuss the findings. This work could benefit many hydrological modeling and water resources management applications.

Another USGS-funded project is using AggieAir high-resolution multi-spectral imagery (RGB, NIR, and thermal imagery) of the lower San Rafael River to provide valuable information to the San Rafael Restoration Committee and the Utah Division of Wildlife Resources in support of ongoing river restoration projects. The imagery provides spatial information regarding thermal refugia and detailed channel information for restoration projects in this region including efforts to restore the river to a more ecologically acceptable state, provide more comprehensive complex native fish habitat, encourage change in channel morphology through Tamarisk removal, and remove man-made barriers to enhance and encourage fish movement/passage throughout the entire drainage. Temperature probes were installed to assist in calibrating the thermal imagery. This project was delayed due to severe low flow conditions in the San Rafael River for several months in the summer 2013 and then higher than expected flows during the summer of 2014. In 2015, a total of nine UAS flights were successfully completed along 55 river miles of the San Rafael River, South-Central Utah to capture a combination of imagery, including RGB, NIR, and thermal.

One USGS-supported project was designed to help local canal and irrigation companies in Northern Utah better understand and adapt to changes associated with the urbanization of an irrigated agricultural landscape. The project objectives included documenting the diverse characteristics of representative shareholders of irrigation companies along a gradient of urbanizing environments, investigating the ways farmer and non-farming shareholders manage secondary water allocations, and identifying the key opportunities and challenges faced by irrigation companies as they adapt to changes in land use and urban pressure. In 2015, a multi-wave mail survey of a random sample of irrigation company shareholders was implemented throughout the summer and fall. Results of the surveys were presented to collaborating irrigation companies and made available on USU’s Digital Commons.

In collaboration with Salt Lake County, Salt Lake City, Sandy City, and the Division of Water Resources in the Utah Department of Natural Resources, A USGS funded project is developing methods for analyzing historical water billing data, acquired from water providers, for identifying water customers with a high capacity to conserve landscape irrigation water. Coupling historical water billing data with the size of specific properties will allow a reasonable estimate of appropriate water use to be made. This information can then be used by cities, counties, and the Division of Water Resources to support efforts to reduce municipal water demand throughout the state. This project completed the first phase of the overall objectives by developing the appropriate database and information systems that will allow for enhanced analysis of relevant data and of water use to help guide water conservancy districts and utilities in their conservation efforts.

Biofiltration of drinking water supplies is a promising method to reduce the potential for production of disinfection by-products and to minimize the regrowth of microorganisms in water distribution systems. A final USGS-funded project investigated biofiltration as an effective way to reduce organic matter from Utah

source waters and reduce potential disinfection by-product production. ATP measurements were also correlated with CBXA as a potential surrogate measure of biological activity and organic compound treatment efficiency. Because of the site specific nature of the implementation of this technology, the proposed project studied, at pilot scale, the potential for using biofiltration for reducing and modifying the organic matter content of drinking water at two Utah water utilities and developed preliminary information pertaining to the design and operation of such utilities.

These projects all involved collaborative partnerships throughout the state with various local, state, and federal agencies.

Estimating Crop Water Use with Remote Sensing: Development of Guidelines and Specifications

Basic Information

Title:	Estimating Crop Water Use with Remote Sensing: Development of Guidelines and Specifications
Project Number:	2011UT164S
USGS Grant Number:	G11AP20229
Sponsoring Agency:	
Start Date:	9/19/2013
End Date:	9/30/2015
Funding Source:	Supplemental
Congressional District:	
Research Category:	Climate and Hydrologic Processes
Focus Category:	Water Use, Agriculture, Methods
Descriptors:	satellite remote sensing, crop water use
Principal Investigators:	Christopher M.U. Neale

Publications

1. Lewis, Clayton; Hatim M. E. Geli, and Christopher M. U. Neale, 2014, Comparison of the NLDAS Weather Forcing Model to Agrometeorological Measurements in the western United States, Journal of Hydrology, Vol. 510, pp. 385-392. DOI: 10.1016/j.jhydrol.2013.12.040.
2. Hobbins, M; H. M. E. Geli; C. S. Lewis; G. Senay; and J. Verdin, 2013, NOAA introduces its first-generation reference evapotranspiration product, poster presented at 2013 Fall Meeting, AGU, San Francisco, California, 9-13 Dec.
3. Lewis, Clayton; Hatim M. E. Geli, and Christopher M. U. Neale, 2014, Comparison of the NLDAS Weather Forcing Model to Agrometeorological Measurements in the western United States, Journal of Hydrology, Vol. 510, pp. 385-392. DOI: 10.1016/j.jhydrol.2013.12.040.
4. Hobbins, M; H. M. E. Geli; C. S. Lewis; G. Senay; and J. Verdin, 2013, NOAA introduces its first-generation reference evapotranspiration product, poster presented at 2013 Fall Meeting, AGU, San Francisco, California, 9-13 Dec.
5. Lewis, Clayton; Hatim M. E. Geli, and Christopher M. U. Neale, 2014, Comparison of the NLDAS Weather Forcing Model to Agrometeorological Measurements in the western United States, Journal of Hydrology, Vol. 510, pp. 385-392. DOI: 10.1016/j.jhydrol.2013.12.040.
6. Hobbins, M; H. M. E. Geli; C. S. Lewis; G. Senay; and J. Verdin, 2013, NOAA introduces its first-generation reference evapotranspiration product, poster presented at 2013 Fall Meeting, AGU, San Francisco, California, 9-13 Dec.
7. Lewis, Clayton S., 2016, Evapotranspiration Estimation: A Study of Methods in the Western United States, Ph.D. Dissertation, Civil and Environmental Engineering, College of Engineering, Utah State University, Logan, Utah, 133.
8. Lewis, Clayton S., Hatim M.E. Geli, Christopher M.U. Neale, James P. Verdin, and Gabriel Senay, 2015, Comparison of the NLDAS Weather Forcing Model with Ground-Based Measurements over

Agricultural Areas Throughout the Western United States, 2015 Spring Runoff Conference, April 2015, poster.

Estimating Crop Water Use with Remote Sensing: Development of Guidelines and Specifications

(USGS Award No G11AP20229)
(2011UT164S)

PART 1

Remote Sensing of Evapotranspiration:

A Review of Models

PART 2

Remote Sensing of Evapotranspiration:

Model Inter-comparison

Hatim M. E. Geli
Department of Civil and Environmental Engineering
Utah State University
Logan, Utah

Christopher M. U. Neale
Daugherty Water for Food Institute
University of Nebraska
Lincoln, Nebraska

Feb 2016

PART 1

Remote Sensing of Evapotranspiration:

A Review of Models

Hatim M. E. Geli
Department of Civil and Environmental Engineering
Utah State University
Logan, Utah

Christopher M. U. Neale
Daugherty Water for Food Institute
University of Nebraska
Lincoln, Nebraska

May 2015

Table of Contents

List of Tables

List of Figures

1. INTRODUCTION

1.1. Definitions

The definitions provided herein are meant to differentiate between the different processes with respect to the transformation of water to vapor state that can generally be defined differently in the literature.

Evaporation (*E*) is the process by which liquid water transforms into vapor and into the atmosphere expressed in terms of mm day^{-1} unless stated otherwise. It includes evaporation from bare soil, wet or dry and all types of water bodies e.g. lakes, ponds, rivers, and intercepted water by plant leaves.

Transpiration (*T*) is the process by which liquid water in the soil strata that is extracted by plant roots moves into the atmosphere through plants stomata as it changes state into water vapor, expressed in terms of mm day^{-1}, unless stated otherwise.

Evapotranspiration (*ET*) as it is practically difficult to separate evaporation and transpiration over surfaces covered with mixed bare soil and vegetation, ET can be defined as the combined process of evaporation and transpiration expressed in terms of mm day^{-1}, unless stated otherwise. ET is the equivalent to the term latent heat flux (*LE* or λE) defined in terms of energy units as W m^{-2} with λ represents latent heat of vaporization of water in MJ kg^{-1}.

Potential Evaporation is the rate of evaporation from an idealized extensive open water body under existing atmospheric conditions.

The *reference evapotranspiration* can be defined as the rate of *ET* from a reference surface specifically an extensive short green cover with a uniform height actively growing and completely shading the ground and not limited of water availability. These conditions defined in literature for a reference grass crop with fixed crop height of 0.12 m, an albedo of 0.23, and surface resistance of 69 s m^{-1} with reference *ET* denoted as ET_o. However, other studies indicated the use of alfalfa as a reference cover with reference *ET* denoted as ET_r and generally is 15-20% larger than grass *ET*.

Consumptive water use (Agriculture) is referred to the amount of water consumed by agricultural activities that cannot be returned or reused. It includes the evaporated water (in terms of or ET) used for crop production. The consumptive water use in irrigation can be identified by subtracting the water returned to the system through runoff and drainage from the total withdrawal.

1.2. Rationale

Consumptive water-use from agricultural activities such as irrigation can be accounted for mainly through estimates of *ET.* In the United States the consumptive water-use in terms of

irrigation represents about 31% of the all water uses. Hence the knowledge of the total amount of ET with a reasonable accuracy plays a great role for better managing valuable water resource. Based on a recent report by the USGS (Kenny et al. 2009), the trend in the water-use in the US for the period 1950-2005 indicated an127% increase in the total amount of water withdrawals with irrigation water diversions representing the second largest increase of about 43%, related to the 100% growth in population. Note that these water-use reports are based on data collected as part of the National Water Use Information Program (NWUIP), compiled by the US Geological Survey (USGS), and provided as a five-year water-use summary at the national level since 1950. Apparently most of this increase in water withdrawals can be attributed to irrigation activities weighted in the 17 western States. About 80% of total water withdrawal in 2005 were from surface water and the remaining 20% were from groundwater sources. Water used for irrigation accounted for 31% of the total withdrawals and about 58% of the total irrigation withdrawals was from surface water sources. The irrigation water withdrawals from the 17 western States accounted for 85% of that total water withdrawal and corresponds to about 74% of the total irrigated area in the US.

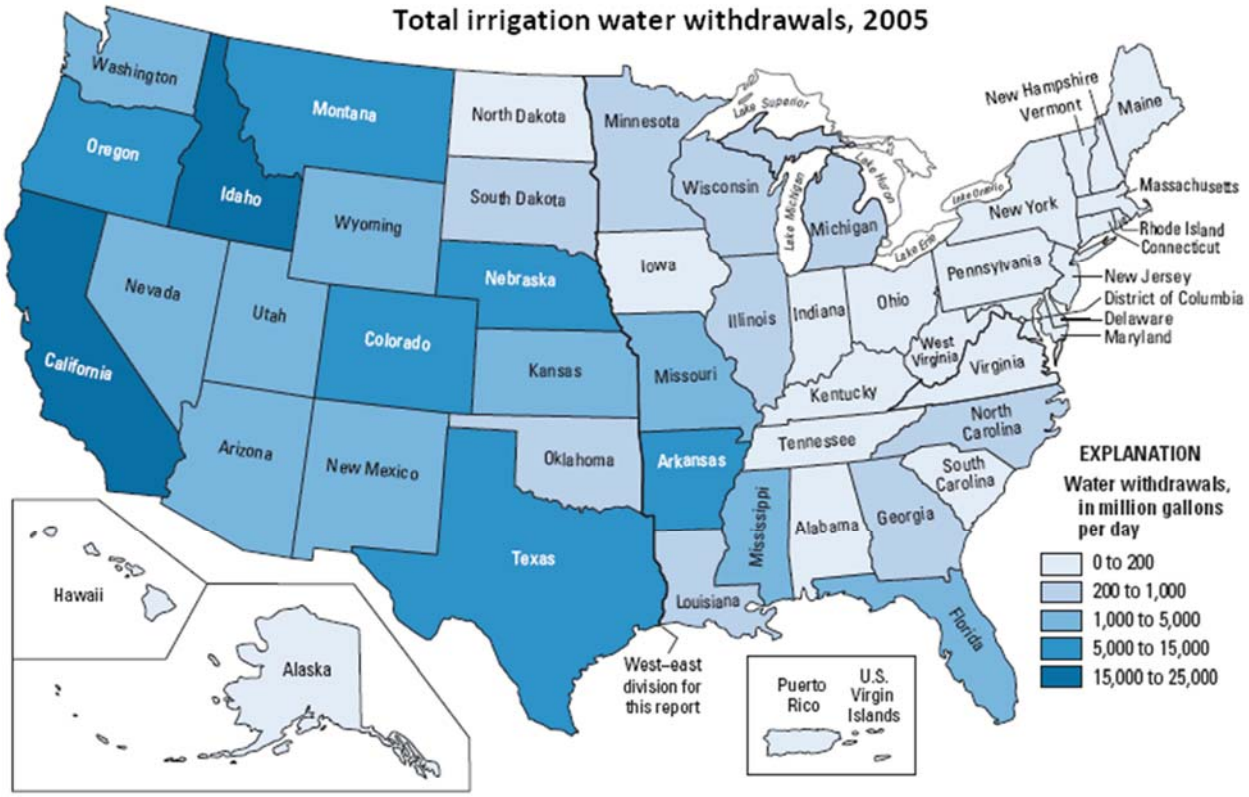

Figure 1: The total water-use for irrigation in the US (reprint from Dickens et al. (2011))

An important observation about the reported water-use as indicated by Dickens et al. (2011)is the inherent inconsistency among the methods used to estimate irrigated withdrawals and their associated uncertainties. Usually water-use information for irrigated agriculture is collected from different sources. The USGS receives information from their representative Water Science Centers (WSCs) which in turn collect information from the individual States at the county level through their respective Division of Water Resources, government agencies as the US Bureau of

Reclamation, river compacts, universities, and others. Reports indicated that different methodologies have been followed to estimate consumptive water-use which are generally based on ET combined with estimates of irrigated acreage. Reported methods included mainly traditional approaches such as a modified Blaney-Criddle method, crop coefficient combined with reference ET approach and meteorological measurements of ET and generally a combination of these methods. Recent activities by some individual States have explored the use of remote sensing approaches, as shown later, which also include a variety of methods that can be used. Most of these method require information about the irrigated acreage which mainly is obtained from the National Agricultural Statistics Service, Census of Agriculture, and Farm and Ranch Irrigation Survey. Uncertainty and inconsistency are evident either at the level of the reported irrigated acreage or the overall method of estimating irrigation withdrawals (Dickens et al. 2011).

However, the usefulness of this water-use information and understanding the challenges to meet the increasing demand due to a growing population and irrigation withdrawals is acknowledged by USGS. By moving forward research and evaluation for managing and predicting future water resources in the US, a major activity is underway by the USGS for improving the quantification of consumptive water-use for irrigated agriculture based on estimates of ET. This activity is carried out by the USGS to comply with the Sustain and Manage America's Resources for Tomorrow program WaterSMART, initiated by the US Department of Interior in 2010 and can also be considered part of the National Water Census. With the availability of numerous sources of remote sensing data that are housed and managed by the USGS and, considering the advances in the use of remote sensing tools for estimating ET, this represents the main theme of this research activity.

The emerging knowledge base of remote sensing and its application in vegetation monitoring potentially provides a promising method for non-traditional monitoring of ET at different spatial and temporal scales. Over the past two decades, remote sensing has made a significant impact in leveraging our understanding of the ET process and in how to provide a more accurate estimates. Note that traditional methods for estimating ET aided with ground-based weather data are still used at field scales and in some cases at regional scales. However, the spatial nature of the ET process imposes some challenges for its estimation at regional scales that could lead to a reduced level of accuracy. Alternatively, remote sensing data are able to capture spatial and temporal variability allowing for better total estimates of ET.

Remote sensing data are provided from a suite of sensors managed by the USGS since 1970's. These sensors, which have been used for estimating ET over agricultural areas, include the Landsat family with its high spatial resolution imagery with a 16-days recurrence. The Landsat sensors include the Multispectral Scanner (MSS) and Thematic Mapper (TM) on Landsat 4 and 5, the Enhanced Thematic Mapper Plus (ETM+) or Landsat 7, and the Operational Land Imager (OLI) or Landsat 8. A relatively coarser resolution sensor includes the Moderate Resolution Imaging Spectroradiometer (MODIS) with a recurrence of 1-2 days. A high recurrence sensor of 15-minute and a coarser spatial resolution of 5-10 km is the Geostationary Operational Environmental Satellite (GOES). All these sensors provide different types of information including surface multispectral reflectance and surface temperature that are sensitive

to plant growth and other relevant changes. All of the above sensors have been explored for the remote sensing of ET either separately or combined from local to field scales.

There are different remote sensing based models available that can be used with these wide range of data to provide estimates of ET. These models range from physically based relatively complex nonlinear models to empirical simple linear models and mixed physical- empirical-based approaches. Some of the methods used include: energy balance at the surface to calculate the latent heat flux, λE, at instantaneous time steps– at the time of image acquisition. Such models usually use radiometric surface temperature (T_R) measured by satellites as a lower boundary condition to estimate sensible heat flux, H, with λE estimated as a residual of the surface energy balance. Another group of models uses aerodynamic resistance approach to directly estimate *ET*. This basically include those models which use Penman-Montieth (P-M) and Priestly-Taylor (P-T) equations. These two groups can be considered as physically based models. A third group of models uses empirical or semi-empirical approaches including the crop coefficient method. A suggested classification of existing models is provided in Section 2.

The availability of these remote sensing data and models allowed different entities to explore their potential for estimating consumptive water-use. Local businesses and government agencies are already implementing remote sensing of *ET* methods such as the U.S. Bureau of Reclamation with its application at Sacramento, CA (Eckhardt 2010). While some States are still using traditional methods for estimating ET such as the Blaney-Criddle method, others are already implementing remote sensing based methods of ET and consumptive use. Examples of such applications include the Idaho Department of Water Resources, Idaho (Allen and Robison 2007), Nevada Division of Water Resources, Nevada (Huntington and Allen 2010). However, major concerns in the application of these non-traditional estimates of ET with respect to differences among methods arises from a) difficulties in applying an integrated river basin water resources management, b) duplication of effort, and certainly c) the related different levels of accuracy for which there is no general agreement yet. The Colorado River basin can be considered an example to further highlight all these issues. As the Colorado River basin encompasses 7 States including Wyoming, Utah, Colorado, New Mexico, Arizona, Nevada and California, an agreement among the States is in place for the allocation of water resources (e.g. Colorado River Compact and the Upper Colorado River Basin Compact). The agreement mainly covers management and allocation of available water resources based on historic water use to meet obligations of all States. River Compact Commission would be providing estimates of ET for the different States while individual States are also required to provide such estimates. Due to the different methods for estimating ET by these different entities the issues above are evident and inevitable unless agreement on approaches and methods for estimating ET via remote sensing is reached.

In this sense, the USGS as part of the WaterSMART is conducting a review of remote sensing methods for estimating ET and consumptive water-use. As there are several models available in literature that can be used for such application, this review considered only a few of them. These models include the two-source energy balance (TSEB) (Kustas and Norman 1999a, b; Norman et al. 1995), the Atmosphere-Land Exchange Invers (ALEXI) (Anderson et al. 1997; Mecikalski et al. 1999), the Disaggregated Atmosphere-Land Exchange Invers (DisALEXI) (Norman et al. 2003), the Mapping Evapotranspiration with Internalized Calibration (METRIC)

(Allen et al. 2007a; Allen et al. 2007b), the Hybrid evapotranspiration (Hybrid ET) (Neale et al. 2012), the MODIS evapotranspiration (MODIS ET) (Mu et al. 2007; Mu et al. 2011), the Simplified Energy Balance System (SEBS) (Su 2002), the Simplified Surface Energy balance (SSEB) (Senay et al. 2011; Senay et al. 2008), and the Priestly-Taylor evapotranspiration (PT-JPL) (Fisher et al. 2008).

The intent of this review is to provide a detailed description of selected candidate models for remote sensing of ET. The review includes description of the model structure and their parameterization, the required input data, the intended use, a general comparison of the models with regards to the objectives of the USGS for crop water use estimates.

2. A CLASSIFICATION OF MODELS

There are several attempts that have aimed to provide a reasonable classification of models that particularly use remote sensing to estimate *ET*. Different classification criteria can be used e.g. some are process-based, method of solution approaches, spatial data analysis and other types of classifications exist in literature. The review by Courault et al. (2005) considered all remote sensing models and suggested four classes that included empirical, residual energy balance, deterministic, and vegetation index. From their definition for each group one can provide a broad classification as empirical, physically-based, and mixed physical and empirical-based classes. Kalma et al. (2008) reviewed models that particularly use thermal remote sensing and they also suggested four major groups including surface energy balance, time rate of change in surface temperature, spatial variability, and direct estimate of *ET* from surface temperature and weather data methods. Similarly, these groups can be collapsed into the three broad methods indicated above. Based on the process criteria the remote sensing of *ET* models can generally be classified into three broad categories as physically-based models, empirical or black box models, and semi-physical semi-empirical, or simply mixed, models. Note that even with this classification a distinct separation between these groups might not be evident. Since with the use of remote sensing there are some empirical relationships need to be included especially with estimation of some biophysical variables such as leaf area index and canopy height that are used to calculate aerodynamic and surface resistances.

2.1. Physically-Based Models

This type of models basically attempts to provide a physical representation of the process under consideration as it occurs in nature--in this case it would be *ET* through modeling the mass/energy exchange at the soil-vegetation atmosphere continuum. Such models usually use the analog of electrical resistance networks for modeling the turbulent H and λE or ET. There are two main groups that can be identified under this category; the first group suggested, or assumes, the use the concept of big leaf (or one-source) to model the mass/energy exchange at the surface. This one-layer approach mainly indicates that the surface needs to be a fairly homogeneous extended horizontal cover. This one-source modeling group can further be classified into: surface energy balance, aerodynamic and surface resistances, and water-energy balance approaches. Example of one-layer models include METRIC, SEBS, and the Hybrid ET. The other group include those recommending and supporting the use of two-source, or in general a multi-source

approach, for modeling the mass/energy exchange at the surface. This group suggests treating surface features separately- bare soil and canopy. Some models allow for interaction between each surface component at some level above the surface while others do not. The rationale behind the multi-source approach is that some surfaces exhibit a level of heterogeneity to the degree that a distinct surface component can be identified. Hence modeling of mass/energy exchange at near-surface atmosphere with the individual features is achievable. However, this approach has also been successfully applied over homogenous surfaces. Example of such models include the TSEB and its descendant ALEXI/DisALEXI approach, MODIS ET, and PT-JPL. As there are many other models that can be included (Courault et al. 2005; Kalma et al. 2008) we limited our examples to those candidate models to this review.

Surface Energy Balance

This type of model is based on the surface energy balance described as

$$Rn = \lambda E + H + G \qquad 2.1.1$$

where Rn is the net radiation (W m^{-2}), G the soil heat flux (W m^{-2}), λE the latent heat flux (W m^{-2}), H the sensible heat flux (W m^{-2}). Canopy heat storage and photosynthesis terms are typically ignored as they are small in comparison to the other terms for most agricultural canopies. Variation between models appear in the way they estimate each of these components. Despite these differences the general notion is that most models tend to provide estimates of Rn and G fairly well with relatively similar level of accuracy. Challenges arises in modeling turbulence heat fluxes H and λE and here lies the differences between the two major groups of one- and two-source modeling approaches. Agreement among these models in providing estimates of Rn using physically based approach which include the use of the incoming shortwave and longwave radiation balance with a simple form used in METRIC and SEBS and a more complex form in TSEB. There is, however, have some level of empiricism in most of these modes as for example in estimating solar transmittance, surface emissivity and other surface properties such as albedo.

One-layer models include METRIC and SEBS with the main difference in the approach for estimating H but applying the general concept of defining upper and lower limits for turbulent heat fluxes. These limits are (1) dry condition where λE approaches 0 and (2) well-watered vegetation conditions were H approaches 0. While METRIC estimates λE as a residual of the surface energy balance equation (see Section 3.4), SEBS uses the concept of evaporative fraction (Section 3.5). An example of a two-layer modeling approach is the TSEB and its descendant ALEXI/DisALEXI. In these models a Priestly-Taylor (PT) equation is used to calculate λE over the canopy at the potential rate and adjusted as needed and the soil component of λE is calculates as a residual of the energy balance.

Aerodynamic and Surface Resistance Approach

This type of model uses mainly a network of resistances to estimate ET. An example of such models is the Penman-Monteith (P-M) equation which can be described

$$\lambda E = \frac{s \cdot A + \rho \cdot C_p \cdot (e_{sat} - e)/r_a}{s + \gamma \cdot (1 + r_s/r_a)} \qquad 2.1.2$$

where e_{sat} the saturated vapor pressure, s the rate of change in e_{sat} to air temperature, A the available energy partitioned between H, λE, and G, ρ the air density, C_p specific heat capacity of air, r_a the aerodynamic resistance, γ the psychrometric constant, r_s the surface resistance.

One of the remote sensing based models that uses P-M equation as the main modeling structure is MODIS ET. While the P-M equations treats the surface as a one-source layer, the MODIS ET approach assumes that the surface consists of multiple sources and applies the P-M model for each to calculate the total ET. The main challenge with such approach lies in the estimation of the different resistances. Deriving estimates of these resistances using remote sensing would still require large amount of information about the specific features on the surface (Section 3.7).

Energy and Water Balance

This group of models tends to couple energy and water balance approaches to estimate ET. Usually, the energy balance approach is used in a diagnostic manner to provide estimates of surface energy balance fluxes (SEBF) at discrete instances in time when remotely sensed inputs are available. Such approach would leave some gaps in estimated ET if Landsat imagery were used. While MODIS provides almost daily maps of earth's surface, it has coarser spatial resolution (250 -1000 m) that are not suitable for field scale estimates of *ET*. The common variables estimated by both approaches are generally daily ET and soil water content, used for the coupling process. On the other hand, water balance models tend to provide estimates of ET, and some other state variables depending on the model, in a prognostic way. Hence coupling these two approaches synergistically provides continuous estimates of daily ET and bridges the gap between satellite image acquisitions in the case of Landsat. The coupling process is generally carried out using data assimilation techniques. An example of such coupled energy-water balance approach is the Hybrid ET model described by Geli (2012) and Neale et al. (2012).

2.2. Empirical Models

This group of models tends to provide a direct, and in some cases indirect, relationship between ET and some land surface features such as vegetation indices (VI) and land surface temperature. The former, as an indirect method, uses VI to estimate crop coefficients (Kc) from remote sensing which in turn can be used to describe the fraction of actual ET with respect to a reference ET. This is similar to the approach followed in the water balance model of the Hybrid ET. Courault et al. (2005) identified this approach as inference method. Direct methods include those use radiometric surface temperature or T_R obtained from remote sensing to directly estimate *ET*. Such as the SSEB. Example of other models that follow such approach can be found in Kalma et al. (2008).

2.3. Mixed Models

Mixed models describes a group of models that use physically-based processes mixed with some level of empirical representations to directly estimate ET. Examples include those that use the Priestly-Taylor approach and the S-SEBI model to estimate actual ET. Note that the P-T (Eq. 2.3.1) is actually a simplification of P-M method in which only the available energy term is kept.

$$LE = f_g \alpha_{PT} \frac{\Delta}{\Delta+\gamma} (Rn - G) \qquad 2.3.1$$

where f_g is the fraction of the green cover, α_{PT} the P-T constant taken as 1.26, Δ the slope of the saturation-vapor pressure curve, and γ the psychrometric constant~$0.066\ kPa\ °C^{-1}$.

As it is developed to estimate potential ET, The P-T equation uses the empirical coefficient α_{PT} as 1.26. To provide estimates of actual ET there are some attempt to estimate α_{PT} from remote sensing as summarized by Kalma et al. (2008). Other approaches such as PT-JPL aimed to maintain the original value of α_{PT} and introduced some constraints based on plants physiological limits (Fisher et al. 2008).

3. DESCRIPTION OF CANDIDATE MODELS

A detailed description of the selected candidate models is provided which includes parameterization, required input data, information about the output, example of reported applications and related accuracies particularly over agricultural areas.

3.1. TSEB Model

General

The development of the TSEB by Norman et al. (1995) was motivated by the resistance network formulation of Shuttleworth and Wallace (1985). The model is mainly designed to account for sparse vegetation conditions that most one-layer models have challenges with modeling, especially in water limited conditions. Over such surface conditions, the resistance to sensible heat flow are different over bare soil and canopy components which in turn defies the assumption of a big leaf of one-layer models. The model also accounts for the differences between the radiometric surface temperature and the aerodynamic temperature (Kustas and Anderson 2009; Norman and Becker 1995) that is used in the bulk heat transfer equation. As the former is used instead of the latter, an empirical adjustment is generally used to account for the excess resistance to heat flow as compared to using aerodynamic resistance based on momentum roughness. The TSEB accounts for such differences by calculating sensible heat flux for each component, bare soil and canopy, based on their respective thermodynamic temperature Ts and Tc.

There are two forms of TSEB; parallel and series resistance network formulations. This review describes the latter as the findings from several comparisons between the two formulations indicated insignificant differences in their respective models estimates of SEBF. Also the TSEB model is a major component of the ALEXI, DisALEXI, and the Hybrid ET models described later.

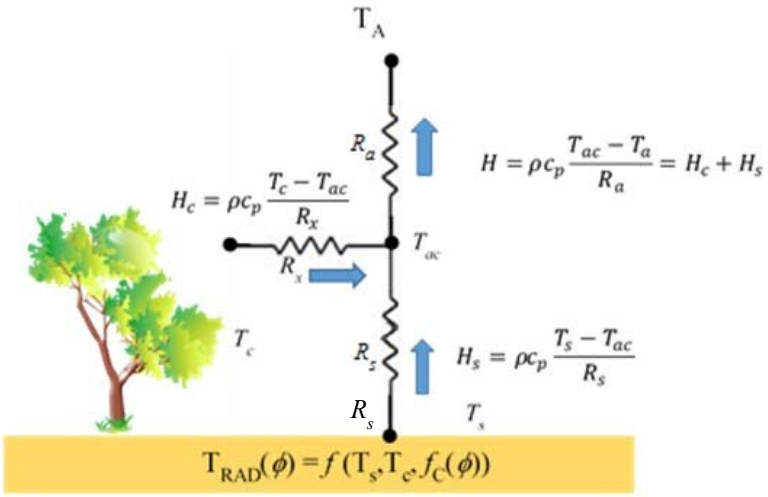

Figure 2: Description of the TSEB model

Model Description

The model treats the bare soil and canopy components of surface energy balance separately. It defines an air-canopy interface at a level above the surface to allow for interaction between each component. By assuming a single emissivity of $\varepsilon(\phi) \cong 0.99$ (Kustas and Norman 1997; Norman et al. 1995) the TSEB makes use of the composite directional radiometric surface temperature T_R to estimate the thermodynamic temperature of soil and canopy T_s and T_c as

$$T_R(\phi) \approx [f_c(\phi)T_c^4(1 - f_c(\phi))T_s^4]^{1/4} \qquad 3.1.1$$

where $f_c(\phi)$ is the fraction of the field of view of the infrared radiometer occupied by vegetation, the subscript s and c refer to soil and canopy components, respectively. The T_R can be estimated from the brightness temperature T_B that is directly measured by a radiometer as

$$T_B(\phi) = [\varepsilon(\phi) \cdot \left(T_R(\phi)\right)^n + (1 - \varepsilon(\phi) \cdot (T_{SKY}^n)]^{1/n} \qquad 3.1.2$$

with T_{SKY} being the hemispherical temperature of the sky and $n \approx 4$. The angular variation in $\varepsilon(\phi)$ is ignored because of the insignificant variations of < 0.005 for view angles between nadir to 60° (Kustas and Norman 1997). Also the use of a single emissivity for soil and canopy has a

minimal effect on the estimated temperatures T_s and T_c as multiple scatter appear to equalize the component emissivity (Anderson et al. 1997; Kustas and Norman 1997).

The directional fraction of vegetation cover, $f_c(\phi)$, can be estimated as a function of the radiometer view zenith angle (ϕ) as

$$f_c(\phi) = 1 - \exp\left(\frac{-0.5 \cdot \Omega(\phi) \cdot LAI}{\cos(\phi)}\right) \quad 3.1.3$$

were LAI is the leaf area index and Ω the clumping factor which can be estimated as described by Campbell and Norman (1998) (Appendix A).

The energy balance equations for canopy, soil, and combined surface components are described as

$$\left.\begin{array}{c} Rn = LE + H + G \\ Rn = Rn_s + Rn_c \\ LE = LE_s + LE_c \\ H = H_s + H_c \\ Rn_s = LE_s + H_s + G \\ Rn_c = LE_c + H_c \end{array}\right\} \quad 3.1.4$$

where subscripts s and c represents soil and canopy components, respectively. The net radiation Rn_c and Rn_s of canopy and soil components, respectively, are estimated using the physically based approach of Campbell and Norman (1998) as

$$\left.\begin{array}{c} Rn_c = Ln_c + (1 - \tau_s) \cdot (1 - \alpha_c) \cdot S \\ Rn_s = Ln_s + \tau_s(1 - \alpha_s)S \end{array}\right\} \quad 3.1.5$$

where τ_s, α_c and α_s are the solar transmittance in canopy, the canopy albedo, and soil albedo, respectively which can be estimated using the formulations described in Campbell and Norman (1998), Ln_c and Ln_s are the longwave radiation, respectively, and can be estimated as

$$\left.\begin{array}{c} Ln_c = [1 - exp(-k_L \cdot \Omega(\phi) \cdot \mathrm{LAI})] \cdot [L_{SKY} + L_s - 2L_c] \\ Ln_s = exp(-k_L \cdot \Omega(\phi) \cdot \mathrm{LAI}) L_{SKY} + [1 - exp(-k_L \cdot \Omega(\phi) \cdot LAI)] L_c - L_s \end{array}\right\} \quad 3.1.6$$

where k_L is an extinction coefficient estimated as described by Campbell and Norman (1998), L_c , L_s , and L_{SKY} are the longwave radiation from the canopy, soil, and sky which can be calculated using Stefan-Boltzmann equation $L = \varepsilon \cdot \sigma \cdot T^4$ with L represents L_c, L_s, or L_{SKY}, ε the emissivity of canopy, soil, or air, and T represents T_c, T_s, or T_a, respectively, and σ the Stefan-Boltzmann constant ($5.67 \cdot 10^{-8} W m^{-2} K^{-4}$). Typical values for leaf absorptivity in the visible, near infrared and thermal infrared, which are required to calculated α_s, α_c and are τ_s provided by Mecikalski et al. (1999) and Anderson et al. (2007).

The soil heat flux, G, is estimated as a function of the soil net radiation Rn_s as

$$G = c_G \cdot Rn_s \quad 3.1.7$$

The value of that c_G varies with soil type, moisture content, and time because of the phase shift between *G* and Rn_s over a diurnal cycle as indicated by Santanello and Friedl (2003). Kustas and Norman (1999a) suggested a time varying value of c_G as

$$st_N = \frac{|t_i - t_{SN}|}{t_{SN}} \quad 3.1.8$$

where t_i is the time representing ±5 hours of t_{SN}, the solar noon local time. However, it is shown that a constant value of c_G can be assumed for midmorning to midday period- typical acquisition time of satellite thermal infrared imagery Santanello and Friedl (2003). For most of the TSEB applications, a constant value is assumed for c_G as ~ 0.3.

The sensible heat fluxes over soil and canopy components are calculated as

$$\left.\begin{aligned} H_c &= \rho \cdot c_P \frac{T_c - T_{AC}}{R_x} \\ H_s &= \rho \cdot c_P \frac{T_s - T_{AC}}{R_s} \\ H &= \rho \cdot c_P \frac{T_{ac} - T_a}{R_a} \end{aligned}\right\} \quad 3.1.9$$

where ρ is the air density, c_P the specific heat of air, T_{ac} air temperature at an air-canopy interface, R_x is the total boundary layer resistance of complete canopy leaves, R_sThe resistance to heat flow in the boundary layer immediately above the soil surface, $R_a$the aerodynamic resistance.

The latent heat flux from canopy LEc is calculated using the Priestly-Taylor (PT) (Priestley and Taylor 1972) formula for the green part of the canopy as

$$LE_c = \alpha_{PT} \cdot f_G \cdot \left(\frac{\Delta}{\Delta+\gamma}\right) \cdot Rn_c \quad 3.1.10$$

where f_G is the fraction of LAI that is green and usually taken as (f_G =1), Δ the slope of the saturation vapor pressure versus temperature curve, and γ the psychrometric constant 0.066 kPa C-1. The PT equation is used to provide an initial, specifically a potential rate of transpiration with the value of $\alpha_{PT} = 1.26$. Two conditions ought to be considered: for well water vegetation under advective conditions a value of $\alpha_{PT} = 2.0$ is used; while for stressed vegetation, as it transpires at a lower rate than the potential rate, using a value of 1.26 will tend to overestimate LEc resulting in unrealistic values of $LE_c < 0$. In this case α_{PT} is iteratively reduced until $LE_c = 0$.

A solution is obtained iteratively until convergence is reached with an acceptable level of error, usually measured by the estimated value of the Monin-Obukov length *L* (Appendix A). For simplification, a linearized form of Eq. 3.1.1 as $T_R(\phi) \approx f_c(\phi)T_c(1 - f_c(\phi))T_s$ to solve for $T_{c,Lin}$ and $T_{ac,Lin}$ and then providing correction terms ΔT_c and ΔT_{ac} to account for nonlinearity. Detailed

descriptions of the methodology to achieve a solution of the series resistance formulation of the TSEB is provided by Norman et al. (1995).

The application of the TSEB requires considerable input information including forcing weather data, surface biophysical features, and remote sensing data represented in terms of radiometric surface temperature and surface reflectance in the shortwave part of the spectrum (Table 1). Some additional required parameters such as soil and vegetation emissivity which usually are assigned typical values of for example. 0.978 and 0.985 from literature and field measurements (Li et al. 2004). Similarly mean leaf size and absorptivity are generally obtained from typical values reported in literature. A major need for a successful application of the TSEB model is the land use map. The required biophysical parameters such as h_c, LAI, and f_c are remote sensing based estimates derived as a function of vegetation indices such as the NDVI. These parameters are needed to calculate the different surface roughness characteristics and the resistances to heat and momentum transfer.

The estimated SEBF are instantaneous sub-hourly values made during satellite overpass time and date. Evaluation of such fluxes is made using sub-hourly measurements. Daily values of actual ET are obtained by extrapolation of instantaneous estimates of LE. Example of the TSEB application particularly over agricultural areas are provided in Table 2.

Table 1: Typical Input data required for the application of the TSEB model

Data	Source	Spatial Resolution
Weather forcing		
Incoming shortwave solar radiation (Rs) Air temperature (Ta) Wind Speed (u) Vapor Pressure (ea) Atmospheric Pressure (P) Height of measurement of Ta (zt) Height of measurement of u (zu)	Ground based observations	Local scale (quasi-point) assumed to be representative of the region under study
Biophysical parameters		
Leaf Area Index (LAI) Canopy Height (hc) Land use classification Mean Leaf size (s) Absorptivity of air, canopy, soil Height and width of clumps	Ground based observations or remote sensing estimates	Local scale (quasi-point) or 30 m
Remote Sensing		
Radiometric surface temperature (TR) Surface Reflectance in the visible and near infrared bands (atmospherically corrected data is required)	Airborne, Landsat Airborne , Landsat	1-30 m 1-30 m

Table 2: Examples of applications of the TSEB model and reported performance

Study area, dataset	Climatic Region	Land Use	Domain	Performance RMSE W m^{-2}					Citation
				Rn	G	H	LE	N	
Ames, Iowa SMACEX, 2002	Humid	Corn soybean	Walnut Creek Watershed	20	31	35	45	38	{Kustas, 2005 #367;Li, 2005 #302}
Maricopa, Arizona, 1987	Semi-arid	Cotton	Research site	21	13	25	37	19	{Kustas, 2000 #297}

3.2. ALEXI/DisALEXI

General

As the ALEXI and DisALEXI models were separately developed based on different motivations, they are in some cases being applied jointly to provide estimates of SEBF at the field scale. The ALEXI model was originally developed by Anderson et al. (1997) and named as the Two-Source Time-Integrated model (TSTIM) for regional scale applications. The motivation behind ALEXI model was to provide an operational scheme with reasonable level of complexity and data need yet acceptable performance to monitor SEBF. As ALEXI uses the TSEB is a major component it alleviates the need for near-surface air temperature (Ta) measurements that would hinder its application at regional scales. The model substituted the need for Ta by using early morning atmospheric soundings to couple the TSEB with atmospheric boundary layer development model. With such an approach, ALEXI provide estimates of SEBF at regional scales using coarse resolution data from GOES. Such estimates are useful for regional applications such as drought monitoring and weather forecasting. On the other hand, for field scale applications such as monitoring vegetation growth and water use, higher resolution estimates of SEBF are needed. The DisALEXI was developed to bridge the gap between regional to field scale estimates of SEBF, avoiding the use of additional weather forcing data. Description of the two models is provided below with examples of some recent applications.

3.2.1 ALEXI

As a progression to the TSEB model that provides fluxes at local scale, the ALEXI model is aimed towards providing fluxes at regional scales with minimal ancillary data needs. The TSEB model is applied at two times during the morning growth phase of the atmospheric boundary layer usually at 1.5 h and 5.5 h after sunrise. At these two times, the radiometric surface temperature from the 5-10 km GOES thermal data is used. In order to provide energy balance closure during this period, a simple slab model is used to relate the rise in air temperature to the time-integrated sensible heat fluxes from the land surface. The modeling approach of ALEXI mitigates problems related to the use of T_R as by differences in surface temperature it eliminates errors caused by atmospheric correction, sensor calibration, and specification of surface emissivity.

The TSEB model serves as the surface component of ALEXI using a simplified linear form of Eq. 3.1.1 as

$$T_R(\phi) \approx f_c(\phi)T_c(1 - f_c(\phi))T_c \qquad 3.2.1$$

This simplification reduces the accuracy by about less than 0.5 °C (Anderson et al. 1997). Also the net radiation components for soil and canopy, Rn_s andRn_c, respectively, are calculated as

$$\left.\begin{aligned} Rn &= Rn_c + Rn_s \\ Rn &= (L_d - L_u) + (S_d - S_u) = L_d - (1-\tau_c)L_c - \tau_c L_s + (1-A)S_d \\ Rn_s &= \left(L_{d,s} - L_{u,s}\right) + \left(S_{d,s} - S_{u,s}\right) = \tau_c L_d - (1-\tau_c)L_c - L_s + (1-\rho_s)S_{d,s} \end{aligned}\right\} \quad 3.2.2$$

where Rn is the net radiation above the canopy, Rn_c and Rn_s are the components absorbed by canopy and penetrating to the soil surface, respectively, the shortwave component depends on insolation values above canopy, S_d, and above soil surface $S_{d,s}$, the reflectivity of the soil-canopy system, A, and the soil surface, ρ_s, and the coefficient of diffuse radiation transmission through the canopy with approximate values provided by Campbell and Norman (1998). S_u and $S_{u,s}$ represents the upwelling shortwave radiation above soil-canopy system and the soil surface, respectively, $L_u$and $L_{u,s}$ are analogous the longwave emissions, L_d, L_c, and L_s are the thermal radiation from the sky, the canopy, and the soil, respectively.

Estimates of surface fluxes components including G, H and LE are provided using a similar parameterization described in the TSEB model (Appendix A and Section 3.1).

The atmospheric boundary layer development component is based on a simple slab model of the mixed layer and the relationship between air $T_a$and potential θ_m temperatures, respectively. The model assumes that the air within the layer, at height z_t at which air temperature is measured, to be at uniform potential temperature as

$$\theta_m = T_a \cdot \left(\frac{100}{P}\right)^{R/c_P} \quad 3.2.3$$

where p is atmospheric pressure (kPa) at height z_t, R and c_P are the gas constant and specific heat capacity with $R/c_P = 0.286$. Using this slab model, the height of the boundary layer z1 at time t1 can be estimated as the height at which an adiabatic laps rate at a potential temperature, θ_m, intersects an early morning temperature sounding (Figure 3).

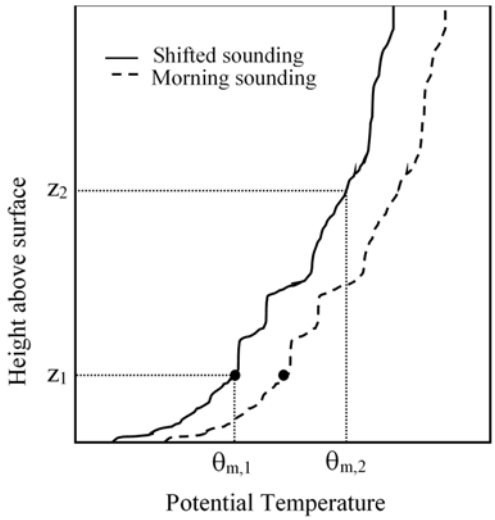

Figure 3: Schematic showing the approach used to diagnose boundary layer growth during a time interval t_1 to t_2 {Anderson, 1997 #114}.

A conservation equation that describes the relationship between the time-integrated sensible heat flux and the growth of the convective ABL is used based on the simplified approach by Mcnaughton and Spriggs (1986) as

$$pc_P\left(z_2\theta_{m,2} - z_1\theta_{m,1}\right) = \int_{t1}^{t2} H(t)dt + pc_P \int_{t1}^{t2} \theta_s(z)dz \qquad 3.2.4$$

where $\theta_{m,i}$ is the potential temperature within the mixed layer at time t_i, $\theta_s(z)$ the potential temperature profile above the mixed layer at time t_1, and p is the air density. Using a simple linear equation, the time-integrated $H(t)$ can be estimated as

$$\int_{t_1}^{t_2} H(t)dt = \frac{1}{2}(H_2 t_2 - H_1 t_1) \qquad 3.2.5$$

where H_1 and H_2 are the estimated sensible heat fluxes at time t_1 and t_2, respectively, using the surface component, TSEB, of ALEXI.

A solution is achieved iteratively by first assuming an initial air temperature to calculate SEBF including sensible heat fluxes from the two components. The air temperature estimates are adjusted during the iterative process until convergence in the sensible heat fluxes from the two components is achieved.

List of input data needed for the application of ALEXI is shown in Table 3. Most of the biophysical parameters were obtained at relatively higher resolution at the MODIS scale of 1 km (Table 3). Weather forcing and GOES remote sensing data are provided at a coarse resolution of 5-40 km scale. Weather forcing data including near surface wind speed, actual vapor pressure and atmospheric pressure were from Automated Service Observation System (ASOS) and Automated Weather Observation System (AWOS). The lapse rate profiles were obtained from the U.S. synoptic network that are at a resolution of ~100 km, and were processed to higher resolution of 40 km within the analysis components of the Cooperative Institute for Meteorological Satellite Studies (CIMSS) mesoscale model (Diak et al. 2004). In some cases (Anderson et al. 2011), the wind speed fields and the lapse rate profile were obtained from North America Regional Reanalysis (NARR). The canopy heights are linearly interpolated between minimum and maximum defined values based on land cover data and fraction of vegetation cover f_c.

Table 3: Summary of input data required for the application of ALEXI model.

Data	Source	Spatial Resolution
Weather forcing		
Incoming shortwave solar radiation (Sd)	GOES	20 km
Downwelling longwave radiation (Ld)	GOES	20 km
Wind Speed (u)	ASOS/AWOS/NARR	40 km
Vapor Pressure (ea)	ASOS/AWOS	40 km
Atmospheric Pressure (P)	ASOS/AWOS	40 km
Lapse rate profile	Radiosonde/NARR	40 km

Biophysical parameters

Leaf Area Index (LAI)	MODIS	1 km
Canopy Height (hc)	Lookup table	1 km
Land use classification	UMD Global	1 km
Characteristic Leaf size (s)	Lookup table	1 km
Absorptivity of air, canopy, soil	Lookup table	1 km

Remote Sensing

Radiometric surface temperature (T_{Rad1}, T_{Rad1})	GOES	5-10 km

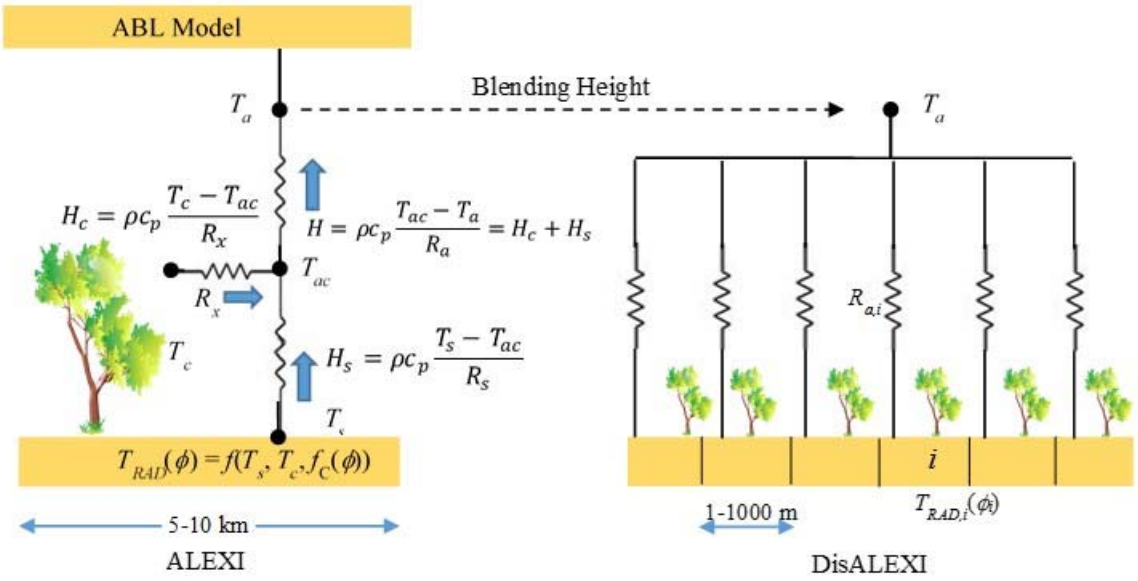

Figure 4: Schematic of ALEXI and DisALEXI models

3.2.2 DisALEXI

The disaggregation scheme (DisALEXI) described by Norman et al. (2003) is developed to bridge the gap between regional and local scale estimates of SEBF. ALEXI provides coarse spatial resolution, regional scale estimates of SEBF, using the 5-km data from GOES. While such scales may be appropriate for weather forecasting and drought monitoring, it limits the application for operational ET at-field scale agricultural monitoring. One of the advantages of DisALEXI is that it requires no additional weather data than those used in ALEXI.

Generally, DisALEXI, mainly applies, again, the TSEB using the same input weather forcing data used in ALEXI including wind speed, downward short- and long-wave radiation as well the estimated Ta at the 50-m. In this sense the blending height concept is employed to allow the use Ta at 50-m as an upper boundary condition for DisALEXI. The high resolution radiometric surface temperature T_R data from either aircraft or Landsat sensors is used as lower boundary condition.

The disaggregation scheme applies the TSEB at the high resolution for all the ith (i=1 to N) contained within each of the 5-km GOES pixels. The 50-m Ta is considered constant for all the ith pixels while the radiometric surface temperature from the high resolution data. Similarly all other surface related parameters are treated at the high-resolution pixel scale including fraction of cover $f_{c,i}$ and vegetation height $h_{c,i}$ which are generally based on NDVI. Note that canopy height data are needed to estimate the related surface roughness and aerodynamic resistance. For the net radiation calculation the surface albedo Ai and emissivity are estimated based on *f*c, following Campbell and Norman (1998) and Anton and Ross 1987, respectively. With this application DisALEXI provide estimates of SEBF at the high-resolution scenes.

Prior to using the high resolution radiometric surface temperature a procedure suggested by Norman et al. (2003) to correct for potential biases between those and the ones from GOES sensor. These biases which needs to be accounted for, could arise from differences in sensor calibration, atmospheric correction, and view angle. For such, correcting all thermal images at low and high resolution should accommodate atmospheric and emissivity effects (Berk et al. 1998; Kustas and Norman 1999a). The bias-corrected high resolution radiometric temperature $T^C_{RAD,i}(\phi_i)$ for all N pixels contained in the GOES pixels can be described as

$$T^C_{RAD,i}(\phi_i) = T_{RAD,i}(\phi_i) + T_{RAD,i}(\bar{\phi}_\iota) - \sum_{i=1}^{N} \frac{T_{RAD,i}(\phi_i)}{N} \qquad 3.2.6$$

where $T_{RAD,i}(\phi_i)$ the high-resolution radiometric surface temperature contained within the GOES pixel, $T_{RAD,i}(\bar{\phi}_\iota)$ the 5-km radiometric temperature from GOES adjusted to the average angle $\bar{\phi}_\iota$ at which the high-resolution sensor views the scene. This adjusted $T_{RAD,i}(\bar{\phi}_\iota)$ is calculated from the estimated soil and canopy temperature from ALEXI at the average angle $\bar{\phi}_\iota$.

Estimated instantaneous SEBF including λE can be extrapolated to daily values using the evaporative fraction (EF) defined as $\lambda E/(R_n - G)$. Several studies indicated that the EF can be considered constant during the daytime hours and can be used to extrapolate instantaneous fluxes to equivalent daily values (Brutsaert and Sugita 1992). Anderson et al. (2012b); Anderson et al. (2007) multiplied the EF fraction defined above by 1.1 i.e. $EF = 1.1\ \lambda E/(R_n - G)$ to account for underestimation of the EF of 5-10 % observed during midday hours as indicated by (Brutsaert and Sugita 1992).

Daily ETa maps throughout a growing season at the Landsat spatial resolution of the surface reflectance can be created following the framework described by Anderson et al. (2011). The optima spatial resolution for agricultural application is that of the Landsat surface reflectance data of 30-m. The Landsat data are available on week to 16-days period. The framework described by Anderson et al. (2011) is based on relying solely on remote sensing data not only

from Landsat but with the utility of information from multiple sensors. This framework uses two different approaches –a thermal sharpening and the Spatial Temporal Adaptive Reflectance Fusion Model (STARFM) to enhance the remote sensing spatial and temporal resolution. The original spatial resolution of TIR bands of the Landsat 5 and 7 is 120 and 60 m, respectively and that of MODIS is 1 km. The thermal sharpening approach developed by Kustas et al. (2003) is used to enhance the spatial resolution of the TIR band of a sensor to its corresponding shorwave bands. For example, the spatial resolution of Landsat 5 at the shortwave bands is 30-m and the corresponding TIR is 120-m. A relationship usually exists between TIR band and the corresponding surface reflectance data in terms of vegetation indices. The STARFM approach developed by Gao et al. (2006) was originally developed to provide surface reflectance at the Landsat spatial resolution of 30-m based on high temporal resolution of MODIS data in between Landsat overpass dates. STARFM follows statistical methods to develop relationships between Landsat and MODIS coincident scenes to map temporal changes based on MODIS. Anderson et al. (2011) applied the STARFM approach directly on ETa maps developed during Landsat and MODIS coincident dates to fuse (or predict) ETa maps in between Landsat overpass dates.

In the application of DisALEXI, four input are held constant. Vegetation height is estimated in a similar way as in ALEXI based on the land use classification. Linear interpolation between the seasonal maximum and minimum canopy height $h_{c,max}$ and $h_{c,min}$, respectively, is applied using the fraction of cover as

$$h_c = h_{c,min} + f_c \cdot \left(h_{c,max} - h_{c,min}\right) \qquad 3.2.7$$

A tabulated values of maximum and minimum canopy height is provided in Anderson et al. (2007). Three inputs to ALEXI are also used as inputs to DisALEXI including the incoming shortwave solar radiation, downwelling longwave radiation S_d and L_d, respectively, and wind speed. The air temperature Ta at the blending height of 50 m at time t_2 estimated by ALEXI is used as an input to DisALEXI. A list of required input data for the application of DisALEXI are shown in Table 4. Examples of DisALEXI model performance over selected areas are shown in Table 5.

Table 4: Summary of input data required for the application of DisALEXI model

Data	Source	Spatial Resolution
Weather forcing		
Incoming shortwave solar radiation (Sd)	GOES	20 km
Downwelling longwave radiation (Ld)	GOES	20 km
Air Temperature Ta at 50 m	Derived from ALEXI	5-10 km
Wind Speed (u)	ASOS/AWOS/NARR	40 km
Vapor Pressure (ea)	Local meteorological	Local scale
Atmospheric Pressure (P)	observations	
Biophysical parameters		
Leaf Area Index (LAI)	Airborne, Landsat, MODIS	1-1000 m
Canopy Height (hc)	Based on land cover type	1-1000 m
Land use classification	Airborne, Landsat, MODIS	1-1000 m

Characteristic Leaf size (s)	Based on land cover type	1-1000 m
Absorptivity of air, canopy, soil	Based on land cover type	1-1000 m
Remote Sensing		
Radiometric surface temperature (T_R)	Airborne, Landsat, MODIS	1-1000 m

Table 5: Examples of applications of DisALEXI model and reported performance.

Study area, dataset	Climatic Region	Land use	Domain	Performance (SEBF) (W/m^2)						Citation
				Rn	G	H	LE	all	N	
Southern Great Plains, Oklahoma SGP79	Humid	Winter wheat, pasture, grassland	Research sites	-	-	-	-	38		{Norman, 2003 #129}
Bushland, Texas, BEAREX08, 2008	Semi-arid	cotton	Research sites	37.7	42.0	54.7	77.2	53.1	66	{Anderson, 2012 #396}

SEBF: surface energy balance fluxes

3.3. Hybrid ET Model

General

The Hybrid-ET couples an energy balance with a water balance model to provide estimates of ET at the field scale. The application of thermal based remote sensing energy balance models using Landsat data provide estimates of SEBF and daily ET during the specified satellite overpass dates that are 8-16 days apart. The imagery from Landsat Thematic Mapper sensors are specifically used as they have a reasonable pixel resolution to provide in-field variability for most agricultural applications. On the other hand, as there are temporal gaps in the Landsat data, so providing continue estimates of ET using a traditional water balance approach can result in continuity in the estimates.

The TSEB developed by Norman et al. (1995) with recent modifications described in Kustas and Norman (1999a, 2000) is used to provide instantaneous estimates of SEBF and daily ET. Detailed description about the TSEB is provided in Section 3.1 and Appendix A.

On the other hand, the tradition water balance approach described by Allen et al. () is used to estimate daily ET. The Hybrid-ET models suggests a modification to the FAO-56 by introducing the use of a reflectance based basal crop coefficient in place of the traditional standards in the FAO-56. In addition to providing estimates of daily ET, Hybrid-ET also provides estimates of soil water content in the root zone of the crop or vegetation. The two models are coupled using data assimilation through the common variable actual ET. While the FAO-56 water balance approach provides estimates of the entire root zone soil water status as an averaged single value, the dynamic soil water content estimates used in the Hybrid-ET approach provides estimates at multiple layers to allow for comparisons with soil water content measurements under different root water extraction models.

Model Description

Energy and Water Balance Models

The hybrid ET model suggested the use of the TSEB model to provide estimates instantaneous SEBF including LE. Daily values of ET during satellite overpass date are calculated using extrapolation methods including the evaporative fraction (EF) and the reference ET fraction (ETrF) methods described in Chavez et al. (2008).

The traditional FAO-56 (Allen et al. 1998a) approach to estimate ET using the dual crop coefficient method represents conditions when crops are under soil water stress as

$$ET_c = (K_s \cdot K_{cb} + K_e) \cdot ET_0 \qquad 3.3.1$$

where ET_c is the crop *ET*, K_s the soil water stress coefficient with $K_s = 1.0$ for no soil water stress and $K_s < 1.0$ is water stress conditions exist, K_e the soil evaporation coefficient, and ET_0 the reference crop *ET* based on a grass reference crop. To estimate K_s and K_e, water balance

calculations for the root zone and the top soil layer are required on a daily bases with more details found in Allen et al. (1998a).

The water balance, WB, of the root zone is

$$SMD_i = SMD_{i-1} - (P_i - RO_i) - I_i - CR_i + ET_{c,i} + DP_i \quad 3.3.2$$

where SMD_i is the soil moisture deficit at the end of day i, P the precipitation, RO the losses due to water runoff, I the irrigation water, CR the capillary rise, ET_c the crop ET, and DP losses due to deep percolation.

Traditionally, tabulated K_{cb} values are used to estimate ET (Allen et al. 1998a). Considerable progress has been made for improving estimates of ET and crop water requirements with remotely sensed values of Kcb (Bausch 1993; Bausch and Neale 1987, 1989; Neale et al. 1989; Neale et al. 2005). For example, the linear relationship between K_{cb} and the soil adjusted vegetation index ($SAVI$) for corn yielding what's known as the reflectance-based basal crop coefficient (K_{cbrf}). The K_{cbrf} for corn are based on the based on the findings of Neale et al. (1989) and Bausch (1993) and for soybean as an adaptation of the dry bean K_{cbrf} developed by Jayanthi et al. (2001).

$$\left.\begin{aligned} K_{cbrf_{corn}} &= 1.835SAVI - 0.034 \\ K_{cbrf\_soybean} &= 1.638SAVI - 0.003 \end{aligned}\right\} \quad 3.3.3$$

The use of K_{cbrf} provides improved estimates of actual ET_c at times when remotely sensed images are available. Also the use of linearly interpolated K_{cb} values in between those K_{cbrf} values instead of the tabulated ones can result in improved estimates of ET between satellite overpass dates. Interpolation of K_{cb} from the K_{cbrf} is more effective, especially under shorter time periods in between satellite image acquisition, as is the case for the current study, compared to the crop growing stages periods suggested by Allen et al. (1998a).

Soil Moisture Model

For the evaluation of estimates of soil moisture content further analysis needs to be carried out to provide soil moisture estimates at multiple layers so it could be compared to the measurements. A soil moisture dynamics model is implemented to provide such estimates. The model used in the Hybrid ET is a simple one-dimensional modeling scheme similar to the modeling approach described in the simple biosphere SiB model by Sellers et al. (1986) and applied as in Luo et al. (2003) (Eq. (3.3.4)).

$$\left.\begin{aligned} D_1 \frac{d\theta_1}{dt} &= I - E - S_1 - Q_{1,2} \\ D_i \frac{d\theta_i}{dt} &= Q_{i-1,i} - S_i - Q_{i,i+1} \\ D_n \frac{d\theta_n}{dt} &= Q_{i-1,n} - S_n - Q_n \end{aligned}\right\} \quad 3.3.4$$

where θ is the soil moisture content, *t* the time increment, *i* number increment from 1 to *n* the total number of soil layers, *D* layer thickness, *I* infiltration rate, *E* evaporation rate from the soil surface and the upper most layer, S_i water uptake from a layer *i* the root zone, $Q_{i,i+1}$ leakage or soil water flux from layer *i* to *i+1*, and Q_n the drainage from the bottom most layer. The root zone up to the maximum root extent of the crops is divided into 7 layers for both corn and soybean fields with the top six layers depths of 0–10, 10–20, 20–30, 30–45, 45–60, and 60–80 cm and the bottom most layer depths of 80–120 and 80–100 cm for corn and soybean fields, respectively.

The *ET* components including soil evaporation *E* and plant transpiration *T*, obtained estimated by the WB model are used as inputs to the soil moisture dynamics model assuming unstressed water condition as initial boundary condition. The soil moisture content at the root zone for each soil layer is then recalculated by introducing the soil water potential ψ with the corresponding Feddes reduction function $\alpha(\psi)$ (Feddes et al. 1976; Feddes et al. 1978) to account for soil moisture stress conditions and to update root water uptake by plants roots. Following an iterative procedure at each time step, the soil moisture content is updated until reaching an acceptable minimum error. Detailed description of how to estimate the different components of soil moisture dynamics models is shown in Appendix B with the corresponding soil water characteristics shown in Table B1.

Data Assimilation Approach

The estimated ET from the TSEB and the WB models is used to couple the two models using data assimilation technique. The hybrid ET suggested the use of the statistical interpolation (SI) method described by Daley (1993). The SI method was generally used since 1940s for improving spatial estimates or forecast of different state variables such as temperature and water vapor using a network of point measurements through minimizing error variances (Daley 1993). To improve model estimates at location r_0 based on measurement points at locations r_k the SI algorithm can be described by as

$$ET_{WB}^{A}(r_0) = ET_{WB}^{B}(r_0) + \sum_{k=1}^{K} W_k\left(ET_{TSEB}(r_k) - ET_{WB}^{B}(r_k)\right) \qquad 3.3.5$$

where superscripts *A* and *B* refer to after and before assimilation, respectively, ET_{WB} and ET_{TSM} are the estimated *ET* based on WB and TSEB models, respectively, and *W* the weight or Kalman gain of the error for each of the observation points.

The least square estimates for *W* can be described as $\sum_{l=1}^{K} W_l[\rho_{kl} + \varepsilon_k^2] = \rho_{k0}$ where $\leq k \leq K$, ρ the model error correlation, ε^2 the normalized observation error equals $\sigma_0^2(r_k)/\sigma_B^2$ with σ_O^2 and σ_B^2 represents the variances in ET_{TSEB} and ET_{WB} estimates with respect to measured *ET*, respectively. With the goal of minimize the after assimilation error variance the normalized error variance can be described as $\varepsilon_A^2 = \sigma_A^2/\sigma_B^2 = 1 - \sum_{k=1}^{K} \rho_{k0} W_k$ where ε_A^2 and σ_A^2 are the error and the error variance after assimilation.

In the hybrid approach each model point is updated from a single observation point hence a single constant *W* applied for each analysis point. Also the observation points and the model points coincide hence $r_0 = r_k$ and $\rho_0 = 1$. Consequently Eq. (3.3.5) is then simplified to

$$ET_{WB}^{A} = ET_{WB}^{B} + W(ET_{TSEB} - ET_{WB}^{B}) \quad 3.3.6$$

with a minimized model variance equal to ε^2 and $W = \varepsilon^2/(1+\varepsilon^2) = \sigma_B^2/(\sigma_B^2 + \sigma_A^2)$

In one of the applications of the hybrid ET (Geli 2012), the analysis of the error in variances showed that the resulting values of *W* for all observation points was approximately equal when compared to each other; hence, a constant value of *W* can be used for all observation points. This is similar to the approach that was followed by Schuurmans et al. (2003) except that they used arbitrary values for *W*.

Geli (2012) applied the SI method is applied using two different options for the value of *W*. The weights can be assumed constant i.e. time invariant hence a constant value of *W* can be applied for entire period of analysis. The weights can be calculated for each satellite overpass date which result in a time variant value for *W*. Consequently, assimilation of ET_{TSEB} into WB result in updated *ET* and root zone soil moisture content.

Update of Ks and SMD

On satellite overpass dates the assimilated *ET* value is used to update the root zone soil moisture status by back calculating new values for K_s and *SMD*. Due to assimilation the resulting new value of *ET* is followed by updating only the values of K_s and K_e since ET_o remains unchanged and K_{cb} is replaced by the remotely sensed value K_{cbrf}. Estimation of K_e is based on moisture conditions of the top 10 cm of the soil hence it is expected to have less variation than the value of K_e, and therefore assumed to remain unchanged after assimilation. As estimation of K_s requires knowing the root zone soil moisture status, the water balance condition is updated by back calculating a new value for K_s and consequently updating the value of *SMD* as well. The updated value of *SMD* is then transferred to the next time step leading to an updated soil moisture status after assimilation for a number of subsequent days depending on the water stress conditions.

A list of required input data for the application of the hybrid ET model is shown in Table 6. Examples of the hybrid ET model performance over selected areas are shown in Table 7.

Table 6: Summary of input data needed for the application of the hybrid ET model.

Data	Source	Spatial Resolution
Weather forcing		
Incoming shortwave solar radiation (Rs) Air temperature (Ta) Wind Speed (u) Vapor Pressure (e_a) Atmospheric Pressure (P) Height of measurement of T_a (z_t) Height of measurement of u (z_u)	Ground based observations	Local scale
Biophysical parameters		
Leaf Area Index (LAI) Canopy Height (hc) Land use classification	Ground based observations or remote sensing estimates	Local scale or 30-m
Mean Leaf size (s)	Lookup table	
Absorptivity of air, canopy, soil	Lookup table	
Height and width of clumps		
Remote Sensing		
Radiometric surface temperature (T_R)	Airborne, Landsat, MODIS	1-1000 m
Surface reflectance in the visible and near infrared bands	Airborne , Landsat, MODIS	1-1000 m
Soil Data		
Field capacity, wilting point Soil type and Texture	Field measurements	Local Scale

Table 7: Example of applications of the hybrid ET model and related performance.

Study area, dataset	Climatic Region	Land Use	Domain	Performance (RMSE)						Citation
				Rn	G	H	LE	ET	N	
Ames, Iowa SMACEX, 2002	Humid	Corn soybean	Walnut Creek Watershed	18	28	30	47	0.67	31	Geli 2012
Bushland, Texas, BEAREX08, 2008	Semi-arid	Dry land and irrigated cotton	Research site	22	50	46	41	0.64	16	Neale et al. 2012

Study area, dataset	Climatic Region	Land use	Domain	Performance (ET mm/month)	Citation
CONUS, Flux NET	Diverse	Crop, forest, shrubland, grassland	CONUS, MODIS	RMSE: 8.5 to 20 mm, single towers	Senay et al, 2013
CONUS, EC Flux Towers	Diverse	crop, forest, shrubland, grassland	CONUS, MODIS	RMSE: 24 - 30 mm multiple towers,	Velpuri et al., 2013
Texas High Plains, Lysimeter	Humid	corn and sorghum	Research site, Landsat	RMSE: 12% of mean at seasonal scale	Senay et al, 2014
Colorado Rivers Basin	Arid-semiarid	Mixed	Basin wide, Landsat	MBE of 10%, single stations	Singh et al, 2014

3.4. METRIC Model

General

The METRIC was conceptualized on the big leaf assumption for modeling mass/energy exchange at the surface. This assumption is mainly utilized to represent the resistance to sensible heat flow above the surface. For most applications over agricultural areas, such an assumption can fairly describe the inherent surface conditions during most of the growing period. METRIC uses a modified version of the bulk sensible heat flux equation that is based on the differences between the aerodynamic and the near-surface air temperature. Instead the model introduces the use of the air temperature difference, dT, at two heights near the surface and empirically relates it to the radiometric surface temperature obtained from remote sensing. With the use of dT, the model manages to avoid the difficulties in estimating the aerodynamic temperature and the potential errors caused by the use to T_R in its place. One of the advantages of the model is that it does not necessarily require the use of a land use map to calculate some related biophysical parameters. However, Allen et al. (2007b) state that it is important to use land use classification maps in the application of METRIC when available as they can be used to specify momentum roughness length values and soil heat flux vs. net radiation relationships as described below.

As the METRIC model is based on the surface energy balance equation it calculates the latent heat flux as a residual. All estimates of SEBF are instantaneous including LE which can be extrapolated to values of daily ETa. METRIC was based on the SEBAL model (Bastiaanssen et al. 1998a; Bastiaanssen et al. 1998b) with some modifications especially regarding the calibration of the latent heat fluxes at the two limiting wet and dry conditions, using pixels identified over well irrigated alfalfa as the wet upper limit instead of a water body. However, the selection of pixels or fields for a given scene with such two limits is subjective by nature and requires some level of experience and knowledge about the area under study. Some challenges might arise with the selection of such pixel when using MODIS date due to its coarser spatial resolution.

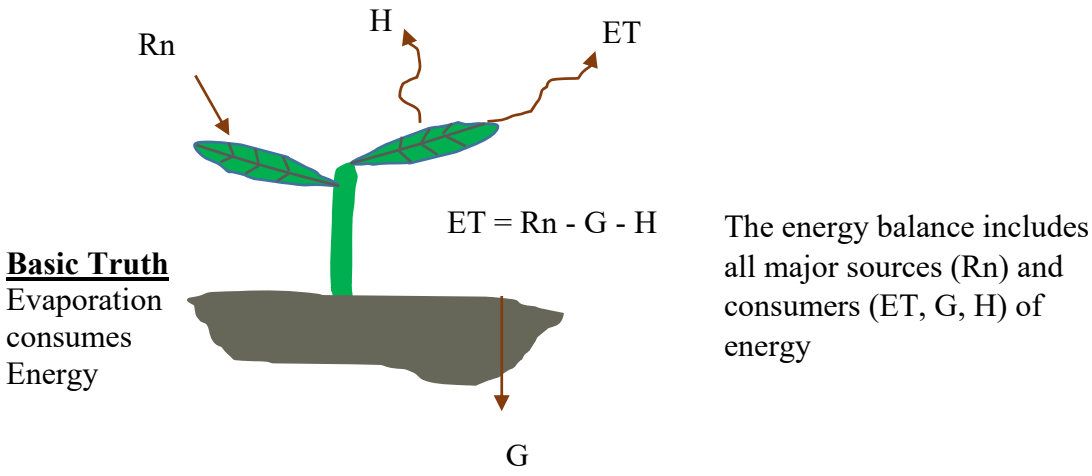

Figure 5: Description of METRIC model

Model Description

The instantaneous LE is estimated as the residual of the energy balance equation as

$$LE = Rn - G - H \quad 3.4.1$$

The net radiation Rn can be estimated as

$$Rn = (1 - \alpha)R_s + R_{L\downarrow} - R_{L\uparrow} - (1 - \varepsilon_o)R_{L\downarrow} \quad 3.4.2$$

where α is the broadband surface albedo, R_s the incoming shortwave radiation, $R_{L\uparrow}$ the outgoing longwave radiation, $R_{L\downarrow}$ the outgoing longwave radiation and ε_o the broadband surface emissivity.

The broadband surface albedo can be estimated as

$$\alpha = \sum_{b=1}^{6} \rho_{s,b} \cdot w_b \quad 3.4.3$$

where w_b is the weighting coefficient with typical values provided by Allen et al. (2007b)Allen et al. 2007 and $\rho_{s,b}$ the at-surface reflectance for each band b and can be estimated as described in Appendix C.

The incoming shortwave radiation R_s, which is considered same for non-mountainous areas, can be estimated as

$$R_s = G_{SC} \cdot cos\ \theta \cdot d_r \cdot \tau_{sw} \quad 3.4.4$$

where $G_{SC}$is the solar constant taken as (1367 W m^{-2}), $cos\ \theta$ the cosine of the solar zenith angle, d_r the inverse squared relative earth-sun distance $1/d^2$ estimated as described in Appendix C, and τ_{sw} the broadband atmospheric transmissiviy which can be estimated following Allen (2005) as described in Appendix C.

The outgoing longwave radiation $R_{L\uparrow}$ can be estimated using the Stefan-Boltzmann equation as

$$R_{L\uparrow} = \varepsilon_o \cdot \sigma \cdot T_S^4 \quad 3.4.5$$

where σ is the Stefan-Boltzmann constant taken as $5.67 \cdot 10^{-8} Wm^{-2}K^{-4}$, ε_o the broadband emissivity (dimensionless), and T_s the surface temperature (K) which basically refers to the radiometric surface temperature T_R.

A corrected radiometric surface temperature T_s can be estimated using a modified Planks equation. This corrections is based on calculating a thermal radiance from the surface R_c (Markham and Barker 1986).

$$T_s = \frac{K_2}{ln\left(\frac{\varepsilon_{NB} \cdot K_1}{R_c} + 1\right)} \quad 3.4.6$$

where K_1 and K_2 are constants for Landsat images for band 6 in $Wm^{-2}sr^{-1}\mu m^{-1}$ (Appendix C), R_c the corrected thermal radiance from the surface ($Wm^{-2}sr^{-1}\mu m^{-1}$), and ε_{NB} the narrow band emissivity. Description of how to estimate ε_o and ε_{NB} is provided in Appendix C. R_C can be estimated following Wukelic et al. (1989) as

$$R_C = \frac{L_6 - R_P}{\tau_{NB}} - (1 - \tau_{NB}) \cdot R_{sky} \quad 3.4.7$$

where L_6 is the spectral radiance of band 6 ($Wm^{-2}sr^{-1}\mu m^{-1}$) which represents the at-sensor radiance, R_P the path radiance in the 10.4-12.5 μm band ($Wm^{-2}sr^{-1}\mu m^{-1}$), R_{sky} the narrow band downward thermal radiation from a clear sky ($Wm^{-2}sr^{-1}\mu m^{-1}$) and $\tau_{NB}$the narrow band transmissivity of air.

R_{sky} can be estimated following Wukelic et al. (1989) as

$$R_{sky} = (1.807 \cdot 10^{-10}) \cdot T_a^4 \cdot [1 - 0.26 \cdot exp(-7.77 \cdot 10^{-4} \cdot (273.15 - T_a)^2)] \quad 3.4.8$$

where T_a is the air temperature (K). Based on analysis carried for several image dates using MODTRAN, (Allen et al. 2007b) suggested that $R_P = 0.91$, $\tau_{NB} = 0.866$, and $R_{sky} = 1.32$ for low aerosol conditions. However these values can be replaced by $R_P = 0$, $\tau_{NB} = 1$, and $R_{sky} = 0$ which leads to ignoring the use of R_C as if L6 is directly used. Using the uncorrected values of L6 has a small effect on the estimated ETa especially over areas with low and high ET values and slightly large for midrange ETa values.

The incoming longwave radiation $R_{L\downarrow}$ can be estimated using Stefan-Boltzmann equation as

$$R_{L\downarrow} = \varepsilon_a \cdot \sigma \cdot T_a^4 \quad 3.4.9$$

where ε_a is the effective atmospheric emissivity which can be estimated originally using an empirical described by Bastiaanssen (1995) adjusted by Allen et al. (2007b) based on data from Idaho as

$$\varepsilon_a = 0.85\left(-ln(\tau_{sw})\right)^{0.09} \quad 3.4.10$$

with the application of SEBAL the coefficients of 1.08 and 0.265, which were based on data from Egypt, were used instead of 0.85 and 0.09, respectively.

The soil heat flux *G* can be estimated using the empirical equation described in SEBAL as based on Bastiaanssen (2000) as

$$\frac{G}{R_n} = T_S \cdot (0.0038 + 0.0074 \cdot \alpha) \cdot (1 - 0.98 \cdot NDVI^4) \quad 3.4.11$$

where α is the surface albedo and T_S surface temperature (C). For recent application of METRIC a different equation provided by Tasumi (2003) based on vegetation cover conditions is used as

$$\left.\begin{array}{ll} \frac{G}{R_n} = 0.05 + 0.18 \cdot e^{(-0.521)\cdot LAI} & for\ LAI \geq 0.5 \\ \frac{G}{R_n} = \frac{1.80\cdot(T_S - 273.16)}{R_n} + 0.084 & for\ LAI < 0.5 \end{array}\right\} \quad 3.4.12$$

As indicated by Allen et al. (2007b) both Eqs. 3.4.11 and 3.4.13 performed similarly well with irrigated crops at Kimberly, Idaho. Noteworthy that these equations are designed to work over tilled agricultural soils. Over desert soil G is adjusted based on Ts (Allen 2012) as

$$G_{adj} = G - 5 \cdot \left(T_{S\,dem} - T_{S\,dem_{thres}}\right) \qquad for\ T_{S\,dem} > T_{S\,dem_{thres}} \quad 3.4.13$$

where $T_{S\,dem}$ and $T_{S\,dem_{thres}}$ are de-lapsed Ts calculated as described later. For water and snow surface G can be estimated as

$$\frac{G}{R_n} = 0.5 \quad 3.4.14$$

where water bodies are identified with areas having NDVI<0 and snow areas with $T_S < 4$ C and $\alpha > 0.47$.

The sensible heat flux, H, can be estimated as

$$H = \frac{\rho\cdot c_P\cdot dT}{r_{ah}} \quad 3.4.15$$

where ρ is the air density kg m^{-3}, c_P the specific heat of air taken as 1004 J kg^{-1} K^{-1}, dT the temperature difference $(T_1 - T_2)$ between two heights (z_1 and z_2), and rah the aerodynamic resistance to heat transport (s m^{-1}). ρ can be estimated as described in Allen et al. 1998 as

$$\rho = \frac{1000\cdot P}{1.01\cdot(T_S - dT)\cdot R} \quad 3.4.16$$

where P is the atmospheric pressure where a single value can be estimated as described in Appendix (C).

The solution to *H* is obtained iteratively as described below with initial estimate of the aerodynamic resistance r_{ah} assuming neutral condition as

$$r_{ah} = \frac{ln\left(\frac{z_2}{z_1}\right)}{u_*\cdot k} \quad 3.4.17$$

where z_2 and z_1 are heights (m) above the zero displacement height, d, of the vegetation, u_* the friction velocity (m s^{-1}), k the von Karman's constant taken as 0.41. Under neutral conditions the friction velocity can be estimated as

$$u_* = \frac{k\cdot u_x}{ln\left(\frac{z_x}{z_{om}}\right)} \quad 3.4.18$$

where u_x is the wind speed (m s^{-1}) at height z_x , z_{om} the momentum roughness length (m) which can be estimated based on the vegetation height h following Brutsaert (1982) as

$$z_{om} = 0.12 \cdot h \qquad 3.4.19$$

The iterative procedure followed to estimate H can be summarized by

1- Estimate the wind speed, u_{200}, at the blending height of 200 m above the weather station which assumed constant for the entire scene as

$$u_{200} = u_* \frac{ln\left(\frac{200}{z_{om}}\right)}{k} \qquad 3.4.20$$

At the weather station u_*can be used to calculate using Eq. (xx) assuming neutral conditions. z_{om} can be estimated as described in Eq. xx using the canopy height at the weather station as h=0.3 which was based on data from Idaho.

2- Spatial estimates of u_* is then calculated for the entire area under study using as

$$u_* = \frac{k \cdot u_{200}}{ln\left(\frac{200}{z_{om}}\right)} \qquad 3.4.21$$

where spatial estimates of z_{om}can be calculated based on the availability of data as

a. In case of a land use map available z_{om} can be estimated for agricultural areas based on LAI (Tasumi 2003) as

$$z_{om} = 0.018 \cdot LAI \qquad 3.4.22$$

For other types of surfaces non-agricultural areas typical z_{om}values are suggested by Allen (2012) (Appendix C). A minimum value for z_{om} can be set as 0.005 for bare agricultural soils. However Tasumi et al. (2005b) indicated the insensitivity of estimated Eta to the value of z_{om}.

b. In case of no land use z_{om} can be estimated based on NDVI (Bastiaanssen 2000) as

$$z_{om} = exp(a \cdot NDVI + b) \qquad 3.4.23$$

Another suggested model by Allen et al. 2001a as

$$z_{om} = exp\left(a \cdot \frac{NDVI}{\alpha} + b\right) \qquad 3.4.24$$

where a and b are regression coefficient that need to be derived from plots of $\ln(z_{om})$ against $NDVI$ or $NDVI/\alpha$. Note that a and b need to be derived for each

vegetation type and local condition. z_{om} can be estimated based on canopy height and different albedo values can be selected for different surface cover types.

3- The aerodynamic resistance r_{ah} is then calculated, assuming neutral atmospheric conditions, using Eq. (3.4.17) along with u_* with the suggested values of z_1 and z_2. The height z_1 is just above the d and z_2 at some distance above d. The study by Bastiaanssen (1995) indicated that $z_1 = 0.1$ and $z_2 = 2.0$ m.

4- H is then calculated using Eq. 3.4.15 based on r_{ah} in step 3 and dT where

$$dT = T_{z_1} - T_{z_2} \quad 3.4.25$$

with T_{z_1} and T_{z_2} are the air temperature at $z_1$and $z_2$respectively. However it is not necessary that T_{z_1} and $T_{z_2}$to be known and as indicated by Bastiaanssen et al. 1995 that dT can be assumed is linearly related to Ts as $dT = b + a \cdot T_{s\_dem}$ with a and b are empirical calibration coefficients determined for a given satellite scene. T_{s_dem} is the radiometric surface temperature delapsed adjusted to a common arbitrary elevation and it can be estimated as $T_{s\_dem} = T_s + Lapse$ with lapse (K) can be estimated based on digital elevation model as described in Appendix C.

The linear relationship between Ts and dT can be developed using information about surface energy budget at two extreme ends of known ET conditions. These two extreme ends are defined at the coldest wet and hot dry agricultural fields for each individual scene. The ET at these two cold and hot pixels defined as ET_{cold} and ET_{hot} will have known values. For the cold pixel ET_{cold} can be estimated as

$$ET_{cold} = 1.05 \cdot ET_r \quad 3.4.26$$

where ETr is the reference ET for alfalfa crop. The 5% increase in ETr was to consider wet soil surface condition under the full cover at LAI >4.0 and dense vegetation conditions. However during non-growing season where the coldest pixel might has ET_{cold} lower than that of ETr the relationship developed by Tasumi et al. (2005a) can be used. H_{cold} and dT at the cold pixel can be calculated based on the surface energy balance as

$$H_{cold} = R_n - G - 1.05 \cdot ET \quad 3.4.27$$

$$dT_{cold} = \frac{H_{cold} \cdot r_{ah\_cold}}{\rho_{cold} \cdot c_P} \quad 3.4.28$$

During non-growing season ET_{cold} can be estimated as $ET_{cold} = a \cdot NDVI \cdot ET_r$ with a varies between 1.25-1.3.

For the hot pixel ET_{hot} is assumed as zero. However, it is recommended to make sure that this assumption is valid by considering the weather data for a period of 10 days before. In some cases, a residual evaporation from the bare soil surface can be considered

as 0.05-0.15 of ETr. Based on this assumption H_{hot} and dT_{hot} can be estimated as $H_{hot} = R_n - G$ and $dT_{hot} = (H\_hot \cdot r\_(ah\_hot))/(\rho\_hot \cdot c\_P)$

Using the information from the hot and cold pixels a linear relationship can be developed and the coefficient a and b in Eq. xx can be estimated as $a = (dT_{hot} - dT_{cold})/(T_{s\_hot} - T_{s\_cold})$ and $b = dT_{hot} - a \cdot T_{s\_hot}$

A map of dT can be calculated using Eq. (3.4.25) which can be used to estimate H. An approximate air temperature can also be estimated as $T_a = T_s - dT$.

5- Correction for atmospheric stability condition is accounted for using Monin-Obukhov similarity theory (MOST) as described in Appendix C. with $z_1 = 0.1$ and $z_2 = 2.0$, Ψ_m and $\Psi_h$can be estimated as described in Appendix C.

6- Using an iterative process steps 4-5 are repeated to calculate the sensible heat flux using the updated values of rah and u_*until the successive values for dT_{hot} and rah at the hot dry pixel stabilized. Generally, this process takes about 4 to 5 steps of iterations at which the correct values of H is estimated.

Note that the METRIC provide estimates of instantaneous LE which can be extrapolated to daily value using the reference ET fraction (ETrF) as $ETrF = ET_{inst}/ET_r$ with $ET_{inst}$is the instantaneous ET in depth of water units (mm hr^{-1}) equivalent to the instantaneous LE (W m^{-1}) which can be estimated as $ET_{inst} = 3600 \cdot LE/\lambda$ with λ is the latent heat for vaporization (J kg^{-1}) calculated as $\lambda = \left(2.501 - 0.00236 \cdot (T_s - 273)\right) \cdot 10^6$

The daily ET in units of mm day^{-1}, ET_{24} , can be estimated s

$$ET_{24} = ETrF \cdot ET_{r\_24} \qquad 3.4.29$$

where ET_{r_24} is the cumulative 24-hour ETr for the day of the image.

Typical data needed for the application of METRIC model are provided in Table 8 with examples of model results over selected areas in Table 9.

Table 8: summary of input data needed for the application of the METRIC model.

Data	Source	Spatial Resolution
Weather forcing		
Air Temperature (Ta)	Ground Observation	Local Scale
Wind Speed (u)	Ground Observation	Local Scale
Vapor Pressure (ea)	Ground Observation	Local Scale
Biophysical parameters		
Leaf Area Index (LAI)	Airborne/ Landsat/ MODIS	1–1000 m
Land use classification (optional)	Airborne/ Landsat/ MODIS	1–1000 m
Digital Elevation Model	Hydro1k/ NED	30 –1000 m
Remote Sensing		
Radiometric surface temperature (T_R) (top of the atmosphere)	Airborne, Landsat, MODIS	1–1000 m
Multispectral reflectance (top of the atmosphere)	Airborne, Landsat, MODIS	1–1000 m

Table 9: Example of applications of METRIC model and the reported performance.

Study area, dataset	Climatic Region	Land Use	Domain	Performance ET	Citation
Ames, Iowa SMACEX, 2002	Humid	Corn, soybean	Walnut Creek Watershed	RMSE: 0.6-0.9 mm/day	(Gonzalez-Dugo et al. 2009)
Montpelier, Idaho, 1985	Semi-arid	Sedge forage crop	Bear River Basin	RE: ±16% mm/day RE: 4% seasonal	(Allen et al. 2007a)

3.5. SEBS Model

General

Similar to SEBAL and METRIC models, the SEBS model treats the surface as one-source to formulate its network resistance for the estimation of the sensible heat flux, H. With the application of energy balance at the surface, the model calculates the latent heat flux using a constrained residual method. The model applies a modified Penman-Monteith equation provided by Menenti (1984) at known limiting surface condition combined with evaporative fraction concept to estimate a constrained values of H and λE. Moreover, a physically based estimate of the roughness length for heat transport is introduced in SEBS. As indicated by Su et al. (2005), the model is designed so that it can be applied at local to regional scales and therefore at different spatial resolutions.

It is observed that differently from the previously described models TSEB and METRIC (Sections 3.1 and 3.4), the SEBS model does not consistently estimate Rn or its components. As indicated by Su et al. (2005); Su (2002), all Rn components can be based on measurements, partially estimated, or parameterized. So when comparing SEBS performance with models that use similar energy balance remote sensing based approaches, this could be in its advantage.

Model Description

The model applies the surface energy balance equation to estimate the different fluxes as

$$R_n = G_0 + H + \lambda E \qquad 3.5.1$$

with R_n calculated as

$$R_n = (1 - \alpha) \cdot R_{swd} + \varepsilon \cdot R_{lwd} - \varepsilon \cdot \sigma \cdot T_0^4 \qquad 3.5.2$$

with α is the broadband albedo in the visible and near-infrared band, R_{swd} the downward shortwave radiation, R_{lwd} the downward longwave radiation, ε the broadband emissivity in the thermal infrared band, σ the Stefan-Boltzman constant, T_0 the radiometric surface temperature. In most of the model applications, ε is calculated based on a model described by Chen et al. (2004) as

$$\varepsilon = \varepsilon_c \cdot f_c + \varepsilon_s \cdot (1 - f_c) \qquad 3.5.3$$

where $\varepsilon_c$and ε_s are the canopy and soil emissivities, respectively, taken as 0.985 and 0.978 when using Landsat data. In some applications of SEBS, the value of ε is estimated based on Ta using the Swinbank equation described in Campbell and Norman (1998). The albedo is obtained from MODIS data for regional applications and sometime typical values from literature are used. R_{swd} and R_{lwd} generally from measurements and in some cases R_{lwd} is estimated using the Stefan-Boltzman equation which require *Ta* measurements at a reference height.

The soil heat flux ,G_0, is estimated as a function of R_n as

$$G_0 = [\Gamma_c + (1 - f_c) \cdot (\Gamma_s - \Gamma_c)] \cdot R_n \quad 3.5.4$$

with $\Gamma_c = 0.05$ for full vegetation cover (Monteith 1973) and $\Gamma_s = 0.315$ for bare soil (Kustas and Daughtry 1990), f_c the fraction of vegetation cover estimated as a function of the vegetation index NDVI (Baret et al. 1995) as

$$f_c = 1 - \left(\frac{NDVI - NDVI_c}{NDVI_s - NDVI_c}\right)^k \quad 3.5.5$$

where $NDVI_s$ and $NDVI_c$ are the NDVI values for bare soil and full canopy cover, respectively, k varies between 0.6-1.25 with a value of 0.6175 used by McCabe and Wood (2006).

The turbulence heat fluxes H and LE are estimated applying the Monin-Obukhov similarity theory MOST. Following MOST the sensible heat flux can be estimated as

$$\theta_0 - \theta_a = \frac{H}{k u_* \rho c_p}\left[ln\left(\frac{z - d_0}{z_{oh}}\right) - \Psi_h\left(\frac{z - d_0}{L}\right) + \Psi_h\left(\frac{z_{0h}}{L}\right)\right] \quad 3.5.5$$

where θ_0 is the potential temperature at the surface, θ_a the potential air temperature at height z above the surface, $\theta_0 - \theta_a$ represents the mean temperature, k Von Karman constant taken as 0.40, c_p is the specific heat of air, d_0 the zero plane displacement height, z_{0m} roughness height for momentum transfer, z_{0h} the roughness height for heat transfer, u_* the friction velocity estimated as $u_* = (\tau_0/p)^{1/2}$ with p the air density, and L is the Obukhov length defined as

$$L = -\frac{\rho C_p u_*^3 \theta_v}{kgH} \quad 3.5.6$$

with θ_v is the potential virtual temperature near the surface and g the gravitational acceleration. The mean wind speed profile can be defined as

$$u = \frac{u_*}{k}\left[ln\left(\frac{z - d_0}{z_{0m}}\right) - \Psi_m\left(\frac{z - d_0}{L}\right) + \Psi_m\left(\frac{z_{0m}}{L}\right)\right] \quad 3.5.7$$

The surface roughness parameters z_{0m}, z_{0h}, and d_0 can be estimated using three different methods depending on the availability of data as indicated by Su (2002) using

a- The model proposed by Massman (1997) and tested by Su et al. (2001) if near surface wind speed, leaf area index, and vegetation height data are available.
b- The empirical relationships proposed by Brutsaert (1982) if only vegetation height data are available.
c- The tabulated values by Wieringa (1986, 1993)

with respect to option (a) tz_{0h} can estimated as

$$z_{0h} = z_{0m}/exp(kB^{-1}) \quad 3.5.8$$

where B^{-1} is the inverse Stanton number. The value of kB^{-1} can be estimated using the proposed model by Su et al. (2001) as

$$kB^{-1} = \left[\frac{kC_d}{4C_t \cdot (u_*/u(h) \cdot (1-e^{-n_{ec}/2}))}\right] \cdot f_c^2 + 2f_c f_s \left[\frac{k \cdot (u_*/u(h) \cdot (z_{0m}/h))}{C_t^*}\right] + kB_s^{-1} f_s^2 \quad 3.5.9$$

where C_d is the drag coefficient of the foliage elements taken as 0.2, C_t the heat transfer coefficient of leaf which has the range of $0.005N \leq C_t \leq 0.075$ with N is the number of sides of a leaf to participate in heat transfer, C_t^* the heat transfer coefficient for soil estimated as

$$C_t^* = Pr^{-2/3} Re_*^{-1/2} \quad 3.5.10$$

with Pr the Prandtl number and Re_* the roughness Reynold number estimated as

$$Re_* = h_s u_* / \nu \quad 3.5.11$$

with hs the roughness height of the soil, ν the kinematic viscosity of the air estimated as

$$\nu = 1.327 \cdot 10^{-5} \cdot (p_0/p) \cdot (T/T_0) \quad 3.5.12$$

with p and T the ambient pressure and temperature and p_0= 101.3 kPa and T_0=273.15K.
The within-canopy wind speed profile extinction coefficient n_{ec} can be estimated as a function of the cumulative leaf drag area at the top of the canopy as

$$n_{ec} = \frac{C_d \cdot LAI}{2u_*^2/u(h)^2} \quad 3.5.13$$

where C_d is the drag coefficient of the foliage elements taken as 0.2, LAI is the leaf area index, u(h) the horizontal wind speed at the top of the canopy. The value of the LAI can be obtained either from ground based measurements (Su et al. 2005) or remote sensing based estimates as a function vegetation indices (McCabe and Wood 2006; Su et al. 2005) as

$$NDVI = 0.6868 \cdot LAI^{0.1810} \quad 3.5.14$$

For a bare soil surface case the kB_s^{-1} is estimated using Brutsaert (1982) model as

$$kB_s^{-1} = 2.46(Re_*)^{1/4} - ln(7.4) \quad 3.5.15$$

By introducing the concept of evaporative fraction (Λ) and using the surface energy balance at two limiting conditions λE can be estimated. During a dry condition when λE_{dry} approaches 0 and sensible heat flux, H_{dry} , is at its maximum value the surface energy balance can be described as

$$\left.\begin{array}{l}\lambda E_{dry} = R_n - G_0 - H_{dry} \equiv 0, \ \ or \\ H_{dry} = R_n - G_0\end{array}\right\} \quad 3.5.16$$

During a wet-limit condition, the sensible heat flux is at its minimum and the latent heat flux, λE_{wet} , approaches its maximum or potential value and the sensible heat flux, H_{wet} , at its lowest value the surface energy balance can be described as

$$\left.\begin{array}{l}\lambda E_{wet} = R_n - G_0 - H_{wet} \equiv 0, \ \ or \\ H_{wet} = R_n - G_0 - \lambda E_{wet}\end{array}\right\} \quad 3.5.17$$

The concept of relative evaporative fraction, Λ_r , can be described as

$$\Lambda_r = \frac{\lambda E}{\lambda E_{wet}} = 1 - \frac{\lambda E_{wet} - \lambda E}{\lambda E_{wet}} \quad 3.5.18$$

Or in terms of sensible heat flux as

$$\Lambda_r = 1 - \frac{H - H_{wet}}{H_{dry} - H_{wet}} \quad 3.5.19$$

The value of H estimated as described in Eq. xx is constrained by the two limiting wet and dry conditions of H_{wet} and H_{dry}. The limiting H_{wet} during wet conditions is estimated using a modified Penman-Monteith P-M equation (Monteith) of λE described by Menenti (1984). When grouping the resistance terms into bulk internal (stomatal) and external (aerodynamic) the P-M equation can be described as indicated by Menenti (1984) as

$$\lambda E = \frac{\Delta \cdot r_e \cdot (R_n - G_0) + \rho C_p \cdot (e_{sat} - e)}{r_e \cdot (\gamma + \Delta) + \gamma \cdot r_i} \quad 3.5.20$$

where Δ the saturation vapor pressure gradient with respect to temperature, e and e_{sat} the actual and saturated vapor pressure, γ the psychrometeric constant, r_e the aerodynamic resistance, and r_i the bulk surface internal resistance. As there is some difficulty in estimating r_i which is function of the water availability using the wet limit eliminate the need to estimate r_i as it approaches 0. Therefore, during wet limit and combining Eqs. Xx and xx H_{wet} can be estimated as

$$H_{wet} = \frac{(R_n - G_0) - \left[\frac{\rho C_p}{r_{ew}}\right] \cdot \left[\frac{e_s - e}{\gamma}\right]}{1 + \frac{\Delta}{\gamma}} \quad 3.5.21$$

The external resistance r_e can be estimated as

$$r_e = \frac{1}{k u_*}\left[ln\left(\frac{z - d_0}{z_{0h}}\right) - \Psi_h\left(\frac{z - d_0}{L}\right) + \Psi_h\left(\frac{z_{0h}}{L}\right)\right] \quad 3.5.22$$

and the external resistance at the wet limit r_{ew} can be estimated as

$$r_{ew} = \frac{1}{ku_*}\left[ln\left(\frac{z-d_0}{z_{0h}}\right) - \Psi_h\left(\frac{z-d_0}{L_w}\right) + \Psi_h\left(\frac{z_{0h}}{L_w}\right)\right] \quad 3.5.23$$

with L_w the wet limit stability length estimated as

$$L_w = -\frac{\rho u_*^3}{0.61 \cdot k \cdot g \cdot [(R_n - G_0)/\lambda]} \quad 3.5.24$$

The latent heat flux, λE can be estimated using the evpoarative fraction Λ as

$$\Lambda = \frac{\lambda E}{R_n - G_0} = \frac{\Lambda_r \cdot \lambda E_{wet}}{R_n - G_0} \quad 3.5.25$$

The model input data provided in Table 10 represents typical requirements as there were variability on the methods followed to obtain values of R_n either from measurements or estimates. Examples of SEBS model application and reported performance is shown in Table 11

Table 10: Summary of input data needed for the application of SEBS model.

Data	Source	Spatial Resolution
Weather forcing		
Incoming shortwave solar radiation (Sd)	Ground Observations/ NLDAS/GOES	14-20 km
Downwelling longwave radiation (Ld)	Ground Observations/ NLDAS/GOES	14-20 km
Air Temperature (Ta)	Ground Observations/ NLDAS	Local scale- 14 km
Wind Speed (u)	Ground Observations/ NLDAS	Local scale- 14 km
Vapor Pressure (e_a)	Ground Observations/ NLDAS	Local scale- 14 km
Atmospheric Pressure (P)	Ground Observations/ NLDAS	Local scale- 14 km
Biophysical parameters		
Leaf Area Index (LAI)	Ground Observations/ Landsat/ MODIS	Local scale -1 km
Canopy Height (hc)	Ground Observations/ Based on land cover type	Local scale -1 km
Land use classification	Landsat/ ASTER/ MODIS	30-1000 m
Albedo	Landsat/ ASTER/ MODIS	30-1000 m
Remote Sensing		
Radiometric surface temperature (T_R) (atmospheric correction)	ASTER/ Landsat/ MODIS	15-1000 m
Multispectral reflectance (atmospheric correction)	ASTER/ Landsat/MODIS	15-1000 m

Table 11: Example of applications of SEBS and the reported performance.

Study area, dataset	Climatic Region	Land Use	Domain	Performance RMSE W/m^2					Citation
				Rn	G	H	LE	N	
Maricopa, AZ, 1987	Semi-arid	Cotton	Research Site	23	5	21	29	19	(Su 2002)
Walnut Gulch, AZ, 1990,	Semi-arid	Shrubland	Walnut Gulch Experimental	35	46	29	83	320	(Su 2002)
MONSOON'90	Semi-arid	Grassland	Watershed	41	43	37	61	281	(Su 2002)
Ames, Iowa SMACEX, 2002	Humid	Corn Soybean	Walnut Creek Watershed				47 44		(Su et al. 2005)

RMSE: root mean square error

3.6. ReSET Model

General

The ReSET model presented by Elhaddad and Garcia (2008) is based on the same modeling concept of SEBAL developed by Bastiaanssen et al. (1998a). To model the exchange of mass and energy at the surface, ReSET assumes the surface as a homogenous extended one-layer. It applies the surface energy balance equation to estimate the latent heat flux, LE, as the residual. These instantaneous estimates of LE can then be extrapolated to daily values of ET. Typically, thermal-based remote sensing models such as TSEB, SEBAL, METRIC and SSEBop including ReSET basically provide estimates of ET during satellite overpass dates. In the case of using Landsat data, which has ideal spatial resolution for agricultural applications, the maps of ET can be obtained every 16-days or sometimes 8 days. To fill in the gap in between satellite overpass dates, different methods were applied and presented in many studies. These gap filling methods are not particularly part of modeling approach such as TSEB, SEBAL, METRIC, ReSET and other thermal-based models. (Elhaddad and Garcia 2008) suggested the use of a simple linear temporal interpolation approach to fill-in the gap based on measured actual ET. To account for regional variation of near surface wind speed, the ReSET model also suggests the use of spatially interpolated ground-based wind speed measurements. As indicated by (Elhaddad and Garcia 2008), these two modifications are meant to account for the spatial and temporal variability of ET estimates to support local to regional scale applications.

Additional modifications to the ReSET model were introduced by (Elhaddad and Garcia 2011) that account for the spatial variability in the hot and cold pixels as well as reference ET (ET0). Typical applications of SEBAL, METRIC which the ReSET is based on, use a single hot and cold pixel as well as reference ET to estimate actual ET for an entire scene regardless of the size of the study area. These modifications include the development of maps of hot and cold pixel and reference ET. Using such maps allows to account for spatial variation of sensible and latent heat fluxes H and LE, respectively. The sensible heat flux, H, in ReSET is estimated based on these two anchoring hot and cold pixels. It is assumed that H at the cold pixel is zero and at the hot pixel LE is zero.

Model Description

The net radiation (R_n) at the surface in the ReSET model is estimated based on the basic principles of radiation balance as

$$R_n = (1 - \alpha)R_s + \varepsilon_a \cdot \sigma \cdot T_a^4 - \varepsilon_s \cdot \sigma \cdot T_s^4 \qquad 3.6.1$$

where Rs is the incoming shortwave solar radiation (W m-2), α the surface albedo, Ta and Ts are the air and radiometric surface temperature (K), respectively, and ε_a and ε_s are the emissivity of air and surface, respectively. The soil heat flux, G, is estimated as a function of Rn, NDVI, Ts and α as shown in Eq. (3.4.12) that was originally described by Bastiaanssen et al. (1998a).

The sensible heat flux, H, is estimated using Eq. (3.4.16) which was originally described by Bastiaanssen (1998). A linear relationship can be developed between *dT* and the radiometric

surface temperature Ts as $dT = aT_s + b$ using information from two anchoring hot and cold pixels. It is assumed that the values of H and LE at the cold and hot pixels are known with and equal zero. At the hot pixel, a value of zero basically indicates that there is no evapotranspiration (ET) occurring over a fallow dry agricultural field. The energy balance equation at surface can be described as $H = R_n - G$. With this value of H at the hot pixel the corresponding value of dT can then be estimated. It is important to account for any wetting events for a period of at least a week before the satellite overpass dates that may induce soil evaporation and hence violating the assumption of zero ET. If such conditions are present, it is recommended that a water balance approach be used to estimate possible ET rates and the corresponding LE values. Over the cold pixel, a zero value of H basically indicates that ET is at its maximum rate at fully irrigated agricultural field. Based on this assumption, the value of dT equals zero. However, in some cases during internally calibrated mode, the model uses reference ETo to estimate the value of H as $H = R_n - G - 1.05 \cdot ET_r$ with ETr is reference ET for an alfalfa reference crop.

As the ReSET model is intended to be used for regional scale applications it accounts for spatial variability of ET by introducing a series of modifications including weather data and the anchoring hot and cold pixels. Instead of using wind speed measured at one weather station, the ReSET applies spatial interpolation approach i.e. ordinary kriging (Elhaddad and Garcia 2008) using information from multiple ground stations. The wind speed is needed during the calculation of aerodynamic resistance and H. Similarly, spatially distributed instantaneous reference ETr is also developed during the application of ReSET and applied during internally calibrated cases. However, it not specified at what conditions the ReSET model uses the internal calibration approach. Moreover, maps of hot and cold pixels account for spatial variability of ET from local to regional scales.

Typical model inputs include, in genera,l ground-based weather forcing data, remote sensing data including radiometric surface temperature and surface reflectance. Table 12 provide more details about the required model input. Example of applications of ReSET model with the resulted performance evaluation is summarized in Table 13. The application of the ReSET model using the described inputs the model performance for estimating ET showed an average relative error of about 12 mm day-1 based on comparison with ground-based lysimeter measurements.

Table 12: Summary of input data needed for the application of ReSET model.

Data	Source	Spatial Resolution
Weather forcing		
Air Temperature (Ta)	Ground Observation	Local Scale
Wind Speed (u)	Ground Observation	Local Scale
Vapor Pressure (ea)	Ground Observation	Local Scale
Biophysical parameters		
Leaf Area Index (LAI)	Landsat	1–1000 m
Land use classification (optional)	Landsat	1–1000 m
Digital Elevation Model	Hydro1k/ NED	30–1000 m
Remote Sensing		
Radiometric surface temperature (T_R) (top of the atmosphere)	Landsat	30–120 m
Multispectral reflectance (top of the atmosphere)	Landsat	30–m

Table 13: Example of applications of ReSET model and the reported performance

Study area, dataset	Climatic Region	Land Use	Domain	Performance ET	Citation
Bushland, TX	Semi-arid	Alfalfa Sorghum	Research sites	RE: 5% mm/day RE:-11% mm/day	(Elhaddad et al. 2011)
PVID, Ca	Semi-arid	Alfalfa	Research sites	RE: -1.5% annual	(Elhaddad et al. 2011)

RE: relative error

3.7. MODIS ET Model

General

The MODIS ET approach described by (Mu et al. 2011) to estimate ET is originally based on Penman-Monteith (P-M) equation of (Monteith 1965). Initial efforts of MODIS ET was presented by Cleugh et al. (2007) and followed by multiple revisions by Mu et al. (2007); Mu et al. (2011). The MODIS ET model is intended for operational regional and global scales applications for ET estimation. As its name suggests, the model utilizes mainly MODIS data at 1 km spatial resolution. However, this review discusses its potential use to monitor ET at field to local scales that is suitable for agricultural water use evaluation.

The P-M equation is originally designed and restricted for the application over vegetated areas assuming the surface as a one-source big leaf to estimate ET. MODIS ET approach, however, considered the surface consists of multiple sources defined by bare soil, canopy, and wet canopy leaves and the P-M equation on each. The MODIS ET approach further considered that each of these sources are formed of multiple sources. This approach has been followed to account for a wide range of surface conditions of bare soil and canopy from wet to dry and stressed to unstressed. The approach has been applied at such scales using.

This physically based approach provides estimates of actual ET by calculating the available energy as well as aerodynamic and surface resistances. As the model is applied at regional scale it uses daily meteorological reanalysis gridded datasets and provides estimates of ET at different temporal resolution including daily, 8-day, monthly and annual values.

Model Description

The MODIS ET is based on the Penman-Monteith (P-M) equation (Monteith 1965) which can be described as

$$\lambda E = \frac{s \cdot A + \rho \cdot C_p \cdot (e_{sat} - e)/r_a}{s + \gamma \cdot (1 + r_s/r_a)} \qquad 3.7.1$$

where λE is the latent heat of evaporation, λ latent heat flux, e_{sat} the saturated vapor pressure, s the rate of change in e_{sat} to air temperature, A the available energy partitioned between sensible, latent, and soil heat fluxes, ρ the air density, C_p specific heat capacity of air, r_a the aerodynamic resistance, γ the psychrometric constant estimated as $\gamma = C_p \cdot P_a \cdot M_a/(\lambda \cdot M_w)$ with M_a and M_w are the molecular masses of dry and wet air, respectively, r_s the effective surface resistance to evaporation from land surface and transpiration from plant canopy, P_a the atmospheric pressure.

The net radiation R_n can be estimated as

$$R_n = (1 - \alpha) \cdot R_s + (\varepsilon_a - \varepsilon_s) \cdot \sigma \cdot T_a^4 \qquad 3.7.2$$

where ε_s is the surface emissivity taken as es=0.97, R_s the downward shortwave radiation, and ε_a the air emissivity which can be estimated as

$$\varepsilon_a = 1 - 0.26exp^{(-7.7\times10^{-4}\times T_a^2)} \quad 3.7.3$$

The surface albedo α is taken from MODIS product, Ta the air temperature in (C).
In MODIS ET A represents the part of Rn that is partitioned between sensible and latent heat fluxes. A special case is introduced which assumes that there is no soil heat flux interaction between the soil and the atmosphere where the surface is 100% covered with vegetation. The available energy A and the related canopy and soil components A_c and A_{soil}, respectively, can be estimated as

$$\left.\begin{matrix} A=R_{net} \\ A_c=f_c\cdot A \\ A_{soil}=(1-f_c)\cdot A \end{matrix}\right\} \quad 3.7.4$$

The fraction of vegetation cover, f_c , is estimated as a function of the enhanced vegetation index (EVI) as

$$f_c = \frac{EVI-EVI_{min}}{EVI_{max}-EVI_{min}} \quad 3.7.5$$

with

$$EVI = Gian \cdot \frac{\rho_{NIR}-\rho_{red}}{\rho_{NIR}+C_1\cdot\rho_{red}-C_2\cdot\rho_{blue}+L} \quad 3.7.6$$

where ρ_{NIR}, ρ_{red}, and ρ_{NIR}, are the surface reflectance in the blue, red and near infrared bands, respectively, $Gian$ the gain factor taken as 2.5, L canopy background adjustment, C1 and C2 coefficients for the aerosol resistance (Huete et al. 2002), EVI_{min} and EVI_{max} are EVI values for bare soil and dense green vegetation and in some case can be taken as 0.05 and 0.95, respectively. However, in a recently revised version of MODIS ET, (Mu et al. 2011) suggested the use of fraction of absorbed photosynthetically active radiation fPARas a surrogate for f_c (Los et al. 2000) as

$$f_c = fPAR \quad 3.7.7$$

Where *f*PAR is obtained from the 8-day 1 km MODIS product.

The soil heat flux, G, can be estimated following Jacobsen and Hansen (1999) as

$$G_{soil} = \begin{cases} 4.73\cdot T_i - 20.87 \quad T_{min_{close}} \le T_{ann_{ave}} < 25°C, T_{day} - T_{night} \ge 5°C \\ 0.0 \quad T_{ann_{ave}} \ge 25°C \; or \; T_{ann_{ave}} < T_{min_{close}} \; or \; T_{day} - T_{night} \ge 5°C \\ 0.39\cdot A_i \end{cases} \quad 3.7.8$$

$$G = G_{soil}\cdot(1-f_c) \quad 3.7.9$$

where T_i is the daytime or nighttime average air temperature (C), $T_{min_{close}}$ the threshold value of air temperature below which the stomata will close completely and halt plant transpiration, $T_{ann_{ave}}$ the annual average daily air temperature in degrees, and G_{soil} represents the soil heat flux when f_c=0.0. The nighttime average air temperature cane be estimated as

$$T_{night} = 2.0 \times T_{ave} - T_{day} \quad 3.7.10$$

with T_{day} is the average daytime air temperature and, T_{ave} the daily average air temperature. The total daily λE and potential λE, λE_{pot} can be estimated as

$$\lambda E = \lambda E_{soil} + \lambda E_{trans} + \lambda E_{wet\_C} \quad 3.7.11$$

$$\lambda E_{pot} = \lambda E_{soil_{pot}} + \lambda E_{trans_{pot}} + \lambda E_{wet\_C} + \lambda E_{wet\_soil} \quad 3.7.12$$

where λE_{soil} is the evaporation from the soil surface, λE_{trans} the plant transpiration, and λE_{wet_C} evaporation from intercepted precipitation by canopy, $\lambda E_{soil_{pot}}$ the potential soil evaporation, $\lambda E_{trans_{pot}}$ the potential plant transpiration, and λE_{wet_soil} the evaporation from wet soil.

The soil evaporation λE_{soil} can be estimated considering different surface components moist (wet) and saturated surface conditions. The evaporation during moist (wet) soil surface λE_{wet_soil} can be estimated as

$$\lambda E_{wet\_soil} = \frac{(s \cdot A_{soil} + \rho \cdot C_p \cdot (1.0 - f_c) \cdot VPD / r_{as}) \cdot f_{wet}}{s + \gamma \cdot r_{tot} / r_{as}} \quad 3.7.13$$

where VPD is the vapor pressure deficit estimated as $(e_{sat} - e)$. The wet and saturated surface components are identified using f_{wet} which represents the fraction of the surface either bare soil of canopy that is covered by water. f_{wet} can be estimated using Fisher et al. (2008) model based on the relative humidity RH as

$$f_{wet} = \begin{cases} 0.0 & RH < 70\% \\ RH^4 & 70\% \leq RH \leq 100\% \end{cases} \quad 3.7.14$$

The aerodynamic resistance at the soil surface,r_{as}, which considered parallel to both resistances to convective and radiative heat transfer r_{hs} and r_{rs}, respectively, and can be estimated as

$$r_{as} = \frac{r_{hs} \cdot r_{rs}}{r_{hs} + r_{rs}} \quad 3.7.15$$

Description of how to estimate r_{hs} and r_{rs} is provided in Appendix D.

The soil evaporation during saturated conditions is at the potential rate and can be estimated as

$$\lambda E_{soil\_pot} = \frac{(s \cdot A_{soil} + \rho \cdot C_p \cdot (1.0 - f_c) \cdot VPD / r_{as}) \cdot (1.0 - f_{wet})}{s + \gamma \cdot r_{tot} / r_{as}} \quad 3.7.16$$

The total soil evaporation λE_{soil} can be estimated following Fisher et al. (2008) and Bouchet (1963) as

$$\lambda E_{pot} = \lambda E_{wet\_soil} + \lambda E_{soil\_pot} \cdot \left(\frac{RH}{100}\right)^{VPD/\beta} \quad 3.7.17$$

where the parameter β is taken as 200.

Evaporation from canopy interception is estimated based on Biome-BGC model by Thornton (1998) to

$$\lambda E_{wet\_C} = \frac{(s \cdot A_C \cdot f_c + \rho \cdot c_P \cdot (e_{sat} - e) \cdot f_c / rhrc) \cdot f_{wet}}{s + \frac{P_a \cdot c_P \cdot rvc}{\lambda \cdot \varepsilon \cdot rhrc}} \quad 3.7.18$$

where rvc is the wet canopy resistance to latent heat transfer estimated as the sum of the aerodynamic resistance, $rhrc$, and the surface resistance r_s. rvc and $rhrc$ can be estimated as described in Appendix F.

Plant transpiration, λE_{trans} , can be estimated as

$$\lambda E_{trans} = \frac{(s \cdot A_C \cdot f_c + \rho \cdot c_P \cdot (e_{sat} - e) \cdot f_c / r_a) \cdot (1 - f_{wet})}{s + \gamma \cdot (1 + r_s / r_a)} \quad 3.7.19$$

where r_a and r_s are the aerodynamic and surface resistances estimated as described in Appendix F.

The MODIS ET model was applied at global scale using local and global metrological data from ground observation and from the global modeling and assimilation office (GMAO). A summary of required input data for the application of MODIS ET is provided in Table 14. Example of model application and related performance statistics are shown in

Table 15. The provided summary results are obtained from the application of MODIS ET at the global scale compared with measured ET at selected FLUXNET sites (Mu et al. 2011).

Table 14: The input data needed for the application of MODIS ET model.

Data	Source	Spatial Resolution
Weather forcing		
Incoming shortwave Solar Radiation	AmeriFlux-GMAO*	Local scale-1 km
Air Temperature (Ta)	AmeriFlux-GMAO*	Local scale-1 km
Humidity (RH)	AmeriFlux-GMAO*	Local scale-1 km
Atmospheric Pressure (P)	AmeriFlux-GMAO*	Local scale-1 km
Biophysical parameters		
Leaf Area Index (LAI)	MODIS	1 km
Fraction of Absorbed Photosynthetic Active radiation (FPAR)	MODIS	1 km
Land use classification	MODIS	1 km
Albedo	CMG	0.05°
Biome Properties (Tmin_open, Tmin_close, VPD_open, VPD_close, gl_sh, gl_e_wv, Cl, RBL_min, RBL_max)	Look-up table	1 km
Remote Sensing		
Multispectral Reflectance/NDVI	MODIS	1 km

The GMAO data is originally at 1.0*1.25 degrees resampled to 1 km resolution (Zhao et al. 2005)
CMG: climate model grid

Table 15: Examples of applications of MODIS ET model and reported performance

Study area, dataset	Climatic Region	Land Use	Domain	Performance ET	Citation
AmeriFlux Sites, 2000-2006	Diverse	Mixed	Global	RMSE:0.9 (mm/day)	{Mu, 2011 #277}

3.8. SSEBop Model

General

The SSEBop model (Savoca et al. 2013)is an extension and operational version of the SSEB approach (Senay et al. 2007) and can be considered a semi-empirical model based on providing a direct relationship between ET_a and radiometric surface temperature. The SSEBop which is developed for operational applications can provide estimates of ET_a at multiple spatial scales including local, regional, and continental. The main assumption of SSEB is that a thermally based scaled evaporative fraction can describe the related vegetation and soil water consumption rate or specificallyET_a. The SSEBop suggests combining of this scaled evaporative fraction with the reference crop to estimate ET_a using a simple linear relationship. With such the SSEBop model assumes the surface as a one-source in modeling the evapotranspiration process. The scaled evaporative fraction can be considered as a normalized temperature difference that ranges between 0-1 developed for a given pixel. This is an important distinction for SSEBop where each pixel has its own lower and upper limits through the pre-defined dT parameter. The rationale of the SSEBop approach, is that models such as METRIC and SEBAL use similar assumptions to estimate the sensible heat flux, based on the differences between near-surface air temperatures. It is also similar in logic to the findings by (Sadler et al. 2000) that differences between soil surface and air temperature is linearly related to soil moisture.

Note that the SSEBop does not provide estimates of surface energy fluxes such as Rn, H, G, and LE but rather directly provides estimates of ET_a on daily and 8-day time scales. On the other hand, the SSEBop provides a parameterization to estimate clear-sky Rn which is key to estimate the pre-defined difference in temperature (dT) between the bare/dry (hot) and vegetated/wet (cold) surfaces. Moreover, the SSEBop suggests a methodology for predefining the limiting conditions that allows for the definition of the hot and cold pixel reference limits. The main input to SSEBop models are the reference ET_o and radiometric surface temperature. As the SSEBop was originally designed to be used over fairly homogenous horizontal agricultural surfaces, recent modifications have been included to account for areas with variable elevation as well as improving its performance over wide range of vegetation conditions.

Model Description

Although the SSEBop model does not solve all the energy balance terms explicitly, it defines the limiting conditions based on clear-sky net radiation balance principles. The SSEBop approach (Senay et al. 2013) pre-defines unique sets of “hot/dry” and “cold/wet” limiting values for each pixel unlike the original SSEB formulation which uses a set of reference hot and cold pixel-pairs applicable for a limited, uniform hydro-climatic region. To estimate ET routinely, the only data needed for the SSEBop method are surface temperature (*Ts,* K), air temperature (*Ta,* K) and grass reference ET (*ETo,* mm).

With this simplification, *ETa* can be estimated using Eqn. (1) as a fraction of the *ETo*. The ET fraction (ET_f) is calculated using Eq. (3.8.2).

$$ETa = ETf * k * ETo \quad (3.8.1)$$

where *ETo* is the grass reference ET for the location; *k* is a coefficient that scales the *ETo* into the level of a maximum ET experienced by an aerodynamically rougher crop such as alfalfa. A recommended value for *k* equal to 1 was used in this study (Senay et al. 2013; Singh et al. 2014). The ET fraction can be estimated as

$$ETf = \frac{Th - Ts}{dT} = \frac{Th - Ts}{Th - Tc} \quad (3.8.2)$$

where *Ts* is the satellite-observed radiometric surface temperature of the pixel whose ET_f is being evaluated on a given image date; *Th* is the estimated *Ts* at the idealized reference "hot/dry" limit of the same pixel for the same time period; *Tc* is the estimated *Ts* at the idealized "cold/wet" limit of the same pixel; dT is a pre-defined temperature difference between *Th* and *Tc;* Negative ET_f is set to zero.

The cold limiting condition, *Tc*, is calculated from *Ta* as follows. Because the satellite thermal data (*Ts*) is acquired during the morning hours at a nominal overpass time of 10:30 am, the daily maximum air temperature is more closely related to it than the daily minimum temperature. The maximum air temperature is more readily available from weather datasets than the hourly temperature for large scale applications. After examining the relationship between *Ts* and Daymet data (Thornton et al. 2014) daily maximum air temperature in well-vegetated pixels, where NDVI is greater than 0.8, a median correction coefficient of 0.985 was established from Landsat images acquisition in the US. (Senay et al. 2013) reported more details on the procedure used for establishing the correction coefficient, *c*. The overall approach of the SSEBop model is presented in Figure 6: Schematic of the SSEBop model methodology.Figure 6.

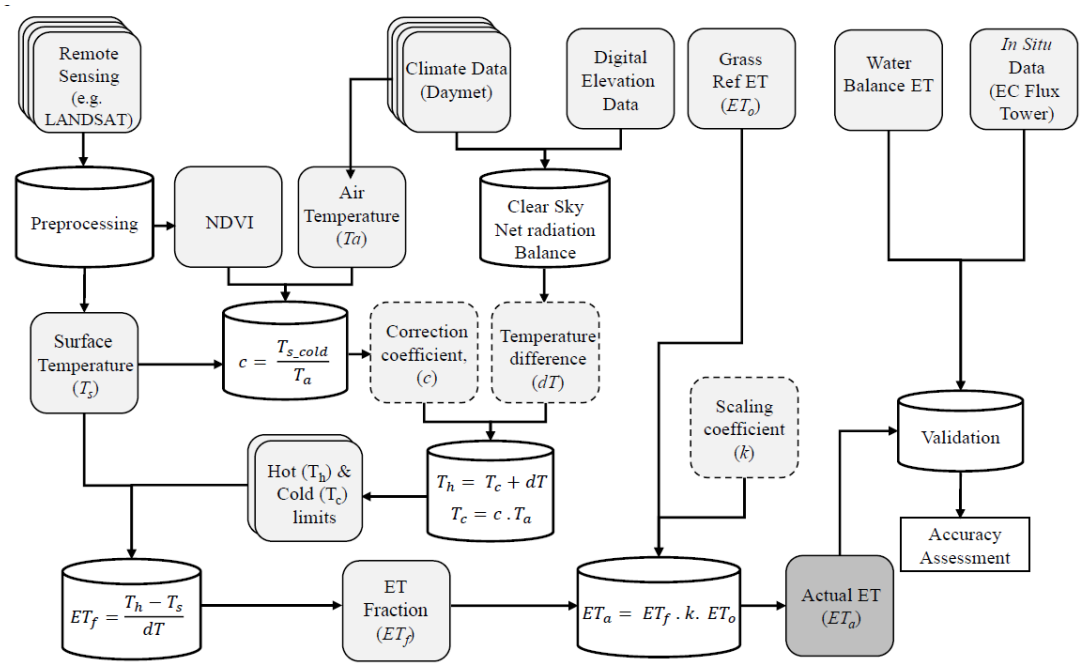

Figure 6: Schematic of the SSEBop model methodology.

In this case, *dT* is pre-defined for the study location as explained in (Senay et al. 2013) using the formulation in Equation 3. It is calculated under clear-sky conditions assumption and assumed not to change much from year to year, but is unique for each day and location.

$$dT = \frac{R_n \cdot r_{ah}}{\rho_a \cdot C_p} \qquad 3.8.3$$

where R_n is daily average clear-sky net radiation J.m^{-2}.s^{-1}, r_{ah} is the aerodynamic resistance to heat transfer from a hypothetical bare and dry surface, taken as 110 sm^{-1} (Senay et al. 2013), ρ_a is the density of air (kg/m^3), estimated as a function of air pressure and Ta (Allen et al. 1998b); C_p is the specific heat of air at constant pressure (1.013 kJ kg^{-1} K^{-1}). All are taken with multiplying factors for consistent energy, mass, volume and time units.

By rearrangement of Eqs. 3.8.1 – 3.8.3, *ETa* can be formulated as the product of commonly used surface energy balance parameters as shown in Eq. 3.8.4.

$$ET_a = \frac{\rho_a \cdot C_p}{R_n \cdot r_{ah}} (Th - Ts) \cdot k \cdot ET_O \qquad 3.8.4$$

The most important simplification is based on the knowledge that the surface energy balance process is mainly driven by the available net radiation (*Rn*). Since thermal remote sensing is conducted under clear-sky conditions, the SSEBop method assumes a location- and date-specific constant temperature difference, *dT,* between the hot/dry and cold/wet limiting reference points. While converting the daily average *Rn* into sensible heat flux at the time of satellite-overpass, we realize the temporal mismatch between the instantaneous satellite-overpass and the daily average *Rn*. As empirical data showed, the daily average clear-sky *Rn* is a good predictor of the available

cumulative energy that would raise the temperature of a bare-dry surface at the time of satellite overpass, with a seasonal range of 2 to 25 K on winter and summer days, respectively. This not only assumes clear-sky at the time of satellite overpass but also clear-sky for the entire day. However, this assumption is only used to get an empirical estimate of *dT*, but not to solve the energy balance at the time of satellite overpass and hence the approach appears to hold as good estimator of *dT*, removing the need to manually select hot and cold pixels.

The input data for the application of SSEBop are summarized in Table 16. Note that SSEB and SSEBop models were designed for applications over agricultural and other vegetated areas at local to continental scales to provide estimates of ET_a at daily-8-day and monthly-annual scales, respectively. Examples of SSEB and SSEBop applications with the reported performance are provided in Table 17.

Table 16: Summary of input required for the application of SSEBop model

Input variable	Source	Spatial Resolution
Weather forcing		
Readily available reference ET (ET_o), or Air temperature (Ta) Temperature correction coefficient (Tc)	Ground Observations, GLDAS, Daymet	Local scale
Biophysical parameters		
Digital elevation Model DEM	SRTM, Hydro1k, NED	30 – 1000 m
Albedo	MODIS	1000 m
Remote Sensing		
Radiometric surface temperature (T_R) (atmospherically corrected)	Landsat, MODIS	100 – 1000 m
Surface Reflectance (atmospherically corrected)	Landsat, MODIS	30 – 250 m

Table 17: Examples of SSEBop model application and reported performance.

Study area, dataset	Climatic Region	Land use	Domain	Performance (ET mm/month)	Citation
CONUS, Flux NET	Diverse	Crop, forest, shrubland, grassland	CONUS, MODIS	RMSE: 8.5 to 20 mm, single towers	Senay et al, 2013
CONUS, EC Flux Towers	Diverse	crop, forest, shrubland, grassland	CONUS, MODIS	RMSE: 24 - 30 mm multiple towers,	Velpuri et al., 2013
Texas High Plains, Lysimeter	Humid	corn and sorghum	Research site, Landsat	RMSE: 12% of mean at seasonal scale	Senay et al, 2014
Colorado Rivers Basin	Arid-semiarid	Mixed	Basin wide, Landsat	MBE of 10%, single stations	Singh et al, 2014

MBE: Mean Bias Error

3.9. PT-JPL Model

General

The PT-JPL model described by Fisher et al. (2008) basically utilizes the Priestly-Taylor (PT) equation (Priestley and Taylor 1972) to estimate latent heat flux LE. It has proven to work well under different land surface conditions. The approach followed by Fisher et al. (2008) is based on reducing the potential to actual rates of LE using plants physiological limits and a soil drought constraint. These physiological limits used in PT-JPL include the leaf area index, the fraction of green canopy cover that is actively transpiring, and plant temperature and soil moisture. The PT equation represents an empirical one-source model parameterization for estimating LE. However, the PT-JPL assumed the surface consists of multiple sources and the PT equation is applied for each. The total actual LE is the sum of the contributions from each of the defined surface components. Fisher et al. (2008) defined three surface components where the PT is applied including bare soil, vegetation canopy, and wet canopy leaves due to precipitation interception. This is similar to the approach followed in MODIS ET when applying P-M equation over different surfaces to estimates the total LE.

The intent of the PT-JPL model is to provide estimates of LE on a monthly basis and at global scales. However, this review explores its potential use for local to regional scales and daily temporal resolutions. The model as described by Fisher et al. (2008) provides only estimates of LE and in some cases the net radiation Rn.

Model description

The original PT equation to estimate LE can be described as

$$LE = f_g \alpha_{PT} \frac{\Delta}{\Delta+\gamma} Rn \qquad 3.9.1$$

where f_g is the fraction of the green cover, α_{PT} known as PT constant taken as 1.26, Δ the slope of the saturation-vapor pressure curve, and γ the psychrometric constant~$0.066\ kPa\ °C^{-1}$. The fraction of green cover $f_g$is calculated as

$$f_g = \frac{f_{APAR}}{f_{IPAR}} \qquad 3.9.2$$

where f_{IPAR} is the fraction of photosynthetically active radiation integrated by total vegetation cover and can be estimated as a linear function of NDVI based on (Zhang et al. 2005) as

$$f_{IPAR} = 1.0 \times NDVI - 0.05 \qquad 3.9.3$$

with $0.05 < NDVI < 1.0$ and $0.0 < f_{IPAR} < 0.95$.

while f_{APAR} is the fraction of photosynthetically active radiation absorbed by green vegetation cover and can be estimated as a linear function of SAVI based on Gao et al. (2000) as

$$f_{APAR} = 1.2 \times 1.136 \times SAVI + 1.2 * (-0.04) \quad 3.9.4$$

Note that was originally obtained using EVI instead of SAVI, however, as indicated by Gao et al. (2000) and Fisher et al. (2008) both behave similarly and account for soil background effects which allow for more accurate estimation of the green vegetation cover.

The net radiation over canopy and bare soil components Rn_c and Rn_s are estimated based on Beer's law (Fisher et al. 2008) as

$$\left.\begin{aligned} Rn_s &= Rn \cdot exp(-k_{Rn} \cdot LAI) \\ Rn_c &= Rn - Rn_s \end{aligned}\right\} \quad 3.9.5$$

with k_{Rn} is the extinction coefficient taken as 0.60, the total green and non-green leaf area index LAI can be estimated based on inverted Beer's low (Ross 1975) as

$$LAI = \frac{-ln(1-f_c)}{k_{PAR}} \quad 3.9.6$$

with k_{PAR} taken as 0.5.

The model provide estimates of LE for different surface components bare soil, canopy cover, and interception defined as LE_S, LE_C, and LE_i , respectively with the total LE equal to

$$LE = LE_C + LE_S + LE_i \quad 3.9.7$$

Canopy transpiration,LE_C, can be estimated as

$$LE_C = (1 - f_{wet}) \cdot f_g \cdot f_T \cdot f_M \cdot \alpha \frac{\Delta}{\Delta+\gamma} Rn_c \quad 3.9.8$$

where f_{wet} is the fraction of the wet surface which can be predicted based on the relative humidity RH as $f_{wet} = RH^4$ with threshold of $RH < 70\%$ for 0%, $RH = 93\%$ for 50%, and $RH = 100\%$ for 100% wet surfaces. This approach is similar to that followed by Stone et al. (1977)

The plant temperature constraint f_T can be estimated as (June et al. 2004)

$$f_T = exp\left(-\left(\frac{T_{max}-T_{opt}}{\lambda}\right)^2\right) \quad 3.9.9$$

where T_{max} is the maximum air temperature, and $\lambda = T_{opt}$. The optimum plant growth temperature, T_{opt}, which is estimated using an updated CASA model (Potter et al. 1993) by Fisher et al. (2008). The CASA model assumes that T_{opt} is the T_{max} at the peak canopy activity. Fisher et al. (2008) suggested that T_{opt} is the T_{max} when light absorptance, green leaf area, and temperature are high and VPD is low or

$$T_{opt} = T_{max} \ \ at\ max\left\{\frac{PAR \cdot f_{APAR} \cdot T_{max}}{VPD}\right\} \quad 3.9.10$$

The plant moisture constraint f_M can be estimated based on the relative change in light absorptance as

$$f_M = \frac{f_{APAR}}{f_{APAR_{max}}} \quad 3.9.11$$

with $f_{APAR_{max}}$ represents the maximumf_{APAR}. The described f_M equation mainly assumes that light absroptance varies in response to plant moisture stress and no moisture stress occur at peak light absorptance. This parameter has effects mainly over sites with seasonal droughts (Fisher et al. 2008).

The soil evaporation LE_s can be estimates as

$$LE_s = \left(f_{wet} + f_{SM}(1 - f_{wet})\right) \cdot \alpha \frac{\Delta}{\Delta+\gamma}(Rn_s - G) \quad 3.9.12$$

where f_{SM} is the soil moisture constraint which represents an index of the soil moisture deficit following the approach of Bouchet (1963) and can be estimated as

$$f_{SM} = RH^{VPD/\beta} \quad 3.9.13$$

with the constant β taken as 1.0 kPa.

The canopy interception evaporation component is estimated as

$$LE_i = f_{wet}\alpha \frac{\Delta}{\Delta+\gamma} Rn_c \quad 3.9.14$$

The PT-JPL was applied at global scale using gridded dataset from the International Satellite Land-Surface Climatology Project, Initiative II (ISLSCP-II) and validated over different climatic regions at FLUXNET sites. The input data required for the application of PT-JPL are provided in Table 18 and example of reported performance statistics shown in
Table 19.

Table 18: summary of input data required for the application of the PT-JPL model.

Data	Source	Spatial Resolution
Weather forcing		
Net Radiation (Rn)	FLUXNET, ISLSCP-II	Local scale-1°
Maximum Air temperature (Ta_max)	FLUXNET, ISLSCP-II	Local scale-1°
Actual Vapor Pressure (ea)	ISLSCP-II	1°
Relative Humidity (RH)	FLUXNET	Local scale
Vapor Pressure Deficit (VPD)	FLUXNET	Local scale
Remote Sensing		
Surface reflectance in the visible and near infrared bands (atmospherically corrected)	MODIS, AVHRR	250m-1°

Table 19: Examples of applications of PT-JPL model and reported performance

Study area, dataset	Climatic Region	Land use	Domain	Performance	Citation
Global/ FLUXNET	Diverse	mixed	Global	RMSE: 16 mm/month RMSE: 12 mm/year	{Fisher, 2008 #270}
Global, FLUXNET	Tropical	Mixed	Global	RMSE: 22.9 W/m^2 Monthly	(Fisher et al. 2009)

4. MODEL INPUTS, OUTPUTS AND EVALUATION

4.1. Model evaluations

The spatial estimates of SEBF and ET provided by most remote sensing based energy balance models are generally evaluated using ground -based measurements. For such, ground based measurements mostly consist of flux towers mounted with Bowen ratio (BR) or Eddy Covariance (EC) energy balance systems, lysimeters, scintillometers, and sapflow methods. Considering the differences in the scale of the measurements among these different methods, evaluation of remote sensing based SEBF is carried out on only small portion of an image map that covers hundreds of meters to a few kilometers due to the characteristics of the method. The general notion is that evaluating a small portion of the image should provide a good indication about the quality of the entire image map. This approach implies that the evaluation of modeled spatial maps of SEBF are based on the notion of synthesizing the comparison with measurements conducted at local scale is representative of the underlying larger scale spatial variability of the of area under study. However, there are a few issues that need to be considered including a) the differences in the spatial scales between estimates and measurements, b) the representativeness of the measurements and their locations with respect to the spatial surface variability, c) time scale of measurement compared to that of the estimates, d) accuracy and related uncertainties of measurements that vary with each of these methods.

Despite the fact that all of these types of ground based measurements have been used and described in the literature individually or combined, the majority of model evaluations have used BR and EC systems, and, to some extent, scintillometers. The use of EC has been favored out these three methods. Site specific, field campaigns, and regional experiments provided some of the SEBF in the US including for example the Soil Moisture-Atmosphere Coupling Experiment (SMACEX) conducted in Iowa (Kustas et al. 2005), the Southern Great Plain Experiment (SGP97) conducted in Oklahoma (Jackson et al. 1999), the First ISLSCP (International Satellite Land Surface Climatology Project) Field Experiment (FIFE) (Sellers et al. 1988, 1992) , and others with a combination of EC and BR systems. Global SEBF are provided for by FLUXNET (Baldocchi et al. 2001) with over 500 EC systems distributed over a wide range of land cover types.

With respect to the quality of the measurements in issues (c) and (d) above, several studies have reported about the performance of EC based flux measurements, as these systems provide independent measurements of turbulent heat fluxes. Studies have indicated that there is a lack of closure in the energy balance of about 20% (Twine et al. 2000). This issue has led to suggested methods (Brotzge and Crawford 2003; Twine et al. 2000) for energy balance closure by using either a Bowen ratio (H/LE) or Residual approach. The former approach is used to distribute the closure error between H and LE while the latter attributes the entire error to the LE measurements. There is no definitive agreement in the literature on which one should be followed. Both approaches have been equally applied and they can provide different indications about the quality of the estimated spatial SEBF.

Regarding the representativeness of measurements described in (a) and (b), studies have showed that direct comparison of measurements for evaluation of estimated SEBF may not be valid (Li et al. 2008) considering the use EC, BR, and scintillometer. Measured fluxes typically originate from an upwind area called source area (SA) or footprint that encompass few hundreds of meters to a few kilometers. The size of the flux footprints is dependent on atmospheric stability, wind direction and speed, surface roughness, and height of measurements. Examples of typical footprint for BR and scintillometer based measurements are shown in Figure 7. This indicates that the spatial extent of the measurements should be the same or larger in size than the spatial resolution of estimates (Brunsell et al. 2011; Li et al. 2008). This issue might be of a lesser effect with the use of scintillometers since they can have a footprint of few kilometers. Several footprint models are available in literature and varies in complexity including the model by Horst and Weil (1992, 1994), {Schmid, 1994 #381@@author-year;Schmid, 1997 #382@@author-year}and Hsieh et al. (2000) with a review provided by Schmid (2002). With other methods of measuring ET such as lysimeter and sapflow, the issue of mismatch of spatial scale between measured and estimated flux, which in this case ET, would be a concern. This issue will be evident except for estimates with spatial resolution on the same order of magnitude as measurements such as those based on airborne remote sensing.

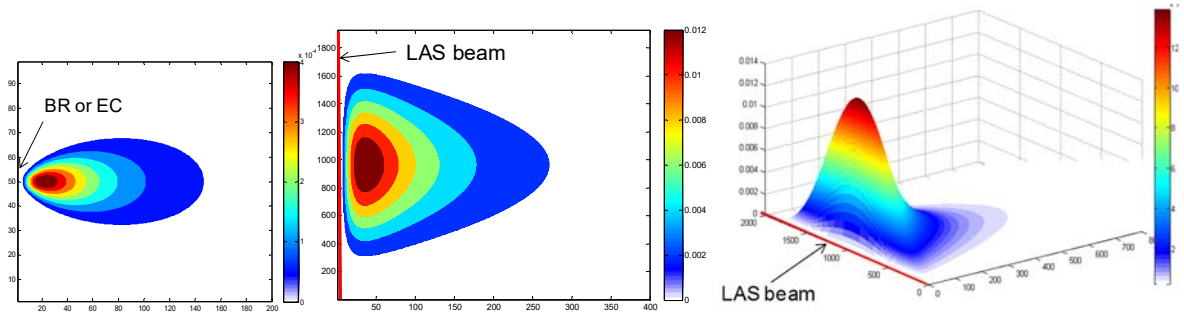

Figure 7: Typical footprints for EC/BR towers and scintillometer path

4.2. Extrapolation of ET across Time Scales

Some of the models, described above, especially those based on thermal remote sensing approaches, provide instantaneous estimates of SEBF at the satellite overpass time. For the interest of evaluating ET the latent heat flux is extrapolated to daily values of ET. Different extrapolation approaches have been used including the evaporative fraction (EF), reference ET fraction (ETrF), and others with variation in both (Chavez et al. 2008; Lhomme and Elguero 1999). Generally, most of these methods are based on preserving a functional ET metrics in terms of a fraction determined at the time of the scene. This fraction can be calculated using the estimated flux combined with meteorological measurements either reference ET or available energy. It is assumed that this fraction, which ranges between 0-1, is constant throughout the day. Several studies have indicated that such assumption is valid for data spanning between midmorning to midday as shown by Brutsaert and Sugita (1992); Lhomme and Elguero (1999) in the case of the EF, and Allen et al. (2007b) for the case of ETrF. Attention should be paid to early morning and late afternoon hours as this assumption might not hold. The preference of

using one method or the other was highlighted by Allen et al. (2007b); Chavez et al. (2008). They indicated that the EF method would work better over cropped lands with soil moisture stress, heterogeneous vegetation cover, and, generally, during non-advective conditions, while the ETrF worked better over unstressed croplands and advective conditions.

Extrapolation of daily ET to monthly and seasonal time period can be obtained by integrating the daily values. In the case of Landsat based estimates of daily ET, interpolation in between image dates can be carried for the ET fraction, e.g. ETrF. Using a reference ET from ground-based weather data, the daily actual ET can be calculated for these dates (Allen et al. 2007b). Another procedure for extrapolating to seasonal ET at the Landsat product resolution is the use of data fusion Spatial Temporal Adaptive Reflectance Fusion Model (STARFM) suggested by Gao et al. (2006). The method basically combines the high temporal, low spatial resolution surface reflectance data from MODIS with the low temporal, high spatial resolution of the Landsat to fill in the gaps between the Landsat-based estimates of ET-typically a thermal based modeled ET. The model predicts the temporal variability in the Landsat-based ET based spectral similarity, temporal difference, and spatial distance information obtained from a set of Landsat-MODIS scenes pairs.

4.3. Spatial and Temporal Resolution of Input Data.

Several studies (Anderson et al. 2012a; Kustas et al. 2003; Li et al. 2008) indicated that for mapping ET for agricultural applications, the moderate resolution of Landsat sensors with a spatial resolution of 60-120 m and 30 m in the thermal and the visible bands respectively, is the most suitable. Such resolution allows for monitoring individual crops that are useful for detailed water-use information and over all agricultural water management. Note that the thermal data of the Landsat at 60-120 m resolution is now provided at a higher resolution of 30 m. However, the coarse temporal resolution of 16-day provides one or two scenes per month during clear sky conditions. In the case of cloudy regions, the number of images per growing season would be limited to only a few which can contribute to reducing the accuracy of estimating seasonal ET. Anderson et al. (2012a)suggested that a 4-day revisit time of with the same nominal spatial resolution of the Landsat sensors would be the optimal for agricultural application. On the other hand, the high temporal spatial resolution data of 1-2 day of MODIS sensors provide a continuous monitoring tool for tracking the variability of the surface and canopy growing conditions. The limiting factor with MODIS data however, is its coarse spatial resolution of 1 km in the thermal band. Such resolution does not allow to discriminate ET from individual cropped fields. With the use of non-thermal based models such as those inferring ET from vegetation indices, the spatial resolution of MODIS data in the visible bands of 250-m could allow for mapping of ET over individual crop fields when these fields are in the same order of magnitude. Based on the findings of Anderson et al. (2012a), it is argued that such VI-based methods would over estimate ET during fast drying periods of canopy.

In an effort to providing continuous remote sensing data that is suitable for agricultural application, a thermal sharpening approach was presented by Agam et al. (2008); Kustas et al. (2003). The main concept of this approach, is to use vegetation variability information accounted for in terms of VIs obtained from the visible bands to increase the resolution of the thermal band i.e. the thermal bands of Landsat and MODIS can be sharpened to 30-m and 250-m, respectively.

As the sharpening approach was applied on Landsat and MODIS datasets it was indicated they work better when variations in surface moisture are already well captured by the thermal signal. This has been typically the case with Landsat data and over some regions with the use of MODIS data (Anderson et al. 2012a). It is suggested that an improved the thermal sharpening algorithm would have the potential of improving MODIS data for its uses in agricultural applications (Anderson et al. 2012a). This will also help to account for periods and regions with considerable cloud cover that could limit the sole use of remote sensing data from Landsat.

5. CONCLUDING REMARKS

The emergence of remote sensing approaches for estimating ETa since 1990s resulted in the development of several modeling concepts based on the intended use and application. The use of remote sensing approaches in general have the advantage of all other traditional methods for estimating ET since it has the ability of capturing the associated spatial and temporal variability. These models which ranged in complexity and data requirements were used in several ways including estimation of actual ETa for detection of crop water stress, crop water requirements at daily to seasonal scales, water rights applications, and several applications related to agricultural water resources management. However, a limited use of the remote sensing of ETa can be observed for applications at basin scale water management such as the Colorado River. This can be attributed to several issues related to

a) Weather forcing and remote sensing data needed at such scales, as well as ground observation for model evaluation
b) Applicability of models at such scales,
c) Wide range of reported model accuracies.

All these models require weather forcing data that represents the particular area of study. Remote sensing estimates of ET at field to local scales can be obtained using ground-based observations and at a reasonably accuracy within agricultural areas. However, for regional scale applications, the use of spatial weather forcing data is eminent obviously due to the associated spatial variability of ET. Different gridded weather forcing datasets are currently available. One of these datasets is the NLDAS-2 that provides the highest spatial and temporal resolution with $1/8^{th}$ degree grids (~ 14 km) and hourly time scales. Comparison of the NLDAS grids with ground-based observations showed variable accuracy depending on the underlying surface heterogeneity from mountain valleys in the western US to the Great Plans as described by Lewis et al. 2014. Under all scenarios, the use of these data adds to the uncertainty of ET estimates that need to be accounted for. Some models such as ALEXI were developed to avoid the use of near surface weather forcing data in order to reduce such uncertainties. There is a need to identify the associated uncertainties in using such gridded data and it is effects on modeling actual ET for agricultural applications.

The different modeling concepts described above ranged from simple one-layer to multilayer multisource approaches. Such modeling concepts were considered in developing the models described in Section 3 to account for homogenous to heterogonous surface conditions and local to regional scales. As shown in Tables 1-18, it appears that there is a wide range of reported accuracies based on different model performance evaluation criteria. Using these reported

accuracies as an inter-comparison of model performance based on their concepts and parameterization rather actual comparison with the same dataset, can be inconsistent and provide misleading indications. This arises from the fact that each of these models uses different kinds of input forcing data and output results in terms of spatial and temporal resolutions. For such, models, an inter-comparison scheme is needed in a way that allows for specifically evaluating their concepts and parameterizations and account for uncertainties related to the forcing data and ground-based observations of estimates of actual ET.

Evaluation of models performance has been achieved by comparing estimates of actual ET and in some cases surface energy balance fluxes with ground-based observations. These observations for example can include point-based eddy covariance, Bowen ratio, lysimeters, and sapflow which provide observations that represent sub-meter to few hundreds of meters of the surface. Other larger scale observations can include scintillometers which provides observations that can represents few hundreds of meters to few kilometers of the surface. The ground-based observations should have spatial extent that is larger or at least same as those of the spatial resolution estimates.

APPENDICES

Appendix A: Description of the TSEB Model

The clumping factor Ω can be estimated following the approach described by Campbell and Norman (1998) as

$$\Omega(\phi) = \frac{\Omega(0)}{\Omega(0)+[1-\Omega(0)\cdot\exp(-2.2[\phi]^P)]} \quad \text{A.1}$$

$$P = 3.8 - 0.46D \quad \text{A.2}$$

where $\Omega(0)$ is the clumping factor when viewed at nadir, and D the ratio of vegetation height vs. width of clumps. Example of some typical values shown in Campbell and Norman (1998). $\Omega(0)$ can be estimated from the general knowledge of vegetation cover and LAI as described in Kustas and Norman (2000). For row crops the fraction of surface covered by bare soil f_s is estimated as the sum of areas of bare soil seen between rows and through farrows assuming random distribution of leaves as

$$f_s = (1 - f_c) + f_c \cdot f_{sr} \quad \text{A.3}$$

$$f_{sr} = exp\left(\frac{-0.5LAI_L}{\cos(0)}\right) \quad \text{A.4}$$

$$f_s = exp\left(\frac{-0.5\cdot\Omega(0)\cdot\text{LAI}}{\cos(0)}\right) \quad \text{A.5}$$

Where LAI_L is the local LAI estimated as $LAI_L = LAI/f_c$, $\Omega(0)$ can then be calculated by solving Eqs. Xx znc xx. There are many equations available in literature to estimate the fractional cover fc where used with TSEB as

$$f_c = 1 - exp(-0.5LAI) \quad \text{A.6}$$

$$f_c = 1 - \left(\frac{NDVI_{max}-NDVI}{NDVI_{max}-NDVI_{min}}\right)^a \quad \text{A.7}$$

where $NDVI_{max}$ and $NDVI_{min}$ are the full cover and bare soil values of NDVI, the coefficient a describes the orientation of leaves of canopy and ranges between 0.6 to 1.0 for erectophile to planophile canopies.

The aerodynamic resistance R_a can be estimated as

$$R_a = \frac{\left[\left(\frac{z_u-d_o}{z_{om}}\right)-\psi_m\right]\left[ln\left(\frac{z_t-d_o}{z_{om}}\right)-\psi_h\right]}{k^2u} \quad \text{A.8}$$

where z_u and z_t are the measurement height for wind speed and air temperature, respectively, d_o the zero-plane displacement height estimated as d_o = (2/3) h_c with h_c the canopy height, z_{om} the roughness length for momentum taken as z_{om} = (1/8) h_c, $\psi_m$and ψ_h the stability correction

functions for momentum and heat, respectively (Brutsaert 1982), k von Karman constant taken as k=0.41.

The resistance R_x can be estimated as

$$R_x = \frac{C'}{LAI}\left(\frac{s}{u_{d+z_{0m}}}\right) \quad \text{A.9}$$

where *s* is the leaf size estimated as four times *LAI* divided by the perimeter. Suggested nominal leaf sizes are provided by Anderson et al. (2007) with a value of s =0.05 is used over most croplands. C' is coefficient derived from weighting a coefficient in the equation for leaf boundary layer resistance over the height of the canopy. Acknowledging uncertainties in C' a value of 90 $s^{-1/2}$ m^{-1} is suggested by Norman et al. (1995). The wind speed $u_{d_o+z_{0m}}$ near canopy elements at height $d + z_{om}$ and can be estimated as

$$u_{d_o+z_{om}} = u_c \cdot exp\left(-a\left(1 - \frac{d_o+z_{om}}{h_c}\right)\right) \quad \text{A.10}$$

where h_c is the canopy height, u_c the wind speed at the top of the canopy and can be estimated as

$$u_c = u\left[\frac{ln\left(\frac{h_c-d_o}{z_{om}}\right)}{ln\left(\frac{z_u-d}{z_{om}}\right)-\psi_m}\right] \quad \text{A.11}$$

where *u* is the wind speed above canopy measured at height z_u , the stability correction function for momentum, ψ_m , is suggested to be negligible due to roughness sublayer as indicated by Norman et al. (1995), a an extinction coefficient estimated as described in Kustas and Norman (2000) as

$$a_x = 0.28(\Omega(\phi) \cdot LAI_L)^{2/3} \cdot h_c^{1/3} \cdot s^{-1/3} \quad \text{A.12}$$

where *s* the mean canopy leaf width, and LAI_L the local leaf area index estimated as $LAI_L=LAI/f_c$. The resistance Rs can be estimated as can be estimated as

$$R_s = \frac{1}{a+bu_s} \quad \text{A.13}$$

where *a* and *b* are constants equals to 0.004 and 0.012, respectively, and u_s the wind speed near soil surface at 0.05-0.20 m where the effect of soil surface roughness is minimal and can be estimated using following Norman et al. (1995) as

$$u_s = u_c \cdot exp\left(-a\left(1 - \frac{0.05}{h_c}\right)\right) \quad \text{A.14}$$

A revised version of Eq. (12) provided by Kustas and Norman (1999a, 2000) in which R_s is updated with the knowledge of T_s and T_c , as *a* was also replaced by $c\ (T_s\text{-}T_c)^{(1/3)}$, with *c* =

0.0025. The extinction coefficient, *a*, can be estimated as indicated by Kustas and Norman (2000) as

$$a_s = 0.28(\Omega(\phi) \cdot LAI)^{2/3} \cdot h_c^{1/3} \cdot s^{-1/3} \quad \text{A.15}$$

The stability correction functions for momentum and heat ψ_m and ψ_h can be estimated using Monin-Obukov stability theory to account for atmospheric stability conditions as correction functions and u_* the friction velocity which can be estimated under neutral atmospheric conditions. Under unstable conditions

$$\Psi_m = 2 \cdot ln\left(\frac{1+x}{2}\right) + ln\left(\frac{1+x^2}{2}\right) - 2 \cdot arctan(x) + \frac{\pi}{2} \quad \text{A.16}$$

$$\Psi_h = 2 \cdot ln\left(\frac{1+x^2}{2}\right) \quad \text{A.17}$$

$$x = \left(1 - 16\frac{x}{L}\right)^{1/4} \quad \text{A18}$$

And for stable conditions

$$\Psi_m = -5 \cdot \left(\frac{2}{L}\right) \quad \text{A.19}$$

$$\Psi_h = -5 \cdot \left(\frac{2}{L}\right) \quad \text{A.20}$$

where L represents the Monin-Obukov length estimated as

$$L = \frac{-\rho \cdot (u_*)^3}{0.4g\left[\left(\frac{H}{c_P \cdot T_a}\right) + 0.61(E)\right]} \quad \text{A.21}$$

where E is the mass evaporation rate and u_* the friction velocity which can be estimated under neutral atmospheric conditions as

$$u_* = \frac{k \cdot u}{ln\left(\frac{z_u - d_o}{z_{om}}\right)} \quad \text{A.22}$$

and for other stability conditions as

$$u_* = \frac{k \cdot u}{ln\left(\frac{z_u - d}{z_{om}}\right) - \psi_m} \quad \text{A.23}$$

Appendix B: Hybrid ET Model

Description of the Soil Moisture Dynamics Model

The soil moisture dynamics model as described in the main body of the paper by Eq. (xx) require the calculation of the infiltration, soil water uptake, leakage between layers and drainage from the bottom most layer.

The infiltration of water at the soil surface in to the soil profile is estimated using Eq. (A1) as described in the daily multi-layered water balance (DAMUWAB) by Verdoodt et al. (2005)

$$I = min\left(P + SS_{ini}, D_1\left(\theta_{sat} - \theta_{fc}\right)\right) \quad \text{B.1}$$

where P is the precipitation, SS_{ini} the initial water storage at the soil surface which represents the amount of water supply that exceeds the infiltration capacity with a maximum storage of SS_{max} and the excess water lost at the surface as runoff Verdoodt et al. (2005).

$$SS_{max} = 0.5 \cdot r \cdot \left(\frac{sin^2(\sigma - \emptyset)}{sin(\sigma)}\right) \cdot \left(\frac{1/tan(\sigma+\emptyset)+1/tan(\sigma-\emptyset)}{2\cdot(cos(\sigma))\cdot(cos(\emptyset))}\right) \quad \text{B.2}$$

where r is the surface roughness which varies between 70 to 15 mm for light tilled and untilled land, respectively, σ the clod angle or furrow angle in radians which varies between 0.5 - 0.8 rad, and ϕ the field declination.

The soil evaporation estimates from the WB were used as an input to the dynamic soil moisture model.

Leakage of water between adjacent layers from layers i to layer i+1 is estimated using Eq. (A3) as described in the BUDGET model by Raes (2002).

$$Q_{i,i+1} = D_i \cdot \tau_i \cdot \left(\theta_{sat,i} - \theta_{fc,i}\right) \cdot \frac{e^{\theta_i - \theta_{fc,i} - 1}}{e^{\theta_i - \theta_{fc,i} - 1}} \quad \text{B.3}$$

$$\tau_i = 0.0866 \cdot e^{0.8063 \cdot log_{10}(K_{sat})} \quad \text{B.4}$$

where θ_s is the soil moisture content at saturation, θ_{fc} the soil moisture content at field capacity, K_{sat} the saturated hydraulic conductivity, and τ the drainage characteristic.
The deep percolation or the drainage from the bottom-most layer is estimated using as $Q_n = K_n \sin x$, where K_n is the hydraulic conductivity of the bottom-most layer, and x the slope angle, taken as 3 degrees as described in the simple biosphere model SiB by Sellers et al. (1986) and Luo et al. (2003).

The water uptake by plants root can be initially estimated using Eq. (A6) as described by Prasad (1988); Verdoodt et al. (2005) assuming unstressed water conditions.

$$S_i = 2 \cdot \left(1 - \frac{D_{ri,0.5}}{D_r}\right) \cdot \left(\frac{D_{ri}}{D_r}\right) \cdot Tr \qquad \text{B.6}$$

where T_r is the total transpiration amount from the entire root zone, D_{ri} the extension of the root zone with in the soil layer i, $D_{ri,0.5}$ the soil depth in the middle of extension of root in the soil layer i, and D_r the rooting depth. The initial value of S_i can be used to initialize soil moisture content all soil layers and the corresponding soil water potential ψ. Under water limited conditions, the water uptake by plant roots is then adjusted to account for water stress conditions using the approach described in the SWATRE model by Feddes et al. (1976); Feddes et al. (1978); Li et al. (2001); Luo et al. (2003) as

$$S_i = \frac{\alpha_i^2 \cdot F^{\lambda}(z)}{\int \alpha \cdot F^{\lambda}(z) \cdot dz} Tr \qquad \text{B.7}$$

where α is the dimensionless Feddes reduction function estimated based on ψ (Eq. A8), λ coefficient with suggested values > 1.1 by Passioura (1985) and 0.5 by Li et al. (2001), and *F(z)* the specific root fraction function with respect to the soil depth z estimated using Eq. (A9) Li et al. (2006).

$$\alpha(\psi) = \begin{Bmatrix} 0 & \psi \geq \psi_1 \\ \frac{\psi_1 - \psi}{\psi_1 - \psi_2} & \psi_2 \leq \psi < \psi_1 \\ 1 & \psi_3 \leq \psi < \psi_2 \\ \frac{\psi - \psi_4}{\psi_3 - \psi_4} & \psi_4 \leq \psi < \psi_3 \\ 0 & \psi \geq \psi_4 \end{Bmatrix} \qquad \text{B.8}$$

$$F(z) = -\beta^z \cdot ln(\beta) \qquad \text{B.9}$$

$$\beta = 0.01^{\left(1/d_r\right)} \qquad \text{B.10}$$

where β is an empirical fitting parameter that determines the root distribution with depth and can be estimated using Eq. (A10), d_r the rooting depth, ψ_1 oxygen deficiency point or soil water potential at saturation, ψ_4 soil water potential at wilting, ψ_2 and ψ_3 are maximum soil water potential head for which the crop is not water stressed with ψ_2 corresponds to soil moisture potential at field capacity and ψ_3 changes with the atmosphere evaporative demand. Different sets of values for the ψ limits are reported in the literature e.g. see Clemente et al. (1994).

The saturated hydraulic conductivity (K_{sat}), θ_{fc}, and the permanent wilting point (θ_{PWP}) for each soil type were estimated using the soil water characteristic model developed by Saxton and Rawls (2006) based on the U.S. Department of Agriculture (USDA) soil database that covers most of the US soils, ψ and K were estimated following the formulation of Clapp and Hornberger (1978) as

$$\psi = \psi_s \cdot \left(\frac{\theta}{\theta_s}\right)^{-b} \qquad \text{B.11}$$

$$K = K_{sat} \cdot \left(\frac{\theta}{\theta_s}\right)^{2b+3} \quad \text{B.12}$$

where ψ_s is the soil water potential at saturation, b empirical constant with different values tabulated for each soil type by Clapp and Hornberger (1978).

Appendix C: METRIC Model

The at-surface reflectance for each of the shortwave bands can be estimated as

$$\rho_{s,b} = \frac{R_{out,s,b}}{R_{in,s,b}} = \frac{\rho_{t,b} - \rho_{a,b}}{\tau_{in,b} \cdot \tau_{out,b}} \quad \text{C.1}$$

where $R_{out,s,b}$ and $R_{in,s,b}$ represent at-surface hemispherical incoming and reflected radiances (W m^{-2} μm^{-1}), $\tau_{in,b}$ effective narrow band transmittance for incoming solar radiation, $\tau_{out,b}$ effective narrow band transmittance for outgoing shortwave radiation, $\rho_{t,b}$ the top of the atmosphere reflectance, $\rho_{a,b}$ the path reflectance estimated as

$$\rho_{a,b} = C_b \cdot \left(1 - \tau_{in,b}\right) \quad \text{C.2}$$

where the typical values of the constant C_b are provided by Allen et al. (2007b), The at-sensor or top of the atmosphere reflectance, $\rho_{t,b}$, which can be estimated as

$$\rho_{t,b} = \frac{\pi \cdot L_{t,b} \cdot d^2}{ESUN_b \cdot \cos\theta_{rel}} \quad \text{C.3}$$

where $L_{t,b}$ the spectral radiance for each band b (W m^{-2} ster^{-1} μm^{-1}) which can be calculated as a function of the digital number (DN) as described in Chander and Markham (2003), the mean solar exoatmospheric irradiance for each band b (W m^{-2} μm^{-1}) with typical values provided by Chander and Markham (2003), θ_{rel} the solar zenith angle relative to the normal to the land surface slope, and d the earth-sun distance in astronomical units and can be estimated as

$$d^2 = \frac{1}{1 + 0.033\cos(DOY \cdot 2\pi/365)} \quad \text{C.4}$$

where DOY is the Julian day of year. $\tau_{in,b}$ and $\tau_{out,b}$ can be estimated as

$$\tau_{in,b} = C_1 \cdot exp\left[\frac{C_2 \cdot P}{K_t \cdot \cos\theta} - \frac{C_3 \cdot W + C_4}{\cos\theta}\right] + C_5 \quad \text{C.5}$$

$$\tau_{out,b} = C_1 \cdot exp\left[\frac{C_2 \cdot P}{K_t \cdot \cos\eta} - \frac{C_3 \cdot W + C_4}{\cos\eta}\right] + C_5 \quad \text{C.6}$$

where the value of the constants C_1 to C_5 are provided in Allen et al. (2007b), η the satellite zenith view angle, θ the solar zenith angle over horizontal surface (radiance). K_t dimensionless turbidity coefficient with $0 < K_t \leq 1.0$ where K_t =1 for clean air and $K_t = 0.5$ for extremely turbid, dusty or polluted air, P the air pressure (kPa) which can be estimated as a function of the elevation above sea level, z, as

$$P = 101.3 \cdot \left(\frac{293 - 0.0065 \cdot z}{293}\right)^{5.26} \quad \text{C.7}$$

The precipitable water, W, (mm) can be estimated as

$$W = 0.14 \cdot e_a \cdot P + 2.1 \qquad \text{C.8}$$

where e_a the vapor pressure (kPa).

The broadband atmospheric transmissivity, τ_{sw}, can be estimated following Allen (1996); Allen (2005) as

$$\tau_{sw} = 0.35 + 0.627 \cdot exp\left(\frac{-0.00146 \cdot P}{K_t \cdot cos\,\theta} - 0.075\left(\frac{W}{cos\,\theta}\right)^{0.4}\right) \qquad \text{C.9}$$

As indicated by Allen et al. (2007b), Eq. (C.9) is valid for values of $\theta < 1.3$ radians.

The constant for K_1 and K_2 needed for estimating top of the atmosphere surface temperature Ts based on the radiances for Landsat images are given in Table C.1 (Allen et al. 2007b).
Table C.1: the values of K_1 and K_2 needed to calculate radiometric surface temperature for Landsat images for band 6.

Table C.1: Summary of K_1 and K_2 values used to estimate TOA radiometric surface temperature with Landsat 5 and 7.

	K_1	K_2
Landsat 5	607.76	1260.56
Landsat 7	666.09	1282.71

The broadband and narrow band emissivities ε_o and ε_{NB}, respectively, can be estimated using empirical equations by Tasumi et al 2003a for different types of surfaces indicated by NDVI (the normalized vegetation index) as

For soil and vegetation covers indicated by $NDVI > 0$

$$\left.\begin{array}{ll} \varepsilon_o = 0.95 + 0.01LAI & for\ LAI \le 3 \\ \varepsilon_o = 0.98 & for\ LAI > 3 \\ \varepsilon_{NB} = 0.97 + 0.0033LAI & for\ LAI \le 3 \\ \varepsilon_o = 0.98 & for\ LAI > 3 \end{array}\right\} \qquad \text{C.10}$$

For water and snow covers with albedo of 0.47 and ≤ 0 , $\varepsilon_o = 0.985$ and $\varepsilon_{NB} = 0.985$, respectively.

The leaf area index LAI can be estimated empirically based on SAVI (Bastiaanssen et al. 1998b) as

$$LAI = \frac{ln\left(\frac{0.69 - SAVI_{ID}}{0.59}\right)}{0.91} \qquad for\ SAVI_{ID} \le 0.687 \qquad \text{C.11}$$

$$LAI = 6 \qquad for\ SAVI_{ID} > 0.687 \qquad \text{C.12}$$

where SAVI is the soil adjusted vegetation index estimated based on the top of the atmosphere reflectance in the red and near infrared bands 3 and 4, $\rho_{t,3}$ and $\rho_{t,4}$, respectively, and calculated as

$$SAVI = \frac{(1+L)\cdot(\rho_{t,4}-\rho_{t,3})}{(\rho_{t,4}+\rho_{t,4})} \quad \text{C.13}$$

Generally, for the calculation of SAVI, the value of L is taken as L=0.5. However, in METRIC applications, SAVI is adjusted to use L=0.1 (Allen et al. 2007b). The NDVI can be estimated as

$$NDVI = \frac{(\rho_{t,4}-\rho_{t,3})}{(\rho_{t,4}+\rho_{t,4})} \quad \text{C.15}$$

The lapse is estimated differently for relatively flat terrain and mountainous slopes (Allen 2012) as

$$Lapse = C_{laspe,flat} \cdot \frac{(z-z_{datum})}{1000} \qquad for\ z \le z_{break} \quad \text{C.16}$$

$$Lapse = C_{laspe,flat} \cdot \frac{(z_{break}-z_{datum})}{1000} + C_{laspe,mountain} \cdot \frac{(z-z_{break})}{1000} \qquad for\ z \le z_{break} \quad \text{C.18}$$

where $C_{laspe,flat}$ is the lapse rate for relatively flat terrain with a range of 0-15 K/km, $C_{laspe,mountain}$ the lapse rate for mountain slopes and taken as 10 K/km, z_{datum} an arbitrary datum specified where $T_{s\_datum} = T_s$, and z_{break} the elevation at the base of a mountainous terrain.

The Monin-Obukhov length is calculated as

$$L = -\frac{\rho\cdot c_P\cdot u_*^3\cdot T_{s\_dem}}{k\cdot g\cdot H} \quad \text{C.19}$$

Note that for unstable condition $L < 0$, for stable conditions $L > 0$ and for neutral conditions $L = 0$. Corrected values for $u_*$and r_{ah} as follows

$$u_* = \frac{u_{200}\cdot k}{ln\left(\frac{200}{z_{0m}}\right)-\Psi_{m(200m)}} \quad \text{C.20}$$

$$r_{ah} = \frac{ln\left(\frac{z_2}{z_1}\right)-\Psi_{h(z_2)}+\Psi_{h(z_2)}}{u_*\cdot k} \quad \text{C.21}$$

The stability correction functions for momentum and heat transport Ψ_m and Ψ_h, respectively, for unstable conditions can be estimated as

$$\left.\begin{aligned}\Psi_{m(200m)} &= 2\cdot ln\left(\frac{1+x_{(200m)}}{2}\right)+ln\left(\frac{1+x_{(200m)}^2}{2}\right)-2\cdot arctan\left(x_{(200m)}\right)+\frac{\pi}{2}\\ \Psi_{h(2m)} &= 2\cdot ln\left(\frac{1+x_{(2m)}^2}{2}\right)\\ \Psi_{h(0.1m)} &= 2\cdot ln\left(\frac{1+x_{(0.1m)}^2}{2}\right)\end{aligned}\right\} \quad \text{C.21}$$

where

$$\left.\begin{aligned}x_{(200m)} &= \left(1-16\frac{200}{L}\right)^{0.25}\\ x_{(2m)} &= \left(1-16\frac{2}{L}\right)^{0.25}\\ x_{(0.1m)} &= \left(1-16\frac{0.1}{L}\right)^{0.25}\end{aligned}\right\} \quad \text{C.22}$$

For stable atmospheric condition Ψ_m and Ψ_h can be estimated as

$$\left.\begin{aligned}\Psi_{m(200m)} &= -5\cdot\left(\frac{2}{L}\right)\\ \Psi_{h(2m)} &= -5\cdot\left(\frac{2}{L}\right)\\ \Psi_{m(0.1m)} &= -5\cdot\left(\frac{0.1}{L}\right)\end{aligned}\right\} \quad \text{C.23}$$

Appendix D: MODIS ET Model

The resistances to radiative and convective heat transfer r_{rs} and r_{hs} , respectively, can be estimated as

$$r_{rs} = \frac{\rho \cdot c_P}{4.0 \cdot \sigma \cdot T_i^3} \quad \text{D.1}$$

$$r_{hs} = r_{tot} \quad \text{D.2}$$

where r_{tot} is the total aerodynamic resistance to vapor transport which represents the sum of the surface and aerodynamic resistances to vapor transport r_s and r_v, respectively and can be estimated as

$$r_{tot} = r_{totc} \cdot r_{corr} \quad \text{D.3}$$

with r_{corr} represents a correction based on atmospheric temperature T_i and pressure P_a taken as 20 C and 101300 Pa, respectively.

$$r_{corr} = \frac{1.0}{\frac{101300}{P_a} \cdot \left(\frac{T_i + 273.15}{293.15}\right)^{1.75}} \quad \text{D.4}$$

$$P_a = P_{STD} \cdot t_1^{t_2} \quad \text{D.5}$$

$$t_1 = 1.0 - \frac{LR_{STD} \cdot Elev}{T_{STD}} \quad \text{D.6}$$

$$t_2 = \frac{G_{STD}}{LR_{STD} \cdot \frac{RR}{MA}} \quad \text{D.7}$$

where LR_{STD} is the standard temperature lapse rate 0.0065 K m^{-1}, T_{STD} the standard temperature at 0.0 m elevation 288.15 K, G_{STD} the standard gravitational acceleration 9.80665 m s^{-1}, *RR* the gas law constant 8.3143 m^3 Pa mol^{-1} K^{-1}, *MA* molecular weight of air 28.9644×10^{-3} kg mol^{-1} and P_{STD} the standard pressure at 0.0 elevation 101.325 Pa.

The variable r_{totc} can be estimated as a function of the boundary layer resistance, *rbl* (s m^{-1}) and VPD as

$$r_{totc} = \begin{cases} rbl_{max}, & VPD \leq VPD_{open} \\ rbl_{max} - \frac{(rbl_{max} - rbl_{min}) \cdot (VPD_{close} - VPD)}{(VPD_{close} - VPD_{open})}, & VPD_{open} < VPD < VPD_{close} \\ rbl_{min}, & VPD \geq VPD_{close} \end{cases} \quad \text{D.8}$$

where VPD_{open} and VPD_{close} (Pa) are the values of VPD when there is no water stress on transpiration and with water stress that leads stomata to close, respectively. Values of rbl_{max} ,

rbl_{min}, VPD_{open} , and VPD_{close} are provided in Mu et al. (2011) in a form of a lookup table for the different biomes.

For the calculation of evaporation from wet canopy leaves due to interception, the aerodynamic resistance $rhrc$ and rvc can be estimated as

$$rhrc = \frac{rhc \cdot rrc}{rhc + rrc} \quad \text{D.9}$$

$$rhc = \frac{1.0}{gl\_sh \cdot LAI \cdot f_{wet}} \quad \text{D.10}$$

$$rrc = \frac{\rho \cdot c_P}{4.0 \cdot \sigma \cdot T_i^3} \quad \text{D.11}$$

$$rvc = \frac{\rho \cdot c_P}{gl\_e\_wv \cdot LAI \cdot f_{wet}} \quad \text{D.12}$$

where rhc is the wet canopy resistance to sensible heat, rrc the resistance to radiative transfer through air, gl_sh the leaf conductance to sensible heat per unit LAI, gl_e_wv the leaf conductance to evaporated water vapor per unit LAI, and σ the Stefan-Boltzman constant. Mu et al. 2011 suggested values for gl_sh and gl_e_wv based on a lookup table for the different biomes.

The aerodynamic and surface resistances r_a and r_s , respectively, required to estimate plant transpiration λE_{trans} can be calculated as

$$r_a = \frac{rh \cdot rr}{rh + rr} \quad \text{D.13}$$

$$rh = \frac{1.0}{gl\_bl} \quad \text{D.14}$$

$$rr = \frac{\rho \cdot c_P}{4.0 \cdot \sigma \cdot T_i^3} \quad \text{D.15}$$

where rh and rr are the resistances to convective and radiative heat transfer, respectively, calculated based on Biome-BCG model of Thornton (1998), and gl_bl the leaf-scale boundary layer conductance estimated as equal to gl_sh. The surface resistance r_s for daytime and nighttime indicated by the subscript *i* can be estimated as the inverse of canopy resistance, C_c, as

$$r_{s\_i} = \frac{1}{C_{c\_i}} \quad \text{D.16}$$

$$C_{c\_i} = \begin{cases} \frac{G_S2 \cdot (G_{S\_i}1 + G_{CU})}{G_{S\_i}1 + G_S2 + G_{CU}} \cdot LAI \cdot (1.0 - f_{wet}), & LAI > 0.0, (1.0 - f_{wet}) > 0.0 \\ 0.0, & LAI = 0.0, (1.0 - f_{wet}) = 0.0 \end{cases} \quad \text{D.17}$$

$$G_s2 = gl\_sh \quad \text{D.18}$$

$$G_{CU} = g\_cu \cdot r_{corr} \quad \text{D.19}$$

$$G_{S\_night}1 = 0.0 \quad \text{D.20}$$

$$G_{S\_day}1 = C_L \cdot m(T_{min}) \cdot m(VPD) \cdot r_{corr} \quad \text{D.21}$$

with the subscript *i* indicates the value during daytime and nighttime, G_s2 the leaf boundary-layer conductance, g_cu the cuticular conductance per unit LAI taken as a constant value of 0.00001 m s^{-1}, $G_{S\_night}1$ and $G_{S\_day}1$ are the nighttime and daytime stomatal conductance.

Appendix E: SSEBop Model

The net radiation component for the application of SSEBop can be estimated as

$$R_n = R_{ns} - R_{nl} \quad \text{E.1}$$

where R_{ns} is the net shortwave solar radiation (MJ/M^2/D) and R_{nl} the net longwave radiation (MJ/M2/D). R_{ns} can be estimated as

$$R_{ns} = (1 - \alpha) \cdot R_s \quad \text{E.2}$$

with α is the albedo with a value of 0.23 used in SSEBop, R_s the incoming shortwave solar radiation (MJ/M^2/D) calculated as a function of the ground surface elevation z (m) and the extraterrestrial radiation (MJ/M^2/D) as

$$R_s = (0.75 + 2 \times 10^{-5} \times z) \cdot R_a \quad \text{E.3}$$

The extraterrestrial radiation, R_a , can be calculated as

$$R_a = \frac{24 \times 60}{\pi} \cdot G_{SC} \cdot d_r [\omega_S sin(\varphi) sin(\delta) + cos(\varphi) cos(\delta) sin(\omega_S)] \quad \text{E.4}$$

where is the solar constant taken as 0.0820 (MJ/m2/min), d_r the inverse of the earth-sun distance, ω_S the sun hour angle (rad), φ the latitude (rad), δ the solar declination. d_r and δ are estimated as a function of the Julian day of year J as

$$d_r = 1 + 0.033 \times cos\left(\frac{2\pi}{365} J\right) \quad \text{E.5}$$

$$\delta = 0.409 \times sin\left(\frac{2\pi}{365} J - 1.39\right) \quad \text{E.6}$$

The sun hour angle, ω_S, is calculated as a function of φ and φ as

$$\omega_S = arccos\left(-tan(\varphi) \cdot tan(\delta)\right) \quad \text{E.7}$$

The net longwave radiation, R_{nl} , is estimated as

$$R_{nl} = \sigma \cdot \left(\frac{T_{max}^4 - T_{min}^4}{2}\right) \cdot \left(0.34 - 0.14\sqrt{e_a}\right) \cdot \left(1.35 \frac{R_s}{R_{so}} - 0.35\right) \quad \text{E.8}$$

where σ is the Stefan-Boltzman costant taken as 4.903×10^{-9} (MJ/K^4/m^2/d), Tmax and Tmin are the maximum and minimum air temperatures, and R_s/R_{so} is the ration between the calculated (R_s) and clear-sky solar radiation (R_{so}). This ration is estimated as 1.0 since the SSEBop operates under the assumption of clear clear-sky conditions. The vapor pressure e_a is calculated as

$$e_a = e^o(T_{min}) = e^{\left(\frac{17.27 \times T_{min}}{T_{min}+237.3}\right)} \quad \text{E.9}$$

with $e^o(T_{min})$ is the saturated vapor pressure at T_{min} as approximation of the dew point temperature.

REFERENCES

Agam, N., Kustas, W.P., Anderson, M.C., Li, F.Q., & Colaizzi, P.D. (2008). Utility of thermal image sharpening for monitoring field-scale evapotranspiration over rainfed and irrigated agricultural regions. *Geophysical Research Letters, 35*

Allen, R., Pereira, L., & Raes, D. (1998a). M. Smith. 1998. Crop evapotranspiration: Guidelines for computing crop water requirements. FAO Irrigation and Drainage Paper No. 56, Rome. *Food and Agricultural Organization. Roma*

Allen, R.G. (1996). Assessing integrity of weather data for reference evapotranspiration estimation. *Journal of Irrigation and Drainage Engineering, 122*, 97-106

Allen, R.G. (2005). *The ASCE standardized reference evapotranspiration equation*: Amer Society of Civil Engineers

Allen, R.G., Pereira, L.S., Raes, D., & Smith, M. (1998b). Crop evapotranspiration-Guidelines for computing crop water requirements-FAO Irrigation and drainage paper 56. *FAO, Rome, 300*

Allen, R.G., & Robison, C.W. (2007). Evapotranspiration and Consumptive Irrigation Water Requirements for Idaho. University of Idaho. In

Allen, R.G., Tasumi, M., Morse, A., Trezza, R., Wright, J.L., Bastiaanssen, W., Kramber, W., Lorite, I., & Robison, C.W. (2007a). Satellite-based energy balance for mapping evapotranspiration with internalized calibration (METRIC) - Applications. *Journal of Irrigation and Drainage Engineering-Asce, 133*, 395-406

Allen, R.G., Tasumi, M., & Trezza, R. (2007b). Satellite-based energy balance for mapping evapotranspiration with internalized calibration (METRIC) - Model. *Journal of Irrigation and Drainage Engineering-Asce, 133*, 380-394

Allen, R.G.T.T.T.M.K.J. (2012). METRIC ^{tm} Mapping Evapotranspiration at High Resolution using Internalized Calibration Application Manual for Landsat Satellite Imagery (Version 2.0.8). In. University of Idaho

Anderson, M.C., Allen, R.G., Morse, A., & Kustas, W.P. (2012a). Use of Landsat thermal imagery in monitoring evapotranspiration and managing water resources. *Remote Sensing of Environment, 122*, 50-65

Anderson, M.C., Kustas, W.P., Alfieri, J.G., Gao, F., Hain, C., Prueger, J.H., Evett, S., Colaizzi, P., Howell, T., & Chavez, J.L. (2012b). Mapping daily evapotranspiration at Landsat spatial scales during the BEAREX'08 field campaign. *Advances in Water Resources, 50*, 162-177

Anderson, M.C., Kustas, W.P., Norman, J.M., Hain, C.R., Mecikalski, J.R., Schultz, L., Gonzalez-Dugo, M.P., Cammalleri, C., d'Urso, G., Pimstein, A., & Gao, F. (2011). Mapping daily evapotranspiration at field to continental scales using geostationary and polar orbiting satellite imagery. *Hydrology and Earth System Sciences, 15*, 223-239

Anderson, M.C., Norman, J.M., Diak, G.R., Kustas, W.P., & Mecikalski, J.R. (1997). A two-source time-integrated model for estimating surface fluxes using thermal infrared remote sensing. *Remote Sensing of Environment, 60*, 195-216

Anderson, M.C., Norman, J.M., Mecikalski, J.R., Otkin, J.A., & Kustas, W.P. (2007). A climatological study of evapotranspiration and moisture stress across the continental United States based on thermal remote sensing: 1. Model formulation. *Journal of Geophysical Research-Atmospheres, 112*

Baldocchi, D., Falge, E., Gu, L.H., Olson, R., Hollinger, D., Running, S., Anthoni, P., Bernhofer, C., Davis, K., Evans, R., Fuentes, J., Goldstein, A., Katul, G., Law, B., Lee, X.H., Malhi, Y., Meyers, T., Munger, W., Oechel, W., U, K.T.P., Pilegaard, K., Schmid, H.P., Valentini, R., Verma, S., Vesala, T., Wilson, K., & Wofsy, S. (2001). FLUXNET: A new tool to study the temporal and spatial variability of ecosystem-scale carbon dioxide, water vapor, and energy flux densities. *Bulletin of the American Meteorological Society, 82*, 2415-2434

Baret, F., Clevers, J.G.P.W., & Steven, M.D. (1995). The Robustness of Canopy Gap Fraction Estimates from Red and near-Infrared Reflectances - a Comparison of Approaches. *Remote Sensing of Environment, 54*, 141-151

Bastiaanssen, W.G.M. (1995). *Regionalization of Surface Flux Densities and Moisture Indicators in Composite Terrain: A Remote Sensing Approach Under Clear Skies in Mediterranean Climates*: DLO Winand Staring Centre

Bastiaanssen, W.G.M. (2000). SEBAL-based sensible and latent heat fluxes in the irrigated Gediz Basin, Turkey. *Journal of Hydrology, 229*, 87-100

Bastiaanssen, W.G.M., Menenti, M., Feddes, R.A., & Holtslag, A.A.M. (1998a). A remote sensing surface energy balance algorithm for land (SEBAL) - 1. Formulation. *Journal of Hydrology, 212*, 198-212

Bastiaanssen, W.G.M., Pelgrum, H., Wang, J., Ma, Y., Moreno, J.F., Roerink, G.J., & van der Wal, T. (1998b). A remote sensing surface energy balance algorithm for land (SEBAL) - 2. Validation. *Journal of Hydrology, 212*, 213-229

Bausch, W.C. (1993). Soil Background Effects on Reflectance-Based Crop Coefficients for Corn. *Remote Sensing of Environment, 46*, 213-222

Bausch, W.C., & Neale, C.M.U. (1987). Crop Coefficients Derived from Reflected Canopy Radiation - a Concept. *Transactions of the Asae, 30*, 703-709

Bausch, W.C., & Neale, C.M.U. (1989). Spectral Inputs Improve Corn Crop Coefficients and Irrigation Scheduling. *Transactions of the Asae, 32*, 1901-1908

Berk, A., Bernstein, L.S., Anderson, G.P., Acharya, P.K., Robertson, D.C., Chetwynd, J.H., & Adler-Golden, S.M. (1998). MODTRAN cloud and multiple scattering upgrades with application to AVIRIS. *Remote Sensing of Environment, 65*, 367-375

Bouchet, R. (1963). Evapotranspiration réelle et potentielle, signification climatique. *IAHS Publ, 62*, 134-142

Brotzge, J.A., & Crawford, K.C. (2003). Examination of the surface energy budget: A comparison of eddy correlation and Bowen ratio measurement systems. *Journal of Hydrometeorology, 4*, 160-178

Brunsell, N.A., Ham, J.M., & Arnold, K.A. (2011). Validating remotely sensed land surface fluxes in heterogeneous terrain with large aperture scintillometry. *International Journal of Remote Sensing, 32*, 6295-6314

Brutsaert, W. (1982). *Evaporation into the Atmosphere: Theory, History and Applications*: Springer

Brutsaert, W., & Sugita, M. (1992). Application of Self-Preservation in the Diurnal Evolution of the Surface-Energy Budget to Determine Daily Evaporation. *Journal of Geophysical Research-Atmospheres, 97*, 18377-18382

Campbell, G.S., & Norman, J.M. (1998). *AN INTRODUCTION TO ENVIRONMENTAL BIOPHYSICS.: 2nd edition*: Springer

Chander, G., & Markham, B. (2003). Revised Landsat-5 TM radiometric calibration procedures and postcalibration dynamic ranges. *Geoscience and Remote Sensing, IEEE Transactions on, 41*, 2674-2677

Chavez, J.L., Neale, C.M.U., Prueger, J.H., & Kustas, W.P. (2008). Daily evapotranspiration estimates from extrapolating instantaneous airborne remote sensing ET values. *Irrigation Science, 27*, 67-81

Chen, L.F., Li, Z.L., Liu, Q.H., Chen, S., Tang, Y., & Zhong, B. (2004). Definition of component effective emissivity for heterogeneous and non-isothermal surfaces and its approximate calculation. *International Journal of Remote Sensing, 25*, 231-244

Clapp, R.B., & Hornberger, G.M. (1978). Empirical Equations for Some Soil Hydraulic-Properties. *Water Resources Research, 14*, 601-604

Clemente, R.S., Dejong, R., Hayhoe, H.N., Reynolds, W.D., & Hares, M. (1994). Testing and Comparison of 3 Unsaturated Soil-Water Flow Models. *Agricultural Water Management, 25*, 135-152

Cleugh, H.A., Leuning, R., Mu, Q.Z., & Running, S.W. (2007). Regional evaporation estimates from flux tower and MODIS satellite data. *Remote Sensing of Environment, 106*, 285-304

Courault, D., Seguin, B., & Olioso, A. (2005). Review on estimation of evapotranspiration from remote sensing data: From empirical to numerical modeling approaches. *Irrigation and Drainage Systems, 19*, 223-249

Daley, R. (1993). *Atmospheric Data Analysis*: Cambridge University Press

Diak, G.R., Mecikalski, J.R., Anderson, M.C., Norman, J.M., Kustas, W.P., Torn, R.D., & DeWolf, R.L. (2004). Estimating Land Surface Energy Budgets From Space: Review and Current Efforts at the University of Wisconsin—Madison and USDA–ARS. *Bulletin of the American Meteorological Society, 85*, 65-78

Dickens, J.M., Forbes, B.T., Cobean, D.S., & Tadayon, S. (2011). Documentation of Methods and Inventory of Irrigation Data Collected for the 2000 and 2005 US Geological Survey Estimated Use of Water in the United States, comparison of USGS-Compiled irrigation data to other sources, and recommendations for future compilations. In: US Geological Survey

Eckhardt, D. (2010). Mapping Evapotranspiration in the Sacramento Valley using the ReSET Model. In, *Technical Memorandum* (p. 51): US Bureau of Reclamation

Elhaddad, A., & Garcia, L.A. (2008). Surface Energy Balance-Based Model for Estimating Evapotranspiration Taking into Account Spatial Variability in Weather. *Journal of Irrigation and Drainage Engineering-Asce, 134*, 681-689

Elhaddad, A., & Garcia, L.A. (2011). ReSET-Raster: Surface Energy Balance Model for Calculating Evapotranspiration Using a Raster Approach. *Journal of Irrigation and Drainage Engineering-Asce, 137*, 203-210

Elhaddad, A., Garcia, L.A., & Chavez, J.L. (2011). Using a Surface Energy Balance Model to Calculate Spatially Distributed Actual Evapotranspiration. *Journal of Irrigation and Drainage Engineering-Asce, 137*, 17-26

Feddes, R.A., Kowalik, P., Kolinskamalinka, K., & Zaradny, H. (1976). Simulation of Field Water-Uptake by Plants Using a Soil-Water Dependent Root Extraction Function. *Journal of Hydrology, 31*, 13-26

Feddes, R.A., Kowalik, P.J., & Zaradny, H. (1978). *Simulation of Field Water Use and Crop Yield*: John Wiley & Sons Australia, Limited

Fisher, J.B., Malhi, Y., Bonal, D., Da Rocha, H.R., De Araujo, A.C., Gamo, M., Goulden, M.L., Hirano, T., Huete, A.R., Kondo, H., Kumagai, T., Loescher, H.W., Miller, S., Nobre, A.D., Nouvellon, Y., Oberbauer, S.F., Panuthai, S., Roupsard, O., Saleska, S., Tanaka, K., Tanaka, N., Tu, K.P., & Von Randow, C. (2009). The land-atmosphere water flux in the tropics. *Global Change Biology, 15*, 2694-2714

Fisher, J.B., Tu, K.P., & Baldocchi, D.D. (2008). Global estimates of the land-atmosphere water flux based on monthly AVHRR and ISLSCP-II data, validated at 16 FLUXNET sites. *Remote Sensing of Environment, 112*, 901-919

Gao, F., Masek, J., Schwaller, M., & Hall, F. (2006). On the blending of the Landsat and MODIS surface reflectance: Predicting daily Landsat surface reflectance. *Ieee Transactions on Geoscience and Remote Sensing, 44*, 2207-2218

Gao, X., Huete, A.R., Ni, W.G., & Miura, T. (2000). Optical-biophysical relationships of vegetation spectra without background contamination. *Remote Sensing of Environment, 74*, 609-620

Geli, H.M.E. (2012). Modeling spatial surface energy fluxes of agricultural and riparian vegetation using remote sensing. In (p. 183). All Graduate Theses and Dissertations: Utah State University

Gonzalez-Dugo, M.P., Neale, C.M.U., Mateos, L., Kustas, W.P., Prueger, J.H., Anderson, M.C., & Li, F. (2009). A comparison of operational remote sensing-based models for estimating crop evapotranspiration. *Agricultural and Forest Meteorology, 149*, 1843-1853

Horst, T.W., & Weil, J.C. (1992). Footprint Estimation for Scalar Flux Measurements in the Atmospheric Surface-Layer. *Boundary-Layer Meteorology, 59*, 279-296

Horst, T.W., & Weil, J.C. (1994). How Far Is Far Enough - the Fetch Requirements for Micrometeorological Measurement of Surface Fluxes. *Journal of Atmospheric and Oceanic Technology, 11*, 1018-1025

Hsieh, C.I., Katul, G., & Chi, T. (2000). An approximate analytical model for footprint estimation of scaler fluxes in thermally stratified atmospheric flows. *Advances in Water Resources, 23*, 765-772

Huete, A., Didan, K., Miura, T., Rodriguez, E.P., Gao, X., & Ferreira, L.G. (2002). Overview of the radiometric and biophysical performance of the MODIS vegetation indices. *Remote Sensing of Environment, 83*, 195-213

Huntington, J.L., & Allen, R.G. (2010). Evapotranspiration and Net Irrigation Water Requirements for Nevada. *Nevada State Engineer's Office Publication, Nevada Division of Water Resources, Carson City, Nevada*

Jackson, T.J., Le Vine, D.M., Hsu, A.Y., Oldak, A., Starks, P.J., Swift, C.T., Isham, J.D., & Haken, M. (1999). Soil moisture mapping at regional scales using microwave radiometry: The Southern Great Plains Hydrology Experiment. *Ieee Transactions on Geoscience and Remote Sensing, 37*, 2136-2151

Jacobsen, A., & Hansen, B.U. (1999). Estimation of the soil heat flux net radiation ratio based on spectral vegetation indexes in high-latitude Arctic areas. *International Journal of Remote Sensing, 20*, 445-461

Jayanthi, H., Neale, C.M., & Wright, J.L. (2001). Seasonal evapotranspiration estimation using canopy reflectance: a case study involving pink beans. *IAHS PUBLICATION*, 302-305

June, T., Evans, J.R., & Farquhar, G.D. (2004). A simple new equation for the reversible temperature dependence of photosynthetic electron transport: a study on soybean leaf. *Functional Plant Biology, 31*, 275-283

Kalma, J.D., McVicar, T.R., & McCabe, M.F. (2008). Estimating Land Surface Evaporation: A Review of Methods Using Remotely Sensed Surface Temperature Data. *Surveys in Geophysics, 29*, 421-469

Kenny, J.F., Barber, N.L., Hutson, S.S., Linsey, K.S., Lovelace, J.K., & Maupin, M.A. (2009). *Estimated use of water in the United States in 2005*: US Geological Survey

Kustas, W., & Anderson, M. (2009). Advances in thermal infrared remote sensing for land surface modeling. *Agricultural and Forest Meteorology, 149*, 2071-2081

Kustas, W.P., & Daughtry, C.S.T. (1990). Estimation of the Soil Heat-Flux Net-Radiation Ratio from Spectral Data. *Agricultural and Forest Meteorology, 49*, 205-223

Kustas, W.P., Hatfield, J.L., & Prueger, J.H. (2005). The soil moisture-atmosphere coupling experiment (SMACEX): Background, hydrometeorological conditions, and preliminary findings. *Journal of Hydrometeorology, 6*, 791-804

Kustas, W.P., & Norman, J.M. (1997). A two-source approach for estimating turbulent fluxes using multiple angle thermal infrared observations. *Water Resources Research, 33*, 1495-1508

Kustas, W.P., & Norman, J.M. (1999a). Evaluation of soil and vegetation heat flux predictions using a simple two-source model with radiometric temperatures for partial canopy cover. *Agricultural and Forest Meteorology, 94*, 13-29

Kustas, W.P., & Norman, J.M. (1999b). Reply to comments about the basic equations of dual-source vegetation-atmosphere transfer models. *Agricultural and Forest Meteorology, 94*, 275-278

Kustas, W.P., & Norman, J.M. (2000). A two-source energy balance approach using directional radiometric temperature observations for sparse canopy covered surfaces. *Agronomy Journal, 92*, 847-854

Kustas, W.P., Norman, J.M., Anderson, M.C., & French, A.N. (2003). Estimating subpixel surface temperatures and energy fluxes from the vegetation index-radiometric temperature relationship. *Remote Sensing of Environment, 85*, 429-440

Lhomme, J.P., & Elguero, E. (1999). Examination of evaporative fraction diurnal behaviour using a soil-vegetation model coupled with a mixed-layer model. *Hydrology and Earth System Sciences, 3*, 259-270

Li, F., Jackson, T.J., Kustas, W.P., Schmugge, T.J., French, A.N., Cosh, M.H., & Bindlish, R. (2004). Deriving land surface temperature from Landsat 5 and 7 during SMEX02/SMACEX. *Remote Sensing of Environment, 92*, 521-534

Li, F.Q., Kustas, W.P., Anderson, M.C., Prueger, J.H., & Scott, R.L. (2008). Effect of remote sensing spatial resolution on interpreting tower-based flux observations. *Remote Sensing of Environment, 112*, 337-349

Li, K.Y., De Jong, R., & Boisvert, J.B. (2001). An exponential root-water-uptake model with water stress compensation. *Journal of Hydrology, 252*, 189-204

Li, K.Y., De Jong, R., Coe, M.T., & Ramankutty, N. (2006). Root-water-uptake based upon a new water stress reduction and an asymptotic root distribution function. *Earth Interactions, 10*

Luo, Y., OuYang, Z., Yuan, G., Tang, D., & Xie, X. (2003). Evaluation of macroscopic root water uptake models using lysimeter data. *Transactions of the Asae, 46*, 625-634

Markham, B.L., & Barker, J.L. (1986). Landsat MSS and TM post-calibration dynamic ranges, exoatmospheric reflectances and at-satellite temperatures. *EOSAT Landsat technical notes, 1*, 3-8

Massman, W.J. (1997). An analytical one-dimensional model of momentum transfer by vegetation of arbitrary structure. *Boundary-Layer Meteorology, 83*, 407-421

McCabe, M.F., & Wood, E.F. (2006). Scale influences on the remote estimation of evapotranspiration using multiple satellite sensors. *Remote Sensing of Environment, 105*, 271-285

Mcnaughton, K.G., & Spriggs, T.W. (1986). A Mixed-Layer Model for Regional Evaporation. *Boundary-Layer Meteorology, 34*, 243-262

Mecikalski, J.R., Diak, G.R., Anderson, M.C., & Norman, J.M. (1999). Estimating fluxes on continental scales using remotely sensed data in an atmospheric-land exchange model. *Journal of Applied Meteorology, 38*, 1352-1369

Menenti, M. (1984). *Physical aspects and determination of evaporation in deserts applying remote sensing techniques*. The Netherlands: Institute for Land and Water Management Research (ICW),

Monteith, J.L. (1965). Evaporation and environment. *Symposia of the Society for Experimental Biology, 19*, 205–234

Monteith, J.L. (1973). *Principles of environmental physics.* : Edward Arnold Press

Mu, Q., Heinsch, F.A., Zhao, M., & Running, S.W. (2007). Development of a global evapotranspiration algorithm based on MODIS and global meteorology data. *Remote Sensing of Environment, 111*, 519-536

Mu, Q.Z., Zhao, M.S., & Running, S.W. (2011). Improvements to a MODIS global terrestrial evapotranspiration algorithm. *Remote Sensing of Environment, 115*, 1781-1800

Neale, C.M.U., Bausch, W.C., & Heermann, D.F. (1989). Development of Reflectance-Based Crop Coefficients for Corn. *Transactions of the Asae, 32*, 1891-1899

Neale, C.M.U., Geli, H.M.E., Kustas, W.P., Alfieri, J.G., Gowda, P.H., Evett, S.R., Prueger, J.H., Hipps, L.E., Dulaney, W.P., Chavez, J.L., French, A.N., & Howell, T.A. (2012). Soil water

content estimation using a remote sensing based hybrid evapotranspiration modeling approach. *Advances in Water Resources, 50*, 152-161

Neale, C.U., Jayanthi, H., & Wright, J. (2005). Irrigation water management using high resolution airborne remote sensing. *Irrigation and Drainage Systems, 19*, 321-336

Norman, J.M., Anderson, M.C., Kustas, W.P., French, A.N., Mecikalski, J., Torn, R., Diak, G.R., Schmugge, T.J., & Tanner, B.C.W. (2003). Remote sensing of surface energy fluxes at 10(1)-m pixel resolutions. *Water Resources Research, 39*

Norman, J.M., & Becker, F. (1995). Terminology in Thermal Infrared Remote-Sensing of Natural Surfaces. *Agricultural and Forest Meteorology, 77*, 153-166

Norman, J.M., Kustas, W.P., & Humes, K.S. (1995). Source Approach for Estimating Soil and Vegetation Energy Fluxes in Observations of Directional Radiometric Surface-Temperature. *Agricultural and Forest Meteorology, 77*, 263-293

Passioura, J. (1985). Roots and water economy of wheat. *NATO advanced study institutes series. Series A. Life sciences, 86*

Potter, C.S., Randerson, J.T., Field, C.B., Matson, P.A., Vitousek, P.M., Mooney, H.A., & Klooster, S.A. (1993). Terrestrial Ecosystem Production - a Process Model-Based on Global Satellite and Surface Data. *Global Biogeochemical Cycles, 7*, 811-841

Prasad, R. (1988). A Linear Root Water-Uptake Model. *Journal of Hydrology, 99*, 297-306

Priestley, C.H.B., & Taylor, R.J. (1972). On the Assessment of Surface Heat Flux and Evaporation Using Large-Scale Parameters. *Monthly Weather Review, 100*, 81-92

Raes, D. (2002). BUDGET: A soil water and salt balance model. *Reference manual. Dep. of Land Manage., Katholieke Univ. Leuven, Leuven, Belgium*

Ross, J. (1975). Radiative transfer in plant communities. *Vegetation and the Atmosphere, 1*, 13-55

Sadler, E.J., Bauer, P.J., Busscher, W.J., & Millen, J.A. (2000). Site-specific analysis of a droughted corn crop: II. Water use and stress. *Agronomy Journal, 92*, 403-410

Santanello, J.A., & Friedl, M.A. (2003). Diurnal covariation in soil heat flux and net radiation. *Journal of Applied Meteorology, 42*, 851-862

Savoca, M.E., Senay, G.B., Maupin, M.A., Kenny, J.F., & Perry, C.A. (2013). Actual evapotranspiration modeling using the operational Simplified Surface Energy Balance (SSEBop) approach. In: US Geological Survey

Saxton, K.E., & Rawls, W.J. (2006). Soil water characteristic estimates by texture and organic matter for hydrologic solutions. *Soil Science Society of America Journal, 70*, 1569-1578

Schmid, H.P. (2002). Footprint modeling for vegetation atmosphere exchange studies: a review and perspective. *Agricultural and Forest Meteorology, 113*, 159-183

Schuurmans, J.M., Troch, P.A., Veldhuizen, A.A., Bastiaanssen, W.G.M., & Bierkens, M.F.P. (2003). Assimilation of remotely sensed latent heat flux in a distributed hydrological model. *Advances in Water Resources, 26*, 151-159

Sellers, P.J., Hall, F.G., Asrar, G., Strebel, D.E., & Murphy, R.E. (1988). The 1st Islscp Field Experiment (Fife). *Bulletin of the American Meteorological Society, 69*, 22-27

Sellers, P.J., Hall, F.G., Asrar, G., Strebel, D.E., & Murphy, R.E. (1992). An Overview of the 1st International Satellite Land Surface Climatology Project (Islscp) Field Experiment (Fife). *Journal of Geophysical Research-Atmospheres, 97*, 18345-18371

Sellers, P.J., Mintz, Y., Sud, Y.C., & Dalcher, A. (1986). A Simple Biosphere Model (Sib) for Use within General-Circulation Models. *Journal of the Atmospheric Sciences, 43*, 505-531

Senay, G.B., Bohms, S., Singh, R.K., Gowda, P.H., Velpuri, N.M., Alemu, H., & Verdin, J.P. (2013). Operational evapotranspiration mapping using remote sensing and weather datasets: A new parameterization for the SSEB approach. *JAWRA Journal of the American Water Resources Association, 49*, 577-591

Senay, G.B., Budde, M., Verdin, J.P., & Melesse, A.M. (2007). A coupled remote sensing and simplified surface energy balance approach to estimate actual evapotranspiration from irrigated fields. *Sensors, 7*, 979-1000

Senay, G.B., Budde, M.E., & Verdin, J.P. (2011). Enhancing the Simplified Surface Energy Balance (SSEB) approach for estimating landscape ET: Validation with the METRIC model. *Agricultural Water Management, 98*, 606-618

Senay, G.B., Verdin, J.P., Lietzow, R., & Melesse, A.M. (2008). Global daily reference evapotranspiration modeling and evaluation. *Journal of the American Water Resources Association, 44*, 969-979

Shuttleworth, W.J., & Wallace, J.S. (1985). Evaporation from Sparse Crops - an Energy Combination Theory. *Quarterly Journal of the Royal Meteorological Society, 111*, 839-855

Singh, R.K., Senay, G.B., Velpuri, N.M., Bohms, S., Scott, R.L., & Verdin, J.P. (2014). Actual evapotranspiration (water use) assessment of the colorado river basin at the landsat resolution using the operational simplified surface energy balance model. *Remote Sensing, 6*, 233-256

Su, H.B., McCabe, M.F., Wood, E.F., Su, Z., & Prueger, J.H. (2005). Modeling evapotranspiration during SMACEX: Comparing two approaches for local- and regional-scale prediction. *Journal of Hydrometeorology, 6*, 910-922

Su, Z. (2002). The Surface Energy Balance System (SEBS) for estimation of turbulent heat fluxes. *Hydrology and Earth System Sciences, 6*, 85-99

Su, Z., Schmugge, T., Kustas, W.P., & Massman, W.J. (2001). An evaluation of two models for estimation of the roughness height for heat transfer between the land surface and the atmosphere. *Journal of Applied Meteorology, 40*, 1933-1951

Tasumi, M. (2003). *Progress in operational estimation of regional evapotranspiration using satellite imagery*

Tasumi, M., Allen, R.G., Trezza, R., & Wright, J.L. (2005a). Satellite-based energy balance to assess with in-population variance of crop coefficient curves. *Journal of Irrigation and Drainage Engineering-Asce, 131*, 94-109

Tasumi, M., Trezza, R., Allen, R., & Wright, J. (2005b). Operational aspects of satellite-based energy balance models for irrigated crops in the semi-arid U.S. *Irrigation and Drainage Systems, 19*, 355-376

Thornton, P.E. (1998). Regional ecosystem simulation: combining surface-and satellite-based observations to study linkages between terrestrial energy and mass budgets

Thornton, P.E., Thornton, M.M., Mayer, B.W., Wilhelmi, N., Wei, Y., Devarakonda, R., & Cook, R.B. (2014). Daymet: Daily Surface Weather Data on a 1-km Grid for North America, Version 2. Data set. In: Oak Ridge National Laboratory Distributed Active Archive Center, Oak Ridge, Tennessee, USA.

Twine, T.E., Kustas, W.P., Norman, J.M., Cook, D.R., Houser, P.R., Meyers, T.P., Prueger, J.H., Starks, P.J., & Wesely, M.L. (2000). Correcting eddy-covariance flux underestimates over a grassland. *Agricultural and Forest Meteorology, 103*, 279-300

Verdoodt, A., Van Ranst, E., Ye, L., & Verplancke, H. (2005). A daily multi-layered water balance model to predict water and oxygen availability in tropical cropping systems. *Soil Use and Management, 21*, 312-321

Wieringa, J. (1986). Roughness-Dependent Geographical Interpolation of Surface Wind-Speed Averages. *Quarterly Journal of the Royal Meteorological Society, 112*, 867-889

Wieringa, J. (1993). Representative Roughness Parameters for Homogeneous Terrain. *Boundary-Layer Meteorology, 63*, 323-363

Wukelic, G.E., Gibbons, D.E., Martucci, L.M., & Foote, H.P. (1989). Radiometric Calibration of Landsat Thematic Mapper Thermal Band. *Remote Sensing of Environment, 28*, 339-347

Zhang, Q.Y., Xiao, X.M., Braswell, B., Linder, E., Baret, F., & Moore, B. (2005). Estimating light absorption by chlorophyll, leaf and canopy in a deciduous broadleaf forest using MODIS data and a radiative transfer model. *Remote Sensing of Environment, 99*, 357-371

Zhao, M., Heinsch, F.A., Nemani, R.R., & Running, S.W. (2005). Improvements of the MODIS terrestrial gross and net primary production global data set. *Remote Sensing of Environment, 95*, 164-176

Remote Sensing of Evapotranspiration

Part 2

Model Inter-comparison

Hatim M. E. Geli
Department of Civil and Environmental Engineering
Utah State University
Logan, Utah

Christopher M. U. Neale
Daugherty Water for Food Institute
University of Nebraska
Lincoln, Nebraska

June 2015

Table of Content

List of Tables

List of Figures

1. INTRODUCTION

Consumptive water-use in agriculture can be defined as the amount of water consumed by agricultural activities that cannot be returned or reused. It includes mainly two components; evaporation, which is the loss of water from wet bare soil or through the irrigation application process; and transpiration, which is the loss of water from plants. Usually over a vegetated surface these two components occur simultaneously and hence are combined and referred to as evapotranspiration (ET). A more specific term is actual ET (ETa) which refers to the ET from growing vegetation at different stages of growth and subject to water availability in the plant root zone. The term "reference ET" –ET_o or ET_r for grass and alfalfa reference crop, respectively, refers to the potential rate of ET under existing climate forcing. Actual evapotranspiration, ETa, can be estimated using different approaches including direct or indirect measurements, process modeling, or combination of both. There are many ETa measurement methods available described in the literature including Bowen ratio, eddy covariance, sap flow gauges, lysimeters, scintillometers, and direct measurements of water balance components such as inflow and outflow at farm to regional scales. Estimation of ETa of agricultural vegetation has also been conducted using the crop coefficient and reference ET method. The reference ET being estimated through different approaches including the Penman-Monteith (P-M), Blaney-Criddle (B-C), Priestly-Taylor(P-T), Hargreaves (H) etc. Actual ET can also be estimated through water balance calculations, surface energy balance and more recently remote sensing techniques. ETa represents the main consumptive component when estimating the total water-use for agricultural systems. The total water requirement for an irrigation system includes, in addition to the consumptive water-use, two other components: conveyance losses in the distribution system and irrigation system application losses on the farm and fields. Typically, these "losses" are non-consumptive in nature, with the excess infiltration water and surface runoff typically available to downstream users. The total irrigation water requirement of a large irrigation system can be accounted for by estimating the consumptive water-use for each crop based on estimates of ETa along with the corresponding cropped area, and estimating related conveyance losses and irrigation application efficiencies. These two components are typically not measured and generally accounted for as a percentage of consumptive/crop water-use that is based on ET estimates. Hence the need for estimating consumptive water-use with a reasonable accuracy clearly rises from the fact that it can help to better manage available water resources.

Irrigation water withdrawal is a major and an important component of the US water use as it represents about 31% of the total water withdrawals. These water use estimates are published by the United State Geological Survey (USGS) in the 5-years reports since 1950 as part of the National Water Use Information Program. Over the years this water-use information is generally based on compilation of data provided by different sources or entities, different methods of measurements, and different methods of estimates of consumptive water-use with each having its own associated level of uncertainty. Because of these uncertainties, any observed trends derived from this water-use information over the years may have lower level of confidence and may not reflect the actual variation (Dickens et al., 2011). In order to provide estimates of irrigation water-use the USGS follow a number of approaches as described in the 5-year reports that include direct measurements and, if not available, in-direct methods such as water-use coefficients that are generally based on published articles, averages from previous report ET models, published plant consumptive water use, and irrigation diversions (Dickens et al., 2011). In recent years one of the most common indirect methods used to estimate consumptive water-

use is modeling ETa using the Blaney-Criddle (B-C), and Penman-Monteith (P-M) equations with crop coefficients (Dickens et al., 2011). The need for a unified, consistent and more accurate method to estimate ETa is important to reduce some of the related uncertainties ETa estimation through different methods. Remote sensing techniques have already shown the potential for meeting these needs with reasonable level of accuracy, even with the fact that they have recently emerged. As there are currently many available remote sensing-based ETa methods, there is still a need to provide a unified, perhaps, agreeable set of methods across wide range of users and decision makers. With this in mind and as part of the Sustain and Manage America's Resources for Tomorrow program (WaterSMART) program under the water census, the USGS is looking towards providing such set of acceptable and agreeable remote sensing methods. This report represents some of the effort towards achieving this goal (DOI, 2012). A recent 3-year report by the USGS states such needs with the ultimate goal of improving the quantification of irrigation water use and consequently irrigation water withdrawal (DOI, 2012).

The recent advances in the use of remote sensing technology showed that it can provide more accurate estimates of ETa and consequently consumptive water-use compared to traditional methods such as B-C (Dickens et al., 2011). These advances were met with a gradual move toward the use of remotely sensed ETa to account for consumptive and total irrigation water-use that are evident in many published reports and articles by government agencies, universities, and other entities (e.g. Allen and Robison, 2007; Eckhardt, 2013). This gradual move was accompanied by different practices that include exploring and developing of a wide range of modeling algorithms, investigation of needed input data and the associated effects of using data for local and regional scales applications, and evaluating the need for trained personnel for efficient application and adoption of such technology by the different entities. As a result many remote sensing-based models have been developed that conceptually ranged from physically based, empirical, and mixed models. Examples of such models include the two-source energy balance (TSEB) (Kustas and Norman, 1999; Norman et al., 1995), the Atmosphere-Land Exchange Inverse (ALEXI) (Anderson et al., 1997; Mecikalski et al., 1999) the Disaggregated Atmosphere-Land Exchange Inverse (DisALEXI) (Norman et al., 2003), the Mapping Evapotranspiration with Internalized Calibration (METRIC) (Allen et al., 2007a, 2007b), the Hybrid ET (Neale et al., 2012), the MODIS ET (Mu et al., 2007, 2011), the Simplified Energy Balance System (SEBS) (Su, 2002), the Simplified Surface Energy balance (SSEB) (Senay et al., 2011, 2008), and the Priestly-Taylor evapotranspiration (PT-JPL) (Fisher et al., 2008). The input data used or needed with these models include multispectral and thermal infrared images that are generally available from a suit of satellites managed by the USGS and NOAA. Other input data requirements include weather forcing data that can be optioned from ground-based observations and/or gridded data that are generally available from multiple sources such as North American Land Data Assimilation System (NLDAS).

It is worth mentioning that most remote sensing ET models are able to provide maps of ETa during the satellite overpass dates. If there is a gap between these dates –due to satellite overpass return period or the presence of clouds – usually other traditional methods need to be applied to fill-in such gaps. Some of the methods that are used for gap filling include the use of weather forcing data and reference ET estimates (Allen et al., 2007b; Elhaddad and Garcia, 2011; Senay et al., 2013), the use of remote sensing information from multiple sources such as data fusion approach (Gao et al., 2006; Norman et al., 2003), coupling remote sensing and water balance

approach (Geli, 2012; Neale et al., 2012), and in some cases a mixture of two or more of these methods. Hence providing seasonal ETa estimates may not necessarily be based solely on remote sensing. With the above described combination of models and wide range of complexity, input data requirement, and the type of the needed of ETa estimates in terms of temporal and spatial resolution have resulted in different types of models applications for reporting consumptive water-use by government agencies. For example the US Bureau of Reclamation has applied interchangeably METRIC and ReSET models (Eckhardt, 2013), the USGS applied SSEBop model (Savoca et al., 2013), and some States (e.g. Nevada and Idaho) have used METRIC (Allen and Robison, 2007).

However, in some cases, when different States share water from the same river basin, or in general the same source of water, if each State applies and uses a different remote sensing model-based ETa estimate, different and inconsistent estimates of total irrigation water withdrawal could result. Consequently, difficulties would arise among users in accepting estimates provided by individual States which could result in improper management of available water resources. Moreover, duplication of effort could also be evident with such practice. A typical example of such case is the Colorado River basin that is shared by 7 States including Wyoming, Utah, Nevada, New Mexico, Arizona, and California. Due to the differences in the methods used for estimating ETa by these States. The above mentioned issues are evident and inevitable unless agreement on approaches and methods for estimating ETa via remote sensing is reached.

This report is intended to provide insight on the potential use of remote sensing for ETa estimation, describing some of the related uncertainties pertained to the application of different modeling approaches, as well as the related input data requirements. The approach followed in this analysis is based on an inter-comparison scheme of candidate models tested over selected sites using unified input datasets. Five candidate models were used in this analysis including METRIC, SEBS, SSEBop, ReSET, and DisALEXI. Two test sites have been selected to test these models that are located in the US with each having different climatic region and vegetation cover type and growing conditions.

2. METHODOLOGY

2.1 Models Description

2.1.1 METRIC and ReSET

A brief description of the models used in this analysis is provided herein with more details available in part 1 of this report (Geli and Neale, 2015). The general "big leaf" concept, or what can be described as a one-layer approach, is used by some models including METRIC, ReSET, and SEBS to provide estimates of ET using the surface energy balance.

$$Rn = \lambda E + H + G \quad (15)$$

where Rn is the net radiation (W m^{-2}), G the soil heat flux (W m^{-2}), λE the latent heat flux (W m^{-2}), H the sensible heat flux (W m^{-2}). Other models such as DisALEXI apply the same

surface energy balance equation but utilize a two-source modeling approach. Generally, most of these models provide reasonable estimates of *Rn* and *G*. The major difference among these models lies in the method used for estimating H and λE. On the other hand, some models estimate ETa directly using empirical approaches such as SSEBop.

The ReSET and METRIC models provide estimates of *Rn* using the basic radiative energy balance at the surface as

$$Rn = (1 - \alpha)R_s + R_{L\downarrow} - R_{L\uparrow} - (1 - \varepsilon_o)R_{L\downarrow} \quad 16$$

where α is the broadband shortwave surface albedo, R_s the incoming shortwave radiation (W m^{-2}), $R_{L\uparrow}$ the outgoing longwave radiation (W m^{-2}), $R_{L\downarrow}$ the outgoing longwave radiation (W m^{-2}) and ε_o the broadband shortwave surface emissivity. R_s can be estimated as $R_s = G_{SC} \cdot cos\ \theta \cdot d_r \cdot \tau_{sw}$ with G_{SC} is the solar constant taken as (1367 W m^{-2}), $cos\ \theta$ the cosine of the solar zenith angle, d_r the inverse squared relative earth-sun distance ($1/d^2$), and τ_{sw} the broadband shortwave atmospheric transmissiviy. $R_{L\uparrow}$ and $R_{L\downarrow}$ are estimated using the Stephan-Boltzmann equation ($R_L = \varepsilon \cdot \sigma \cdot T^4$) applied either on the surface or the sky using the corresponding surface or atmospheric emissivity (ε) and temperature (T^4).

The soil heat flux, G, can be estimated the equation provided by Tasumi (2003), as function of Rn , leaf area index (*LAI*), and radiometric surface temperature (T_R) and is applicable for tilled agricultural areas as

$$\frac{G}{R_n} = 0.05 + 0.18 \cdot e^{(-0.521) \cdot LAI} \qquad for\ LAI \geq 0.5 \quad 17$$

$$\frac{G}{R_n} = \frac{1.80 \cdot (T_R - 273.16)}{R_n} + 0.084 \qquad for\ LAI < 0.5 \quad 18$$

The two models estimate *H* following a semi-empirical approach that relates *H* with the temperature difference at two reference heights above the surface as

$$H = \frac{\rho \cdot c_P \cdot dT}{r_{ah}} \quad 19$$

where ρ is the air density kg m^{-3}, c_P is the specific heat of air taken as 1004 J kg^{-1} K^{-1}, dT is the temperature difference $T_1 - T_2$ (K) between two heights z_1 and z_2, and $r_{ah}$is the aerodynamic resistance to heat transport (s m^{-1}). The solution to *H* is obtained iteratively to account for atmospheric stability conditions initialized with the neutral case. *dT* can be estimated based on a linear relationship as $dT = b + a \cdot T_R$ that needs to be developed for each scene using two reference hot and cold anchoring temperature limits. The general concept behind this linear relationship is that at the hot pixel (with known T_R value) there is minimal or no *ETa* ($ET_{hot} = 0$) and that at the cold pixel (ET_{cold}) can be estimated as a fraction of the reference ET for alfalfa crop (*ETr*) as 1.05 * *ETr*. The latent heat flux λE is estimated as the residual of the surface energy balance (Eq. 15). The instantaneous values of λE can be extrapolated to daily values using the reference evaporative fraction (*ETrF*) method. These two models mostly follow the same concepts including the fact that both models do not necessary need atmospherically

corrected multispectral reflectance and thermal imagery as raw digital number (DN) data can be used. Both models have their own approach for atmospheric correction. Some of the differences between the two models is that ReSET describes and uses an approach to generate gridded weather forcing data based on available ground-based observations as well as developing gridded dT information.

2.1.2 SSEBop

The SSEBop model (Senay et al., 2013) represents an operational version of SSEB developed by Senay et al. (2007). Both SSEB and SSEBop models are based on a simplified semi-empirical approach that directly provide estimates of ETa as a function of grass reference ET (ET_0) as

$$ETa = ETf \cdot k \cdot ET_0 \quad (20)$$

where ETf is the ETa fraction that can be estimated using an empirical scaling approach (Eq. 21) based on the radiometric surface temperature T_R (Senay et al., 2013) as

$$ETf = \frac{T_h - T_R}{T_h - T_C} = \frac{T_h - T_R}{dT} \quad (21)$$

with T_h and T_C are hot and cold surface temperatures estimated at idealized reference hot/dry and cold/wet limits for a given scene and dT is a predefined temperature difference ranges between 0-1. The cold surface temperate limit can be estimated as a function of the near surface Ta and an adjustment coefficient as described in (Senay et al., 2013) . The temperature difference can be estimated as a function of Rn and aerodynamic resistance (γ_{ah}). The hot surface temperature can then be calculated as $T_h = dT - T_C$. Hence ETa can be estimate as

$$ETa = \frac{\rho \cdot C_P}{Rn \cdot \gamma_{ah}} \cdot (T_h - T_R) \cdot k \cdot ETo \quad (22)$$

2.1.3 SEBS

Similar to METRIC and ReSET models, SEBS model solves the energy balance equation at two wet and dry limits surface conditions during which H and λE can be estimated. The model provides estimates of Rn using the basic radiative balance equation as

$$R_n = (1 - \alpha) \cdot R_s + \varepsilon \cdot R_{L\downarrow} - \varepsilon \cdot \sigma \cdot T_R^4 \quad (23)$$

where ε the broadband emissivity in the thermal infrared band. G can be estimated as

$$G = [\Gamma_c + (1 - f_c) \cdot (\Gamma_s - \Gamma_c)] \cdot R_n \quad (24)$$

with $\Gamma_c = 0.05$ for full vegetation cover (Monteith, 1973) and $\Gamma_s = 0.315$ for bare soil (Kustas and Daughtry, 1990), and f_c is the fraction of vegetation cover.

By introducing the concept of evaporative fraction (Λ) as $\Lambda = \lambda E/(Rn - G)$ and the relative evaporative fraction as $\Lambda_r = \lambda E/\lambda E_{wet} = 1 - (\lambda E_{wet} - \lambda E)/\lambda E_{wet} = 1 - (H - H_{wet})/(H_{dry} - H_{wet})$ with subscripts wet and dry refer to the wet and dry surface conditions. The SEBS model applies the energy balance at the two dry and wet limits to estimate H_{dry} and H_{wet}. Note that H_{wet} is estimated using a modified Penman-Monteith equation and H is estimated using the bulk resistance equations as $\theta_0 - \theta_a = H/ku_*\rho c_p \cdot [ln(z - d_0/z_{oh}) - \Psi_h(z - d_0/L) + \Psi_h(z_{0h}/L)]$. Knowing H, H_{wet}, and H_{dry}; both Λ_r and Λ can then be estimated and consequently λE as

$$\lambda E = \Lambda \cdot (Rn - G) \qquad 25$$

2.1.3 DisALEXI

The disaggregation modeling scheme DisALEXI was developed to provide surface energy balance fluxes estimates at the desired field scale of 1-1000 m that is typical to airborne, Landsat, and MODIS based on ALEXI output that is estimated at a coarser resolution of 5-10 km typical to GOES (Norman et al., 2003). One of the advantages of the model is that it alleviates the need for using near surface air temperature Ta observations that most models depend on. The Tow-Source Energy Balance (TSEB) model represents the main modeling components of DisALEXI as it is being applied at the desired pixel scale that is based on the T_R of the high resolution imagery. The T_R represents the lower boundary condition and Ta at the blending height is the upper boundary condition. The TSEB is applied at the high resolution for all the i^{th} pixels (i =1 to N) contained within each of the 5-km GOES pixel. The 50-m Ta is considered constant for all the i^{th} pixels while using the T_R at the high resolution data. Similarly all other surface related parameters are treated at the high-resolution i^{th} pixel scale such as the $f_{c,i}$ and canopy height $h_{c,i}$ which are generally based on NDVI.

It is worth mentioning that the use of T_R images from multiple sensors in the application of ALEXI and DisALEXI could result in some biases due to differences in sensors calibration, view angle, and atmospheric correction (Norman et al., 2003). A bias correction procedure is described by Norman et al. (2003) that needs to be performed prior to the use of these images.

The TSEB model treats surface components, bare soil and canopy, separately when applying the surface energy balance equation. The model allows the interaction between the two energy balance components at an air-canopy interface just above the surface. The energy balance equations for canopy, soil, and combined surface components can be described as **Error! Reference source not found.Error! Reference source not found.Error! Reference source not found.Error! Reference source not found.Error! Reference source not found.**

$$\left.\begin{aligned} Rn_s &= LE_s + H_s + G \\ Rn_c &= LE_c + H_c \\ Rn &= Rn_s + Rn_c \end{aligned}\right\} \qquad 26$$

The net radiation Rn_c and Rn_s of the canopy and soil components, respectively, are estimated using the physically based approach of Campbell and Norman (1998) as

$$\left.\begin{aligned} Rn_c &= Ln_c + (1-\tau_s)\cdot(1-\alpha_c)S \\ Rn_s &= Ln_s + \tau_s(1-\alpha_s)S \end{aligned}\right\} \quad 27$$

where τ_s, α_c and α_s are the solar transmittance in canopy, the canopy albedo, and soil albedo, respectively, and can be estimated as described in Campbell and Norman (1998), and G can be estimated as a function of Rn_s as

$$G = c_G \cdot Rn_s \quad 28$$

The value of that c_G varies with soil type, moisture content, and time because of the phase shift between *G* and Rn_s over a diurnal cycle as indicated by Santanello and Friedl (2003). However, a constant value of c_G can be used for midmorning to midday period- typical acquisition time of satellite thermal infrared imagery (Santanello and Friedl, 2003). Typical value for c_G as ~ 0.3 was used in most of the TSEB applications.

The directional radiometric surface temperature T_R can be decomposed into the thermodynamic temperature of soil and canopy T_s and T_c , respectively, as

$$T_R(\phi) \approx [f_c(\phi)T_c^4(1-f_c(\phi))T_s^4]^{1/4} \quad 29$$

where $f_c(\phi)$ is the directional fraction of the field of view of the infrared radiometer occupied by vegetation which can be estimated as

$$f_c(\phi) = 1 - \exp\left(\frac{-0.5\cdot\Omega(\phi)\cdot LAI}{\cos(\phi)}\right) \quad 30$$

where Ω is the clumping factor and ϕ the radiometer view zenith angle. Ω can be obtained following Campbell and Norman (1998).

The sensible heat fluxes over soil and canopy components are calculated as

$$\left.\begin{aligned} H_c &= \rho\cdot c_P\frac{T_c-T_{AC}}{R_x} \\ H_s &= \rho\cdot c_P\frac{T_s-T_{AC}}{R_s} \\ H = H_c + H_s &= \rho\cdot c_P\frac{T_{ac}-T_a}{R_a} \end{aligned}\right\} \quad 31$$

where T_{ac} is the air temperature at an air-canopy interface, R_x is the total boundary layer resistance of complete canopy leaves, R_sThe resistance to heat flow in the boundary layer immediately above the soil surface, $R_a$the aerodynamic resistance. These resistances can be estimated as described in Li et al. (2005).

The latent heat flux from canopy LE_c is calculated using the Priestly-Taylor (P-T) (Priestley and Taylor, 1972) formula for the green part of the canopy as

$$LE_c = \alpha_{PT} \cdot f_G \cdot \left(\frac{\Delta}{\Delta+\gamma}\right) \cdot Rn_c \quad 32$$

where f_G is the fraction of LAI that is green and usually taken as (f_G =1), Δ the slope of the saturation vapor pressure versus temperature curve, and γ the psychrometric constant 0.066 kPa C^{-1}.

The P-T equation is used to provide an initial, specifically a potential rate of transpiration with the value of $\alpha_{PT} = 1.26$ that needs to be adjusted for actual surface conditions. For example two conditions ought to be considered: for well water vegetation under advective conditions a value of $\alpha_{PT} = 2.0$ is used; while for stressed vegetation which usually transpires at a lower rate than the potential rate, using a value of 1.26 will tend to overestimate LE_c resulting in unrealistic values of $LE_c < 0$. In this case α_{PT} is iteratively reduced until it reaches in some case $LE_c = 0$. Another approach to estimate LE_c was introduced by Anderson et al. (2000) that utilizes light use efficiency. This approach has recently been applied over different surfaces and showed promising results. More details on this approach is provided in part 1 of this report (Geli and Neale, 2015).

DisALEXI provides estimates of instantaneous surface energy balance fluxes including λE (W m^{-2}) during the overpass time and date of any particular sensor. Estimates of daily ET can be obtained by extrapolation of instantaneous estimates of λE using the evaporative fraction (EF) method defined as $\lambda E/(R_n - G)$ (Norman et al., 2003). In some cases (Anderson et al., 2012, 2007) the EF is adjusted by a factor of 1.1 to account for underestimation of the EF of 5-10 % observed during midday hours as indicated by Brutsaert and Sugita (1992).

To provide daily ETa in between Landsat overpass dates, Anderson et al. (2011) followed a data fusion framework that uses remote sensing data from multiple sensors. The intent of this framework is to provide enhanced remote sensing data temporal resolution at Landsat scale throughout the growing season. The framework is based on two algorithms – thermal sharpening (Kustas et al., 2003) and the Spatial Temporal Reflectance Fusion Model (STARFM) (Gao et al., 2006). The former is used to improve the spatial resolution of TIR band of a specific sensor to that of the shortwave bands. Usually the TIR bands are available at a relatively coarse resolution compared to that of the shortwave bands due to sensors configurations and signal to noise issues. The spatial resolution of the TIR band for Landsat 5 is 120-m and it can be enhanced to be at 30-m of the visible bands. The latter uses statistical methods to develop relationships between Landsat and MODIS coincident images. These relationships can then be used to fill the gap between Landsat overpass dates that are usually 16-days. Hence the STARFM fuses (predict) Landsat scale data based on MODIS. (Gao et al., 2006) developed STARFM to provide surface reflectance data, later (Anderson et al., 2011) followed this approach to directly fuse ETa maps.

2.2 Evaluation of Models

Estimates of spatially distributed surface energy balance fluxes and ETa are evaluated against ground-based observations from Bowen ratio (BR) and eddy covariance (EC) towers. The

ground-based measurements either from BR or EC originate from a source area, called the footprint, located in the upwind direction of the measurement tower and with a variable weight of contribution according to several factors including atmospheric stability conditions. The footprint represents a 3D weights of the contribution of each defined pixel in the upwind direction to the integrated measured flux. In this analysis the footprint model by Horst and Weil (1994, 1992) is used. The integrated vertical flux measurements $F(x, y, z_m)$ at a height z_m can be estimates as the integral of the spatially distributed fluxes $F_0(x', y', z' = 0)$ multiplied by the footprint weight function *f* and can be described as

$$F(x, y, z_m) = \int_{-\infty}^{\infty} \int_{-\infty}^{x} F_0(x', y', z' = 0) \cdot f(x - x', y - y', z_m) dx' dy' \quad 33$$

where x and y are the upwind and crosswind distances, respectively, from the point measurement. The estimated footprint from this model can provide 90% representation of the total contributed source area.

Another issue that needs to be considered is related to the lack of energy balance closure of EC systems measurement. Such lack of closure can be up to 20% as described by Twine et al. (2000). The closure of energy balance can be achieved following one of the methods suggested by Twine et al. (2000) that include the Bowen ratio (BR) defined as H/LE and the Residual (Re) approaches. The Re method tends to attributes all the error to the measurements of LE while the BR method distribute this error between H and LE. As there is no definitive agreement in the literature on which one should be followed both methods were used in this analysis to highlight the related differences when evaluating models results.

Statistical performance evaluation in this analysis were based on root mean square difference RMSD, the mean absolute difference MAD, mean difference or bias (BIAS).

$$\left.\begin{aligned} RMSD &= \frac{1}{n}\sqrt{\sum_{i=1}^{n}(P_i - O_i)^2} \\ BIAS &= \frac{1}{n}\sum_{i=1}^{n}|P_i - O_i| \\ MAD &= \frac{1}{n}\sum_{i=1}^{n}(P_i - O_i) \end{aligned}\right\} \quad 34$$

where P and O are the estimated and measured values, respectively, n the number of record.

The accuracy of the water balance component was estimated using the coefficient of variation (CV) and confidence interval (CI). The 95% CI is estimated as ±2 CV following the approach described by Clemmens (2009). CV is estimated as the standard deviation divided by mean of the values. To estimate CI for the ETa that is estimated as the residual of water balance components as

$$\mu_0^2 \cdot CV_0^2 = \sum_{i=1}^{n} \mu_i^2 \cdot CV_i^2 \quad 35$$

with the subscript i represents the water balance component.

3. DATA

Two testing sites were selected to perform the model inter-comparison analysis. These sites are located in different climatic regions and exhibit different land cover types and vegetation growing conditions. These sites are agricultural fields at the Palo Verde Irrigation District (PVID), Palo Verde, CA, and Mead (Mead), Ne.

Different dataset used were used in this analysis including remote sensing data, weather forcing data, water balance components (e.g. canal inflow, drains outflow and groundwater fluctuations), and surface energy balance fluxes from eddy covariance and Bowen ratio flux towers. Unified dataset were meant to be used during the analysis for all models applications, however, some models required different input data than the unified dataset provided by USU. A brief description of these data is provided in this section.

3.1 Site 1 at PVID

3.1.1 Site Description

The PVID is an irrigated agricultural area located in Riverside and Imperial counties, CA and it is a privately owned entity (PVID, 2015). The total area of the PVID is about 440 km^2 mostly covered with alfalfa (70%), cotton (15%) and the remaining (15%) covered with mixed vegetable crops (Figure 8). The area diverts irrigation water from the Colorado River via a diversion dam at Palo Verde. A network of irrigation and drainages canals supports the gravity-fed surface irrigation system. The PVID is located in a climatic region that is characterized by arid to semi-arid conditions where it receives an average annual precipitation of 50 mm. The eastern side of the PVID agricultural area is bordered by the Colorado River and desert lands surround the northern and western boarders. The area is relatively level ranging in elevation from 290 amsl at the northeast end to 220 m at the southwest end. The underlying soils are alluvial having a texture of mixed fine grain clays, silty loams, and sand. The long growing season at the PVID allows for year-round harvested agriculture suitable for many crops such as the perennial alfalfa crop and some vegetables grown during the winter months.

3.1.2 Remote Sensing Data

The remote sensing data used in this analysis include images in the multispectral reflectance and thermal infrared (TIR) bands. Multiple Landsat 5 scenes during the year of 2008 were obtained from the USGS data portal. The data were provided based on the current processing system as Level 1 Product Generation System (LPGS). It is worth noting that the raw thermal infrared data provided as Band 6 were collected at 120 m pixel resolution and the USGS provides a resampled 30 m product processed using cubic convolution resampling method. Standardized at-surface reflectance product were provided by the USGS that have already been atmospherically corrected. The thermal infrared data were atmospherically corrected to provide at-surface radiometric temperatures as described in Section 3.1.3. A list of all Landsat 5 scenes used during this analysis is provided in Table 20.

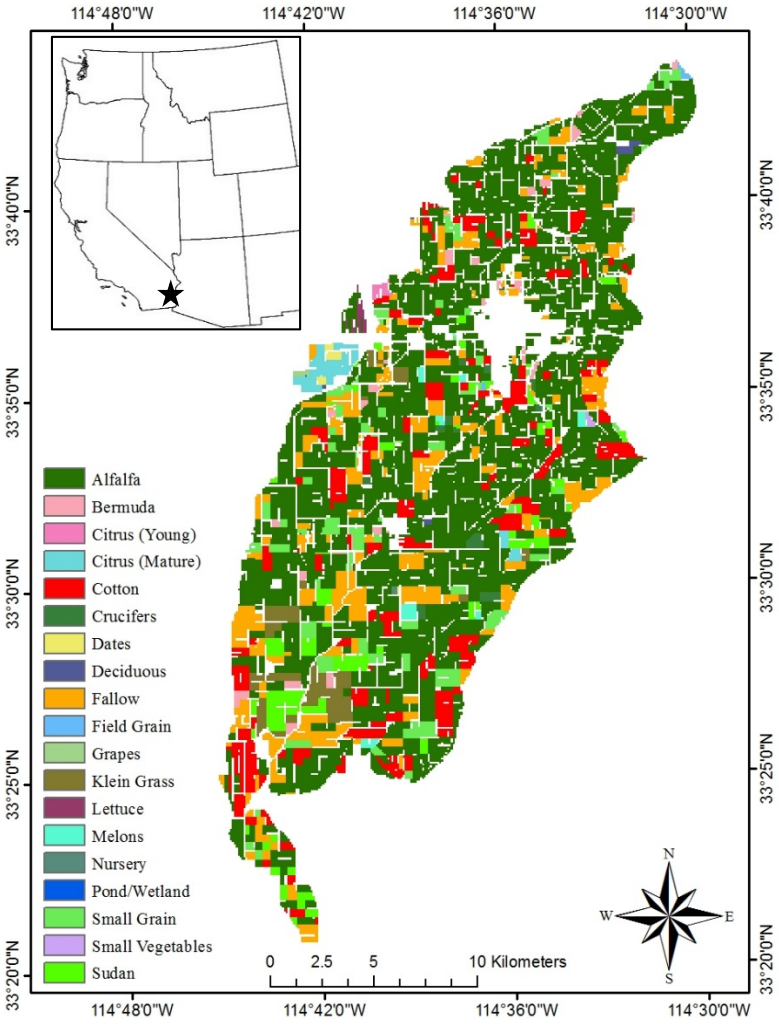

Figure 8: The location of the Palo Verde Irrigation District (PVID) along with the land use during the growing season of 2008.

3.1.3 Atmospheric correction of TIR data

The Landsat 5 imagery in the TIR band are currently provided in calibrated digital numbers (DN) that can be converted to radiance values. These at-sensor radiance values can then be used to estimate at-surface brightness temperatures (T_B) as

$$T_B = \frac{k_2}{ln[k_1/L+1]} \quad 36$$

where Ts is the surface brightness temperature (K), L is the integrated at-sensor band radiance (W m^{-2} sr^{-1} μm^{-1}), and k_1 and k_2 are calibration constants. For Landsat 5, k_1 =607.76 W m^{-2} sr^{-1} μm^{-1} and k_2= 1260.56 K (Chander and Markham, 2003). The radiance can be calculated based on the DN as follows

$$L_\lambda = G_{rescale} \cdot Q_{cal} + B_{rescale} \quad 37$$

with

$$G_{rescale} = \frac{LMAX_\lambda - LMIN_\lambda}{Q_{cal\,max}} \text{ and } B_{rescale} = LMIN_\lambda \quad (38)$$

where $G_{rescale}$ (W m^{-2} sr^{-1} μm^{-1}) and $B_{rescale}$ W m^{-2} sr^{-1} μm^{-1} are band-specific rescaling factors (Chander and Markham, 2003) provided in the header/metadata file that is associated with each Landsat scene.

A radiative transfer model is used to correct for atmospheric effects when estimating Ts based on the brightness temperature. MODTRAN 4.1 and 5 radiative transfer model (Berk et al., 1998) was used during the analysis along with radiosonde data from the nearest station to the specified site. The model provides estimates of the corresponding at-sensor radiance and bright ness temperature for a given set of surface temperature and surface emissivity, and sensor response function. A set of different surface emissivity and surface brightness temperatures are estimated. This information is then used to create a linear regression equation as

$$T_R = a + b \cdot T_B + c \cdot \varepsilon_{surface} \quad (39)$$

where a, b, and c are regression coefficients that corresponds to each scene, and $\varepsilon_{surface}$ is the surface emissivity estimated as a function of the vegetation fraction of cover fc as

$$\varepsilon_{surface} = fc \cdot \varepsilon_{veg} + (1 - fc) \cdot \varepsilon_{soil} \quad (40)$$

with ε_{veg} and $\varepsilon_{surface}$ are the soil and vegetation emissivity, respectively and

$$f_c = 1 - \left(\frac{NDVI_{max} - NDVI}{NDVI_{max} - NDVI_{min}}\right)^a \quad (41)$$

where $NDVI_{max}$ and $NDVI_{min}$ are the NDVI for full cover vegetated surface and bare soil and a is a coefficient that ranges between 0.6 to 1.25 for electrophile to planophile canopies. Figure 9 provides a comparison between T_B and T_R for one of the Landsat scenes used in this analysis. Other models such as METRIC (Allen et al., 2007a, 2007b) uses a different approach to estimate T_R.

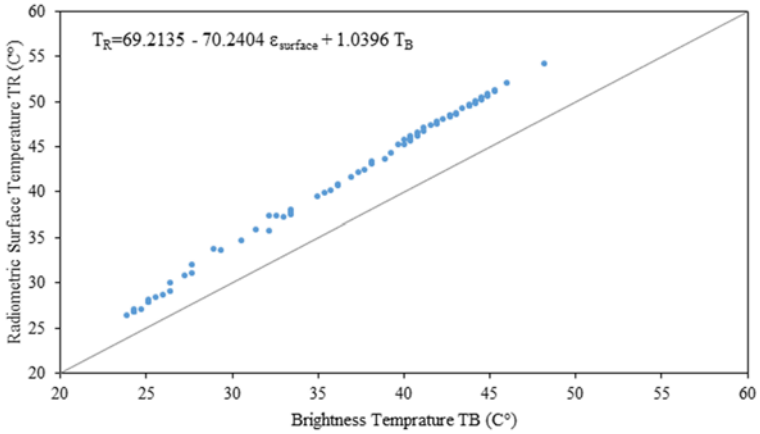

Figure 9: scatterplot of showing a comparison between brightness and radiometric surface temperatures before and after corrections, respectively, for DOY 131.

Table 20: List of Landsat 5 scenes over the PVID and used in the analysis

NO.	DATE	DOY (2008)	PATH	RAW
1	19-Jan-2008	19	38	37
2	11-Feb-2008	42	39	37
3	27-Feb-2008	58	39	37
4	07-Mar-2008	67	38	37
5	23-Mar-2008	83	38	37
6	08-Apr-2008	99	38	37
7	24-Apr-2008	115	38	37
8	10-May-2008	131	38	37
9	17-May-2008	138	39	37
10	26-May-2008	147	38	37
11	11-Jun-2008	163	38	37
12	18-Jun-2008	170	39	37
13	13-Jul-2008	195	38	37
14	29-Jul-2008	211	38	37
15	05-Aug-2008	218	39	37
16	21-Aug-2008	234	39	37
17	15-Sep-2008	259	38	37
18	01-Oct-2008	275	38	37
19	17-Oct-2008	291	38	37
20	09-Nov-2008	314	39	37
21	18-Nov-2008	323	38	37

3.1.4 Weather Forcing Data

The weather forcing data were obtained from the California Irrigation Management Information System (CIMIS) weather stations. The data from three stations located within the PVID were used including stations no. 135, 151, and 175 at Blythe NE, Ripley, and Palo Verde II (Figure 10). These weather forcing data include measurements of incoming solar radiation (Rs), air temperature (Ta), wind speed (U), relative humidity (RH), as well as calculated Penman-Monteith grass and/or alfalfa reference ET (ETo/ETr) at hourly and daily time scales. The measurements were at 2 m agl for U and Rs and at 1.5 m agl for Ta and RH. An example of measured daily average Ta grass reference ET (ETo) is shown in Figure 11.

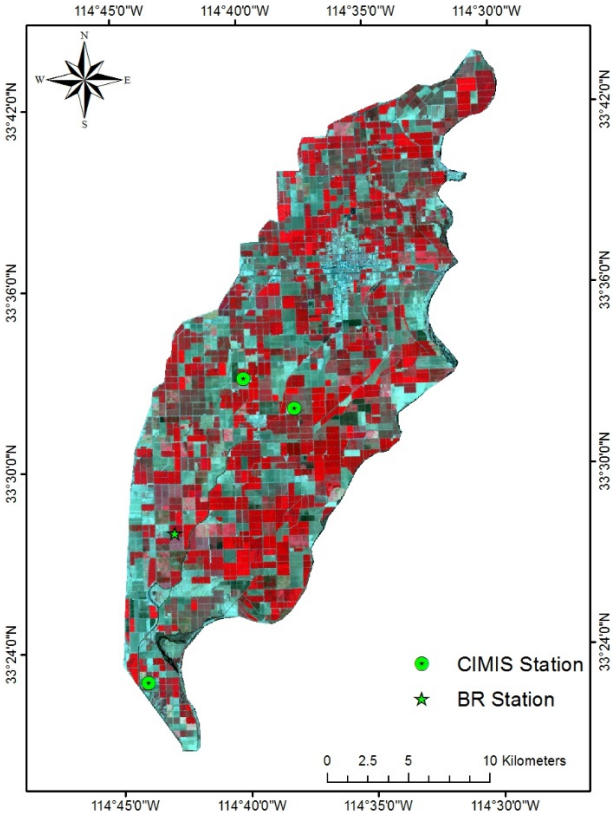

Figure 10: location of weather stations and energy balance flux tower measurements.

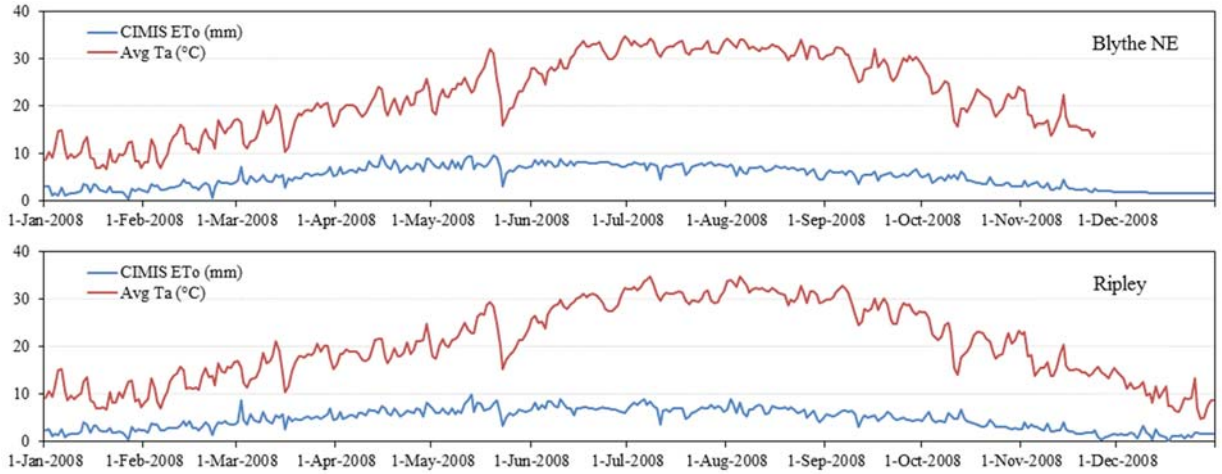

Figure 11: Timeseries of daily average air temperature Ta and CIMIS grass reference ET (ETo) during 2008.

3.1.5 Surface Energy Balance Fluxes

Surface energy balance flux measurements were obtained from an alfalfa field using a Bowen ratio (BR) system developed by Radiation and Energy Balance Systems (REBS) Inc., Seattle, WA. The BR system was installed at an alfalfa field (Figure 12) taking measurements at an average height of 2 m agl. The system consists of an Automatic Exchange Mechanism that switch the height of the lever arms that holds the air temperature and humidity sensors every 15 minutes to reduce biases. These 15-minute data are then used to calculate surface energy balance fluxes including H and LE at 30-minute averages. Soil related measurements at an average depth of 10 cm below the surface include soil heat flux using, soil temperature and water content using soil heat flux plate, soil temperature props, and soil moisture sensor, respectively, provided by REBS Inc. This set of soil measurements were installed at three locations below a set of two Q7.1 net radiometers by REBS Inc. the set of measurements include also air temperature, humidity, pressure using temperature, humidity, wind speed and direction. These data were managed using a CR10X datalogger by Campbell Scientific Inc., Logan, Utah. Timeseries of calculated daily actual ET (ETa) based on the BR measurements during 2008 is shown in Figure 13.

Figure 12: layout of the BR system located over an alfalfa in PVID

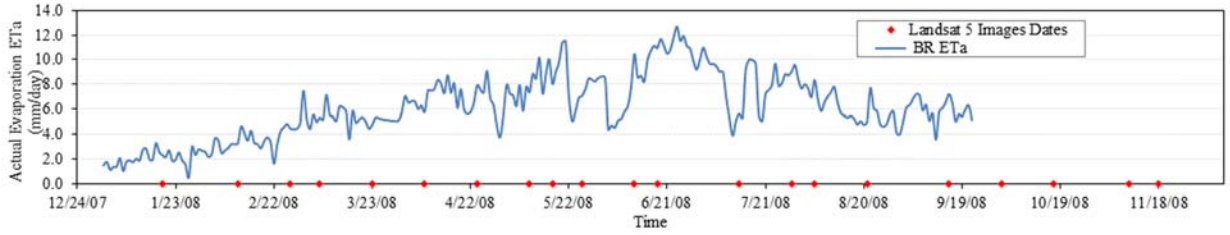

Figure 13: Plot of daily ETa (mm/day) during 2008 as measured by the BR system along with the Landsat overpass dates.

3.1.6 Water Balance Components

The PVID can be considered as a controlled hydrologic system with defined input and output water quantities that are routinely measured with a reasonable accuracy. The PVID receives its irrigation water from the Colorado River via the Palo Verde diversion dam located at the northeast side of the area. The water gets distributed within the PVID via 440 km of irrigation canal network and the excess water is collected and returned to the river via a network of 230 km of drains. Another source of water input, yet minimal, is the precipitation that accounted for ~ 75 mm during 2008. Hence the main water input include inflow from the diversion dam, precipitation, and the main outflows include drainage water measured at the main outflow drain, infiltration percolated to groundwater, lateral canal spills measured before returning to the Colorado River and ET. Measured inflow and outflow are shown in Figure 14 and it can be obtained from the USGS data portal. Groundwater table fluctuations is monitored using 260

wells distributed on one-mile grid with measurements made once at the beginning of each month (Figure 15).

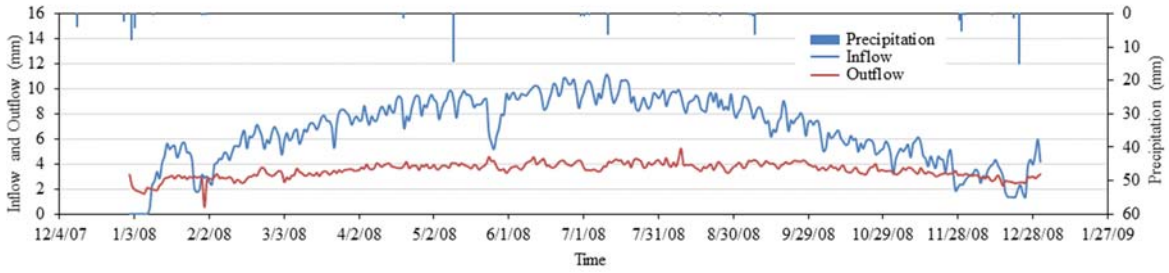

Figure 14: Measured inflow, outflow, and precipitation at the PVID during 2008

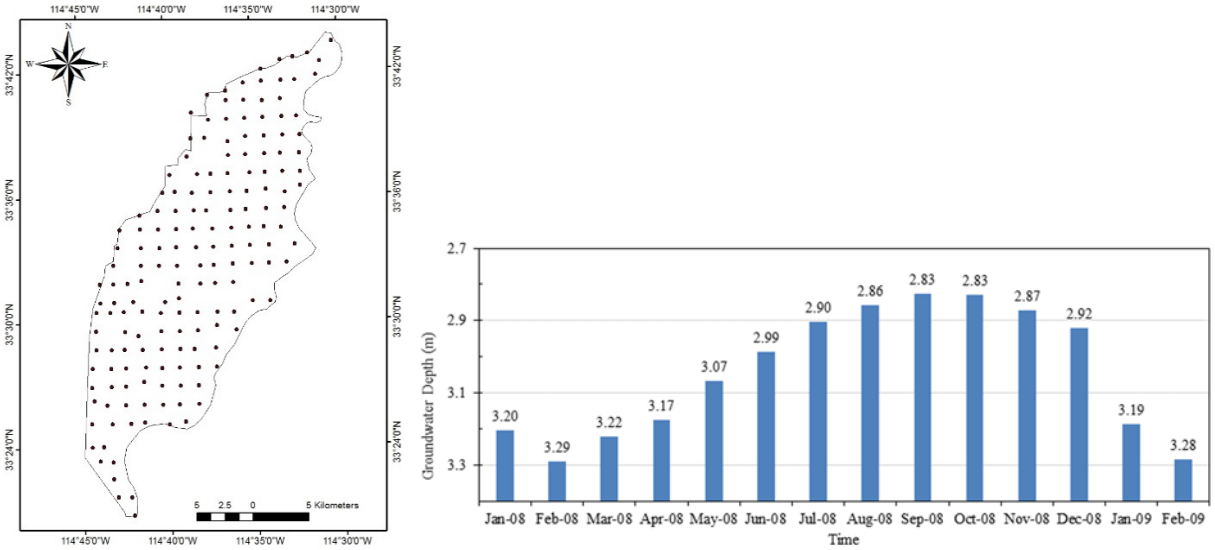

Figure 15: Groundwater piezometers distribution and the corresponding fluctuations for the calendar year 2008.

3.2 Site 2 at Mead

3.2.1 Site Description

The site consist of irrigated and dryland agricultural fields located at the University of Nebraska Agricultural Research Center (Figure 16), Lincoln, NE. There are three fields cultivated with maize and soybean crops with two of them supported with pivot irrigation systems and the third is a rainfed field. Planting and harvesting of the maize crop occur during summer between Late April/ Early May and Late October, respectively (Table 20). Hydrometeorological measurements at the three sites are obtained using EC systems as part of the Ameriflux network. The EC towers height is 6 m and the maximum crop height at full cover ranges between 1.7 to 2.9 m.

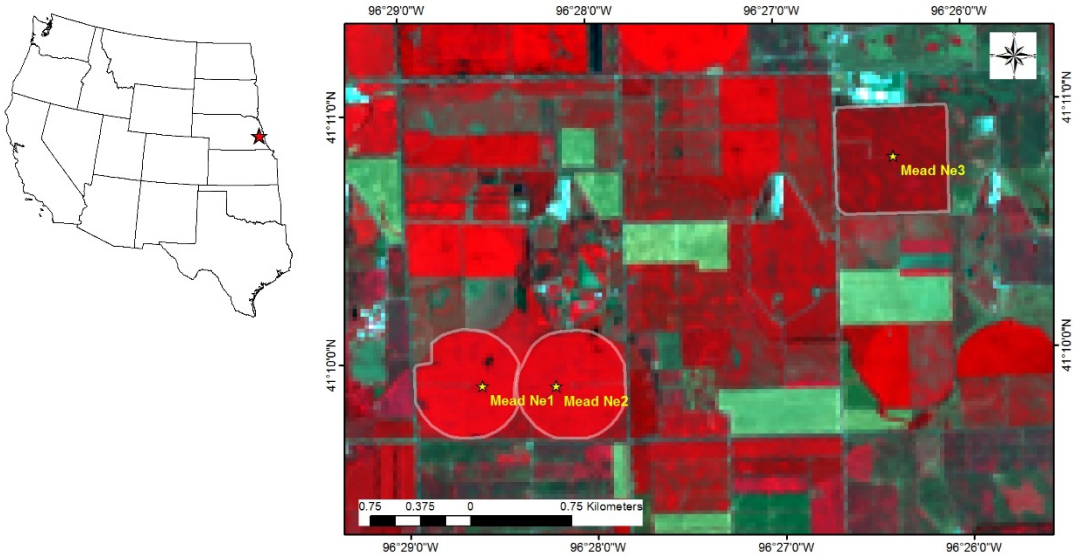

Figure 16: Location of dryland (US-Ne 3) and irrigated (US-Ne 1 and US-Ne 2) maize fields in Mead, NE.

Table 21: Description of the growing season and crop rotation for the three sites near Mead, NE

Site	Irrigation	Crop Type/hybrid	Planting Date	Emergence Date	Harvesting Date	Density Plant/ha
US – Ne 1	Irrigated	Maize (DKC 61-16-RIB)	29-April-2013	14-May-2013	22-October-2013	80,400
US – Ne 2	Irrigated	Maize (DKC 61-16-RIB)	30-April-2013	15-May-2013	22-October-2013	78,900
US – Ne 3	Rainfed	Maize (DKC 62-98-RIB)	13-May-2013	21-May-2013	21-Ocotber-2013	50,200

3.2.2 Remote Sensing Data

Remote sensing data from Landsat 7 and Landsat 8 were used in this analysis. Multispectral reflectance and TIR imagery were obtained during satellite overpass dates. Nine scenes were identified that have no or minimal cloud contamination. Apparently there are periods with considerable gaps with no data as shown in

Table 22**Error! Reference source not found.**. Multispectral reflectance for Landsat 7 are available for bands 1-5 and 7 while for Landsat 8 are for bands 2-7. TIR image are available in band 6 for Landsat 7 with a band width of 10.44-12.5 μm while that for Landsat 8 are available for bands 10 and 11 with band width of 10.6-11.19 μm and 11.5-12.51 μm and xx, respectively. Band 10 for Landsat 10 is used during this study. All thermal bands were atmospherically corrected using MODTRAN to provide surface temperature TR and reflectance data were provided via LPDAAC system available through the USGS data portal.

Table 22: List of Landsat 7 and 8 scenes provided over Mead, NE site during 2013

No.	Date	DOY (2013)	Landsat Sensor	Path	Raw
1	24-April-2013	114	7	28	31
2	3-June-2013	154	8	28	31
3	19-June-2013	170	8	28	31
4	21-July-2013	202	8	28	31
5	30-August-2013	242	7	28	31
6	23-September-2013	266	8	28	31
7	1-October-2013	274	7	28	31
8	9-October-2013	282	8	28	31
9	25-October-2013	289	8	28	31

3.2.3 Weather Forcing and Flux data

Three ground-based observation towers located within each of the fields provide measurements of weather forcing and fluxes. The towers are instrumented with EC systems and are part of the AmeriFlux network. The meteorological data were observed by the stations US-Ne1, US-Ne2, and US-Ne3 with irrigated maize, irrigated rotational maize and soybeans, and rainfed (dryland) maize, respectively.

4. RESULTS AND DISCUSSION

4.1 Palo Verde Irrigation District (PVID)

An example of spatially distributed estimates of daily ETa for May 10, 2008 -one of the satellite overpass dates-for each model including their average is shown in Figure 17. Visual inspection of this result clearly showing considerable spatial variability when compared to each other. Using the same ETa categories for all maps; four models including their average (Average) showed daily ETa values ranging between 0 to 10 mm/day except DisALEXI model which did not provide estimates of ETa in 0-1 mm/day category. Figure 18 shows plots of histogram – plot of ETa versus their frequency- that correspond to those on Figure 17. The METRIC model resulted in ETa values mostly in > 6 mm/day category followed by ReSET (Figure 18) with both models showed similar frequency distribution. It is noticed that SSEBop model resulted in ETa estimates mostly in only two categories 0-1 and > 6 mm/day with relatively similar ETa frequencies in all other ETa categories (Figure 18). This behavior of the SSEBop model can be explained by the model parametrization that is based on scaling its estimates between 0-1 as described in Eq. 21. These histogram plots provide clear indication of how these ETa estimates could be different in terms of spatial variability of daily ETa. These differences could have some effects on applications that require daily ETa information such as detection of water stress condition, irrigation scheduling, and precision agriculture. On applications that require estimates of annual water requirements such differences

on daily ETa between these model results might have minimum effects as discussed below. The corresponding area-average and total ETa values in mm/day and m^3/day, respectively, for each model are shown in Figure 18. The results show that the area-average values fall within a range of 0.5 mm/day when excluding the results of SSEB models that provided relatively the lowest mean value. The area-average values are 4.5, 4.4, 4.0, and 4.2 mm/day for DisALEXI, METRIC, ReSET, and SSEBop, respectively, while SEBS model provided 2.4 mm/day which is nearly half of all others. Considering the total area of the PVID of 440 km^2 (or 439,094, 000 m^2) a small ETa difference of 0.5 mm/day will result in a total volume water of 220 x 10^3 m^3/day or 58 Million gallons/day.

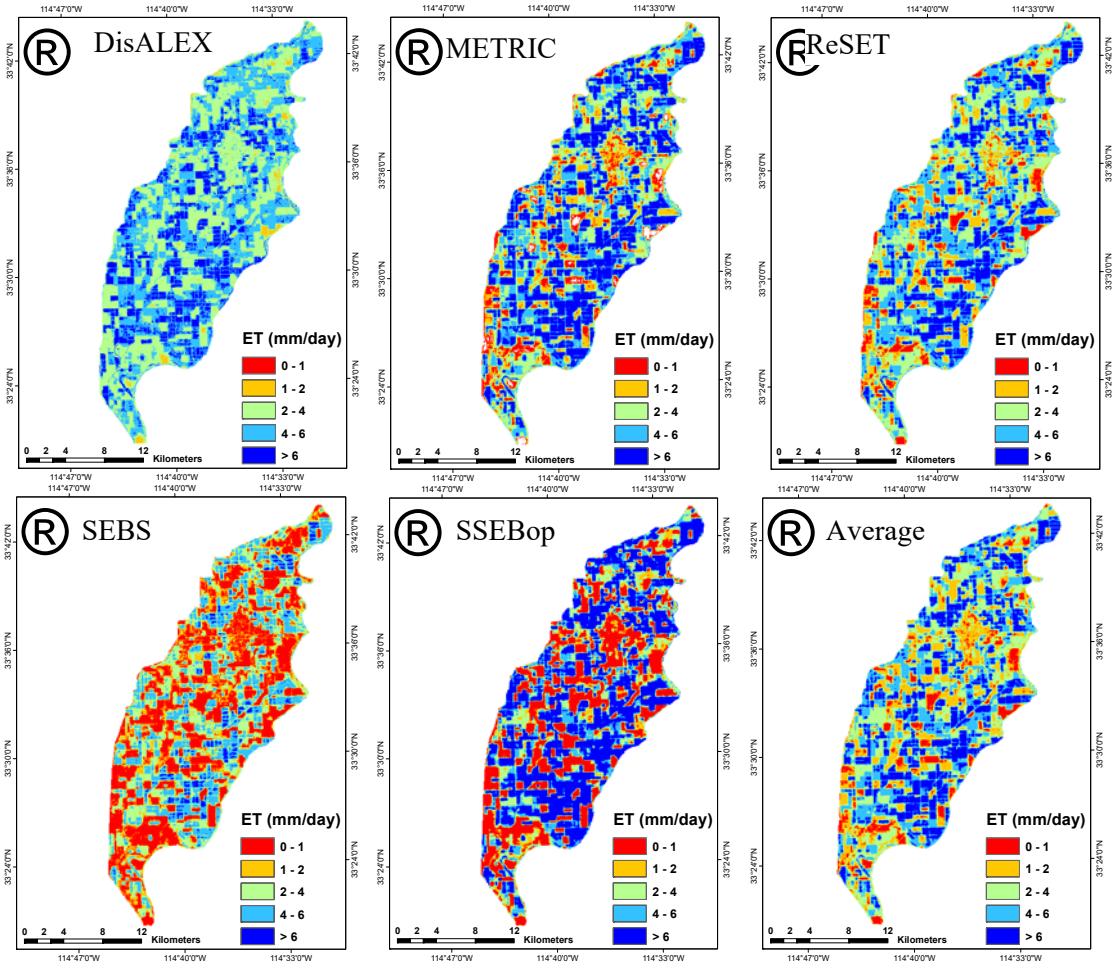

Figure 17: Estimates of daily ETa over the PVID based on METRIC, SEBS, SSEBop, ReSET, DisALEXI, and average of all models (Average) for day of year (DOY) 131 or May 10, 2008.

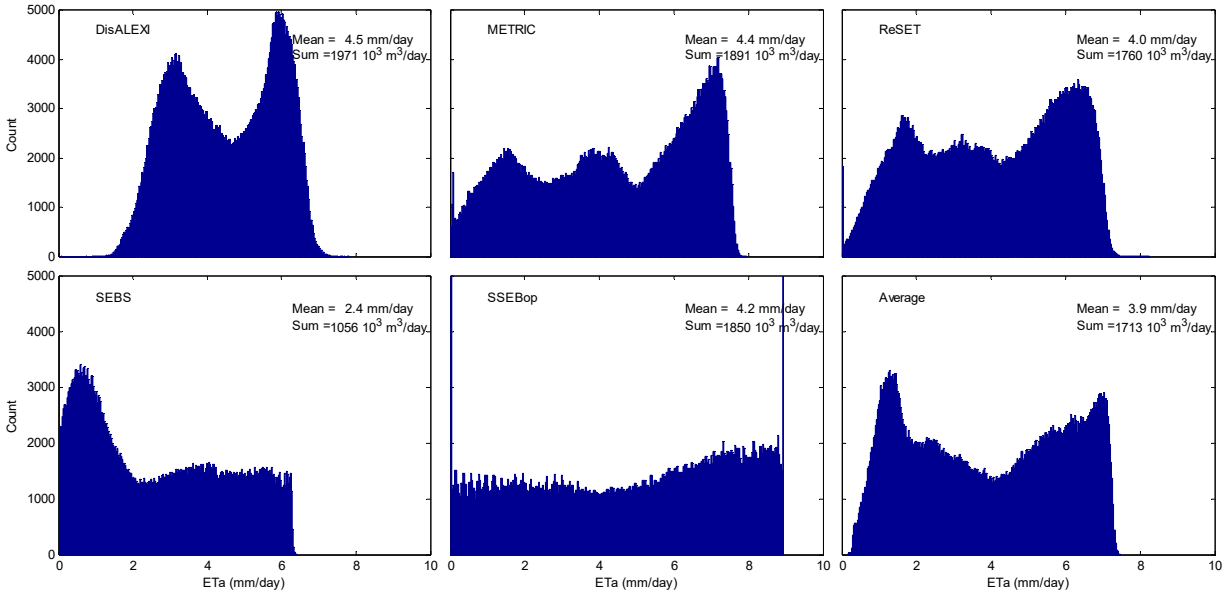

Figure 18: Histogram of estimated daily ETa based on all models and their average (Average) for DOY 131 May 10, 2008 over the PVID for the results shown in Figure 17

Figure 18The area-average daily ETa estimates during satellite overpass dates are shown in Figure 19 with the corresponding values shown in Table A1 (Appendix A). The seasonal variation of ETa is clearly shown with values increasing during the summer growing season April-August. The variation among models estimates of ETa within each satellite overpass date can also be observed with METRIC and SEBS models showing relatively the highest and the lowest estimates of ETa, respectively, while the rest of the models showing relatively similar behavior. Such variable models behavior shown in Figure 19 during satellite overpass dates throughout the growing season supports the fact that evaluating crop water requirements, irrigation scheduling, and water stress conditions using different models could result in variable crop growth behavior and eventually leading to mismanaged agricultural water resources.

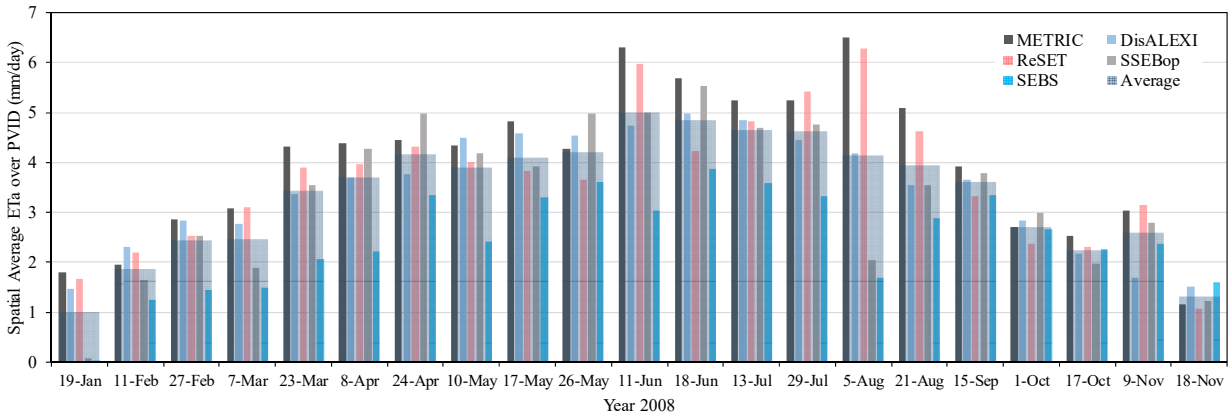

Figure 19: Plot of area-average daily ETa (mm/day) for all images and model estimates and their average (Average) for satellite overpass dates. The corrsponding values used to create the figure are provided in Table A1 (Appendix A).

Estimates of ETa during satellite overpass dates were compared against BR measurements obtained at one of the alfalfa fields to evaluate the models performance. Generally, fluxes measured by point-based system such as the BR towers are based on weighted area integrated from the upwind direction or footprint and were estimated as described in Section 2.2. The footprint of the BR tower measurements is estimated for each satellite overpass time and overlaid over the corresponding ETa images. An example of footprint analysis is shown in Section 0. The integrated footprint ETa values during each day were calculated and compared with the corresponding ETa measurements by the BR (ET_{BR}) as shown in Figure 20. Two models ReSET and METRIC showed narrow scattering around the 1:1 line while SSEBop model showed slightly larger scatter. DisALEXI model showed a slight underestimation while SEBS model showed considerable underestimation. Generally, all models resulted in an underestimation of daily ETa values as indicated by the negative BIAS. Based on the RMSD described in Table 23 the models can be ranked starting with METRIC with the lowest value followed in order by ReSET, SSEBop, DisALEXI, and SEBS.

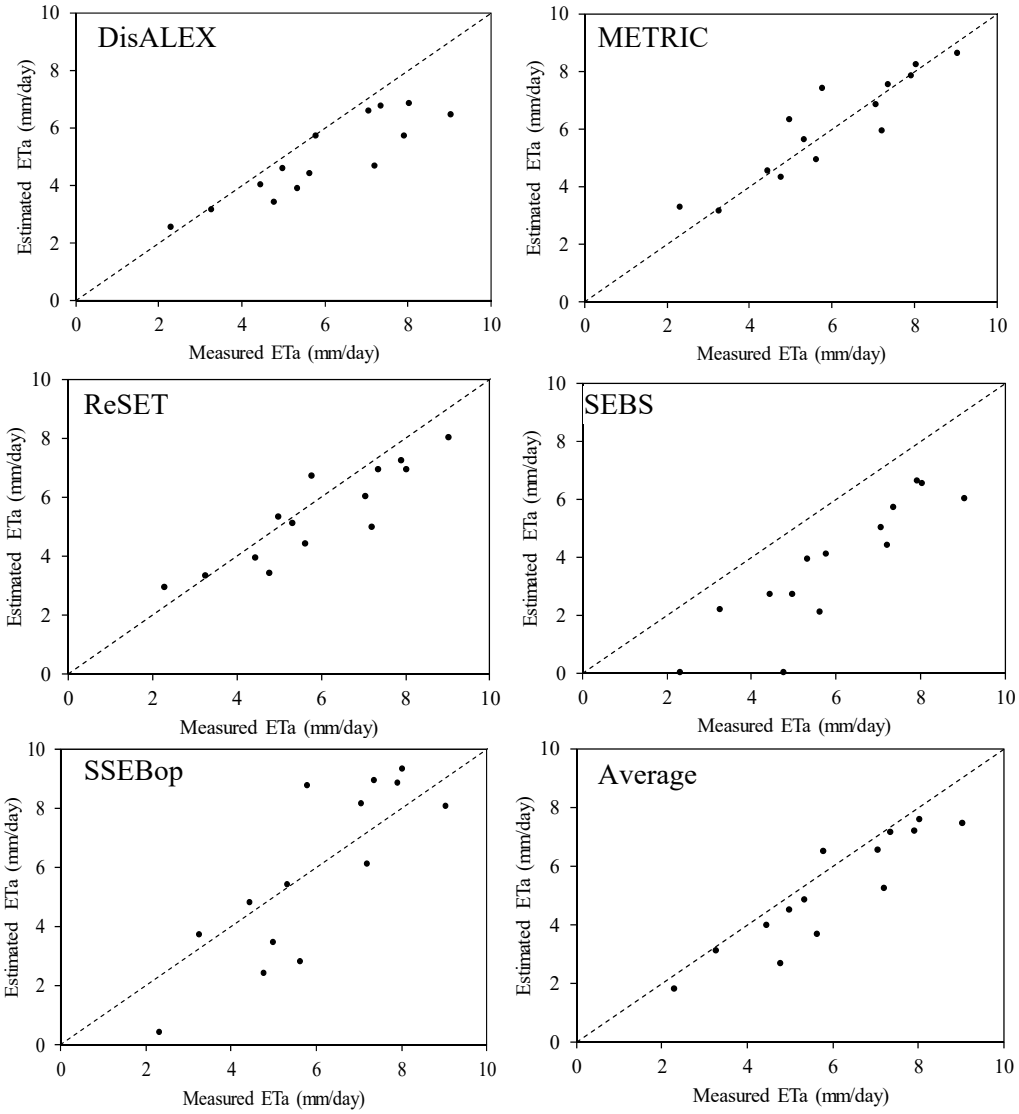

Figure 20: Comparison of estimated and measured daily ETa (mm/day) based on all models and their average (Average).

Table 23: Comparison of measured ET_{BR} based Bowen ratio method and estimated ETa based on DisALEXI, METRIC, ReSET, SEBS, and SSEBop, and their average (Average).

	RMSE mm/day	BIAS mm/day	BIAS (%)	MAE mm/day	Sample	Mean mm/day	Std. Dev. mm/day
Measured					16	6.55	2.4
SSEBop	1.5	-0.2	-7.2	1.3	16	6.35	2.8
SEBS	2.7	-2.5	-42.0	2.5	16	4.09	2.1
METRIC	0.9	-0.1	1.6	0.6	16	6.45	1.9
ReSET	1.3	-0.8	-9.8	1.1	16	5.70	1.7
DisALEXI	1.8	-1.4	-18.9	1.7	16	5.20	1.4
Average	1.3	-1.0	-15.3	1.4	16	5.54	1.9

Seasonal ETa can be based on approaches that combine remote sensing and traditional methods. As described in Section **Error! Reference source not found.** three models including ReSET, METRIC and SSEBop used this approach while DisALEXI used the STARFM algorithm (Gao et al., 2006)–a data fusion approach that combines multispectral data from multiple sensors to fill-in the gap between Landsat 5 scenes–in addition to a thermal sharpening model (Agam et al., 2008; Kustas et al., 2003). Both approaches are described in (Geli and Neale, 2015). The seasonal ETa estimates from each model as well as their average is shown in Figure 21 with the total annual ETa values and the corresponding uncertainties shown in Table 25.

Another approach to estimate seasonal ETa based on the water balance calculation was used to provide additional estimates for comparison purposes (ETa_{WB}). Estimates of ETa based on remote sensing models were compared to ETa_{WB}. The water balance components considered include diverted inflow water to the main canal, measured returns that include canal spills and outfall drains for the site, unmeasured return flow, and precipitation. For the calendar year of 2008 these values are 2,475 mm, 1,283 mm, 139 mm, and 75 mm over the area of 439.093 km^2. It is worth noting that the unmeasured return flows are reported by the USBR as constant percentage of ~ 5.6% with little information about how it was estimated.

Typically the uncertainty of these components (i.e. inflow and measured return flow) are based on gage or device used and may include a number of uncertainties such as reading error, device calibration and other potential sources of error (Wahlin et al., 1997). A number of studies (e.g. Allen et al., 2005; Clemmens, 2009; Wahlin et al., 1997) were conducted to evaluate the uncertainty of flow measurements of water balance components of agricultural areas specifically in California. In this study, the CI's obtained by Wahlin et al. (1997) for some canals and drains in Imperial Irrigation District were used since the PVID has flow measurement systems that are similar to those evaluated by Wahlin et al. (1997). The uncertainty of the water balance components including the inflow, measured returned flow, and unmeasured return flow is

assumed to have CI of ±2.1% based on the average CI value of those obtained by Wahlin et al. (1997). The accuracy for the precipitation is based on the reported accuracy of the rain gage of ±1% as indicated by CIMIS. Following Eq. (2.1.1) and using the value of ETa_{WB} for year 2008 of 1128 mm (when considering the unmeasured return flow) or 1267 mm (without considering the unmeasured return flow), the estimated accuracy of ETa_{WB} is ±5.2% or ±4.6%, respectively (Table 24). Note that the ETa_{WB} was calculated for the growing season to minimize uncertainties that arise from groundwater table fluctuations. These uncertainties in ETa_{WB} are relatively comparable to those reported for the Imperial Valley that fall within ±10% (Allen et al., 2005).

Comparison of seasonal ETa estimates based on remote sensing with ET_{a_WB} showed that, given the uncertainty in ET_{a_WB}, only two models provided estimates of ETa that fall within the 95% confidence interval of ET_{a_WB} in both cases, with or without considering unmeasured return flow. When considering the unmeasured return flow, the accuracy of ETa estimates based on DisALEXI and SSEBop fall within the CI of the ET_{a_WB} of ±5.2% with +2.8% and -3.2%, respectively. While when not considering the unmeasured return flow, two different models METRIC and ReSET provided ETa estimate that fall with the CI or ET_{a_WB} of ±4.6% with +3.5% and -3.6%, respectively. Three models, ReSET, DisALEXI, and SSEBop underestimated ETa_{WB} (1267 mm ±4.6% at 95% confidence level) by -3.6%, -8.6%, and -13.9%, respectively while METRIC model overestimated ET_{a_WB} by +3.5% (Table 25). By considering the unmeasured return flow as part of the water balance components, ETa_{WB} becomes 1128 mm with a CI of ±5.2% at 95% confidence level. In this case, at ET_{a_WB} = 1128 mm, three models including DisALEXI, ReSET, and METRIC, overestimated ETa_{WB} by +2.8%, + 8.4%, and +16.3%, respectively, while SSEBop underestimated ET_{a_WB} by -3.2%. Moreover, the results based on the two cases of ETa_{WB} –with or without considering the unmeasured return flow component –show that METRIC and SSEBSop have consistent behavior by always providing either overestimation or underestimation of ET_{a_WB}, respectively. On the other hand, DisALEXI and ReSET models changed their behavior from overestimation to underestimation when including the unmeasured return flow component.

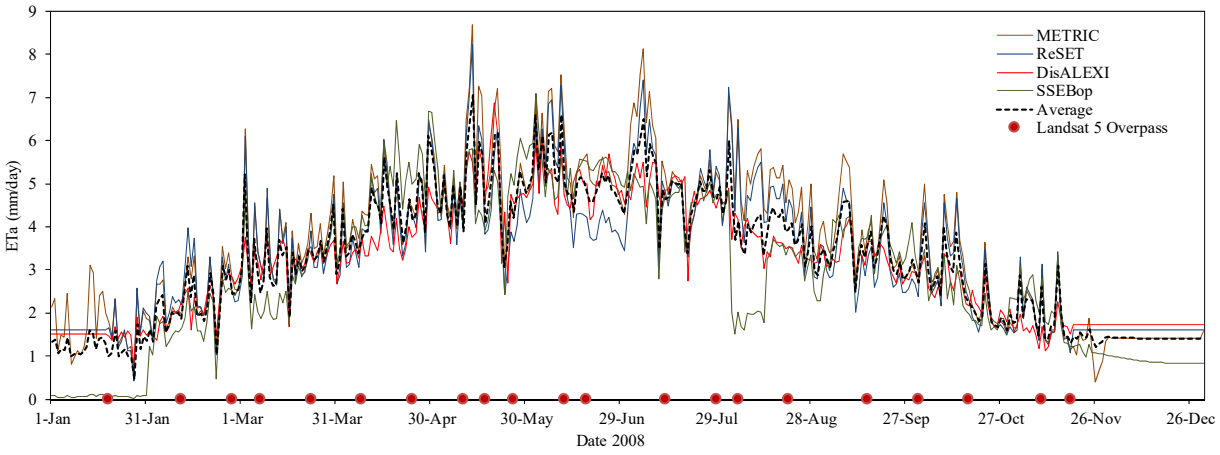

Figure 21: timeseries of modeled dailyETa (mm/day) based on METRIC, ReSET, DisALEXI, SSEBop, and their average (Average) along with the satellite overpass dates during 2008.

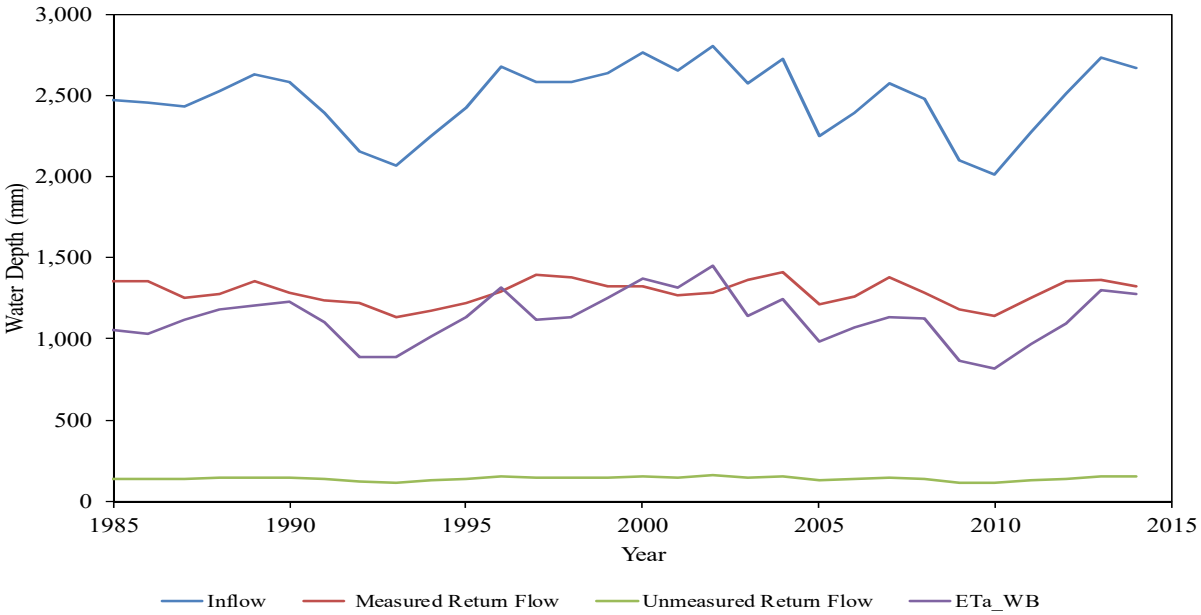

Figure 22: Historical 30 years record (1985-2014) of water balance components that include measured inflow, outflow, unmeasured return flow, and calculated ETa (ET_{a_WB}).

Table 24: Uncertainties of PVID water balance components based on 30 years of measurements and the estimated uncertainty of ETa_{WB} based on Eq. 2.1.1
.

Water Balance Components	Water Balance	Uncertainty *
Inflow:		
Precipitation (mm) [a]	75	± 1%%
Inflow Main Canal (mm) [b]	2,475	± 2.2% %
Outflow:		
Canal Spills + Outfall Drain (mm) [c]	1,283	± 2.2 %
Unmeasured Returns [d]	139	± 2.2%
Evapotranspiration (ETa) [e] $(\boldsymbol{e = a + b - c - d})$	1,128 (1,267)[#]	± 5.2 % (± 4.6 %)[#]

* numbers indicate the 95% confidence level for water balance components
# the unmeasured returns were estimated by USBR as fixed percentage of ~5.6% of the total inflow from the main canal with no information of how this was estimated. In case we considered this as part of the ETa_WB as shown in bracket, the corresponding 95% confidence level is shown as 4.6%.

Table 25: Comparison of water balance-based ET_{a_WB} and remote sensing-based ETa on annual based for PVID for year 2008

	Water Balance	METRIC	ReSET	DisALEXI	SSEBop
Actual Evapotranspiration (ETa) (mm)	1,128 (1,267)	1,312	1,223	1160	1,092
Uncertainty (%)	±5.2 % (± 4.6%)	+16.3% (+3.5%)	+8.4 (-3.6%)	+2.8% (-8.6%)	-3.2 (-13.9%)
Total Inflow (mm)	2,550	2,550	2,550	2,550	2,550
Total Outflow (mm)	2,550	2,595	2,506	2,443	2,375
Inflow – Outflow (mm)	(0)	+45	-45	-108	-175

The uncertainty values by each model indicate the diversion of remote sensing estimates of ETa from water balance based $ETa_{\_WB}$.

4.2 Irrigated and Dryland Fields Mead, NE

Estimates of spatially distributed daily ETa over the three agricultural fields US-Ne 1, and US-Ne 2 and US-Ne 3 as well as the surrounding areas based on all models and their average (Average) are shown in Figure 23. The example shown is for ETa during DOY 202 July 21, 2013. The model estimates showed relatively similar patterns in terms of the spatial variability of ETa. Areas with relatively low or high ETa values were observed on the same regions by all models with some minor differences as indicated by the assigned categories. The corresponding histograms of ETa estimates are shown in Figure 24. These histograms indicate that ReSET and SEBS model resulted in values ranging from 0-8 mm/day, METRIC and SSEBop models showing values ranging from 0-7 mm/day, and DisALEXI model resulting in a narrow distribution of values ranging from 2-6 mm/day. In general, these histograms show relatively similar distribution or pattern which supports the observed spatial variability shown in Figure 23.

Spatially distributed ETa for all models during all 9 satellite overpass dates is shown in Figure 25. The observed similarity of the spatial variability pattern shown in Figure 23 for DOY 202 July 21 can also be observed on DOY 242, August 30. It should be noted that based on the growing season for all three fields, the crops are at their peak growth stage and hence having higher ETa rates. Differences in spatial variability pattern can be observed among models estimates of ETa on other overpass dates. However, METRIC and ReSET models showed similar behavior throughout the growing season when compared to each other. The other three models DisALEXI, SEBS, and SSEBop behaved relatively similar when compared to each other but as a group they behaved differently compared to METRIC and ReSET models. It should be noted that on June 19 the satellite image was slightly contaminated with some clouds which is a typical condition over humid regions such as the Mead site. Due to this issue three models DisALEXI, ReSET and SEBS did not provide estimates of ETa indicating the possibility of obtaining misleading results. In the case of the METRIC model during such cloudy days, nearby fields were used as surrogate to obtain estimates of ETa.

Comparison of model estimates with ground-based EC measurements of ETa was carried out by integrating the weights of footprint measurements over each model spatial ETa estimates. The upwind footprints were calculated for all Landsat overpass dates and times at each of the three towers US-Ne 1, US-Ne 2, and US-Ne 3. The footprint typically provides 90% of the total source area of measurements. For this study the footprint comprised 2-4 Landsat visible band pixels (Landsat pixel size in the visible band is 30-m) on the upwind direction and 2-3 in the crosswind direction. An example of flux footprint overlaid with estimates of ETa from DisALEXI is shown in Figure 26 at US-Ne 1 for DOY 202 July 21 2013. Following this approach all models estimates of ETa were compared with measurements and shown in Figure 27.

Three model estimates showed reasonable scatter around the 1:1 line including DisALEXI, SEBS, and SSEBop while the two other models METRIC and ReSET showed relatively large scatter away from the 1:1 line. The resulting model average (Average) showed reasonable scatter around 1:1 line. The corresponding model performance statistics are provided in Table 26. The results indicate that DisALEXI resulted in the lowest RMSE of 1.00 mm/day and the highest was from ReSET model followed by METRIC model as 3.2 and 2.9 mm/day, respectively. The other two models showed relatively similar behavior having RMSD of 1.3 mm/day for both SSEBop

and SEBS models. Generally, all models provided overestimation of ETa with the lowest BIAS of 0.2 mm/day provided by SSEBop and the highest BIAS of 2.7 mm/day provided by ReSET.

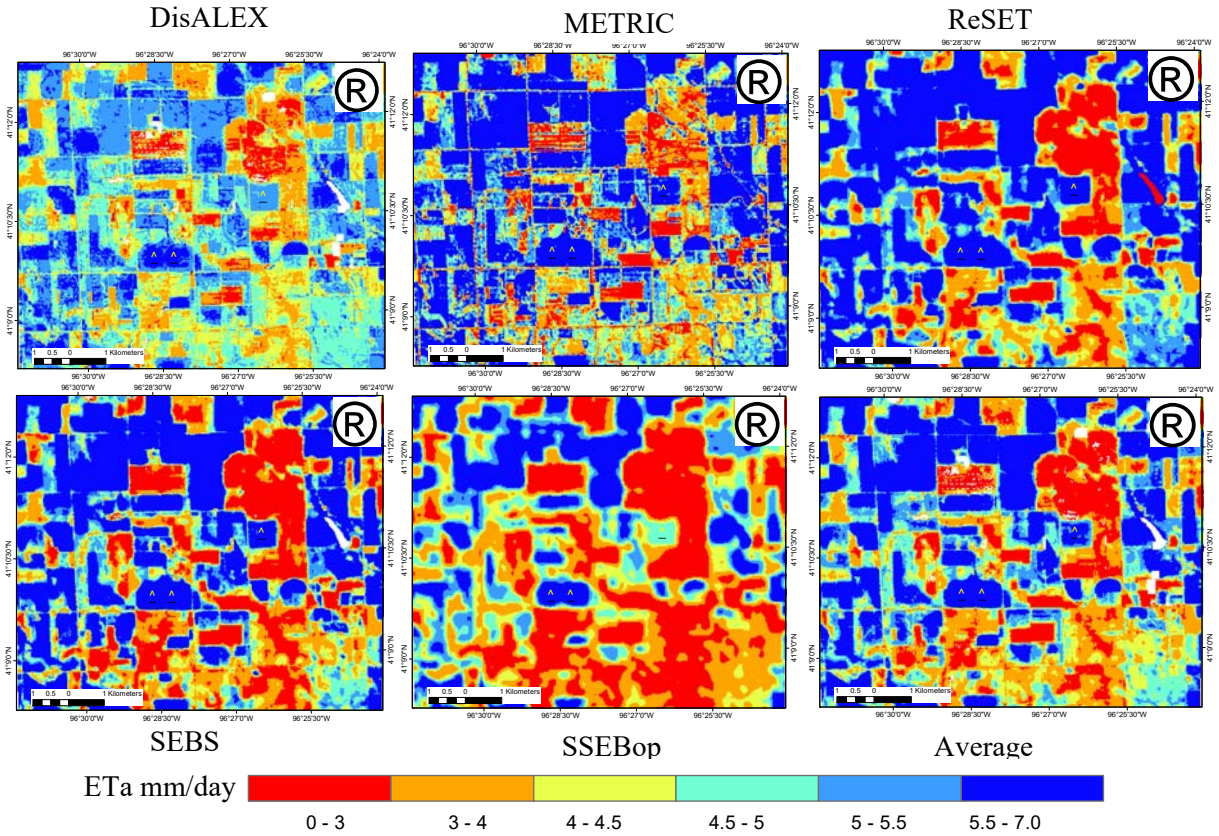

Figure 23: Estimates of actual evapotranspiration ETa based on DisALEXI, METRIC, ReSET, SEBS, and SSEBop models as well as their average (Average) on DOY 202, July 21, 2013.

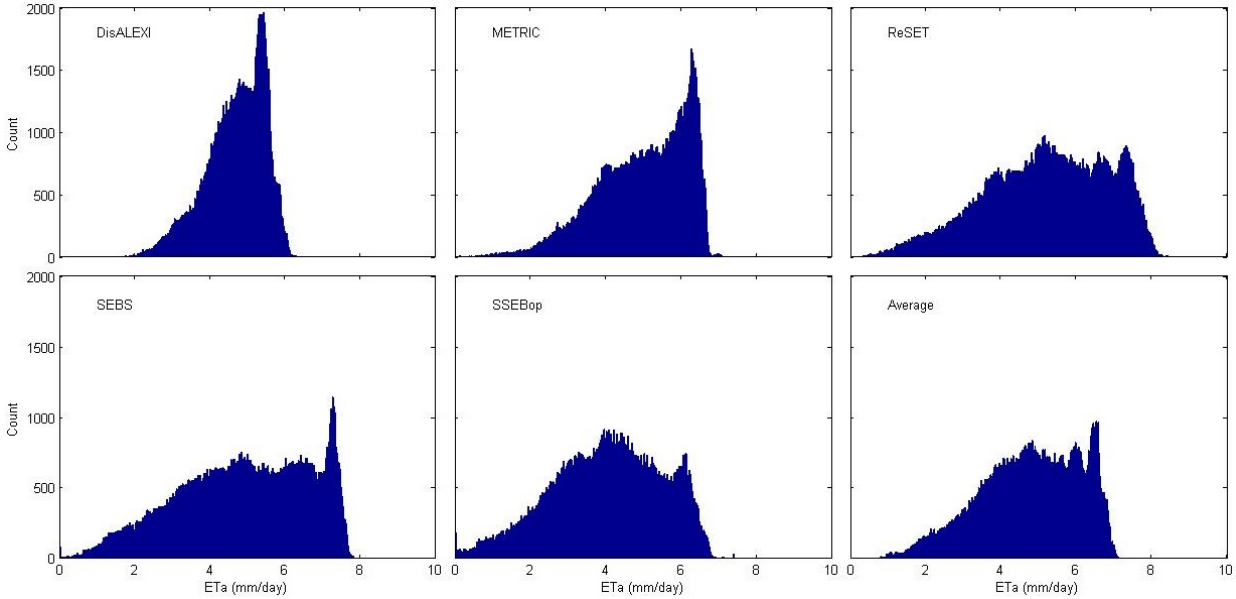

Figure 24: Histogram of estimated daily ETa based on all models and their average for DOY 131 May 10, 2008 over Mead for the results shown in Figure 23.

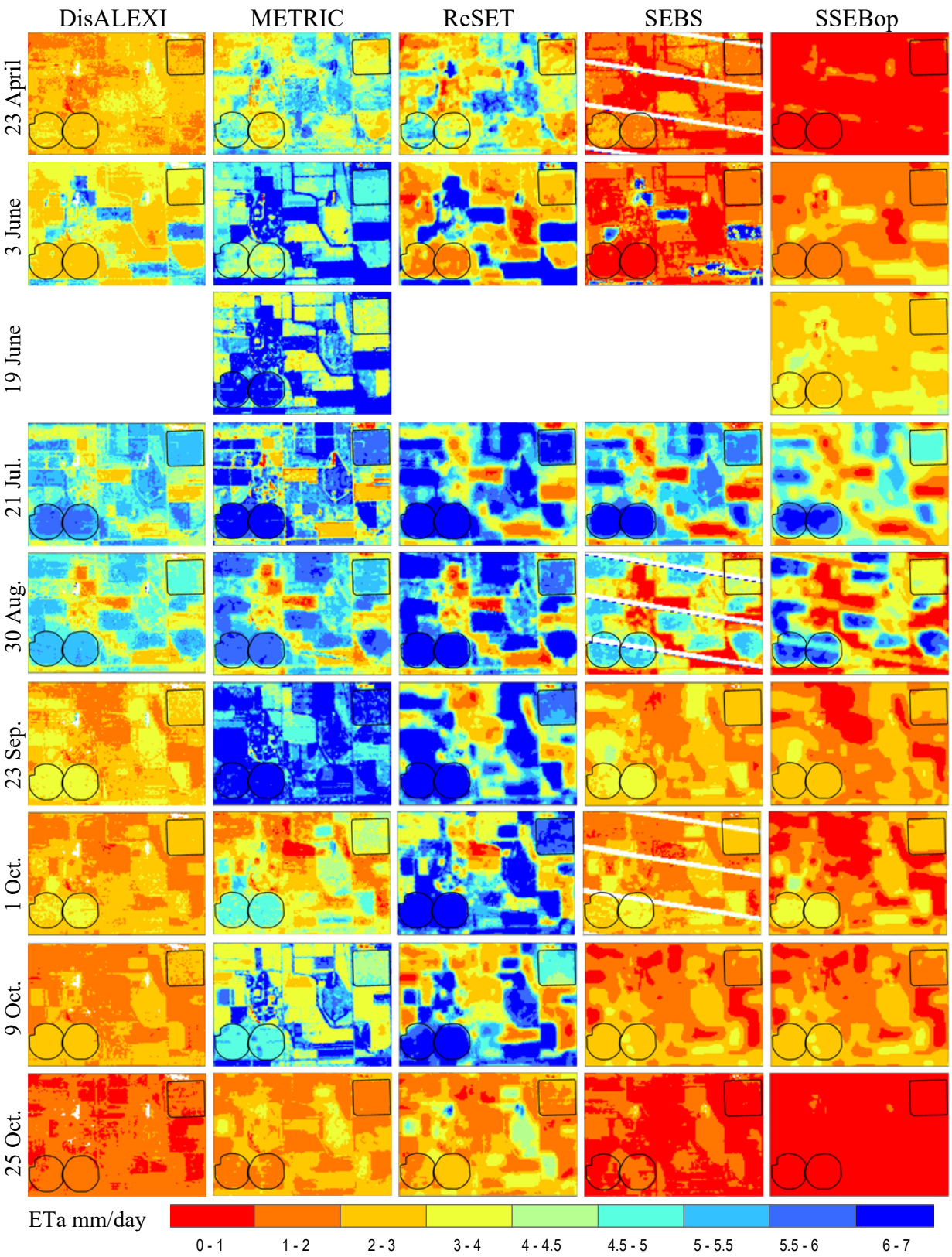

Figure 25: Maps of actual evapotranspiration (ETa) in mm/day during Landsat overpass dates resulting from each model. Study sites US-Ne 1 and US-Ne 2 are shown as two circles (black) left and right, respectively, and US-Ne 3 square (black).

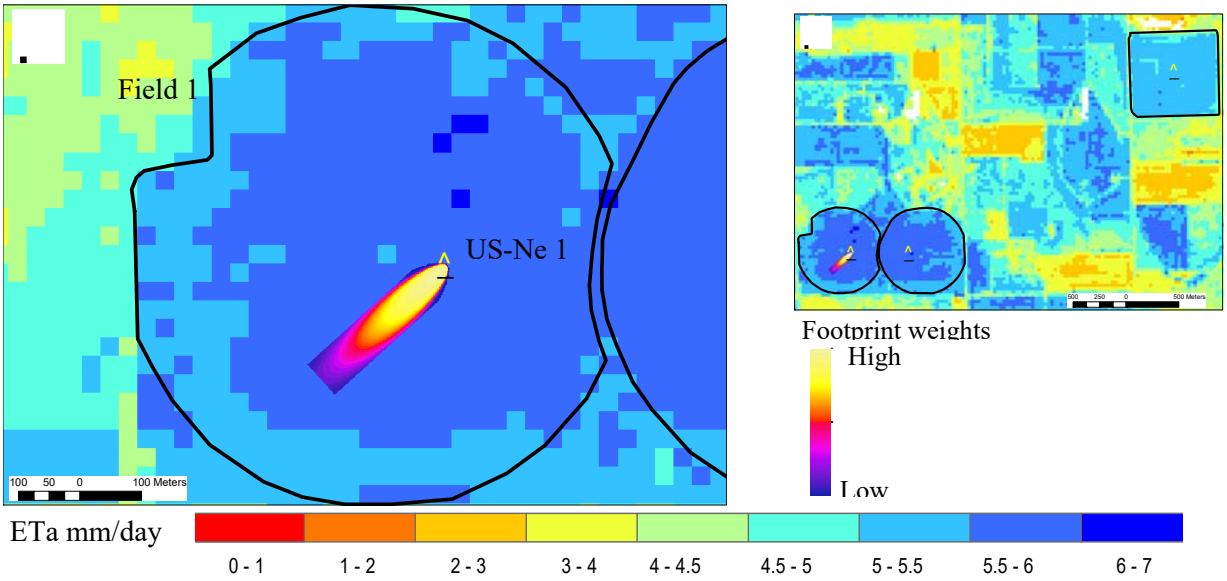

Figure 26: Flux measurement upwind footprint overliad on DisALEXI model estimates of daily ETa at field 1 (irrigated maize) and US-Ne 1 eddy covariance tower on DOY 202, July 21, 2013.

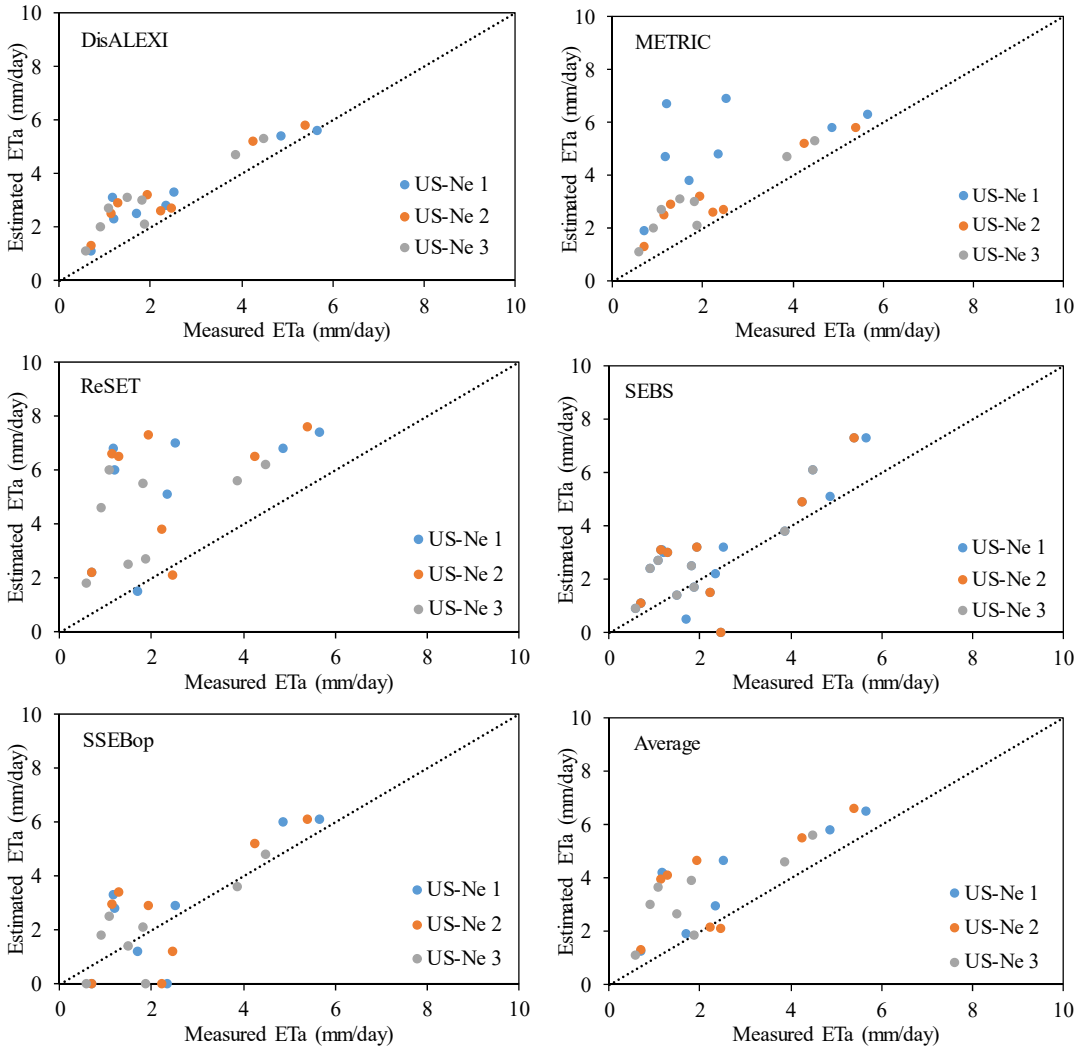

Figure 27: Comparison of estimated and measured ETa based on DisALEXI, METRIC, ReSET, SEBS, SSEBop, and their average (Average) and ground-based EC measurements. Models estimates are based on footprint integrated values.

Table 26: Summary of model performance statistics for DisALEXI, METRIC, SEBS, SSEBop, ReSET, and their average (Average) for estimates of daily ETa during Landsat overpass dates at Mead, Ne site.

	DisALEXI	METRIC	SEBS	SSEBop	ReSET	Average	N
RMSD (mm/day)	1.0	2.9	1.3	1.3	3.2	1.7	24
BIAS (mm/day)	0.9	2.5	0.6	0.2	2.7	1.4	24
MAD (mm/day)	0.9	2.5	1.0	1.1	2.7	1.4	24

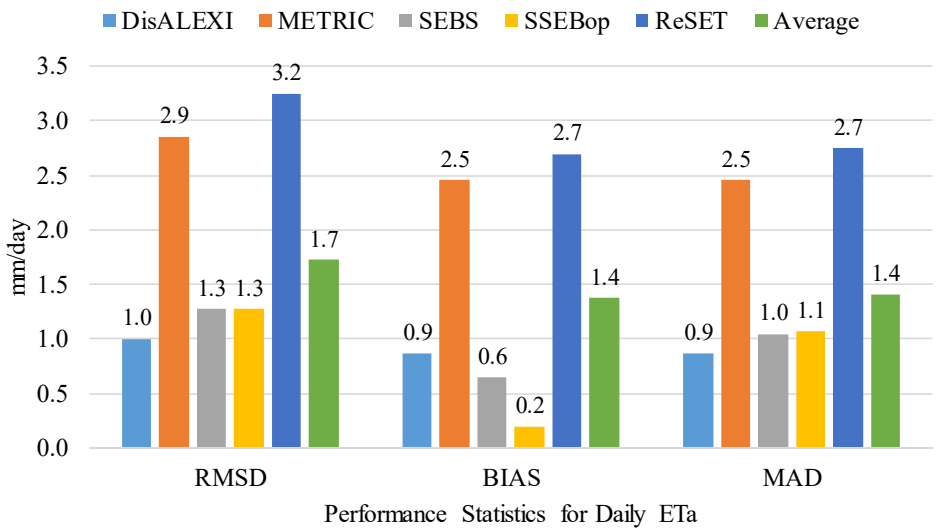

Figure 28: Barplot of model performance statistics for DisALEXI, METRIC, SEBS, SSEBop, ReSET, and their average (Average) for daily ETa during Landsat overpass dates for Mead, Ne (Table 26).

The crop growth at the three fields can be described by the observed ETa that is based on EC system measurements at the center of each field. Measured seasonal daily and monthly total ETa are shown in Figure 29 and Figure 30, respectively. As the three fields are geographically close to each other, the observed daily ETa showed similar temporal variability throughout the growing season that spans between the End of April and the End of October. The monthly ETa can show that the two irrigated fields US-Ne 1 and US-Ne 2 have relatively similar amounts of total monthly ETa that are higher than that of the dryland field but not by much.

A comparison of estimated and measured monthly ETa over the three sites is shown in Figure 31. Based on visual inspection of Figure 31, it can be observed that METRIC and ReSET models provided the largest overestimation of monthly ETa followed to a lesser extent by DisALEXI model when compared to EC measurements. The SSEBop model underestimated monthly ETa during April-August and overestimated on the rest of the growing season. As shown in Figure 32, DisALEXI and SSEBop models provided a narrow scatter of data around the 1:1 line while METRIC and ReSET models showed wider scattering away from the perfect match line. This performance on a monthly basis by SSEBop and DisALEXI models is supported by the evaluation statistics (Figure 33 and Table 27) as the two models show relatively low values of RMSD of 23 and 28 mm, respectively. The results provided by METRIC and ReSET models had higher RMSD of 49 and 59 mm indicating relatively lower performance compared to DisALEXI and SSEBop models. Generally, three models overestimated the monthly ETa values including METRIC, ReSET, and DisALEXI, models while SSEBop model slightly underestimated monthly ETa. DisALEXI model slightly overestimated monthly ETa as indicated by BIAS of 25 mm while METRIC and ReSET models considerably overestimate monthly ETa by BIAS of 45 and 46 mm. SSEBop model slightly underestimated monthly ETa by a BIAS of -8 mm.

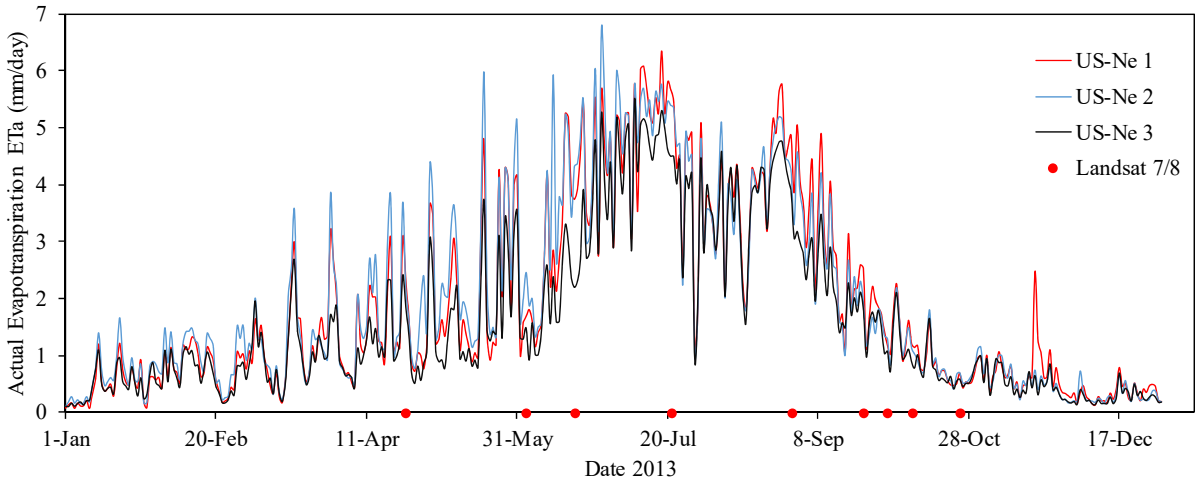

Figure 29: Seasonal ETa based on ground-based eddy covariance (EC) tower measurements at the three sites US-Ne 1 (irrigated maize), US-Ne 2 (irrigated maize), and US-Ne 3 (dryland maize) along with the Landsat 7/8 overpass dates

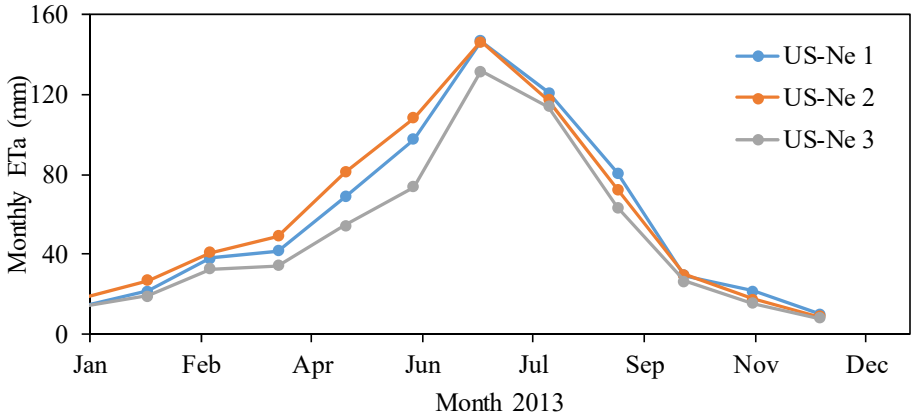

Figure 30: Monthly total ETa based on ground-based eddy covariance (EC) tower measurements at the three sites US-Ne 1 (irrigated maize), US-Ne 2 (irrigated maize), and US-Ne 3 (dryland maize).

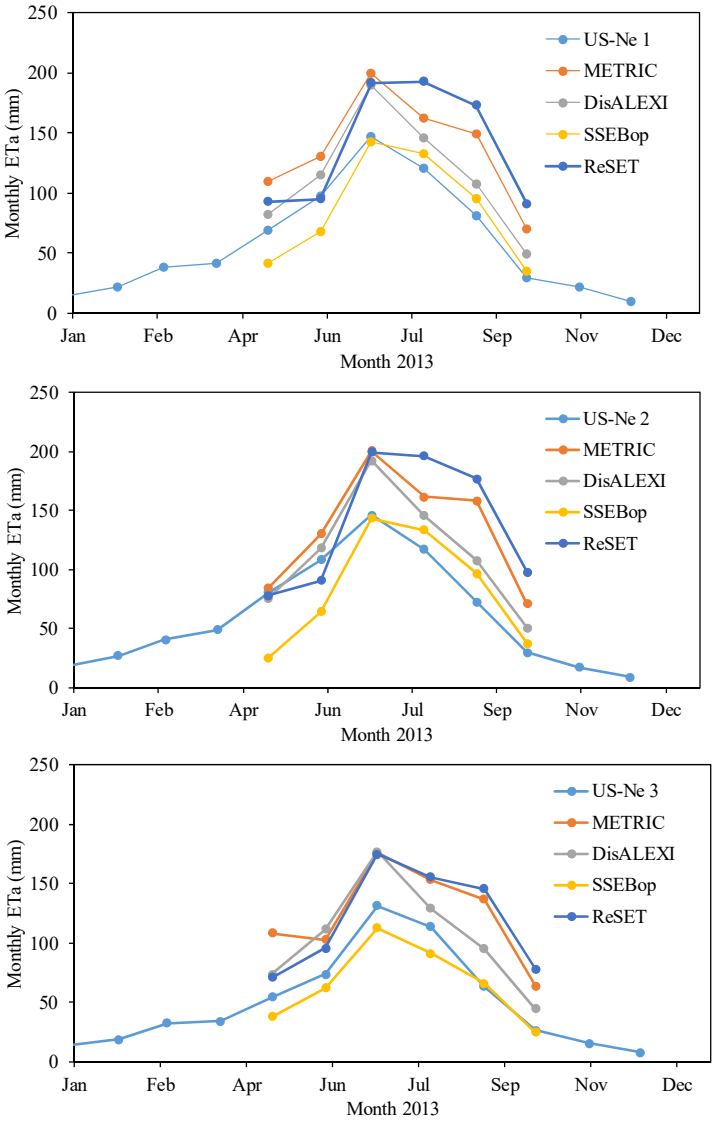

Figure 31: Comparison of measured total monthly ETa based on ground-based EC measurements at the three fields US-Ne 1 (irrigated maize), US-Ne 2 (irrigated maize), and US-Ne 3 (dryland maize) with estimated values by DisALEXI, METRIC, SSEBop, and ReSET models

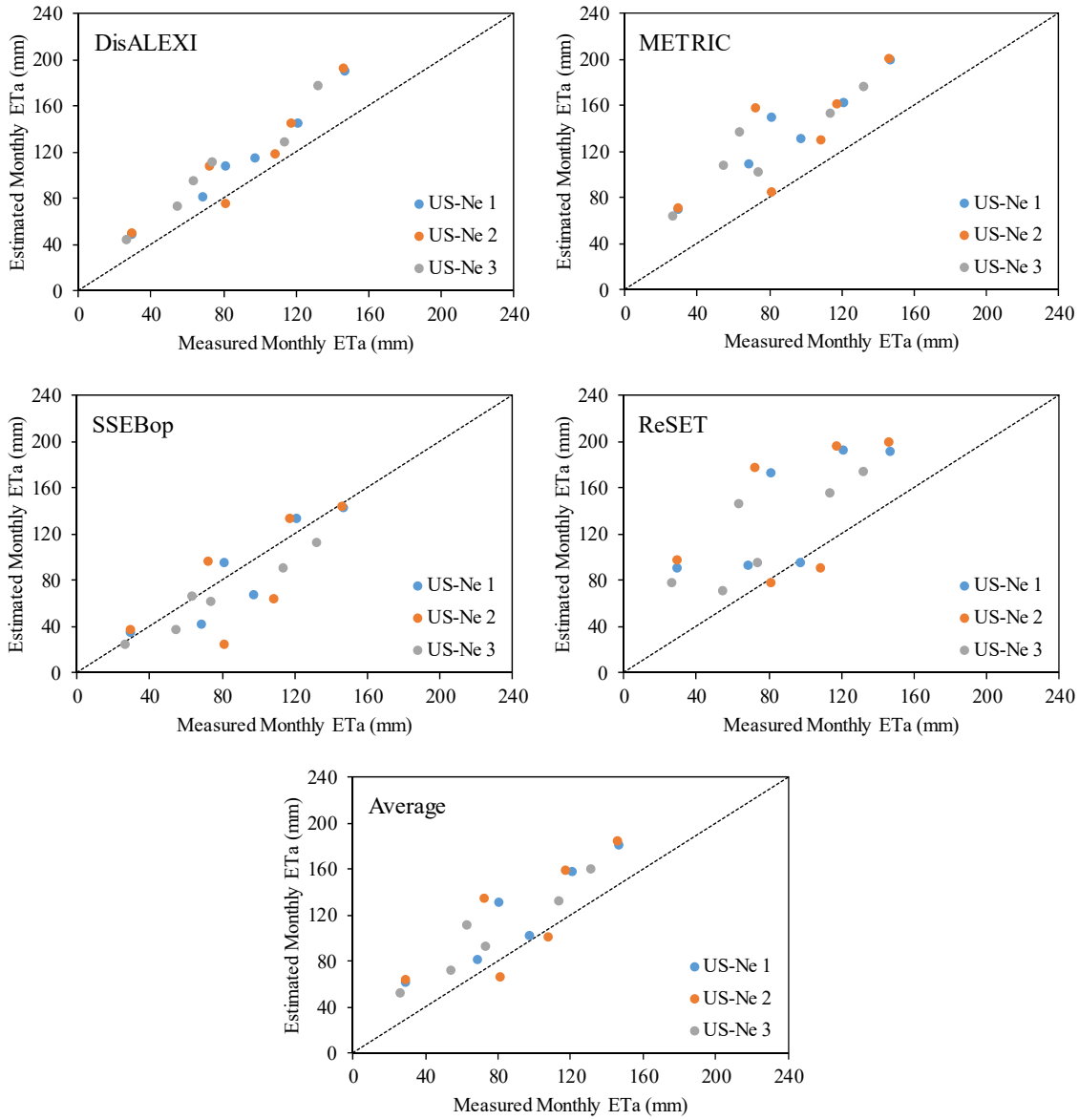

Figure 32: Comparison of estimated monthly ETa (mm) based on DisLAEXI, METRIC, ReSET, SSEBop models and their average (Average) with EC measurements.

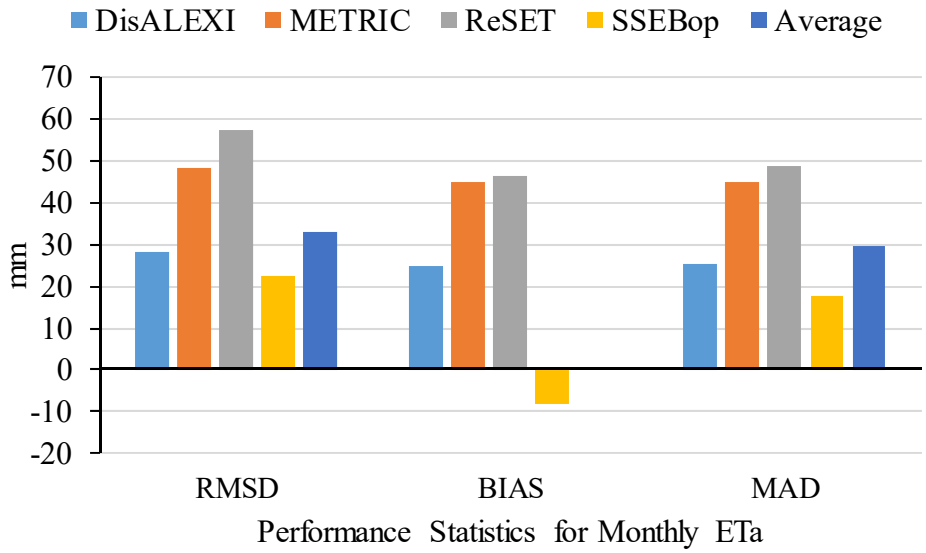

Figure 33: Summary of models performance statistics for monthly ETa (mm) for DisLAEXI, METRIC, ReSET, SSEBop, and their average (Average)

Table 27: Summary of model performance statistics for monthly ETa (mm) for DisLAEXI, METRIC, ReSET, SSEBop, and their average (Average)

	DisALEXI	METRIC	ReSET	SSEBop	Average
RMSD (mm)	28	49	57	23	33
BIAS (mm)	25	45	46	-8	0.0
MAD (mm)	26	45	49	18	30

In addition to evaluating the performance of the models on estimates of monthly ETa, estimates of total seasonal ETa are also evaluated as summarized in Figure 34 and Table 28. The total ETa between April-October for each field is 543, 555, and 464 mm for US-Ne 1, US-Ne 2, and US-Ne 3, respectively. As shown in Figure 33 three models including ReSET, METRIC, and DisALEXI overestimated the total seasonal ETa while SSEBop provided slightly underestimated values. ReSET and METRIC models provided relatively similar overestimation of total seasonal ETa at all three fields followed to a lesser extent by DisALEXI model. The SSEBop model slightly underestimated total seasonal ETa. The relative error of these models estimates at each field is calculated based on the EC measurements as shown in Table 28. It can be noticed that the RE is higher for all models at the dryland field US-Ne 3 and similar at the two irrigated fields US-Ne 1 and US-Ne 2. For example, the overestimation of total seasonal ETa at the dryland field US-Ne 1 by the three models of 36, 55, and 60 %, respectively, is higher than that at the irrigated fields. The underestimation of total seasonal ETa at the dryland field US-Ne 1 of -15% provided by SSEBop is higher than that at the two irrigated fields. The average RE for all three fields indicated significant overestimation of total seasonal ETa by METRIC and ReSET models by over 50% while that for the DisALEXI model by about 30%. The percentage overestimation of total seasonal ETa by DisALEXI model is about 29% while SSEBop model underestimated the total seasonal volume by -10%.

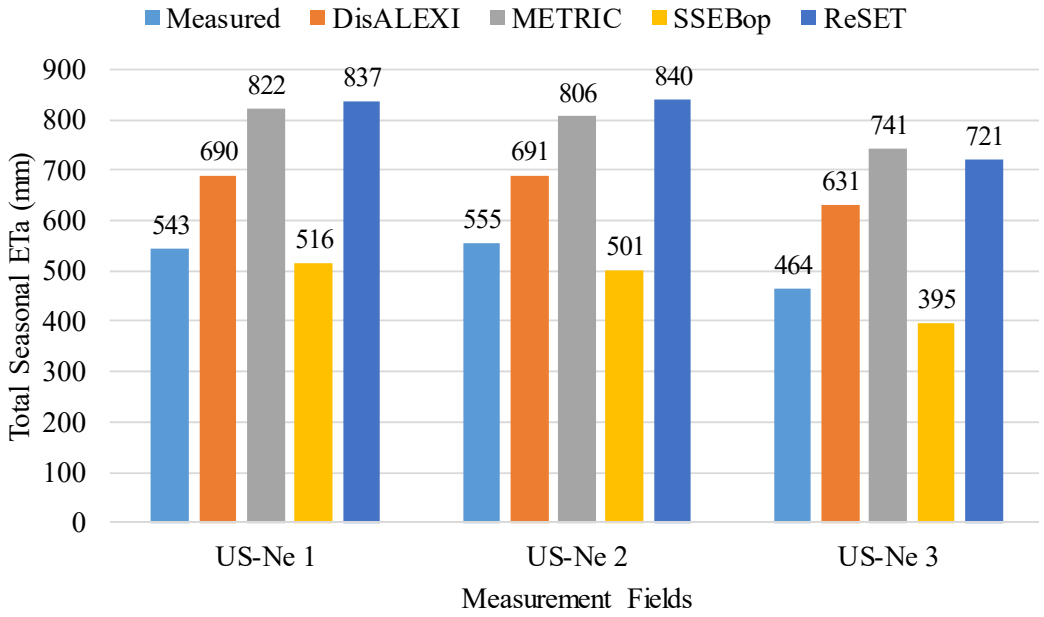

Figure 34: Summary of seasonal total ETa (mm) for the months April-October for DisALEXI, METRIC, ReSET, and SSEBop models and ground-based EC measurements.

Table 28: Summary of models performance on the total seasonal ETa estimates compared to measurements.

	Total Seasonal ETa (mm)			RE (%)			
	US-Ne 1	US-Ne 2	US-Ne 3	US-Ne 1	US-Ne 2	US-Ne 3	Average
Measured	543	555	464				
DisALEXI	690	691	631	27%	25%	36%	29%
METRIC	822	806	741	51%	45%	60%	52%
SSEBop	516	501	395	-5%	-10%	-15%	-10%
ReSET	837	840	721	54%	51%	55%	54%

RE: relative error = (estimated-measured)/measured

APPENDICES

Appendix A

Summary of area average daily ETa estimates for PVID during satellite overpass dates based on all models including their average (Average).

Table A1: List of Landsat 5 scenes over the PVID and used in the analysis spatial average ETa

No	DOY (2008)	DisALEXI	METRIC	ReSET	SEBS	SSEBop	Average
1	*19*	1.47	1.79	1.67	0.02	0.07	1.00
2	*42*	2.30	1.96	2.20	1.25	1.65	1.87
3	*58*	2.84	2.85	2.52	1.45	2.53	2.44
4	*67*	2.78	3.08	3.09	1.49	1.88	2.47
5	*83*	3.37	4.32	3.89	2.07	3.55	3.44
6	*99*	3.71	4.37	3.96	2.23	4.27	3.71
7	*115*	3.75	4.46	4.31	3.33	4.98	4.17
8	*131*	4.49	4.35	4.01	2.43	4.19	3.89
9	*138*	4.58	4.83	3.82	3.29	3.93	4.09
10	*147*	4.54	4.27	3.65	3.61	4.98	4.21
11	*163*	4.74	6.30	5.98	3.03	5.00	5.01
12	*170*	4.98	5.68	4.22	3.88	5.53	4.86
13	*195*	4.85	5.24	4.81	3.60	4.69	4.64
14	*211*	4.45	5.25	5.41	3.32	4.75	4.63
15	*218*	4.18	6.50	6.29	1.69	2.03	4.14
16	*234*	3.53	5.09	4.62	2.87	3.54	3.93
17	*259*	3.66	3.91	3.33	3.35	3.79	3.61
18	*275*	2.83	2.70	2.38	2.66	2.99	2.71
19	*291*	2.18	2.52	2.30	2.26	1.97	2.24
20	*314*	1.68	3.04	3.14	2.36	2.79	2.60
21	*323*	1.51	1.16	1.07	1.60	1.22	1.31

REFERENCES

Agam, N., Kustas, W.P., Anderson, M.C., Li, F.Q., Colaizzi, P.D., 2008. Utility of thermal image sharpening for monitoring field-scale evapotranspiration over rainfed and irrigated agricultural regions. Geophys. Res. Lett. 35.

Allen, R.G., Clemmens, A.J., Burt, C.M., Solomon, K., O'Halloran, T., 2005. Prediction accuracy for projectwide evapotranspiration using crop coefficients and reference evapotranspiration. J. Irrig. Drain. Eng. 131, 24–36.

Allen, R.G., Robison, C.W., 2007. Evapotranspiration and Consumptive Irrigation Water Requirements for Idaho. University of Idaho.

Allen, R.G., Tasumi, M., Morse, A., Trezza, R., Wright, J.L., Bastiaanssen, W., Kramber, W., Lorite, I., Robison, C.W., 2007a. Satellite-based energy balance for mapping evapotranspiration with internalized calibration (METRIC) - Applications. J. Irrig. Drain. Eng. 133, 395–406. doi:Doi 10.1061/(Asce)0733-9437(2007)133:4(395)

Allen, R.G., Tasumi, M., Trezza, R., 2007b. Satellite-based energy balance for mapping evapotranspiration with internalized calibration (METRIC) - Model. J. Irrig. Drain. Eng. 133, 380–394. doi:Doi 10.1061/(Asce)0733-9437(2007)133:4(380)

Anderson, M.C., Kustas, W.P., Alfieri, J.G., Gao, F., Hain, C., Prueger, J.H., Evett, S., Colaizzi, P., Howell, T., Chavez, J.L., 2012. Mapping daily evapotranspiration at Landsat spatial scales during the BEAREX'08 field campaign. Adv. Water Resour. 50, 162–177.

Anderson, M.C., Kustas, W.P., Norman, J.M., Hain, C.R., Mecikalski, J.R., Schultz, L., Gonzalez-Dugo, M.P., Cammalleri, C., d'Urso, G., Pimstein, A., Gao, F., 2011. Mapping daily evapotranspiration at field to continental scales using geostationary and polar orbiting satellite imagery. Hydrol. Earth Syst. Sci. 15, 223–239.

Anderson, M.C., Norman, J.M., Diak, G.R., Kustas, W.P., Mecikalski, J.R., 1997. A two-source time-integrated model for estimating surface fluxes using thermal infrared remote sensing. Remote Sens. Environ. 60, 195–216. doi:Doi 10.1016/S0034-4257(96)00215-5

Anderson, M.C., Norman, J.M., Mecikalski, J.R., Otkin, J.A., Kustas, W.P., 2007. A climatological study of evapotranspiration and moisture stress across the continental United States based on thermal remote sensing: 1. Model formulation. J. Geophys. Res. 112. doi:Artn D10117Doi 10.1029/2006jd007506

Anderson, M.C., Norman, J.M., Meyers, T.P., Diak, G.R., 2000. An analytical model for estimating canopy transpiration and carbon assimilation fluxes based on canopy light-use efficiency. Agric. For. Meteorol. 101, 265–289.

Berk, A., Bernstein, L.S., Anderson, G.P., Acharya, P.K., Robertson, D.C., Chetwynd, J.H., Adler-Golden, S.M., 1998. MODTRAN cloud and multiple scattering upgrades with application to AVIRIS. Remote Sens. Environ. 65, 367–375. doi:Doi 10.1016/S0034-4257(98)00045-5

Brutsaert, W., Sugita, M., 1992. Regional Surface Fluxes under Nonuniform Soil-Moisture Conditions during Drying. Water Resour. Res. 28, 1669–1674.

Campbell, G.S., Norman, J.M., 1998. AN INTRODUCTION TO ENVIRONMENTAL BIOPHYSICS.: 2nd edition. Springer.

Chander, G., Markham, B., 2003. Revised Landsat-5 TM radiometric calibration procedures and postcalibration dynamic ranges. Geosci. Remote Sensing, IEEE Trans. 41, 2674–2677.

Clemmens, A.J., 2009. Accuracy of project-wide water uses from a water balance: a case study from Southern California. Irrig. Drain. Syst. 22, 287–309. doi:10.1007/s10795-008-9057-3

Dickens, J.M., Forbes, B.T., Cobean, D.S., Tadayon, S., 2011. Documentation of Methods and

Inventory of Irrigation Data Collected for the 2000 and 2005 US Geological Survey Estimated Use of Water in the United States, comparison of USGS-Compiled irrigation data to other sources, and recommendations for future compil. US Geological Survey.
DOI, 2012. WaterSMART A Three-Year Progress Report. doi:http://www.usbr.gov/watersmart/docs/WaterSMART-thee-year-progress-report.pdf
Eckhardt, D., 2013. Mapping Evapotranspiration in the Upper Colorado River Basin using the ReSET Energy-Balance Model.
Elhaddad, A., Garcia, L.A., 2011. ReSET-Raster: Surface Energy Balance Model for Calculating Evapotranspiration Using a Raster Approach. J. Irrig. Drain. Eng. 137, 203–210. doi:Doi 10.1061/(Asce)Ir.1943-4774.0000282
Fisher, J.B., Tu, K.P., Baldocchi, D.D., 2008. Global estimates of the land-atmosphere water flux based on monthly AVHRR and ISLSCP-II data, validated at 16 FLUXNET sites. Remote Sens. Environ. 112, 901–919. doi:DOI 10.1016/j.rse.2007.06.025
Gao, F., Masek, J., Schwaller, M., Hall, F., 2006. On the blending of the Landsat and MODIS surface reflectance: Predicting daily Landsat surface reflectance. Ieee Trans. Geosci. Remote Sens. 44, 2207–2218.
Geli, H.M.E., 2012. Modeling spatial surface energy fluxes of agricultural and riparian vegetation using remote sensing. Utah State University, All Graduate Theses and Dissertations.
Geli, H.M.E., Neale, C.M.U., 2015. Remote Sensing of Evapotranspiration - Part 1- A Review of Models.
Horst, T.W., Weil, J.C., 1994. How Far Is Far Enough - the Fetch Requirements for Micrometeorological Measurement of Surface Fluxes. J. Atmos. Ocean. Technol. 11, 1018–1025.
Horst, T.W., Weil, J.C., 1992. Footprint Estimation for Scalar Flux Measurements in the Atmospheric Surface-Layer. Boundary-Layer Meteorol. 59, 279–296.
Kustas, W.P., Daughtry, C.S.T., 1990. Estimation of the Soil Heat-Flux Net-Radiation Ratio from Spectral Data. Agric. For. Meteorol. 49, 205–223. doi:Doi 10.1016/0168-1923(90)90033-3
Kustas, W.P., Norman, J.M., 1999. Evaluation of soil and vegetation heat flux predictions using a simple two-source model with radiometric temperatures for partial canopy cover. Agric. For. Meteorol. 94, 13–29. doi:Doi 10.1016/S0168-1923(99)00005-2
Kustas, W.P., Norman, J.M., Anderson, M.C., French, A.N., 2003. Estimating subpixel surface temperatures and energy fluxes from the vegetation index-radiometric temperature relationship. Remote Sens. Environ. 85, 429–440. doi:Doi 10.1016/S0034-4257(03)00036-1
Li, F.Q., Kustas, W.P., Prueger, J.H., Neale, C.M.U., Jackson, T.J., 2005. Utility of remote sensing-based two-source energy balance model under low- and high-vegetation cover conditions. J. Hydrometeorol. 6, 878–891. doi:Doi 10.1175/Jhm464.1
Mecikalski, J.R., Diak, G.R., Anderson, M.C., Norman, J.M., 1999. Estimating fluxes on continental scales using remotely sensed data in an atmospheric-land exchange model. J. Appl. Meteorol. 38, 1352–1369. doi:Doi 10.1175/1520-0450(1999)038<1352:Efocsu>2.0.Co;2
Monteith, J.L., 1973. Principles of environmental physics. . Edward Arnold Press.
Mu, Q., Heinsch, F.A., Zhao, M., Running, S.W., 2007. Development of a global evapotranspiration algorithm based on MODIS and global meteorology data. Remote Sens. Environ. 111, 519–536. doi:DOI 10.1016/j.rse.2007.04.015

Mu, Q.Z., Zhao, M.S., Running, S.W., 2011. Improvements to a MODIS global terrestrial evapotranspiration algorithm. Remote Sens. Environ. 115, 1781–1800. doi:DOI 10.1016/j.rse.2011.02.019

Neale, C.M.U., Geli, H.M.E., Kustas, W.P., Alfieri, J.G., Gowda, P.H., Evett, S.R., Prueger, J.H., Hipps, L.E., Dulaney, W.P., Chávez, J.L., French, A.N., Howell, T.A., 2012. Soil water content estimation using a remote sensing based hybrid evapotranspiration modeling approach. Adv. Water Resour. 50, 152–161.

Norman, J.M., Anderson, M.C., Kustas, W.P., French, A.N., Mecikalski, J., Torn, R., Diak, G.R., Schmugge, T.J., Tanner, B.C.W., 2003. Remote sensing of surface energy fluxes at 10(1)-m pixel resolutions. Water Resour. Res. 39. doi:Artn 1221Doi 10.1029/2002wr001775

Norman, J.M., Kustas, W.P., Humes, K.S., 1995. Source Approach for Estimating Soil and Vegetation Energy Fluxes in Observations of Directional Radiometric Surface-Temperature. Agric. For. Meteorol. 77, 263–293. doi:Doi 10.1016/0168-1923(95)02265-Y

Priestley, C.H.B., Taylor, R.J., 1972. On the Assessment of Surface Heat Flux and Evaporation Using Large-Scale Parameters. Mon. Weather Rev. 100, 81–92. doi:10.1175/1520-0493(1972)100<0081:otaosh>2.3.co;2

PVID, 2015. Palo Verde Irrigation District [WWW Document]. URL http://www.pvid.org/

Santanello, J.A., Friedl, M.A., 2003. Diurnal covariation in soil heat flux and net radiation. J. Appl. Meteorol. 42, 851–862. doi:Doi 10.1175/1520-0450(2003)042<0851:Dcishf>2.0.Co;2

Savoca, M.E., Senay, G.B., Maupin, M.A., Kenny, J.F., Perry, C.A., 2013. Actual evapotranspiration modeling using the operational Simplified Surface Energy Balance (SSEBop) approach. US Geological Survey.

Senay, G.B., Bohms, S., Singh, R.K., Gowda, P.H., Velpuri, N.M., Alemu, H., Verdin, J.P., 2013. Operational Evapotranspiration Mapping Using Remote Sensing and Weather Datasets: A New Parameterization for the SSEB Approach. J. Am. Water Resour. Assoc. 49, 577–591. doi:Doi 10.1111/Jawr.12057

Senay, G.B., Budde, M., Verdin, J.P., Melesse, A.M., 2007. A coupled remote sensing and simplified surface energy balance approach to estimate actual evapotranspiration from irrigated fields. Sensors 7, 979–1000.

Senay, G.B., Budde, M.E., Verdin, J.P., 2011. Enhancing the Simplified Surface Energy Balance (SSEB) approach for estimating landscape ET: Validation with the METRIC model. Agric. Water Manag. 98, 606–618. doi:DOI 10.1016/j.agwat.2010.10.014

Senay, G.B., Verdin, J.P., Lietzow, R., Melesse, A.M., 2008. Global daily reference evapotranspiration modeling and evaluation. J. Am. Water Resour. Assoc. 44, 969–979. doi:DOI 10.1111/j.1752-1688.2008.00195.x

Su, Z., 2002. The Surface Energy Balance System (SEBS) for estimation of turbulent heat fluxes. Hydrol. Earth Syst. Sci. 6, 85–99.

Tasumi, M., 2003. Progress in operational estimation of regional evapotranspiration using satellite imagery.

Twine, T.E., Kustas, W.P., Norman, J.M., Cook, D.R., Houser, P.R., Meyers, T.P., Prueger, J.H., Starks, P.J., Wesely, M.L., 2000. Correcting eddy-covariance flux underestimates over a grassland. Agric. For. Meteorol. 103, 279–300. doi:Doi 10.1016/S0168-1923(00)00123-4

Wahlin, B.T., Replogle, J.A., Clemmens, A.J., District, I.I., 1997. Measurement accuracy for major surface-water flows entering and leaving the Imperial Valley. US Department of Agriculture, Agricultural Research Service, US Water Conservation Laboratory.

Capturing Aerial Imagery on the San Rafael River, Utah, Using an Unmanned Aerial Vehicle (UAV) to Monitor and Assist in Evaluating Restoration Efforts

Basic Information

Title:	Capturing Aerial Imagery on the San Rafael River, Utah, Using an Unmanned Aerial Vehicle (UAV) to Monitor and Assist in Evaluating Restoration Efforts
Project Number:	2013UT190B
Start Date:	3/1/2015
End Date:	2/28/2016
Funding Source:	104B
Congressional District:	UT3
Research Category:	Biological Sciences
Focus Category:	Geomorphological Processes, Invasive Species, Management and Planning
Descriptors:	None
Principal Investigators:	Bethany T. Neilson

Publications

There are no publications.

Capturing Aerial Imagery on the San Rafael River, Utah, Using an Unmanned Aerial Vehicle (UAV) to Monitor and Assist in Evaluating Restoration Efforts

Introduction

The San Rafael River in South-Central Utah, is in a severely degraded state and on the 303(d) list of degraded waters, with a low abundance of native fish species, poor fish habitat quality, limited native riparian vegetation recruitment, and abundant stands of non-native tamarisk (UWDR 2006; Budy et al. 2009). A large-scale restoration scheme is being implemented by both federal and state agencies and other entities, including the Utah Center for Water Resources Research (UCWRR) at the Utah Water Research Laboratory, Utah State University. As part of the monitoring program, the UCWRR flew an Unmanned Aerial System (UAS) over the river during the autumn of 2015. The resulting data and analyses provided by the AggieAir™ Flying Circus will be used to support the ongoing efforts of the San Rafael restoration process. The research results from this project also add to the body of knowledge regarding the accuracy and limitations of the use of inexpensive UAS platforms to provide data, such as digital elevation and terrain models, in place of more conventional and expensive approaches (e.g., LiDAR).

Methods

The Minion 2.0 UAS was the aerial platform employed by the AggieAir Flying Circus ™ Service Center (aggieair.usu.edu) for this project. Minion 2.0 is a traditional fixed-wing aircraft with a 2.7-m wingspan and 1.2-m total length that carries a payload of two Lumenera Lt965R industrial-grade cameras (RGB & NIR 12 MP) and one ICI 9640 Thermal camera (TIR). Minion was deployed at multiple locations along the San Rafael River to capture aerial imagery of the river channel and riparian corridor. The UAS was pre-programmed with individual flight lines (9 in total) at 450 m above ground level (AGL) to obtain a pixel resolution of approximately 0.10 m for RGB and NIR and 0.57 m for TIR

Orthomosaic Generation

The imagery captured over the San Rafael River was processed through Agisoft PhotoScan Professional (Agisoft LLC, 2016). This is a stand-alone software product that performs photogrammetric processing of digital images and generates 3D spatial data. During each flight, the UAS continually records its position as each frame is captured along with yaw, pitch, and roll. This information is used to produce an orthorectified digital number mosaic. Additionally, the software creates a high-density point cloud surface, which is exported as a point file or as a digital surface model (DSM). Imagery from both the RGB and NIR was processed to produce a DSM with a similar pixel resolution of 10.5 cm (Figure 1). The DSM's that were created for each of the 9 flights along the San Rafael River were analyzed and ultimately compared to the 2013 Bare Earth LiDAR (San Rafael LiDAR 2013) data for vertical and horizontal accuracy.

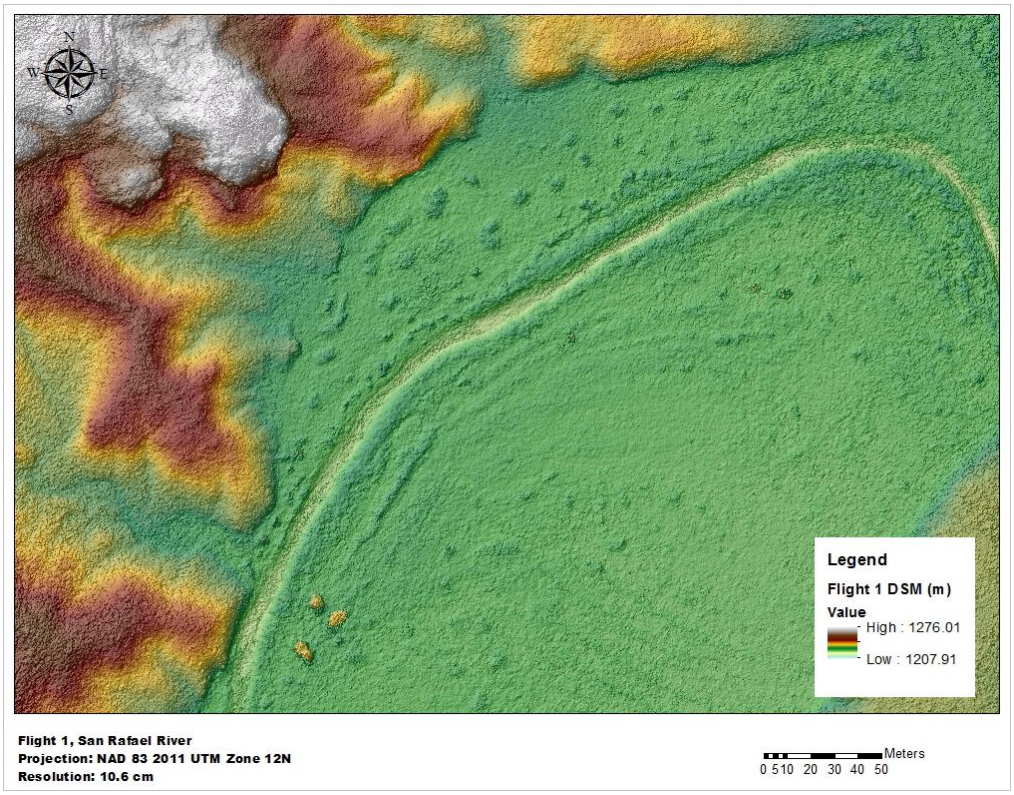

Figure 1. Example digital surface model (meters) from Agisoft PhotoScan Professional, (Flight 1, San Rafael River 2015).

Thermal Image Calibration

Thermal imagery was captured during all flights, clipped to the pixels representing the river channel, and then calibrated using temperature sensors that were located within the river. A relationship was established between these deployed instream temperature probes and the temperature values extracted from the mosaic at the corresponding locations and used to calibrate the thermal imagery. Figure 2 below represents a close up of the clipped calibrated thermal imagery for the river in Flight 1.

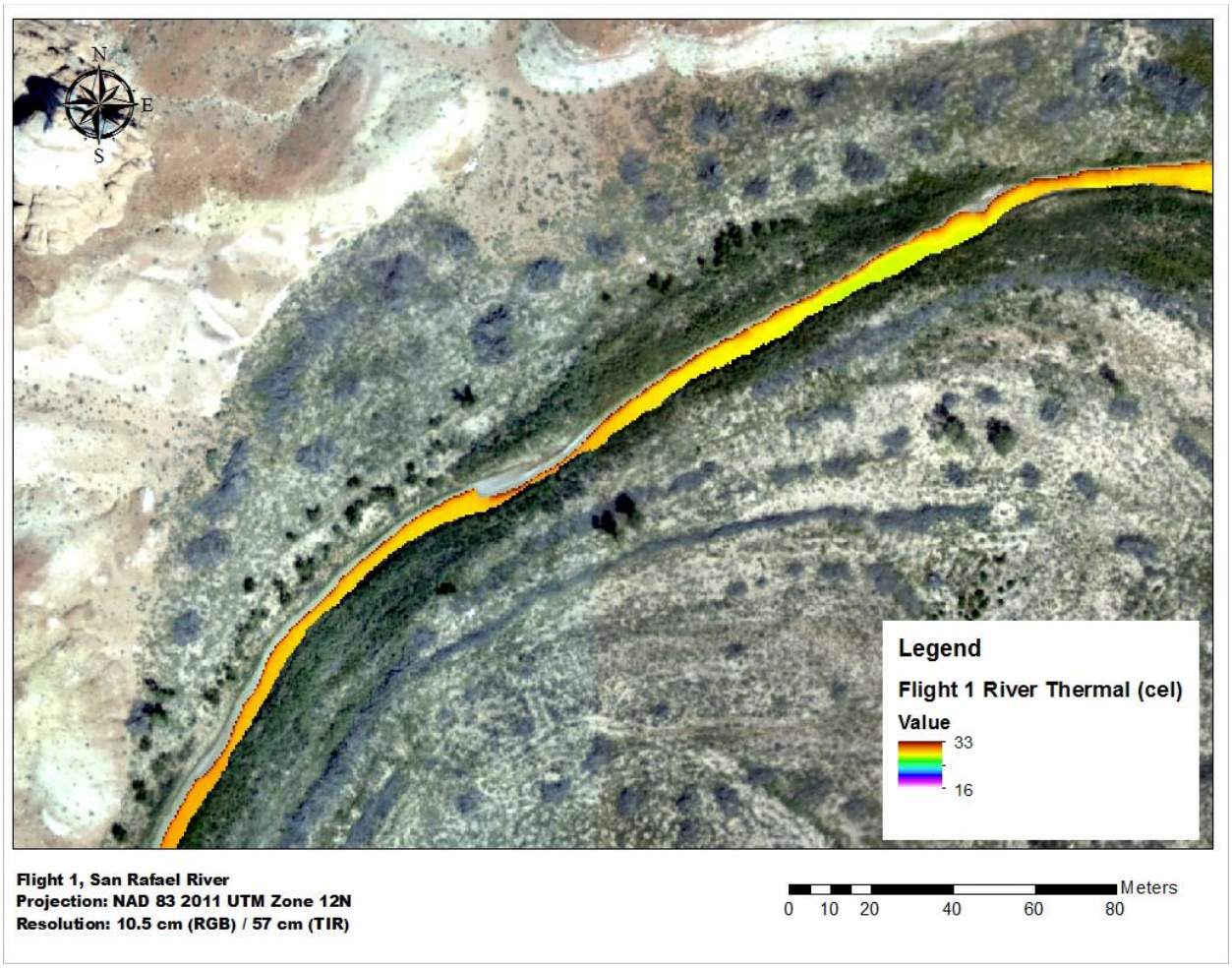

Figure 2. Thermal output from Agisoft Photoscan Professional, (Flight 1, San Rafael River).

Horizontal and Vertical Accuracy Assessment

The main objective of this research was to compare relative vertical and horizontal value estimates from the AggieAir derived DSM data with data captured from a LiDAR flight (San Rafael LiDAR 2013). The vertical assessment was performed using the Agisoft DSM output (one for RGB and one for NIR for each flight). The horizontal assessment was performed using the RGB digital number mosaic. Due to the 2013 LiDAR having been captured 2 years prior to the AggieAir imagery, the areas selected for analysis were refined to stable non-changing surfaces (i.e., bare ground, rock, or other hard surfaces) and avoiding any steep slopes. The horizontal and vertical accuracy was characterized using the National Spatial Data Accuracy Statistic and Root Mean Square Error as outlined in Minnesota Planning. Land Management Information Center, 1999, P.4

The National Standard for Spatial Data Accuracy (NSSDA) statistic is obtained by calculating three values:

- The sum of the set of squared differences between the test dataset and the independent data set.

- The average of the sum, obtained by dividing the sum by the number of test points evaluated.
- The root mean square error statistic (RMSE), which is the square root of the average.

The NSSDA statistic is determined by multiplying the RMSE by a value that represents the standard error of the mean at the 95 percent confidence level:

1.7308 when calculating horizontal accuracy
1.9600 when calculating vertical accuracy

The percentage of random points and level of accuracy assessed for Flight 1 (Table 1) shows that 2930 points fell within the Flight 1 RGB DSM Footprint. Using 100% of the points resulted in a Root Mean Square Error (RMSE) of 0.774, with a vertical accuracy of 1.52 m National Standard for Spatial Data Accuracy, (NSSDA) (Minnesota Planning 1999). Also shown in Table 1 are a 20% sample of randomly selected points for each flight and all points with difference values (Z^2) less than 1, 0.5, 0.2, 0.1, and 0.05. More than half (54.5%) of all of the points within the Flight 1 RGB DSM had an RMSE of 0.121 with an NSSDA vertical accuracy of 0.237 m.

Table 1. Vertical accuracies for Flight 1 San Rafael River RGB DSM versus 2013 Bare earth LiDAR.

Flight 1	PCT	Points	RMSE	NSSDA (m)	Description	Level (diff z^2)
	100.00%	2930	0.774	1.517	100 % of random points	100%
	20.00%	587	0.812	1.592	20 % of random points	20% random
	88.87%	2604	0.311	0.61	eliminate all points >1	1
	84.47%	2475	0.253	0.495	eliminate all points >0.5	0.5
	77.27%	2264	0.201	0.394	eliminate all points >0.2	0.2
	67.17%	1968	0.159	0.312	eliminate all points >0.1	0.1
	54.54%	1598	0.121	0.237	eliminate all points >0.05	0.05

The highest vertical accuracies have the smallest difference (Z^2) values. Initial investigations have determined that points with lower accuracy are close to vegetation, near the edge of the imagery, or near areas of high relief.

In this specific example, horizontal accuracy was calculated for Flight 1 (Table 2) with a RMSE of 0.577 and an NSSDA of <1 m. Twenty points were selected from well-distributed points with identifiable features. American Society of Photogrammetry & Remote Sensing (ASPRS) class values and appropriate scales for horizontal accuracy were determined from the RMSE and the (NSSDA) values.

An alternative method to the NSSDA is provided by the American Society of Photogrammetry & Remote Sensing (ASPRS) as explained below:

Explanation of ASPRS Accuracy Standards for Large-Scale Maps

ASPRS Accuracy Standards for Large-Scale Maps (ASPRS Specifications and Standards Committee, 1990) provide accuracy tolerances for maps at 1:20,000-scale or larger

> "prepared for special purposes or engineering applications." RMSE is the statistic used by the ASPRS standards. Accuracy is reported as Class 1, Class 2, or Class 3. Class 1 accuracy for horizontal and vertical components is discussed below. Class 2 accuracy applies to maps compiled within limiting RMSE's twice those allowed for Class 1 maps. Similarly, Class 3 accuracy applies to maps compiled within limiting RMSE's three times those allowed for Class 1 maps.
>
> (Geospatial Positioning Accuracy Standards, 1998, 3.1, p. 3-22, 23)

Flight 1 differs from all other flights for accuracy as horizontal control came in the form of air photo targets with RTK GPS post-processed to cm level accuracy.

Table 2. Horizontal accuracy using 20 points from Flight 1.

ASPRS			sum	6.659
Class 1	Class 2	Class 3	average	0.333
0.577	0.29	0.19	RMSE	0.577
1:4,000	1:2,000	1:1,000	NSSDA	0.999

Conclusions

A total of 9 UAS flights were successfully completed along 55 river miles of the San Rafael River, South-Central Utah. A combination of imagery was captured, including RGB, NIR, and thermal. This has allowed the following to be developed;

1. Color visual (RGB) orthorectified mosaics for all 9 flights at 0.1 m pixel resolution
2. Near-infrared (NIR) orthorectified mosaics for all 9 flights at 0.1 m pixel resolution
3. Calibrated orthorectified thermal mosaics for all 9 flights at 0.57 m pixel resolution
4. Digital Surface Models (DSMs) in raster format for all 9 flights in RGB and NIR at 0.1 m pixel resolution

DSMs derived from RGB mosaics in Agisoft had higher accuracies as a whole than DSMs derived from NIR mosaics, which we believe is due to the image quality. NIR capture data is inherently "noisy" due to the NIR long pass band filter. Color imagery (RGB) also has more noticeable features.

The highest vertical accuracies have the smallest difference Z^2 values. Initial investigations have determined that points with lower accuracies are placed close to vegetation, near the edge of the imagery, or near areas of high relief, and all of these situations are expected outcomes.

References

Budy, Pl, J. Bottcher, and G. P. Thiede, 2009, Habitat needs, movement patterns, and vital rates of endemic Utah fishes in a tributary to the Green River, Utah. 2008 Annual Report to the Bureau of Reclamation, Upper Colorado Region. UTCFWRU 2009(4):1-56.

Agisoft PhotoScan. Professional Edition, Version 1.2.4. 2016, AgiSoft LLC, [online] Available: http://www.agisoft.ru/products/photoscan.

Minnesota Planning. Land management Information Center. Positional Accuracy Handbook-Using the National Standard for Spatial Data Accuracy to measure and report geographic data quality, October 1999.

NSPDA (National Standard for Spatial Data Accuracy), Geospatial Positioning Accuracy Standards, Part 3, FGDC-STD-007.3-1998.

San Rafael LiDAR, Technical Data Report. WSI. May 20, 2013.

UDWR (Utah Division of Wildlife Resources), 2006, Conservation and management plan for three fish species in Utah, Publ. No. 06-17, pp. 1-82. Salt Lake City, UT.

Managing Western Irrigation Systems in the Face of Urbanization

Basic Information

Title:	Managing Western Irrigation Systems in the Face of Urbanization
Project Number:	2014UT195B
Start Date:	3/1/2014
End Date:	2/28/2016
Funding Source:	104B
Congressional District:	UT 1
Research Category:	Social Sciences
Focus Category:	Irrigation, Law, Institutions, and Policy, Water Use
Descriptors:	None
Principal Investigators:	Douglas Jackson-Smith

Publication

1. Armstrong, Andrea, 2015, Organizational Adaptation in Local Stormwater Governance, Ph.D. Dissertation, Department of Sociology, College of Humanities and Social Sciences, Utah State University, Logan, Utah, 272.

Managing Western Irrigation Systems in the Face of Urbanization
2014UT195B
May 1, 2016

PROJECT LEAD: Douglas Jackson-Smith

Problem and Research Objectives:

Most irrigation water in the Intermountain West region is managed, distributed, and delivered to individual farmers by thousands of local irrigation or canal companies who operate an estimated 72,000 km of main irrigation canals (and much larger amounts of minor canals and ditches) in mountain valleys across the West. While much less studied than the much larger federal dam and water distribution systems in the West, these organizations remain a vital link in the agricultural irrigation systems throughout this region. In recent decades, the growth of residential settlement in the Intermountain West is occurring mostly on formerly irrigated agricultural lands. The shifts in the socio-demographic characteristics of shareholders and changes in land use patterns associated with urbanization pose new challenges to the performance and long-term viability of local irrigation systems. This project will provide irrigation and canal companies in Northern Utah with scientifically-based data on the characteristics, behaviors, attitudes, and information needs of their shareholders. Since most contemporary shareholders do not actively participate in company planning or decision-making processes, these companies have few opportunities to learn about many of their members. In this project, we are collaborating with leaders of three irrigation companies in Northern Utah to develop, distribute, and analyze results from a mail survey instrument to be sent to a sample of their shareholder members representing a diverse set of land use contexts along the gradient of urbanization. Results will be useful to the participating companies as they make plans for future investments in new infrastructure and/or operating procedures.

This project is designed to help local canal and irrigation companies in Northern Utah better understand and adapt to changes associated with the urbanization of an irrigated agricultural landscape. The specific objectives that guide project activities include:

- document the diverse characteristics of representative shareholders of irrigation companies located along a gradient of urbanizing environments
- better understand the ways that farmer vs. non-farming shareholders of irrigation companies manage their secondary water allocations
- identify the key opportunities and challenges faced by irrigation companies as they adapt to changes in land use and urban pressure

Methodology:

Activities (since the May 15, 2015 report):

- We received agreements from four irrigation companies to gain access to their shareholder lists in mid-summer 2015, and implemented a multi-wave mail survey of a random sample of these shareholders beginning on July 31, 2015. The survey data collection extended until October 15, 2015.
    - Overall, surveys were sent to 1,161 shareholders across the four companies. Just over half of the surveys went to members of the largest company (the Cache Highline Water Association). To be eligible to complete the survey, shareholders had

to currently own shares and have utilized their water shares themselves at some point during 2015. About 15 percent of all shareholders in our sample were disqualified because their surveys were undeliverable to the address we were provided, were not using their shares themselves, or represented a large number of separate water users who had combined membership in a smaller irrigation group or association (which then held shares in the larger company from which we drew our sample). The disqualification rates were higher for the smaller irrigation companies (perhaps because their lists were less frequently updated).

    - Of the remaining 987 eligible households, we received responses from 649, an overall response rate of 65.8%. Response rates across the four companies ranged from 55-58% in Benson and Midway to 64-70% in the Cache Highline Water Association and Logan Northwest Field Canal samples. These high response rates are a testament to the relevance and importance of the survey to most respondents, and suggest that the findings are a reasonably accurate estimate of the characteristics of shareholders throughout the respective irrigation companies.
- We spent the fall and mid-winter processing the surveys and analyzing the data. A draft report of the results was shared with the board of the Logan Northwest Field Irrigation Company in early March, and we revised the report significantly based on their input. We then made formal presentations at the LNFIC Annual Shareholders meeting (on March 25, 2016), and to the CHWA board on May 5, 2016. We have scheduled to present to the Midway Irrigation Company board on July 11, 2016.
- The full written technical report was finalized in early May, 2015, and will be posted to the USU Digital Commons report shortly. We also plan to send postcards with links to the on-line final report to survey respondents to enable them to see the full survey results.

Principal Findings and Significance:

- The survey findings have been summarized for each of the four companies and for the combined sample in a technical report "A Profile of Irrigation Company Members in Utah's Urbanizing Landscapes." Key findings include:
    - Farming is still an important goal, but that it is changing with the gradual acquisition of shares by nonfarming members.
    - Each company has a relatively small number of shareholders who control the large majority of shares in the company, so most water in these companies is still used for commercial agricultural operations.
    - Most shareholders have been long-time members and are relatively familiar with the procedures for using their shares and participating in company decisions. That said, newer members and those with relatively few shares are less well acquainted with how the irrigation company operates, and many feel unsure how to get involved in company governance.
    - The factors that irrigators consider when making irrigation decisions did not differ dramatically between farming and nonfarming (or large vs. small shareholder) respondents.
    - Many said they use less water than their shares allow them to use, and a minority say they always use their full water share, though larger shareholders were more likely to report using their full shares.

- Informal social ties remain important to sharing knowledge about how to irrigate and to address issues that arise during the irrigation season. However, nonfarmers and those with fewer shares relied more on previous owners than relatives to learn about their irrigation system, and not many were deeply involved in company decisions.
- Most shareholders are satisfied with their irrigation shares and the irrigation company.
- Our results did not uncover evidence of high levels of tension between farmer and nonfarmer shareholders, but a small minority of large shareholders with commercial farming operations did indicate significant number of negative experiences and conflicts. Similarly, impacts from urbanization and land use change were more commonly reported by larger shareholders and in companies that have fewer non-farming members.
- The most commonly cited problems were impacts associated with city stormwater running into company canals, and impacts associated with new housing development and encroachment by new residents onto irrigation company infrastructure.
- Over two-thirds of shareholders expressed concern about whether there is sufficient water to meet the current or future needs of all shareholders in the company. A majority recognized that increasing water conveyance efficiency could increase their available water supply, but less than a third said they were willing to pay more to reduce seepage if they got more irrigation water. Larger shareholders were most likely to see benefits from piping irrigation canals.
- Taken as a whole, there is evidence that the changing face of irrigation company membership will introduce new challenges for irrigation company management and operations. These companies appear to have developed infrastructure and decision-making processes that are primarily targeted at meeting the needs of the largest shareholders (who use the vast majority of the water supplied by the company. Yet the overwhelming bulk of their shareholders (who admittedly own just a minority of total water shares) have less and less interest in using their water for productive agricultural uses, and have different concerns and priorities than the large shareholding farmers.

- Results of the surveys were also presented (or are planned to be presented) to the Boards of Directors of three of the four companies.
- The final technical report will be posted to USU's Digital Commons and information about how to access the report will be sent to the Boards of Directors for each company, and to

REPORTABLE PRODUCTS:

Over the past year, the project has resulted in three potential publications, seven research presentations at professional conferences and stakeholder meetings, and one graduate degrees.

Publications:

1. Armstrong, A. and D. Jackson-Smith. Under Review. Connections and collaborations in local water management organizations of Utah. Submitted to *Society and Natural Resources* February 2016.

2. Jackson-Smith, D., B. Nielsen, and A. Armstrong. In Preparation. New Faces in Old Places: Impacts of Urbanization and Social Change on Irrigation Companies in Northern Utah. Paper manuscript planned for submission to *Rural Sociology*.
3. Jackson-Smith, D. and B. Nielsen. "A Profile of Irrigation Company Members in Utah's Urbanizing Landscapes." Technical Research Report. Plans to publish on USU Digital Commons May 2016.

Presentations:

Research Presentation (based on above project(s) - citation)

1. Armstrong, A. and D. Jackson-Smith. 2015. "Cross-boundary Connections in Sustainable Stormwater Policy and Management." Presentation at 2015 Meetings of the Association for Environmental Studies and Sciences (AESS), San Diego, CA, June 25.
2. Nielsen, B. and D. Jackson-Smith. 2016. "Impacts of Urbanization and Social Change on Dynamics of Water Management in Local Irrigation Companies in Northern Utah." Presentation at USU Student Research Symposium, Logan, UT, April 14.
3. Nielsen, B. and D. Jackson-Smith. 2016. "Impacts of Urbanization and Social Change on Dynamics of Water Management in Local Irrigation Companies in Northern Utah." Presentation at International Symposium on Society and Natural Resources, Houghton, MI, June 22-26.

Stakeholder Research Presentation (based on above project(s) - citation)

4. Jackson-Smith, D and B. Nielsen. 2016. "Highlights of Results of Irrigation Shareholder Survey" Presentation to Board of Directors, Logan Northwest Field Irrigation Company, Logan, UT, March 10.
5. Jackson-Smith, D and B. Nielsen. 2016. "Highlights of Results of Irrigation Shareholder Survey" Presentation at Annual Shareholder Meeting, Logan Northwest Field Irrigation Company, Logan, UT, March 25.
6. Jackson-Smith, D and B. Nielsen. 2016. "Highlights of Results of Irrigation Shareholder Survey" Presentation to Board of Directors, Cache Highline Water Association, Logan, UT, May 5.
7. Jackson-Smith, D and B. Nielsen. 2016. "Highlights of Results of Irrigation Shareholder Survey" Presentation to Board of Directors, Midway Irrigation Company, Logan, UT, July 11.

Degrees granted:

Armstrong, A. Sociology PhD. June, 2015. (professional placement—obtained a tenure-track faculty position in the Department of Environmental Studies at LaFayette College in Easton, PA. Started January 2016).

Information Systems for Landscape Water Conservation

Basic Information

Title:	Information Systems for Landscape Water Conservation
Project Number:	2015UT196B
Start Date:	3/1/2015
End Date:	2/29/2016
Funding Source:	104B
Congressional District:	01
Research Category:	Climate and Hydrologic Processes
Focus Category:	Conservation, Irrigation, Water Supply
Descriptors:	None
Principal Investigators:	Kelly Kopp

Publications

There are no publications.

NIWR Report: **Information Systems for Landscape Water Conservation** (104B)
2015UT196B
Kelly Kopp and David K. Stevens

Problem Description

Drought and the increase in population in Utah and throughout the Intermountain West have created water shortages in the region. The population continues to grow faster than anywhere else in the United States and homeowners in Utah use approximately 60% of potable water to irrigate landscapes (Utah Division of Water Resources, 2003). Because water is a limited resource, the need for conservation of landscape irrigation water has become increasingly important.

Although water is used in high amounts for other purposes as well, "a landscape may serve as a visual indicator of water use to the general public due to its visual exposure" (Thayer, 1976). As homeowners become more aware of landscape water conservation alternatives, attitudes toward drought tolerant landscapes may change throughout the United States. In 1979, Hancock suggested that residential landscape water conservation is "essential to establishing a successful water policy aimed at curbing use in all sectors of water conservation" (Hancock, 1979). The use of non-adapted plant species, irrigation system non-uniformity, poor landscape management, and poor landscape design all contribute to excessive water use on landscapes in the state.

Many difficulties arise, however, at the prospect of improving landscape irrigation efficiency. Obstacles to improvement such as initial startup costs, lack of adequately trained industry professionals, and unfavorable consumer reaction are all concerns facing municipalities as they encourage landscape irrigation efficiency. Perceived fairness and equity also become an obstacle when water conservation measures are applied uniformly to all users at all times, when excess irrigation often is greatest in certain segments of the water-consuming public (Kjelgren, 1999). Consequently, those persons watering their landscapes in an efficient manner only serve to subsidize any costs arising from those persons who are watering inefficiently. Identifying the 'who' and 'when' of landscape water demand will help water suppliers to better target conservation measures. In this technology-oriented society, many water suppliers have the capacity to analyze landscape water use by using their existing water billing data, including such information as lot size, tax identification information, and historical water use.

Since 1999, the Center for Water Efficient Landscaping at Utah State University has been cooperating with the state's major water agencies and suppliers to provide landscape irrigation system evaluations for residential and commercial irrigators. Voluntary participants receive customized irrigation schedules based on their irrigation systems' efficiency. The program quantifies water use improvements by combining water use and billing records, dynamic evapotranspiration (ET) rates and information regarding landscape size and irrigation system efficiency. Over time, estimations of landscape water demand from reference ET rates can be

compared to historical water use and billing records in order to create profiles of landscape water users within a given service area. Conservation measures may then be more appropriately directed toward those consumers who are using water inefficiently.

Research Objectives

Methods for analyzing historical water billing data, acquired from water providers, for identifying water customers with a high capacity to conserve landscape irrigation water are complex due to the nature of the data. High capacity to conserve water customers are those customers that utilize irrigation water in great excess of actual plant water requirements. Using historical water billing data, and coupling the information with the size of specific properties, a reasonable estimate of appropriate water use may be made.

Appropriate database and information systems are needed to mine the large datasets associated with water billing data and to perform customized calculations appropriate to different water providers. This project began the development of appropriate database and information systems and the association of these systems with existing landscape irrigation system evaluation data (gathered since 1999) with the ***overall objective of helping the state's water agencies identify consumers with a high capacity to conserve landscape irrigation water***.

A further objective of the project is to identify obstacles to landscape water conservation for consumers with a high capacity to conserve, such as inefficient irrigation systems, a lack of education, or general unwillingness to conserve water (due to attitudes or improper water pricing signals).

The project, which began in 2015/2016, will be completed in stages over a period of 3 years, which is the typical time frame for the completion of a doctoral level research project. This proposal funded the first stage of the project (1 year), and included the development of the database required to meet the overall project objective.

Historically, accessing water billing data across multiple agencies has been difficult because of data inconsistencies and general difficulty of use. Automating billing data analysis eliminates the arguably tedious task of going through billing data line-by-line, trying to ensure proper formatting. This project identified and utilized new methods of mining water billing data and combined these methods with existing landscape irrigation system evaluation data to identify properties and water customers with the highest potential to conserve water, as well as to determine the overall water-saving benefits of an existing landscape irrigation system evaluation program. We refined current methods for determining the capacity of water customers to conserve by analyzing historical water use and comparing it to an estimated water use budget.

Methodology

Related to this project, a Utah-based irrigation system evaluation program, a.k.a. The Water Check Program (WCP), has developed a mobile application (app) to aid in the collection of program data, calculations of complicated equations, and the production of educational materials for program clients.

In concert with the app for program data collection, a Structured Query Language (SQL) database was developed from the WCP's original Microsoft Access database. SQL is a programing language designed for managing data held in relational databases. Relational databases store information about data and how variables are related to each other. Since 1986, SQL has been the database standard in the American National Standards Institute (ANSI).

When used in conjunction with the WCP app, the SQL database allows for the acceptance of field data collection by one or multiple users remotely, while also allowing system administrators the ability to generate custom reports and user access modifications. A customized, web-based database query tool was also developed as part of this project.

The information system and database development were integrated with statistical modeling tools for mining water billing data. These were combined with existing landscape irrigation system evaluation data in order to identify water consumers with a high capacity to conserve. Training for a graduate student in database development and use, along with relevant statistical methods, was initiated.

We accessed the water billing databases for one major water retailer in Salt Lake County, Utah. This retailer, the Salt Lake City Department of Public Utilities (SLCDPU), allowed us to use their water billing databases and staff resources for the purposes of this project. The SLCDPU water data are especially desirable due to the general accessibility of their consumption data. However, additional water utilities/providers will be incorporated over time.

One obstacle to using water billing data among different water agencies is in the formatting of the data. Each water agency uses a different, and sometimes custom, format for their data. Many fields have differing names (i.e., Account Number versus Service ID), text-based or numerical fields, ordering of fields, etc. CWEL developed a tool to import relevant water use data from SLCDPU so the data were more easily used for common analyses.

Principal Findings and Significance

One year into this 3-year project, the SQL database that has been developed is allowing for enhanced analysis of WCP program participant data, as well as analysis of the water use of the entire Salt Lake City Department of Public Utilities (SLCDPU) service area. For example, 2013 WCP program participants were found to be using 25,000 gallons of water monthly for outdoor irrigation. The average single family home in the service area during the same time period was using 17,000 gallons of water monthly for outdoor irrigation. Following WCP participation,

2013 participants reduced their monthly irrigation by 8000 gallons monthly, bringing their overall water use down significantly and bringing them more in line with other city residents.

Customized reporting based on specific data fields such as zip code, landscaped area (and more), plus the ability for advanced statistical analyses, including regression, correlations or analysis of variance are now possible. For example, with the new database, we can easily identify the total area of turf area audited in the SLCDPU. This data is now being associated with water savings and efficiency and will help guide water conservancy districts and utilities in their conservation efforts.

References

Hancock, J.C. 1979. Water conservation in housing. Water Conservation Needs and Implementing Strategies Conference. The Franklin Pierce College, Rindge, NH.

Kjelgren, R., F. A. Farag, C. Neale, and D. Itenfisu. 1999. Determining conservable landscape water through remote sensing. *In:* 1999 Proceedings of the Irrigation Association. Nov. 7-9, Orlando FL, pp 193-197.

Thayer, R.L. 1976. Visual ecology: revitalizing the esthetics of landscape architecture. *Landscape,* 20, 37-43.

Utah Division of Water Resources. 2003. Utah State Summary 2000. Municipal and Industrial Water Supply Studies. Division of Water Rights. Salt Lake City, Utah, Utah Department of Natural Resources.

Biofiltration of Utah Municipal Drinking Water

Basic Information

Title:	Biofiltration of Utah Municipal Drinking Water
Project Number:	2015UT197B
Start Date:	3/1/2015
End Date:	2/29/2016
Funding Source:	104B
Congressional District:	01
Research Category:	Water Quality
Focus Category:	Treatment, Water Quality, None
Descriptors:	None
Principal Investigators:	David K. Stevens, Eva Nieminski, Darwin L. Sorensen

Publications

There are no publications.

Biofiltration of Utah Municipal Drinking Water

Pilot Plant Testing of Biofiltration at the Central Utah WCD Treatment Plant in Duchesne, UT

Stetson Bassett[1], David Stevens[1], Eva Nieminski[2], Michael Rau[3], Monica Hoyt[3], Joe Crawford[3]

(2015UTxyz)

Abstract

Biofiltration of drinking water supplies is a promising method to reduce the potential for production of disinfection by products and to minimize the regrowth of microorganisms in water distribution systems. Because of the site-specific nature of the implementation of this technology, the proposed project will study, at pilot scale, the potential for using biofiltration for reducing and modifying the organic matter content of drinking water at the Duchesne, Utah plant managed by the Central Utah Water Conservancy District water utilities, and to develop preliminary information pertaining to the design and operation of such utilities.

Problem Description

Organic compounds have been problematic in source waters for municipal water supplies since the advent of modern filtration. Historically, organic compounds caused operational problems due to the promotion of uncontrolled biological growth on treatment plant surfaces and in plant piping. They have also caused problems in finished water related to the residual taste and odor that prompt consumer complaints. Since the 1970s it has been recognized in the water treatment community that some organic compounds in source waters may react unfavorably with chlorine-containing disinfectants to form trihalomethanes (THMs) and haloacetic acids (HAAs) in finished water, of which some are known or suspected human carcinogens. In addition, some organic compounds found in source water are toxic in their own right; microcystin and geosmin are often present in surface water supplies influenced by certain cyanobacteria.

Biofiltration has been used to some extent in Europe to remove these naturally occurring organic compounds from source waters since the 1970s, and in North America since the later 1980s. The biological processes currently in engineering practice in North America include natural processes such as slow sand and river bank filtration both of which are currently regulated. Additional processes include anoxic treatment during which oxidized organic compounds are reduced to forms more readably

[1] Utah Water Research Laboratory

[2] Utah Division of Drinking Water

[3] Central Utah Water Conservancy District

removed by conventional or advanced physical/chemical water treatment, or natural organic matter is used to reduce nitrate concentrations via denitrification. More recently, aerobic granular filters, in which existing granular rapid sand filters are allowed to develop aerobic biofilms capable of reducing the concentrations of assimilable organic carbon (AOCs). A review of biological filtration in both water and wastewater treatment is found in Chaudhary et al. (2003).

An important element in the use of any new technique is to be able to measure its performance. Traditionally, the performance of BWT systems is determined via the measurement of the amount of organic matter at each stage of treatment in the form of overall measures such as AOC (above), carboxylic acid concentration (CBXA), among others. Though well established, these measures are time consuming multistep lab methods that are unwieldy to use for process control. Using the idea that more pertinent measures for incremental biological activity in a biofilter may be suitable, another option may be to using a direct measure of metabolic activity, the adenosine triphosphate (ATP) concentration (Pharand *et al*. 2014), for which instrumentation is now in common use, may yield a process activity measure that can be correlated with treatment performance measures, such as carboxylic acids (CBXA).

In as much as every engineering problem is local, the history of biological water treatment in Utah is short and it's necessary to assess the potential for biofiltration water treatment in Utah Drinking Water Treatment Plants. Biofiltration for drinking water has been more extensively applied in Europe than in the U.S., though significant research was carried out in the U.S. to study the science of biofilm formation and activity in granular filters, primarily reported by the American Water Works Association (e.g., Ahmad *et al.* 1998a,b, Alonso *et al.* 1998, Bablon, *et al.* 1988, Boe-Hansen *et al.* 2002). We are proposing here a preliminary study of the application of biofiltration in Utah Drinking Water Plants.

This report describes monitoring results from the Duchesne Drinking Water Biofiltration project in conjunction with the Utah Department of Environmental Quality, Division of Drinking Water (UDEQ), the Central Utah Water Conservancy District (CUWCD), and Utah State University (USU). A pilot plant located at the CUWCD's Duchesne Water Treatment plant has been operated in parallel with the main plant to test three methods related to biofiltration for the control of organic matter that may be disinfection byproduct precursors (DBPp). Details of the filters are provided below. Weekly Monitoring at several locations in the main plant and the pilot plant, and in the distribution system commenced in April 2015 and samples of the pilot plant filter media were obtain less frequently. This report is a preliminary assessment of the results.

Research Objectives

Objectives

The proposed project has as its primary objective the assessment and optimization of biofiltration in selected Utah Drinking Water Treatment plants at pilot scale.

Hypotheses

The research effort was built around the following scientific/engineering hypotheses:

1. Biofiltration is an effective way to reduce organic matter from Utah source waters

2. Biofiltration can be used to gain the following potential benefits: enhanced organics removal, enhanced turbidity removal, improvement of taste & odor, potential reduction in coagulant and polymer dose, reduction in disinfection by-products formation, and improvement of biological stability of water in distribution systems

3. ATP measurements, along with CBXAs, could provide accurate, inexpensive, and easy to use tools to monitor the performance of biologically active filters and measure stability of filtered water.

Methodology

A series of designed experiments were carried out at the Central Utah Water Conservancy District's water treatment plant in Duchesne, UT (Figure 1), to test the hypotheses outlined above. The plant was chosen in consultation with project partners from the Utah Division of Drinking Water, and the Utah Water Quality Alliance, composed of the staff from large and small water treatment plants in Utah and devoted to optimize treatment effectiveness to produce the highest drinking water quality possible. Pilot-scale filters were available at the plant that could be easily retrofitted to carry out biofiltration. . Three parallel process trains were used. In Pilot plant 1, prechlorination of the water was withheld. In Pilot plant 2, both prechlorination and backwash water chlorination were withheld. In Pilot plant 3, all chlorination was withheld and nitrogen and phosphorus were added to promote biological activity Influent, intermediate, and effluent water samples were collected weekly during this period and assayed for general water chemistry, heterotrophic plate count (HPC), dissolved and total organic carbon, UV_{254}, ATP, nutrients (N and P), and other measures, and regular samples of the biofiltration media were collected during the study to assess the development of the biological consortia through microbiological analyses.

Due to the short duration of the proposed project (April 2015 – March 2016), factorial experiments to assess how operational and source water variables influence biofiltration performance were not possible. Though we see these types of experiments as critical for future application of the technology, the experiments carried out here under naturally occurring variability provide sufficient preliminary information to seek external funds in a follow-on project.

Based on USU's experience with development of biological activity on filtration media (McNeill et al 2015), it was anticipated that some time would be required for biofilter start-up.

Figure 1 Central Utah Water Conservancy District – Duchesne Water Treatment Plant

Figure 2 Pilot Biofilters at the CUWCD Duchesne WTP

Detailed Methods

Filter operation

The pilot plant receives raw water from the influent line to the DWTP. Ferric chloride ($FeCl_3$) is added to a static rapid mixer. Flow then passes to a flocculator with three basins, each with a residence time of 12 min and a shear rate, *G* of 35 1/sec. After settling, flow is split between the three filters with the treatments given below. The filtration rate was the same for each filter of 0.2 m^3/m^2-min. The filters were backwashed every 20-50 hours when either the headloss or turbidity exceeded guidelines.

Water quality monitoring

During operation of the pilot-scale systems, each pilot treatment train was monitored weekly at three locations with replication of ~10% of the total samples. These samples were analyzed in the field for temperature, pH, dissolved oxygen, specific conductance, turbidity, UV_{254}, and ATP. The methods are found in Table 1 in the Appendix. The samples were then split and preserved as needed for analysis at the UPHL using methods found in Tables 2-3 (Appendix A) and in the SHL Standard Operating Procedures (State of Utah, 2014).

Bioactivity monitoring

On a weekly basis throughout the pilot study, we assessed the ATP concentration associated with the filtration media within the biofiltration pilot plants to be used as a surrogate of the microbial activity. This was accomplished by sampling the filter media from each system, and measuring the ATP of a suspension of the washed medium. Samples were obtained weekly from each pilot plant, and assayed for ATP within 24 hours.

Statistical analysis

The monitoring data were collected in spreadsheets and entered into a Microsoft SQL Server database housed at the UWRL. Statistical analysis of the data was carried out using the statistical package R (R Core Team, 2016). Analysis methods included the analysis of variance and the Tukey HSD test.

Principal Findings and Significance

Statistical Analysis

R was used to determine statistical significance between (1) the influent and effluent concentrations of the pilot plant, (2) the three different types of filters, and (3) the full-scale plant and pilot plant. The analysis of variance (ANOVA) method was used to determine these differences. The ANOVA method compares the amount of variation *within* treatments with the amount of variation *between* treatments (Berthouex and Brown, 2002). If the variation between treatments is significantly larger than the variation within treatments then there is evidence to suggest that the mean values of the samples are different. The Tukey's Honest Significant Difference (Tukey HSD) method was then be used to determine *which* treatments differ from one another. The Tukey method uses a 95% family-wise confidence interval to compare the means between each pair of samples; therefore a *p*-value less than 0.05 would suggest statistical significance.

Pilot Plant

Description of Filters (Figure 2)

- Pilot Plant 1: Easy Biofilter
    - No pre-chlorine
    - Chlorinated backwash
- Pilot Plant 2: Biofilter
    - No pre-chlorine
    - Non-chlorinated backwash
- Pilot Plant 3: Engineered Biofilter
    - No pre-chlorine
    - Non-chlorinated backwash
    - Added P and N

Comparison of Influent and Effluent Water Quality

Comparisons of influent and effluent concentrations within the pilot plant were made to determine the effect of biofiltration. These results cannot be compared directly with the full scale plant since CUWCD is practicing prechlorination at the Duchesne plant and the PP influent samples were taken on the raw water.

NOM removal. TOC, UV_{254}, and SUVA (specific ultraviolet absorption at 254 nm) are all commonly used to characterize natural organic matter (NOM) in raw and treated drinking water. One purpose of a biofilter is to reduce the amount of NOM in the effluent of a distribution system. A decrease in NOM would reduce the potential of forming disinfection by-product's (DBPs) as well as improve the aesthetics of the water (taste and odor, primarily). Therefore, TOC, UV_{254}, and SUVA (dissolved and total) were measured to determine if organic material was reduced across each filter. Time series plots showing change in concentration over time are found in Figure 3, and boxplots and 95% confidence intervals were plotted to show the spread of the data in Figure 4. For the 95% confidence level plots, statistical significance is implied if an interval does not cross zero (vertical dashed line in the right hand panel in Figure 4).

Figures 3 and 4 demonstrate that TOC, UV_{254}, and SUVA concentrations were decreased across all three filters for all sampling events from May through November 2015. An ANOVA plus TukeyHSD test found that the influent and effluent concentrations of all 4 parameters at each filter were statistically different. A table of the *p*-values can be found in the Appendix, Table A1. It can therefore be concluded that each biofilter captured and consumed NOM, as expected. Though significant statistically, the actual change in TOC was quite small compared to the surrogate measures suggesting that the changes in NOM due to bioactivity acted primarily to change the nature of the NOM to a form less sensitive to UV detection.

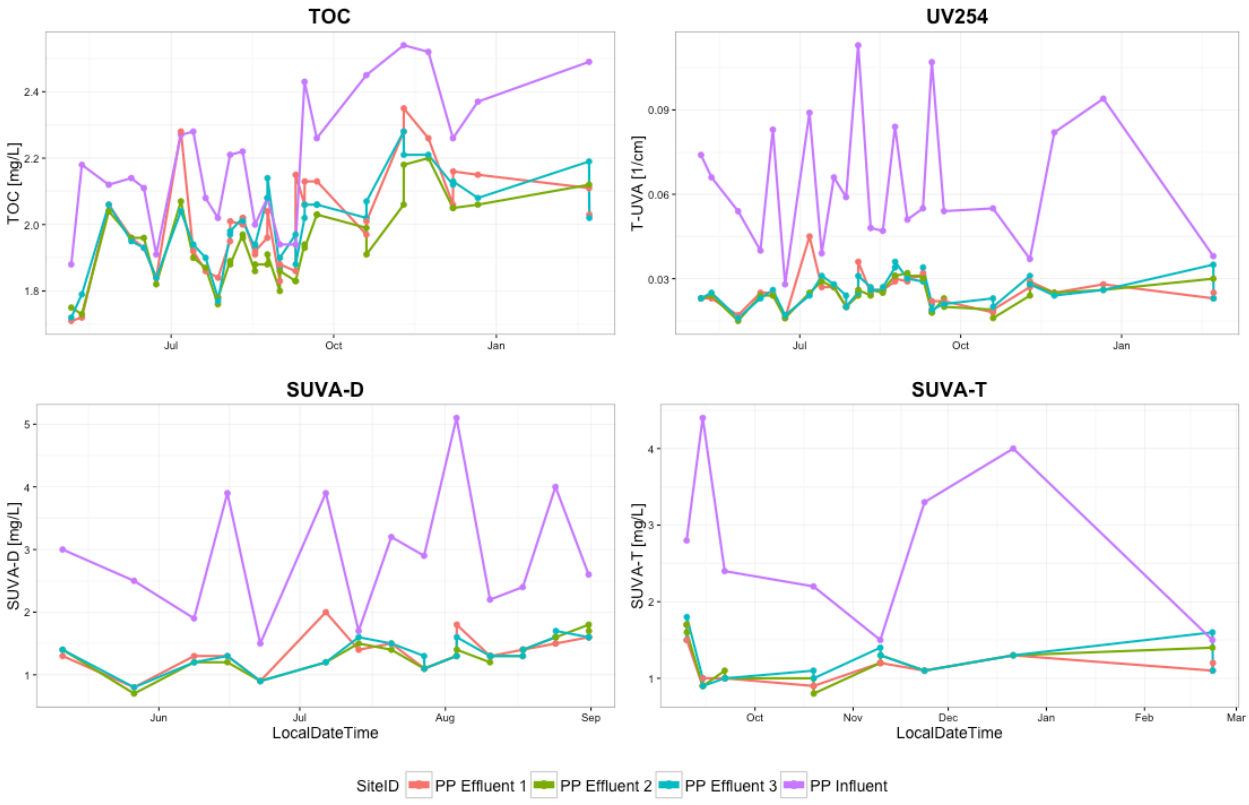

Figure 3. Time series plot of TOC, UV_{254}, and SUVA (dissolved and total) to compare influent vs. effluent concentrations.

Carboxylic Acid Removal. One type of ozone by-product is low-molecule-weight organic molecules such as carboxylic acids (e.g. Acetate, Formate, and Oxalate) (Crittenden 2012). Therefore, carboxylic acids can also be used as a surrogate to estimate the amount of organic matter in a system if ozonation precedes filtration. A decrease in carboxylic acids across a filter would indicate good filter performance. Figures 5 and 6 show the pilot plant results. Figures 5 and 6 demonstrate that carboxylic acids were decreased across all three filters. An ANOVA and TukeyHSD test were conducted and found that the influent and effluent concentrations of all 4 parameters at each filter were statistically different. A table of the *p*-values can be found in the Appendix, Table A2. This is another confirmation that the biofilters are indeed capturing and consuming organic matter.

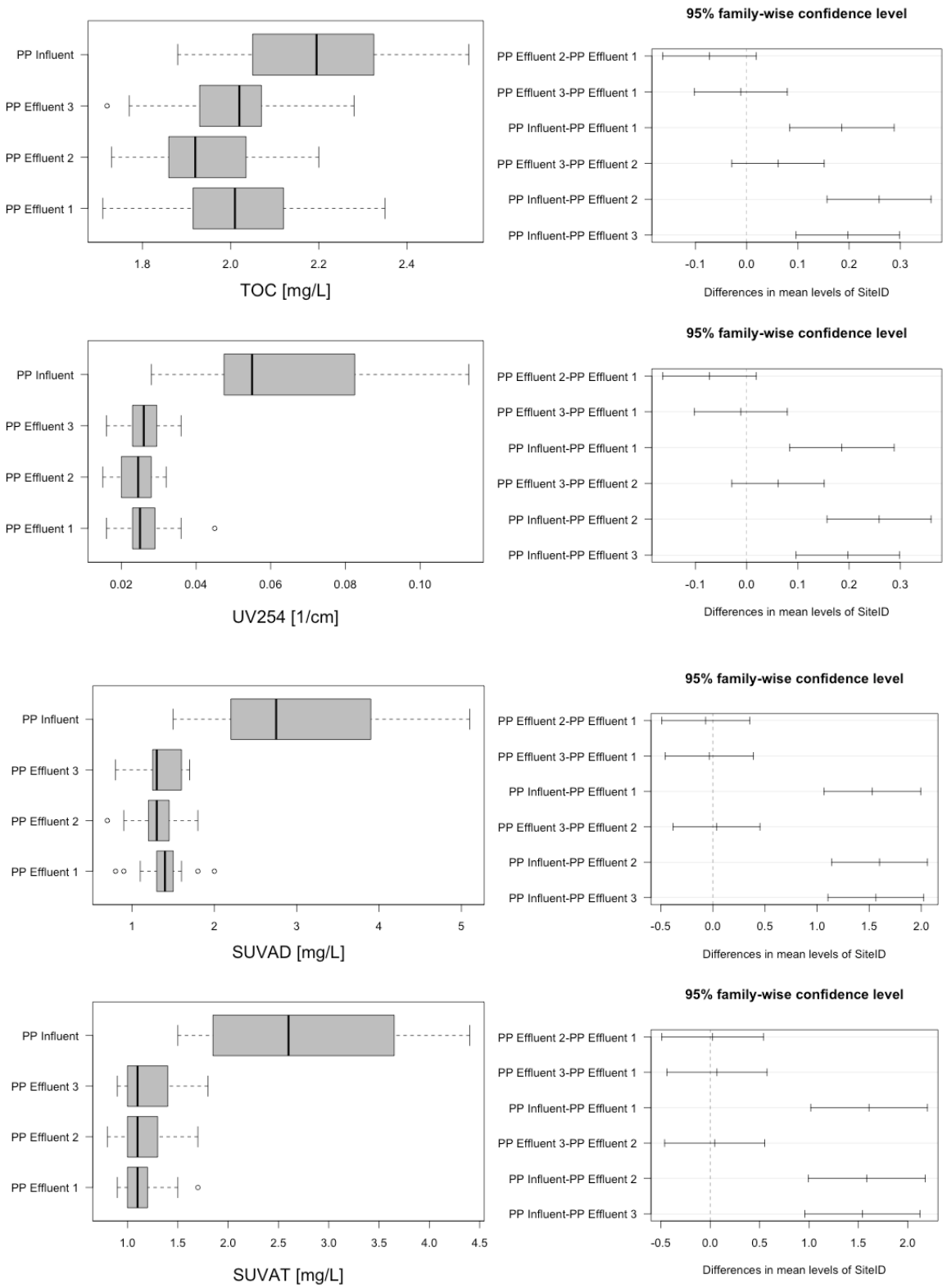

Figure 4. Boxplots and 95% confidence intervals of TOC, UV_{254}, and SUVA (dissolved and total) to compare influent vs. effluent concentrations.

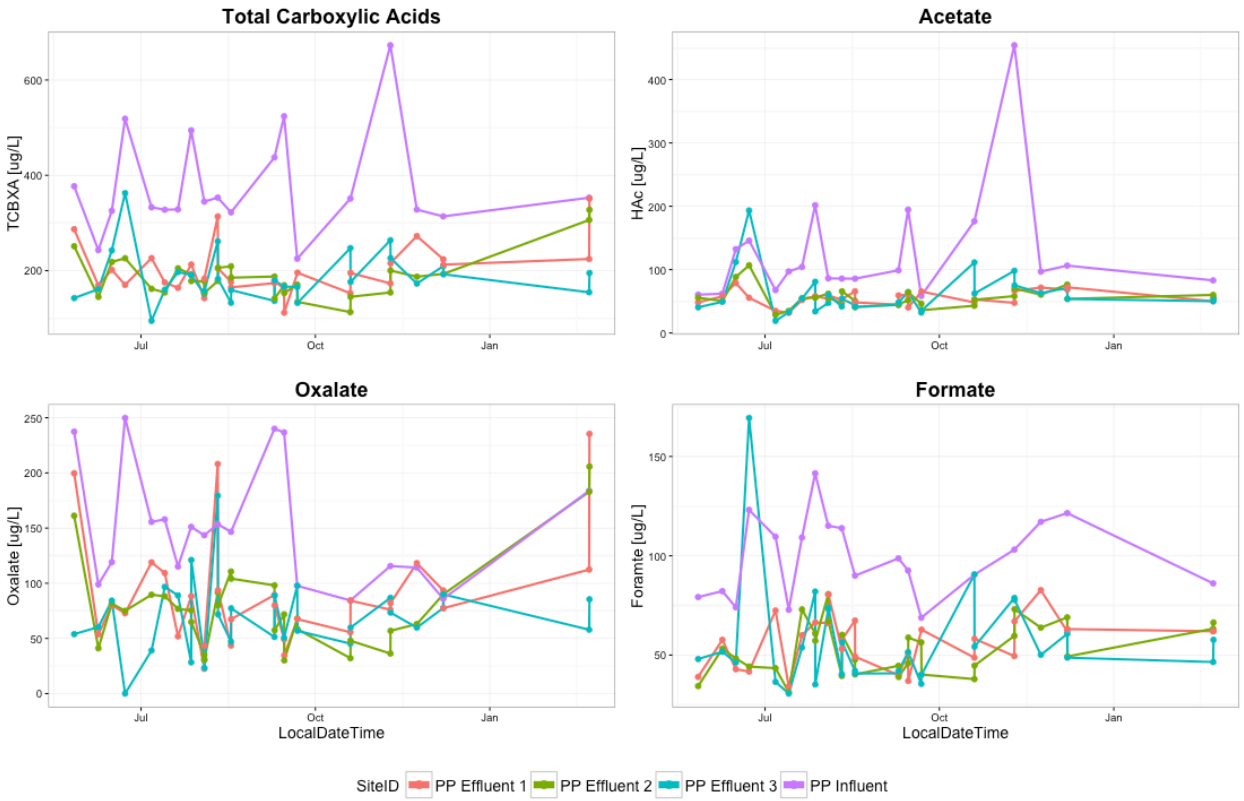

Figure 5. Time series plot of Total Carboxylic Acids, Acetate, Oxalate, and Formate to compare influent vs. effluent concentrations.

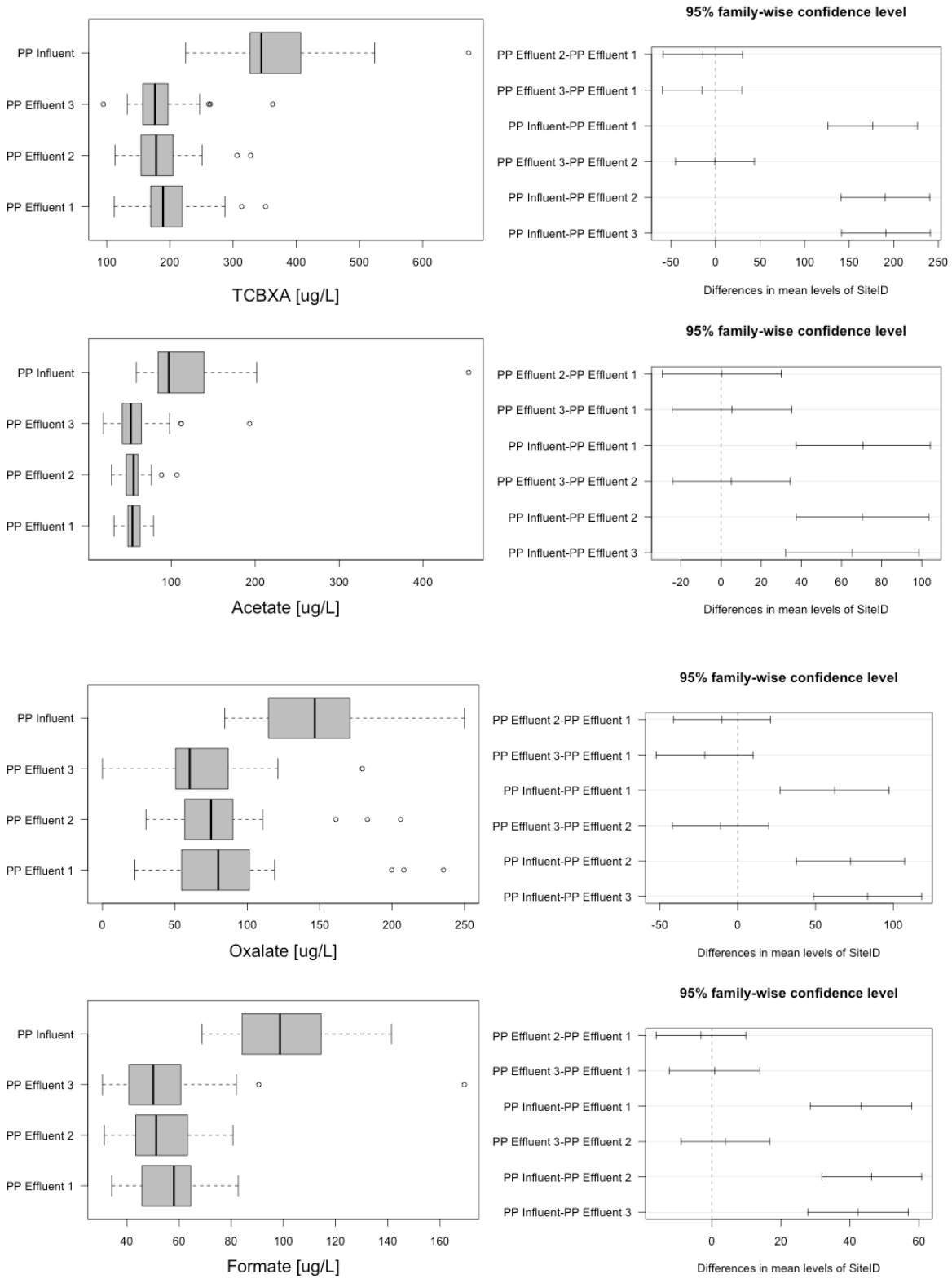

Figure 6. Boxplots and 95% confidence intervals of Total Carboxylic Acids, Acetate, Oxalate, and Formate to compare influent vs. effluent concentrations.

Turbidity Removal. The primary purpose of any filter is to remove stray particles from the chemical treatment portion of the plant. Changes in turbidity are commonly measured to determine how effective a filter is at particle removal. High turbidity removal and low effluent turbidity would indicate an effective filter. Figures 7 and 8 show the pilot plants turbidity results.

The large difference in turbidity from the influent to the effluent as well as the large turbidity removal demonstrated by each filter (Figures 7 and 8) suggests that all of the filters were working effectively. An ANOVA and TukeyHSD test were also conducted and found that the influent and effluent concentrations of the turbidity at each filter were statistically different. A table of the p-values can be found in the Appendix, Table A3.

Biological Activity. One indicator of microbial activity is ATP; thus high ATP concentrations would suggest high biological activity. ATP concentrations were collected at the influent, at the three different filter effluents, and from the filter media. Filter media ATP concentrations will be considered in a later section. The concentrations were calculated in both units of RLU and pg ATP/mL. The ATP results in pg ATP/mL may have not been calculated correctly (Appendix, Figure A1), so Figures 9 and 10 only show ATP in units of RLU. The values were plotted on a log scale.

Figures 9 and 10 show that the highest concentrations of ATP were seen at the influent. An ANOVA and TukeyHSD test were conducted and found that both Filters 2 and 3 were statistically different than the influent, but that filter 3 was not statistically different. It is not surprising that there are relatively high ATP concentrations in the plant influent since the raw water is from Starvation Reservoir with typical amounts of bacteria and algae, both of which produce ATP, especially at elevated water temperatures.

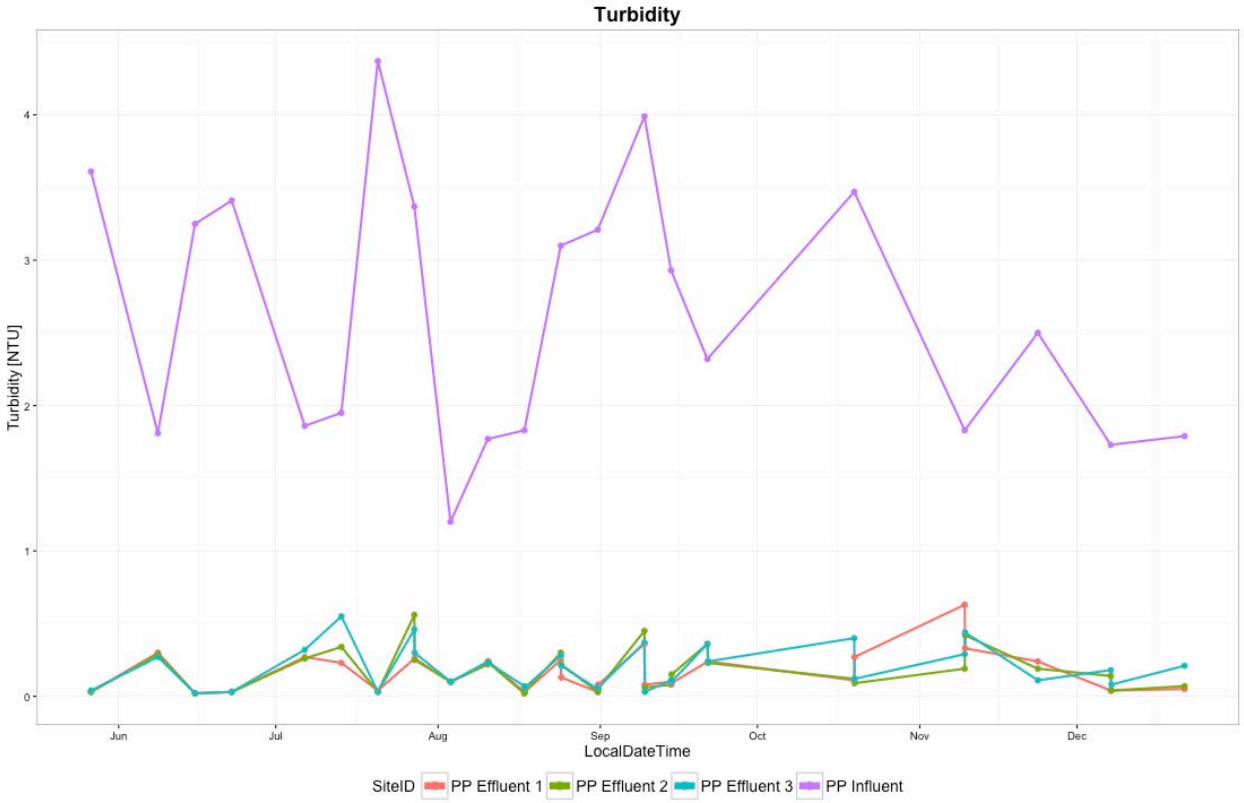

Figure 7. Time series plot of turbidity to compare influent vs. effluent concentrations.

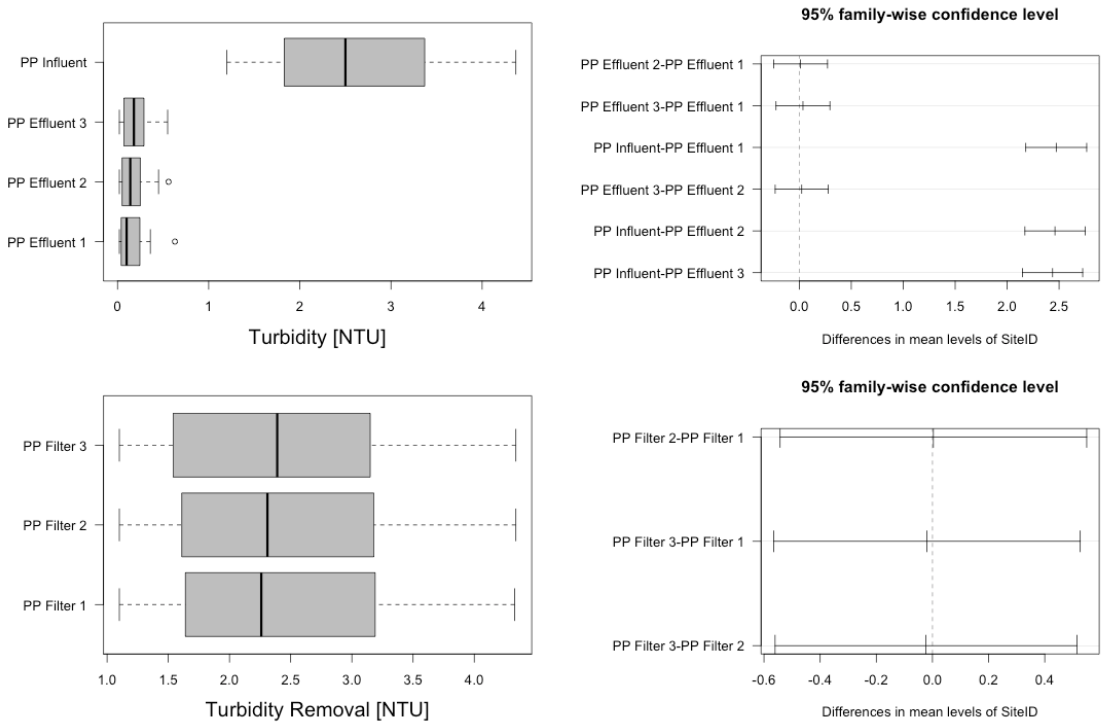

Figure 8. Boxplots and 95% confidence intervals of turbidity and turbidity removal concentrations.

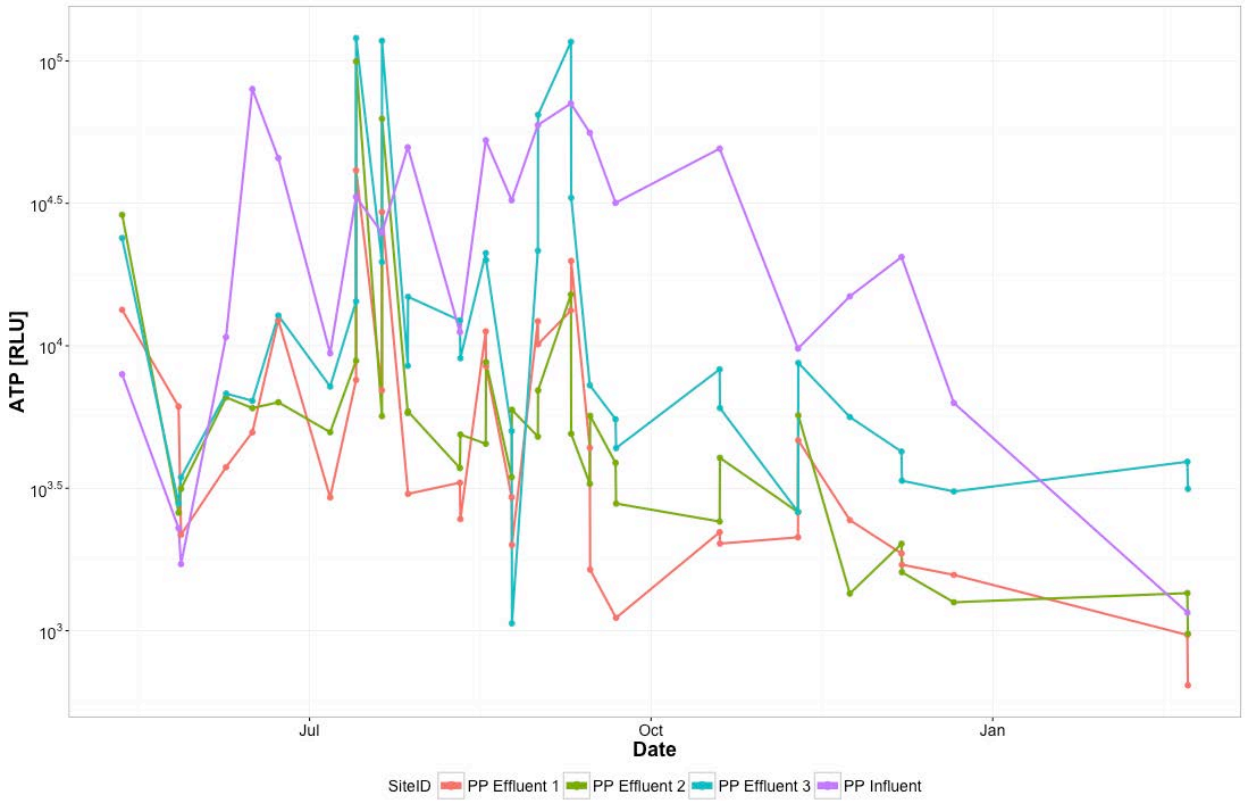

Figure 9. Time series plot of ATP (on a log scale) to compare influent vs. effluent concentration. ATP was calculated in units of RLU.

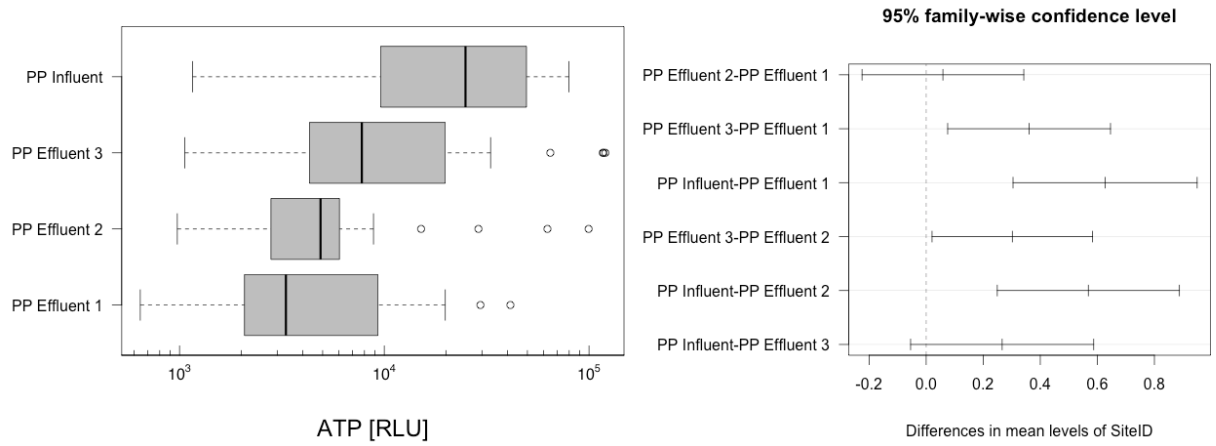

Figure 10. Boxplot and 95% confidence interval of ATP (on a log scale).

These ATP observations were then correlated with CBXA observations in the water phase samples from the water quality monitoring (Figure 11) for the pilot plant. This figure shows that Carboxylic Acid, total is well correlated with the individual acid components, and ATP is moderately correlated with total CBXA and acetate (r = 0.47 and 0.45, respectively). However, when replotted for each sampling location (not shown), the only significant correlation with ATP in the pilot plant influent with acetate (*r* = 0.59), while for the pilot plant effluents, significant ATP correlations are in pilot plants 1 and 2 (*r* = 0.58 and 0.53, respectively) with formate, with none in pilot plant 3. These results suggest that the form of the CBXA depends on the biofiltration option with the effluent from pilot plants 1 and 2 favoring oxalate with pilot plant 3 slightly favoring acetate.

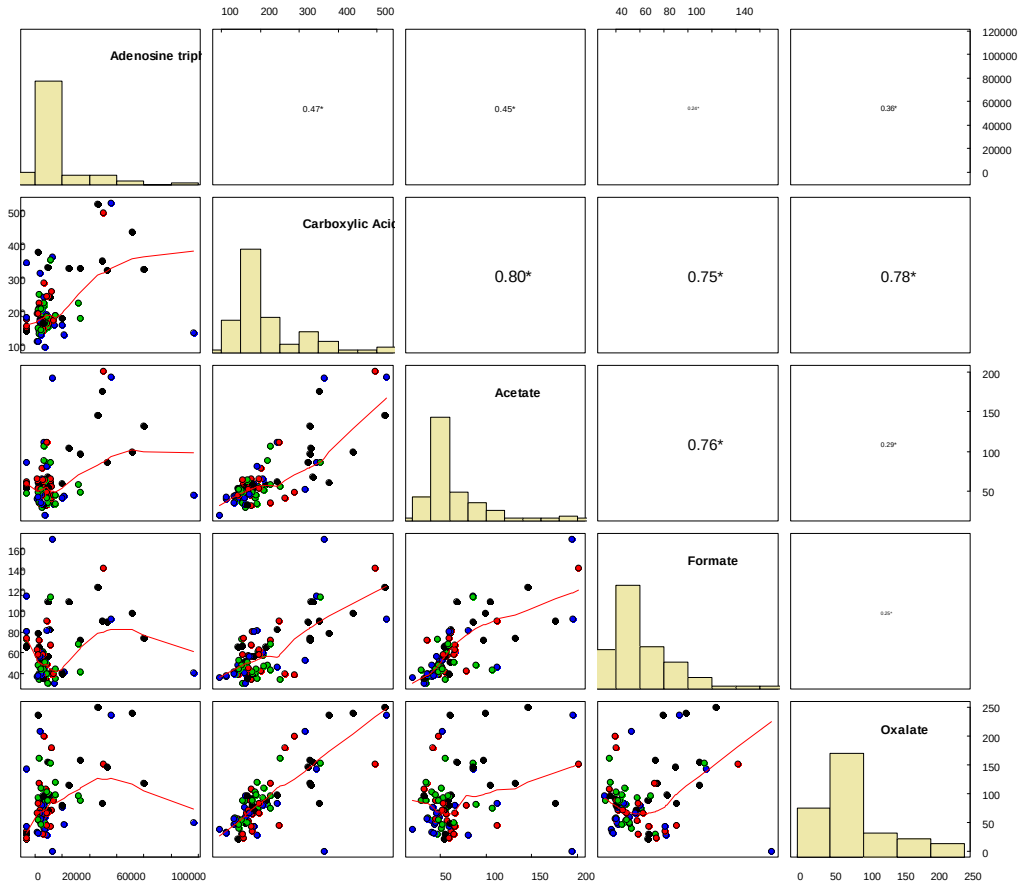

Figure 11 Correlation Matrix for ATP and Carboxylic Acids – Pilot Plant Influent and Effluent. '*' means correlation is significant at α = 0.05. Black points are pilot plant influent, red, blue, and green are pilot plant effluent 1, 2, and 3, respectively.

Comparison of Biofiltration Methods

A comparison of each biofilter was made to determine if the biofiltration management approach (i.e. chlorinated backwash or nutrient addition) had an impact on filter performance.

NOM removal. A separate ANOVA and Tukey test was made to compare each filter individually. Both the ANOVA and Tukey test found that there was no statistical difference between filter performance, within a 95% confidence interval, for TOC, UV254, or SUVA. The results can be found in the Appendix, Table A5.

Carboxylic Acid Removal. The results for carboxylic acids were very similar to that of TOC, UV_{254}, and SUVA; there was no statistical difference between the 3 different filters for total carboxylic acid removal, though which of the three CBXA components did differ somewhat. The findings can be found in the Appendix, Table A6.

Turbidity Removal. There was also no statistical difference between each filter for final turbidity or turbidity removal. These results can also be found in the Appendix, Table A3.

Biological Activity. The highest concentrations of ATP should be found on the filter media. Therefore it was concluded that the best comparison of microbial activity should be from filter media. Filter 3 should have the highest ATP concentrations due to nutrient additions and Filter 1 should have the lowest ATP concentrations due to the chlorinated backwash. Figures 12 and 13 show the results of ATP concentrations on filter media. ATP concentrations were plotted on a log scale. An ANOVA and Tukey test were conducted for the ATP concentrations on the media of each individual filter. It was found that each filter is statistically different than each other, the results can be found in the Appendix, Table A7. ATP concentration followed the expected trend. Filter 3 had the highest ATP concentrations and Filter 1 had the lowest concentrations. The ATP results therefore suggest that there is a difference in biofilm makeup between each filter.

Full Scale

The full-scale and pilot plants were also compared to determine if the pilot plant exhibited similar characteristics to the full-scale plant. NOM and turbidity removal for the full scale and pilot plants were plotted together to make the comparison. The results can be found in Figures 14 through 17. For NOM removal (Figures 14 and 15) the influent concentrations of the full-scale plant were around the effluent concentrations of the pilot plant. The only variable that differed was TOC removal. For turbidity the pilot plant and full-scale plant showed similar results (Figures 16 and 17). The effluent concentrations of the pilot and full-scale plant for both NOM removal and turbidity were similar in all cases.

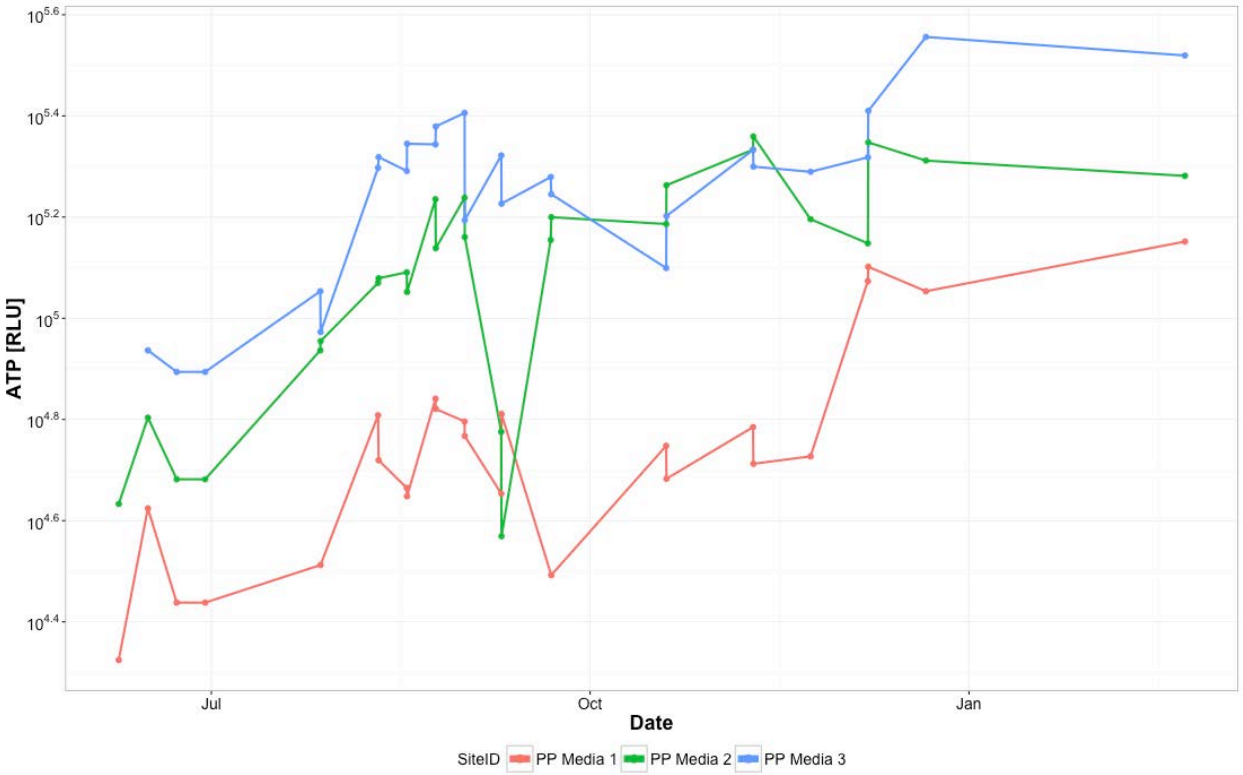

Figure 12. Time series plot of ATP on filter media (on a log scale). ATP was calculated in units of RLU.

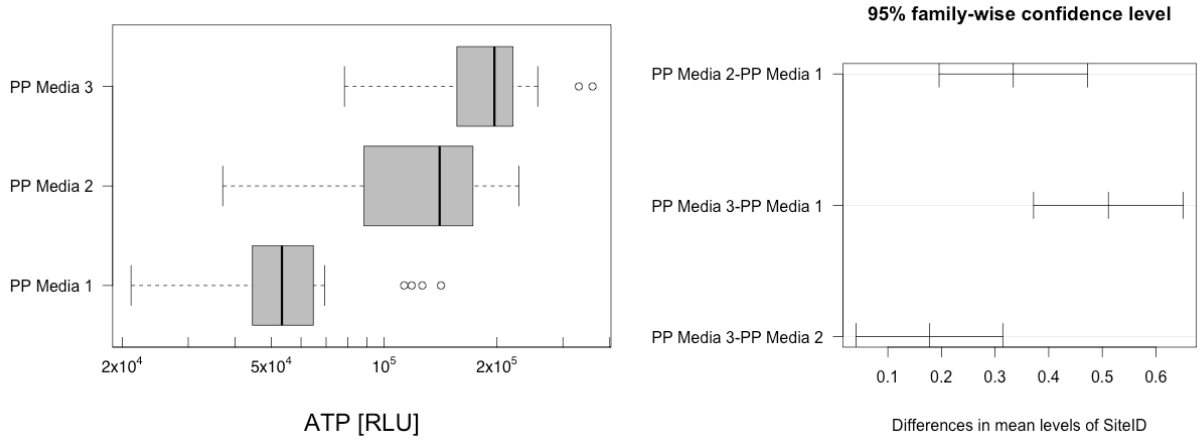

Figure 13. Boxplot and 95% confidence interval of ATP on filter media (on a log scale). ATP was calculated in units of RLU.

Figure 14. Time series plot of NOM removal to compare the full-scale plant (Filter Influent/Effluent) and pilot plant (PP Influent/Effluentx).

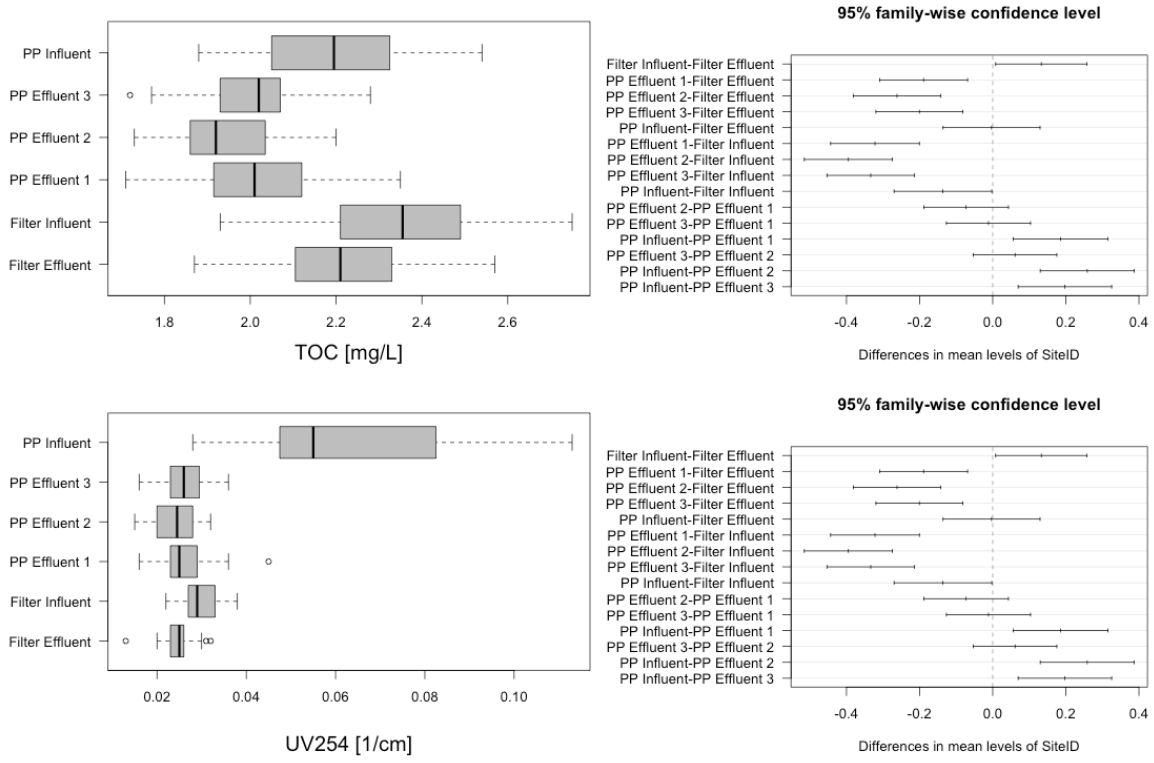

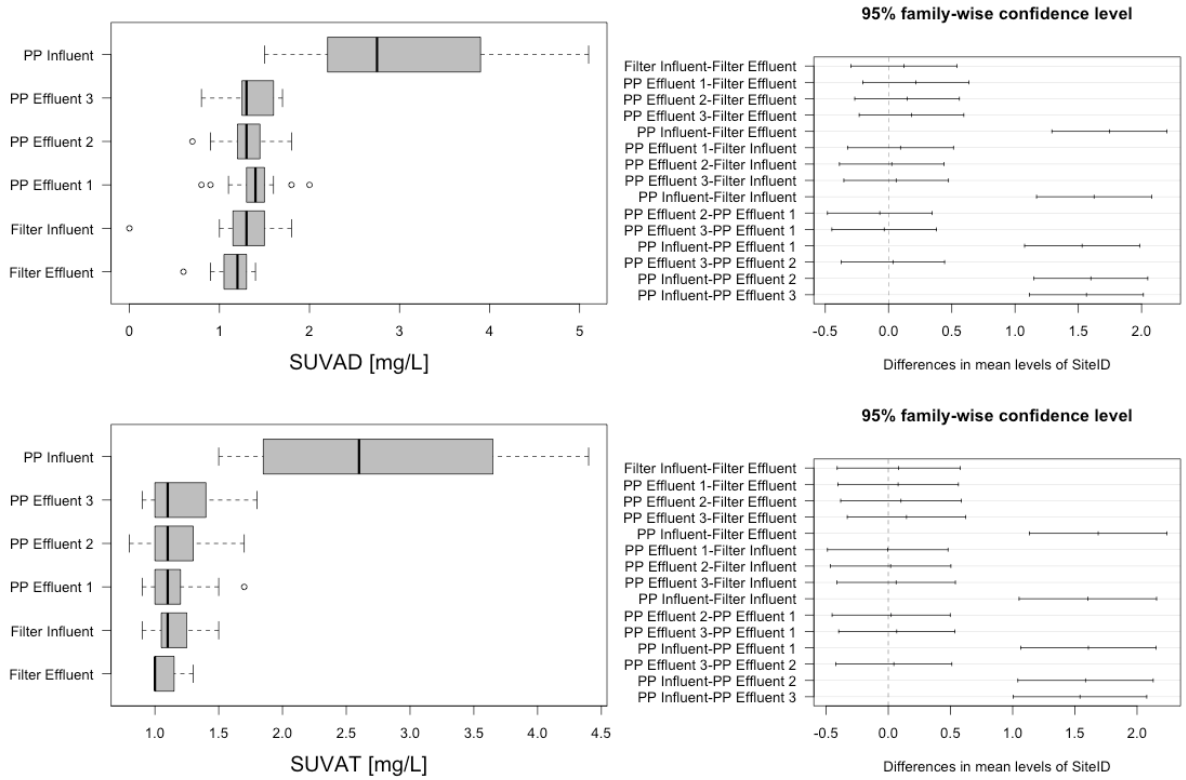

Figure 15. Boxplot and 95% confidence interval of NOM removal to compare the full-scale plant and pilot plant.

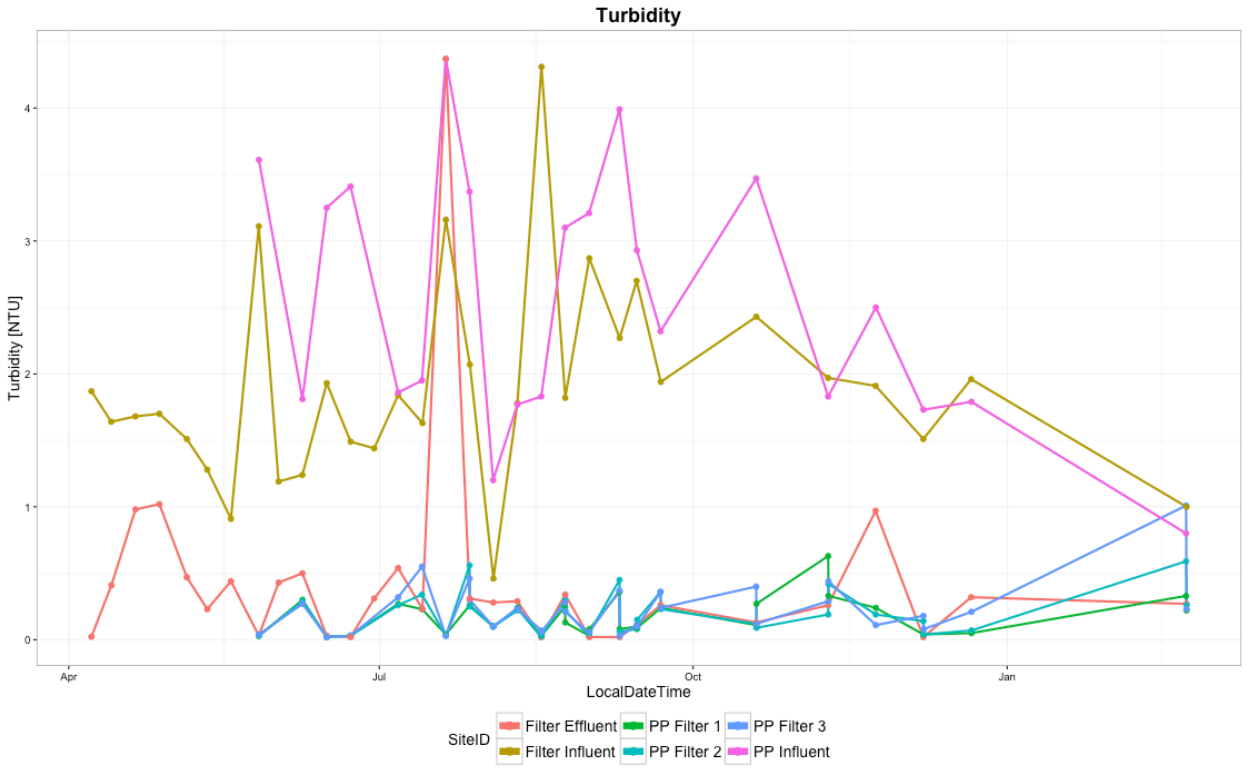

Figure 16. Time series plot turbidity to compare the full-scale plant and pilot plant.

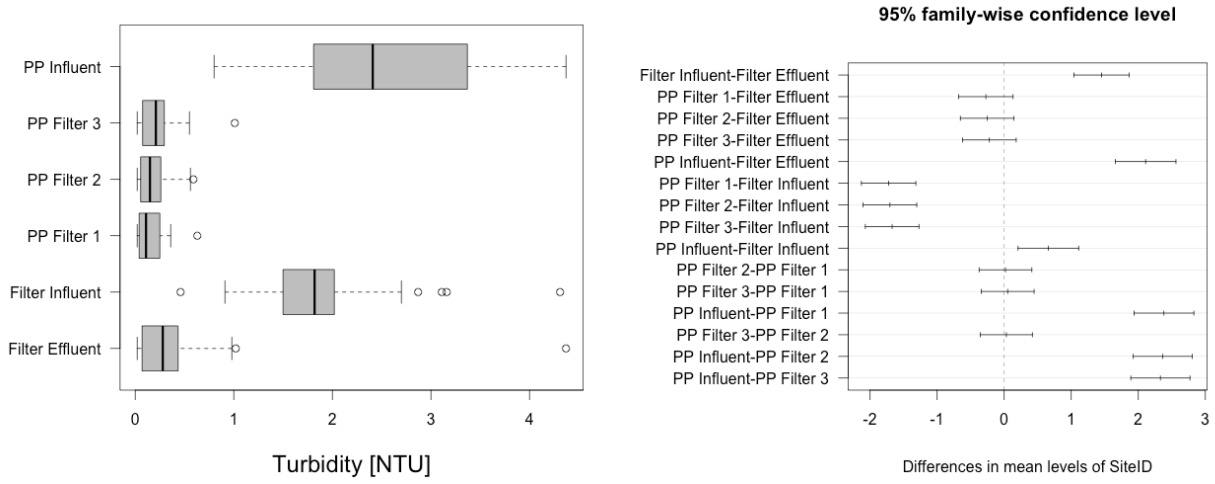

Figure 17. Boxplot and 95% confidence interval of turbidity to compare the full-scale plant and pilot plant.

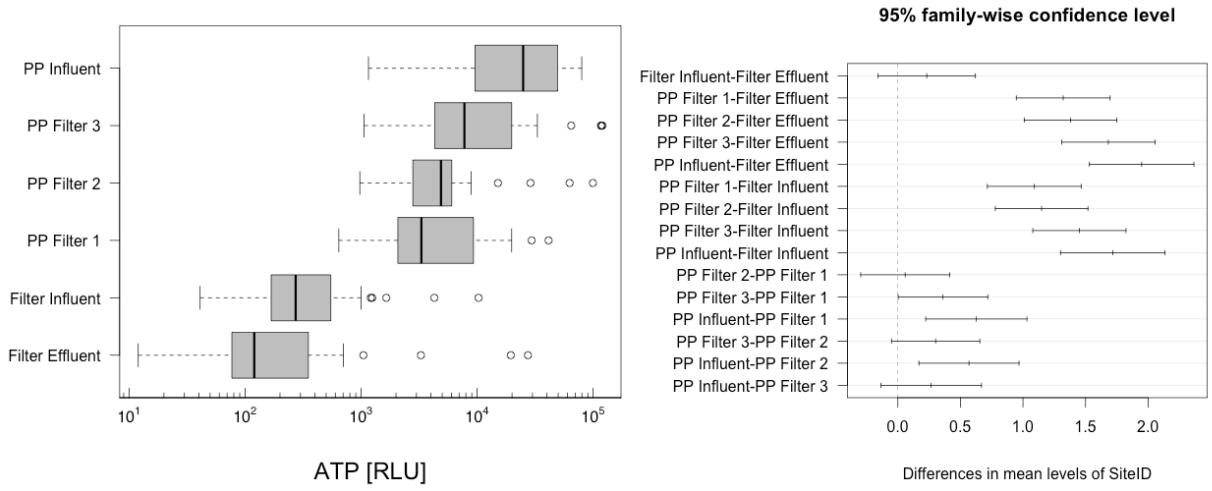

Figure 18 Boxplot and 95% confidence interval of ATP in water (on a log scale) to compare full-scale and pilot plant.

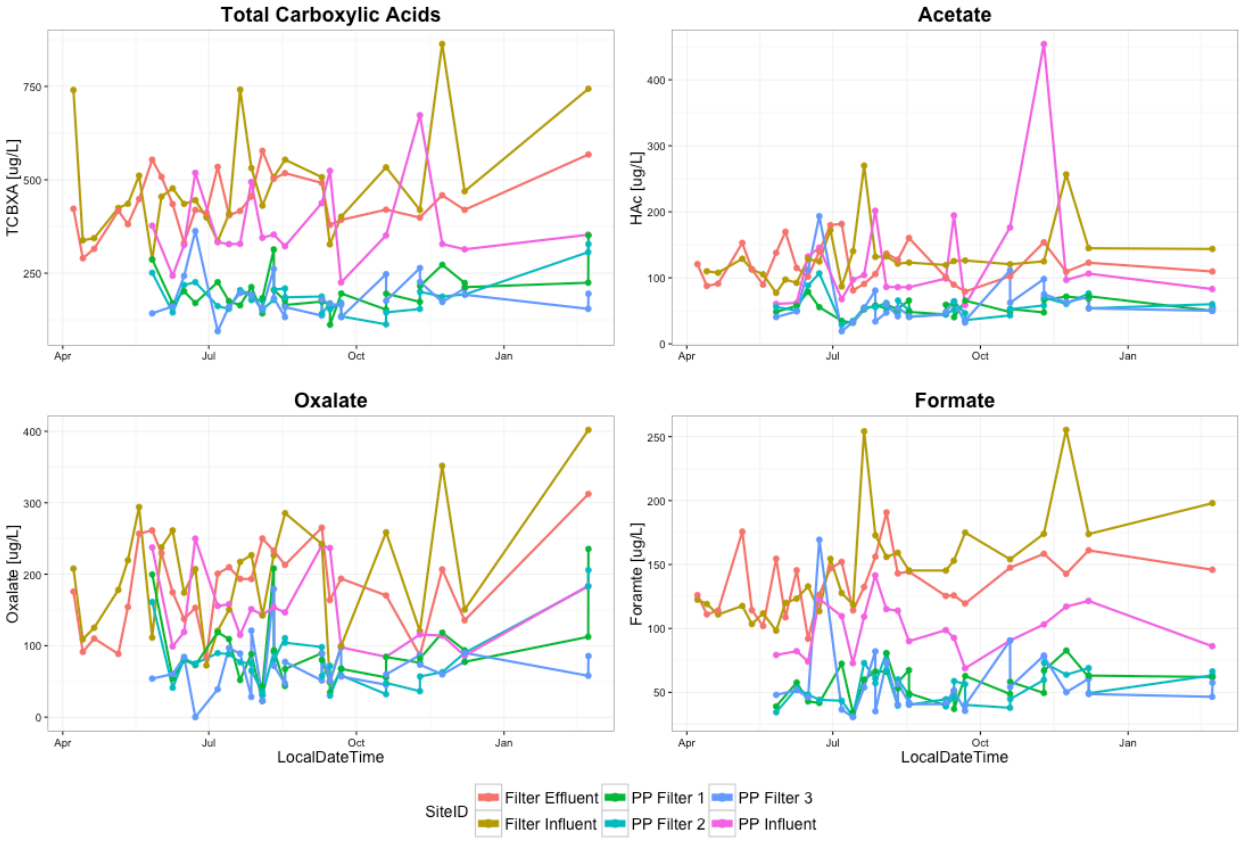

Figure 19 Time series plot of Carboxylic Acid removal to compare the full-scale plant (Filter Influent/Effluent) and pilot plant (PP Influent/Effluent).

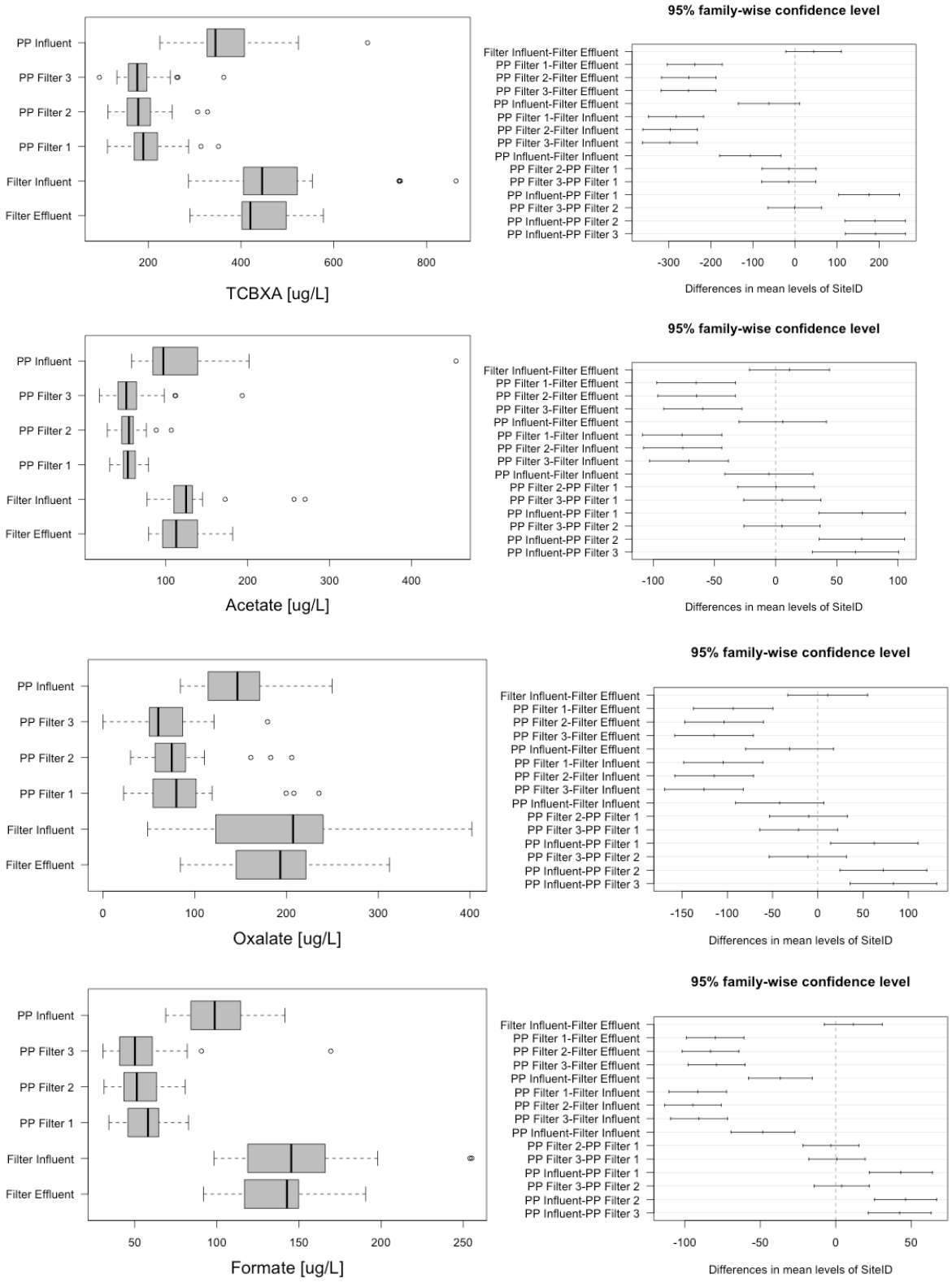

Figure 20 Boxplot and 95% confidence interval of Carboxylic Acids to compare the full-scale plant and pilot plant.

Summary and Conclusions

A pilot water treatment system at the Central Utah Water Conservancy District's Duchesne Water Treatment Plant consisting of three parallel units was operated for 12 months in a manner that promotes biological development in the filters. This was done by simple operational changes limiting the application of chlorine at intermediate process stages in all units and by adding nutrients (nitrogen and phosphorus) in the third unit. In units 1, 2, and 3, prechlorination was suspended, in units 2 and 3 chlorination of the backwash water was suspended and in unit 3 nutrients were added to promote biological activity. Observations were made weekly from April 2015-March 2016 for a variety of water quality measures, including routine operational measures (turbidity, pH, dissolved oxygen, specific conductance, others), measures of organic matter (total organic carbon, UV absorbance, carboxylic acids), and a measure of biological activity (adenosine triphosphate, or ATP). The systems were sampled at the pilot plant filter influent and effluent, the full scale plant filter influent and effluent, and at a number of locations in the water distribution system. Additional samples for ATP were obtained from the filter media, where microorganisms tend to congregate.

Comparisons of the influent and effluent concentrations of the pilot plant was made to determine the impact of biofiltration on water quality. It was found that NOM removal and turbidity were drastically decreased across all 3 filters. A comparison between each filter was also made to determine the impact of nutrient addition and chlorinated backwash. There was no statistical difference between filters for NOM removal or turbidity, but there was a statistical difference for ATP concentrations. Filter 3, which was the engineered biofilter, had the highest ATP concentrations and Filter 1, which had chlorinated backwash, had the lowest ATP concentrations. The pilot plant and full-scale plant was also compared. The influent concentrations for NOM removal and turbidity of the pilot and full-scale plant were dissimilar, but effluent concentrations were similar.

This study demonstrated that the pilot scale biofilters effectively reduced the amount of organic matter measured both as UV254 (~60% removal) and carboxylic acids (~50% removal) from pilot filter influent to effluent in all three biofiltration modes. There was not difference in treatment performance between the three biofiltration alternatives, though there were small differences in the ATP content of the filter media. The removal of organic matter in the full scale plant operated in conventional mode was negligible.

This project represents a first step toward making biofiltration a viable option in Utah Water Treatment Plants. Elimination of prechlorination appears to promote the development of a robust biological fauna in the filter media with no apparent impact of conventional filter performance (as measured by effluent turbidity). This may be beneficial for several reasons: 1) chlorine is expensive and can be hazardous to store at a water treatment plant, 2) chlorine production produces significant amounts of air and water pollution, imposing public health costs borne by the public, 3) the use of chlorine on raw water may lead to the lysing of cells from reservoir and some river sources that contain cyanobacteria, releasing cyanotoxins to the water that are soluble and difficult to remove by conventional treatment.

References

Ahmad, R., Amirtharajah, A., Al-Shawwa, A. and Huck, P. M. 1998a. Effects of Backwashing on Biological Filters. *J. AWWA*. **90**(12): 62.

Ahmad, R. and Amirtharajah, A. 1998b. Detachment of Particles during Biofilter Backwashing. *J. AWWA*. **90**(12):74.

Alonso, C., Suidan, M. T., Kim, B. R. and Kim, B. J. 1998. Dynamic Mathematical Model for the Biodegradation of VOCs in a Biofilter: Biomass Accumulation Study. *Env. Sci. Tech.*. **32**(20): 3118 (1998).

APHA, AWWA, and WEF. 2011. Standard Methods Online [Online]. Available: <http://www.standardmethods.org/>. [cited August 1 2011].

APHA, AWWA, and WEF. 2014. Standard Methods Online [Online]. Available: <http://www.standardmethods.org/%3E. [cited August 1 2014].

AWWA Research and Technical Practice Committee on Organic Contaminants. 1981. An Assessment of Microbial Activity of GAC. *J. AWWA*. **73**(8):447.

Bablon, G. P., Ventresque, C. and Ben Aim, R. 1988. Developing a Sand-GAC Filter to Achieve High Rate Biological Filtration. *J. AWWA*. 80(12):47.

Berthouex, P. Mac and L.C. Brown, 2002. Statistics for Environmental Engineers. CRC Press, Boca Raton.

Crittenden, J. C., Trussell, R. R., Hand, D. W. Howe, K. J., Tchobanoglous G. (2012). *Water Treatment Principles and Design* (3rd ed.) John Wiley & Sons, Inc., Hoboken, NJ.

Boe-Hansen, R., H. Albrechtsen, E. Arvin, C. Jorgensen. 2002. Bulk water phase and biofilm growth in drinking water at low nutrients conditions. *Water Research*. **36**:447-4486.

Chaudhary, D.S., S. Vigneswaran, H.H. Ngo, W.G. Shim, and H. Moon. 2003. Biofilter in Water and Wastewater Treatment. *Korean J. Chem. Eng.,* **20**(6): 1054-1065)

Dionex. 2001. Application Note 141: Determination of Inorganic Cations and Ammonium in Environmental Waters by Ion Chromatography Using the Ionpac Cs16 Column [Online]. Available: <http://www.dionex.com/en-us/webdocs/4211-AN141_LPN1404-R2.pdf%3E. [cited August 1 2014].

Dionex. 2003. Application Note 154: Determination of Inorganic Anions in Environmental Waters Using a Hydroxide-Selective Column [Online]. Available: <http://www.dionex.com/en-us/webdocs/4117-AN154_V19_releasedJC052703.pdf%3E. [cited August 1 2014].

McNeill, L.S., M. Friedman, M. deHaan, J.E. McLean, D.L. Sorensen, A. Hill, D.K. Stevens and others. 2015. Metals Accumulation And Release Within The Distribution System: Evaluation Of Mechanisms And Mitigation - Park City, Ut. Draft Final Report to the Water Research Foundation. 6666 West Quincy Avenue, Denver, CO 80235.

O'Dell, J.W. 1984. The Determination of Inorganic Anions in Water by Ion Chromatography -- Method 300.0. Cincinnati, OH: USEPA Environmental Monitoring and Support Laboratory.

Pharand, L., M.I. Van Dyke, W.B. Anderson, P.M. Huck. 2014. Assessment of biomass in drinking water biofilters by adenosine triphosphate. *J. AWWA.* **106**(10):433-444.

R Core Team. 2016. R: A Language and Environment for Statistical Computing. [Online]. Available: <http://www.R-project.org/%3E. [cited April 1 2016].

Uhl, W. 2008. Biofiltration Processes for Organic Matter Removal. In: Biotechnology Set, 2nd Edition, H.J. Rehm, G. Reed, ed., Chapter 22. 457-478. DOI: 10.1002/9783527620999.ch22n.

USEPA. 2011. USEPA SW-846 [Online]. Available: <http://www.epa.gov/osw/hazard/testmethods/sw846/>. [cited July 27, 2011].

Appendix

Table A1. Comparison of NOM removal from influent to effluent.

Variable	Sites Compared	p-value	Statistical Diff.
TOC [mg/L]	PP Effluent 2-PP Effluent 1	0.203	No
	PP Effluent 3-PP Effluent 1	0.998	No
	PP Influent-PP Effluent 1	0.000	Yes
	PP Effluent 3-PP Effluent 2	0.266	No
	PP Influent-PP Effluent 2	0.000	Yes
	PP Influent-PP Effluent 3	0.000	Yes
UV254 [1/cm]	PP Effluent 2-PP Effluent 1	0.946	No
	PP Effluent 3-PP Effluent 1	1.000	No
	PP Influent-PP Effluent 1	0.000	Yes
	PP Effluent 3-PP Effluent 2	0.965	No
	PP Influent-PP Effluent 2	0.000	Yes
	PP Influent-PP Effluent 3	0.000	Yes
SUVA-D [mg/L]	PP Effluent 2-PP Effluent 1	0.973	No
	PP Effluent 3-PP Effluent 1	0.997	No
	PP Influent-PP Effluent 1	0.000	Yes
	PP Effluent 3-PP Effluent 2	0.996	No
	PP Influent-PP Effluent 2	0.000	Yes
	PP Influent-PP Effluent 3	0.000	Yes
SUVA-T [mg/L]	PP Effluent 2-PP Effluent 1	1.000	No
	PP Effluent 3-PP Effluent 1	0.999	No
	PP Influent-PP Effluent 1	0.000	Yes
	PP Effluent 3-PP Effluent 2	0.999	No
	PP Influent-PP Effluent 2	0.000	Yes
	PP Influent-PP Effluent 3	0.000	Yes

Table A2. Comparison of Carboxylic Acid removal from influent to effluent.

Variable	Sites Compared	p-value	Statistical Diff.
TCBXA [ug/L]	PP Effluent 2-PP Effluent 1	0.888	No
	PP Effluent 3-PP Effluent 1	0.974	No
	PP Influent-PP Effluent 1	0.000	Yes
	PP Effluent 3-PP Effluent 2	0.991	No
	PP Influent-PP Effluent 2	0.000	Yes
	PP Influent-PP Effluent 3	0.000	Yes
Acetate [ug/L]	PP Effluent 2-PP Effluent 1	1.000	No
	PP Effluent 3-PP Effluent 1	0.924	No
	PP Influent-PP Effluent 1	0.000	Yes
	PP Effluent 3-PP Effluent 2	0.934	No
	PP Influent-PP Effluent 2	0.000	Yes
	PP Influent-PP Effluent 3	0.000	Yes
Oxalate [ug/L]	PP Effluent 2-PP Effluent 1	0.896	No
	PP Effluent 3-PP Effluent 1	0.630	No
	PP Influent-PP Effluent 1	0.000	Yes
	PP Effluent 3-PP Effluent 2	0.955	No
	PP Influent-PP Effluent 2	0.000	Yes
	PP Influent-PP Effluent 3	0.000	Yes
Formate [ug/L]	PP Effluent 2-PP Effluent 1	0.931	No
	PP Effluent 3-PP Effluent 1	0.978	No
	PP Influent-PP Effluent 1	0.000	Yes
	PP Effluent 3-PP Effluent 2	0.737	No
	PP Influent-PP Effluent 2	0.000	Yes
	PP Influent-PP Effluent 3	0.000	Yes

Table A3. Comparison of final turbidity from influent to effluent and of turbidity removal.

Variable	Sites Compared	p-value	Statistical Diff.
Turbidity [NTU]	PP Effluent 2-PP Effluent 1	0.995	No
	PP Effluent 3-PP Effluent 1	0.978	No
	PP Influent-PP Effluent 1	0.000	Yes
	PP Effluent 3-PP Effluent 2	0.998	No
	PP Influent-PP Effluent 2	0.000	Yes
	PP Influent-PP Effluent 3	0.000	Yes
Turbidity Removal [NTU]	PP Filter 2-PP Filter 1	0.997	No
	PP Filter 3-PP Filter 1	0.988	No
	PP Filter 3-PP Filter 2	0.997	No

Table A4. Comparison of ATP concentrations from influent to effluent in both units of RLU and pg ATP/mL.

Variable	Sites Compared	p-value	Statistical Diff.
ATP [RLU]	PP Effluent 2-PP Effluent 1	0.954	No
	PP Effluent 3-PP Effluent 1	0.019	Yes
	PP Influent-PP Effluent 1	7.23E-05	Yes
	PP Effluent 3-PP Effluent 2	0.066	No
	PP Influent-PP Effluent 2	3.31E-04	Yes
	PP Influent-PP Effluent 3	0.201	No
ATP [pg ATP/mL]	PP Effluent 2-PP Effluent 1	0.958	No
	PP Effluent 3-PP Effluent 1	0.015	Yes
	PP Influent-PP Effluent 1	2.20E-05	Yes
	PP Effluent 3-PP Effluent 2	0.051	No
	PP Influent-PP Effluent 2	1.00E-04	Yes
	PP Influent-PP Effluent 3	0.129	No

Table A5. Comparison of NOM removal by each individual filter.

Variable	Sites Compared	p-value	Statistical Diff.
TOC [mg/L]	PP Effluent 2-PP Effluent 1	0.078	No
	PP Effluent 3-PP Effluent 1	0.977	No
	PP Effluent 3-PP Effluent 2	0.112	No
UV254 [1/cm]	PP Effluent 2-PP Effluent 1	0.519	No
	PP Effluent 3-PP Effluent 1	0.984	No
	PP Effluent 3-PP Effluent 2	0.617	No
SUVA-D [mg/L]	PP Effluent 2-PP Effluent 1	0.685	No
	PP Effluent 3-PP Effluent 1	0.911	No
	PP Effluent 3-PP Effluent 2	0.905	No
SUVA-T [mg/L]	PP Effluent 2-PP Effluent 1	1.000	No
	PP Effluent 3-PP Effluent 1	0.978	No
	PP Effluent 3-PP Effluent 2	0.972	No

Table A6. Comparison of Carboxylic Acid removal by each individual filter.

Variable	Sites Compared	p-value	Statistical Diff.
TCBXA [ug/L]	PP Effluent 2-PP Effluent 1	0.647	No
	PP Effluent 3-PP Effluent 1	0.860	No
	PP Effluent 3-PP Effluent 2	0.929	No
Acetate [ug/L]	PP Effluent 2-PP Effluent 1	0.998	No
	PP Effluent 3-PP Effluent 1	0.724	No
	PP Effluent 3-PP Effluent 2	0.747	No
Oxalate [ug/L]	PP Effluent 2-PP Effluent 1	0.726	No
	PP Effluent 3-PP Effluent 1	0.396	No
	PP Effluent 3-PP Effluent 2	0.839	No
Formate [ug/L]	PP Effluent 2-PP Effluent 1	0.817	No
	PP Effluent 3-PP Effluent 1	0.913	No
	PP Effluent 3-PP Effluent 2	0.561	No

Table A7. Comparison of ATP concentrations on the media of each filter in units of RLU and pg ATP/mL.

Variable	Sites Compared	p-value	Statistical Diff.
ATP [log(RLU)]	PP Media 2-PP Media 1	2.10E-06	Yes
	PP Media 3-PP Media 1	0.00E+00	Yes
	PP Media 3-PP Media 2	0.004	Yes
ATPpg [log(pg/mL)]	PP Media 2-PP Media 1	0.710	No
	PP Media 3-PP Media 1	0.534	No
	PP Media 3-PP Media 2	0.952	No

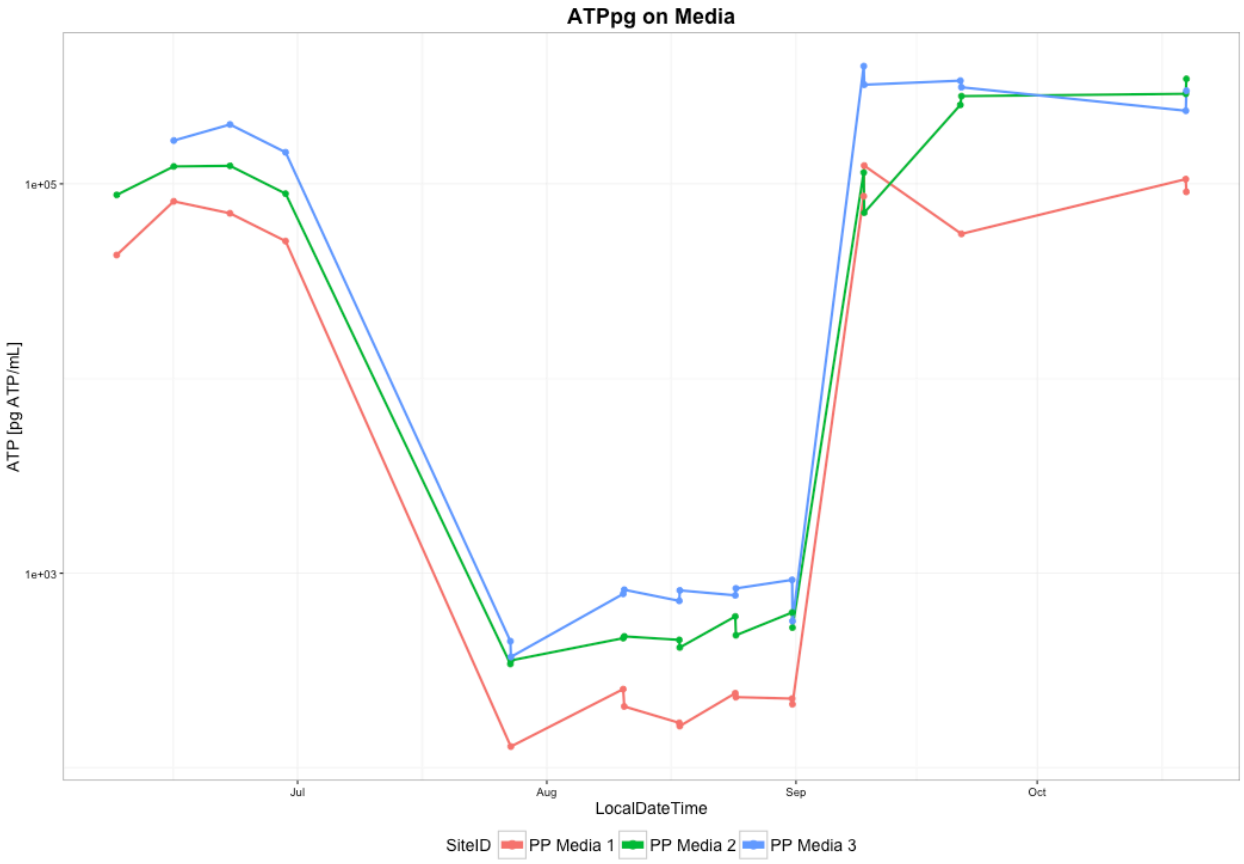

Figure A21. Time series plot of ATP concentrations on the media of each filter in units of pg ATP/mL (plotted on a log scale).

Information Transfer Program Introduction

The individual research projects documented in the Research Project section of this report have information and outreach components integrated within them. These include research findings published in the technical literature and findings and water management models and tools provided on the web pages of the Utah Center for Water Resources Research (UCWRR) and individual water agencies. Beyond this, Information Transfer and Outreach activities through the UCWRR, the Utah Water Research Laboratory (UWRL), and Utah State University (USU) have had an impact on the technical and economic development of the State of Utah. As part of the UCWRR outreach activities supported by USGS 104 funds, there continues to be a vigorous dialogue and experimentation with regard to the efficiency and effectiveness of outreach activities of the UCWRR. Faculty are engaged in regular meetings with State of Utah water resources agencies, including the Department of Environmental Quality (DEQ), the Department of Natural Resources (DNR), the State Engineer's Office, and numerous municipal water supply and irrigation companies to provide assistance in source water protection, on-site training, non-point source pollution management, technology transfer, development of source water protection plans (SWPPs), and efficient management of large water systems within the context of water-related issues in Utah. UCWRR staff, through the facilities at the UWRL, provides short courses both on- and off-site within the State of Utah, regionally, and internationally. Generally offered from one to five days in duration, short courses are tailored to meet the needs of the requestor. The following is a partial list of information transfer and outreach activities, short courses, and field trainings that involve UCWRR staff.

Principal Outreach Publications

Principal outreach items include our two newsletters and other reports:

1. “The Water bLog” (http://uwrl.usu.edu/partnerships/ucwrr_newsletter), which highlights research projects and their findings,
2. “The Utah WaTCH” (http://uwrl.usu.edu/onsite_utahwatchnewsletter), which addresses on-site and wastewater issues; and
3. The Mineral Lease Report (http://uwrl.usu.edu/media/uwrl_reports) submitted to the Utah Office of the Legislative Fiscal Analyst.

Additional publications from the UCWRR and UWRL appear regularly as technically-reviewed project reports, professional journal articles, other publications and presentations, theses and dissertation papers presented at conferences and meetings, and project completion reports to other funding agencies.

Short Courses

None of the short-courses conducted were related to USGS funded projects in FY 15.

Information Transfer in Support of the Utah Center for Water Resources Research (UCWRR)

Basic Information

Title:	Information Transfer in Support of the Utah Center for Water Resources Research (UCWRR)
Project Number:	2015UT198B
Start Date:	3/1/2015
End Date:	2/29/2016
Funding Source:	104B
Congressional District:	01
Research Category:	Not Applicable
Focus Category:	Education, None, None
Descriptors:	None
Principal Investigators:	R. Ivonne Harris, Carri Lyn Richards

Publications

1. UCWRR, July 2015, The Water bLog, newsletter from the Utah Center for Water Resources Research, Vol. 6, No. 1, http://uwrl.usu.edu/sites/default/files/pdf/waterblog_july2015.pdf
2. UCWRR, Dec. 2015, The Water bLog, newsletter from the Utah Center for Water Resources Research, Vol. 6, No. 2, http://uwrl.usu.edu/sites/default/files/waterblog/waterblog_december2015.pdf

Information Transfer in Support of the Utah Center for Water Resources Research (UCWRR)

(2015UT198B)
R. Ivonne Harris

Problem

The Water Resources Research Act of 1964 established the Utah Center for Water Resources Research (UCWRR). The Center is housed at Utah State University in Logan, Utah. The general purposes of the UCWRR are to foster interdepartmental research and educational programs in water resources; administer the State Water Research Institute Program funded through the U.S. Geological Survey at Utah State University for the State of Utah; and provide university-wide coordination of water resources research.

Objectives

The center plays a vital role in the dissemination of information. Utah is home to approximately 50,000 miles of rivers and streams and 7,800 lakes. This water is an essential resource for the economic, social, and cultural well-being of the State of Utah. As one of 54 water research centers, the UCWRR works to "*make sure that tomorrow has enough clean water*."

A major component of the information transfer and outreach requirements of the UCWRR is the development of appropriate vehicles for dissemination of information produced by research projects conducted at the Center. This project provides on-going updates of the UCWRR web page, with information transfer specifically identified as the key objective. This project is in the process of disseminating semi-annual newsletters for the Utah Center that feature research projects and their findings, water-related activities in the state, and on-going work by researchers affiliated with the Center.

Methods

Web Pages

A vital objective in the dissemination of information for the UCWRR was the development of an up-to-date web page. The UCWRR web pages have been developed to make information available, thus creating a tool wherein interested parties can find solutions to water problems. The design of the web pages is developed with Adobe "Dreamweaver" software and CSS. Pictures are taken from the various on-going projects and added to the web pages. The address for the UCWRR is http://uwrl.usu.edu/partnerships/ucwrr/. Figures 1 and 2 are pictures of two of the pages. The web pages are works-in-progress and the pages are periodically updated.

1. The "Homepage" explains the Center's purpose.

2. The "About Us" gives an overview of the center and its affiliations.

3. The “People” page gives an overview of the governing body of the center as well as key contact staff.

4. The “Research and Publications” page guides readers to the various projects and reports. This page is updated periodically.

5. “The Water bLog” page provides access to current and past issues of the Center’s newsletter (described in the next section).

6. The “Contact” page has the center’s address and mode of contact.

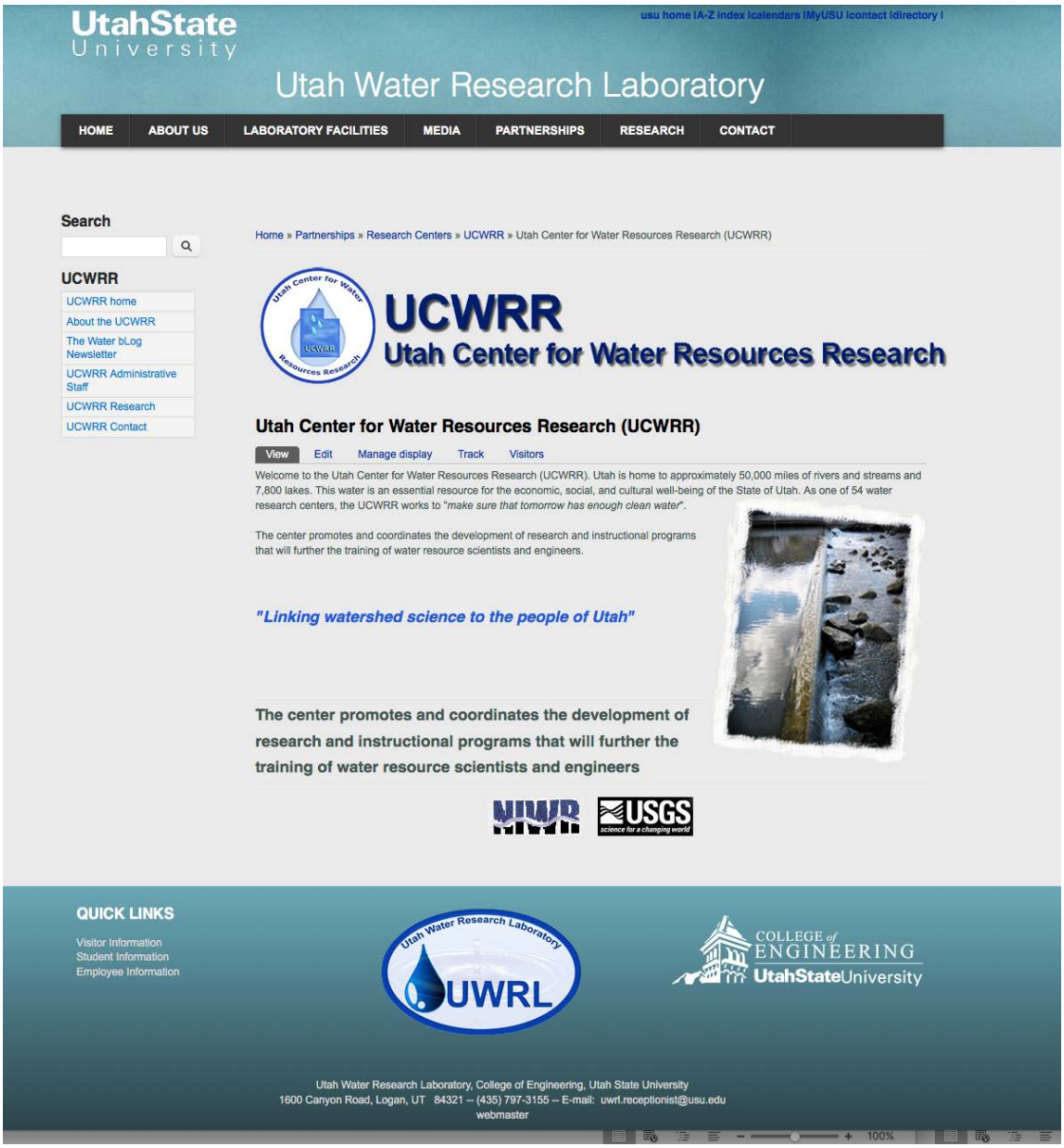

Figure 1. Home page for the UCWRR.

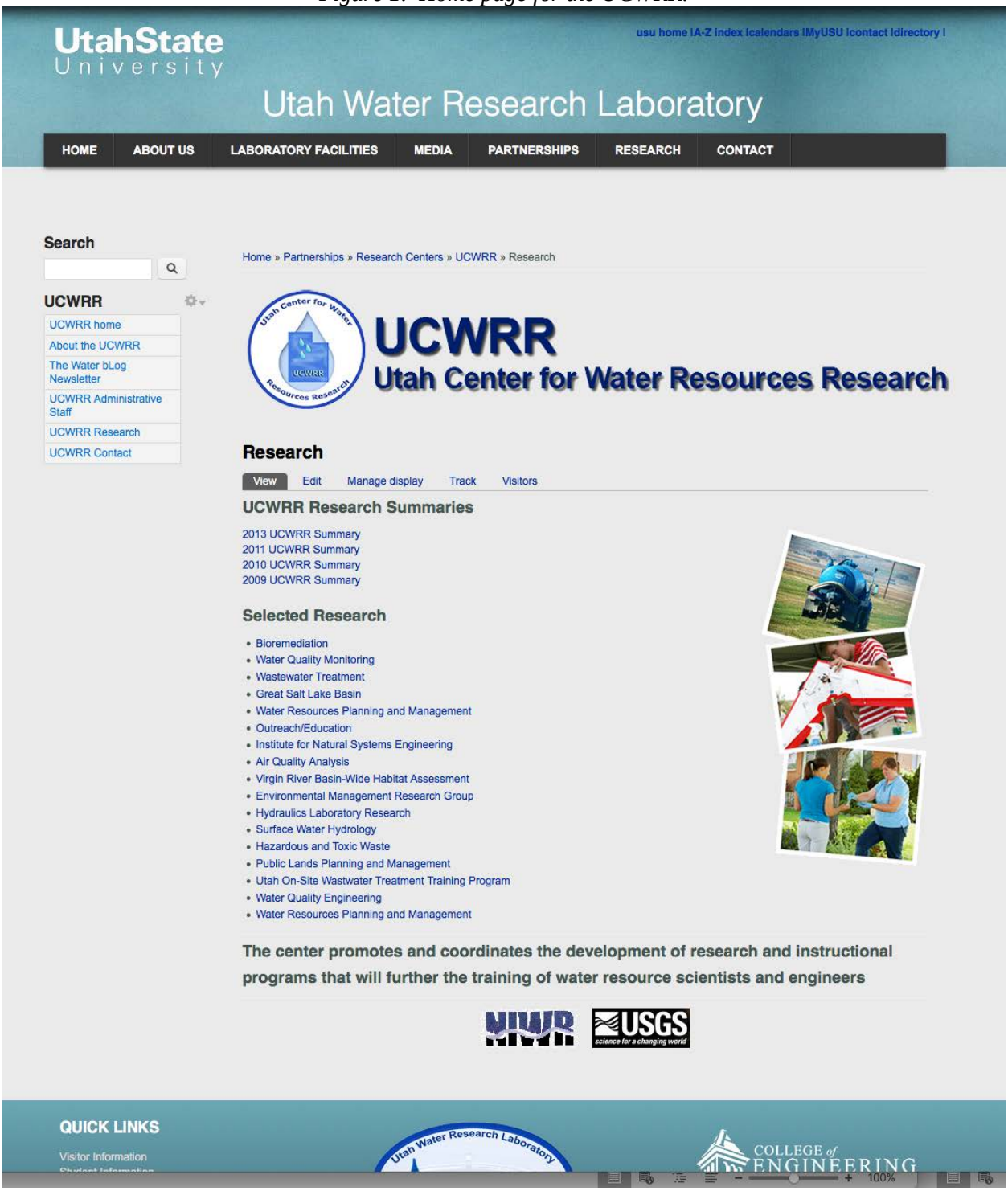

Figure 2. Research and Publications page for the UCWRR.

Newsletter

A semi-annual newsletter *The Water bLog* continues to be published. *The Water bLog* is disseminated electronically at the UCWRR web site at

http://uwrl.usu.edu/partnerships/ucwrr/ucwrrnewsletter

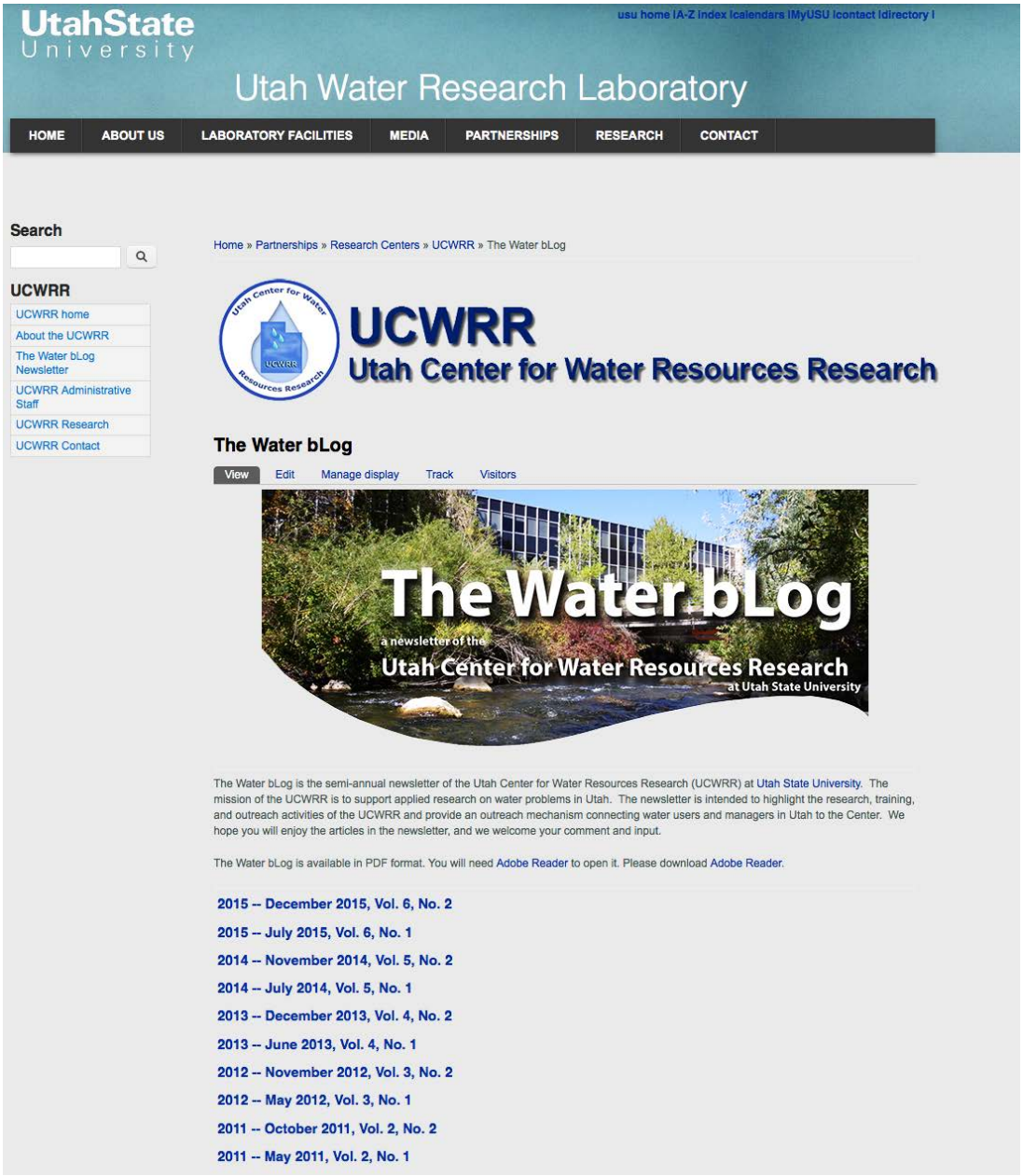

Figure 3: The Water bLog Newsletter home page.

It is also disseminated through e-mail. The newsletter is e-mailed to approximately 350 readers. The main purpose of the newsletter is to highlight research projects and their findings. These will be of great interest and value to the State of Utah, as well as nationally and internationally.

A recent copy of the newsletter was sent out December 2015 and a new one will go out in June 2016. One of the research projects featured in the December 2015 newsletter was "**Virgin River Fish Barrier Modification Model**." UCWRR researchers designed and implemented physical and numerical models to develop a modification to the Virgin River fish barrier that would prevent non-native red shiner from migrating upstream during flood conditions.

Red shiner is a non-native fish species in Utah's Virgin River that often out-competes desirable native fish species for food and habitat. Incremental chemical treatments starting in 1984 have proven to be successful in eradicating red shiner in specific reaches of the river. Structures such as the Virgin River Gorge fish barrier constructed in 2009 about 20 miles southwest of Saint George, Utah, protect native species by preventing red shiner from migrating further upstream. This barrier was effective until September 2014 when a major storm event elevated the river flow rates beyond the fish barrier's ability to function as it was originally designed. After the flood event, red shiner were again found in significant numbers upstream of the barrier.

UCWRR researchers at the Utah Water Research Laboratory were commissioned to implement physical and numerical model studies of the Virgin River Gorge fish barrier. Protecting native fish species from invasive red shiners is a long-term goal of the Washington County Water Conservancy District. This research helps facilitate that goal.

The Current Virgin River Gorge Fish Barrier

Physical and numerical model at the Utah Water Research Laboratory test the effectiveness of structural modifications to the Virgin River Gorge Fish Barrier

Utah State University (USU) and the Utah Water Research Laboratory (UWRL) celebrated 2015 as the **Year of Water**. The year 2015 was also the 50th anniversary of the dedication of the UWRL, home of the Utah Center for Water Resources Research (UCWRR). Students and faculty were busy this past fall presenting research and welcoming visitors to the facility through Open Houses, Alumni Get-Together and other events.

Visitors to the Open House and Alumni Get-Together

For an electronic copy of current or past newsletters, please go to:

http://uwrl.usu.edu/partnerships/ucwrr/newsletter/

December 2015, Vol. 6, No. 2

The Water bLog

a newsletter of the

Utah Center for Water Resources Research

at Utah State University

Welcome!

The Water bLog is the semi-annual newsletter of the Utah Center for Water Resources Research (UCWRR), housed at the Utah Water Research Laboratory. The Center supports the development of applied research related to water resources problems in Utah and promotes instructional programs that will further the training of water resource scientists and engineers. Each issue of The Water bLog reports on a small selection of the current or recently completed research projects conducted at the center. More information is available online at:

http://uwrl.usu.edu/partnerships/ucwrr

Message from the Director

Mac McKee, Director

For more than 50 years, the UCWRR has been conducting water-related research and finding practical solutions to water resources problems in Utah and beyond.

As we wrap up the 2015 'Year of Water' celebrations with Utah State University and the Utah Water Research Laboratory, we are delighted with the positive feedback we have received for this focus on water in all its forms and functions.

This issue of the Water bLog highlights projects in Utah that address the challenges of both surface water and groundwater. One project engineered a solution that will extend the usefulness of a fish barrier in Utah's Virgin River that was found to be ineffective at very high river flows. The other project addressed the more urban challenge of optimizing aquifer recharge and aquifer storage and recovery to better manage variable water supplies along the Wasatch Front.

These projects represent only a tiny fraction of the active research underway at the UCWRR aimed at solving water-related natural resources problems throughout Utah, the nation, and the world. ■

INSIDE:

Research Highlights:

- Virgin River Fish Barrier Modification Model
- ASR Optimization Protocol and Decision Support

In the News

- Year of Water 2015 Celebrations

RESEARCH HIGHLIGHT

Virgin River Fish Barrier Modification Model

UCWRR researchers designed and implemented physical and numerical models to develop a modification to the Virgin River fish barrier that would prevent non-native red shiner from migrating upstream during flood conditions

Red shiner is a non-native fish species in Utah's Virgin River that often out-competes desirable native fish species for food and habitat. Incremental chemical treatments starting in 1984 have proven to be successful in eradicating red shiner in specific reaches of the river. Structures such as the Virgin River Gorge fish barrier constructed in 2009 about 20 miles southwest of Saint George, Utah, protect native species by preventing red shiner from migrating further upstream. This barrier was effective

The current Virgin River Gorge fish barrier

UtahStateUniversity

The Water bLog December 2015, Vol. 6, No. 2

Figure 4. The Water bLog, *the Newsletter for the UCWRR*

Data Base

Another concern the UCWRR has is making available electronic copies of research projects and reports. These are being converted to PDF format and have been added to a database to make them available on-line. This is a work in progress and some of the publications can be found in our website at http://uwrl.usu.edu/publications.

USGS Summer Intern Program

None.

Student Support					
Category	**Section 104 Base Grant**	**Section 104 NCGP Award**	**NIWR-USGS Internship**	**Supplemental Awards**	**Total**
Undergraduate	4	0	0	0	4
Masters	4	0	0	0	4
Ph.D.	3	0	0	0	3
Post-Doc.	0	0	0	0	0
Total	11	0	0	0	11

Notable Awards and Achievements

Dr. Bethany Neilson was awarded a travel grant in 2015 as a visiting researcher at the University of New South Wales.

Publications from Prior Years

1. 2014UT193B ("Influence of Groundwater/Surface Water Interactions in High Gradient Mountain Streams") - Articles in Refereed Scientific Journals - Majerova, M., B.T. Neilson, N.M. Schmadel, C. Snow, J. Wheaton. "Impacts of beaver dams on hydrologic and temperature regimes in a mountain stream." Hydrology and Earth System Sciences. In Preparation.
2. 2007UT87B ("Two-Zone Temperature and Solute Model Testing and Development in the Virgin River") - Articles in Refereed Scientific Journals - Schmadel, N. M., B.T. Neilson, J. Heavilin. "Spatial considerations of stream hydraulics in reach scale temperature modeling." Water Resources Research, In Preparation.
3. 2013UT189B ("Quantification of Water Quality Improvements Through the 900 S Oxbow Restoration and Stormwater BMP Renovation Project") - Other Publications - Richardson, Jake, 2015, Presentation to Jordan River Research Synthesis Workshop, Technical Memo related to the Jordan River, September 2015.
4. 2006UT69B ("Irrigation Demand Forecasting for Management of Large Water Systems") - Articles in Refereed Scientific Journals - Bachour R., I. Maslova, A.M. Ticlavilca, W.R. Walker, M. McKee. 2015. Wavelet-Multivariate Relevance Vector Machine Hybrid Model for Forecasting Daily Evapotranspiration. Stochastic Environmental Research and Risk Assessment, DOI 10.1007/s00477-015-1039-z.
5. 2006UT69B ("Irrigation Demand Forecasting for Management of Large Water Systems") - Articles in Refereed Scientific Journals - Hassan-Esfahani, L., A. Torres-Rua, A. Jensen, and M. McKee. 2015. Assessment of Surface Soil Moisture Using High-Resolution Multi-Spectral Imagery and Artificial Neural Networks. Remote Sensing, 2015, 7, 2627-2646; doi:10.3390/rs70302627.
6. 2006UT69B ("Irrigation Demand Forecasting for Management of Large Water Systems") - Articles in Refereed Scientific Journals - Hassan-Esfahani, Leila; Alfonso Torres-Rua; and Mac McKee, 2015, Assessment of optimal irrigation water allocation for pressurized irrigation system using water balance approach, learning machines, and remotely sensed data, Agricultural Water Management, 153(2015):42-50.
7. 2006UT69B ("Irrigation Demand Forecasting for Management of Large Water Systems") - Articles in Refereed Scientific Journals - Elarab, Manal; Andres Ticlavilca; Alfonso Torres-Rua; Inga Maslova; and Mac McKee, 2015, Estimating chlorophyll with thermal and broadband multispectral high resolution imagery from an unmanned aerial system using relevance vector machines for precision agriculture, International Journal of Applied Earth Observation and Geoinformation. http://dx.doi.org/10.1016/j.jag.2015.03.017.
8. 2006UT ("Irrigation Demand Forecasting for Management in Large Water Systems") - Articles in Refereed Scientific Journals - Maslova, Inga; Andres M. Ticlavilca; and Mac McKee, 2015, Adjusting wavelet-based multiresolution analysis boundary conditions for long-term streamflow forecasting, Hydrological Processes, DOI: 10.1002/hyp.10564.